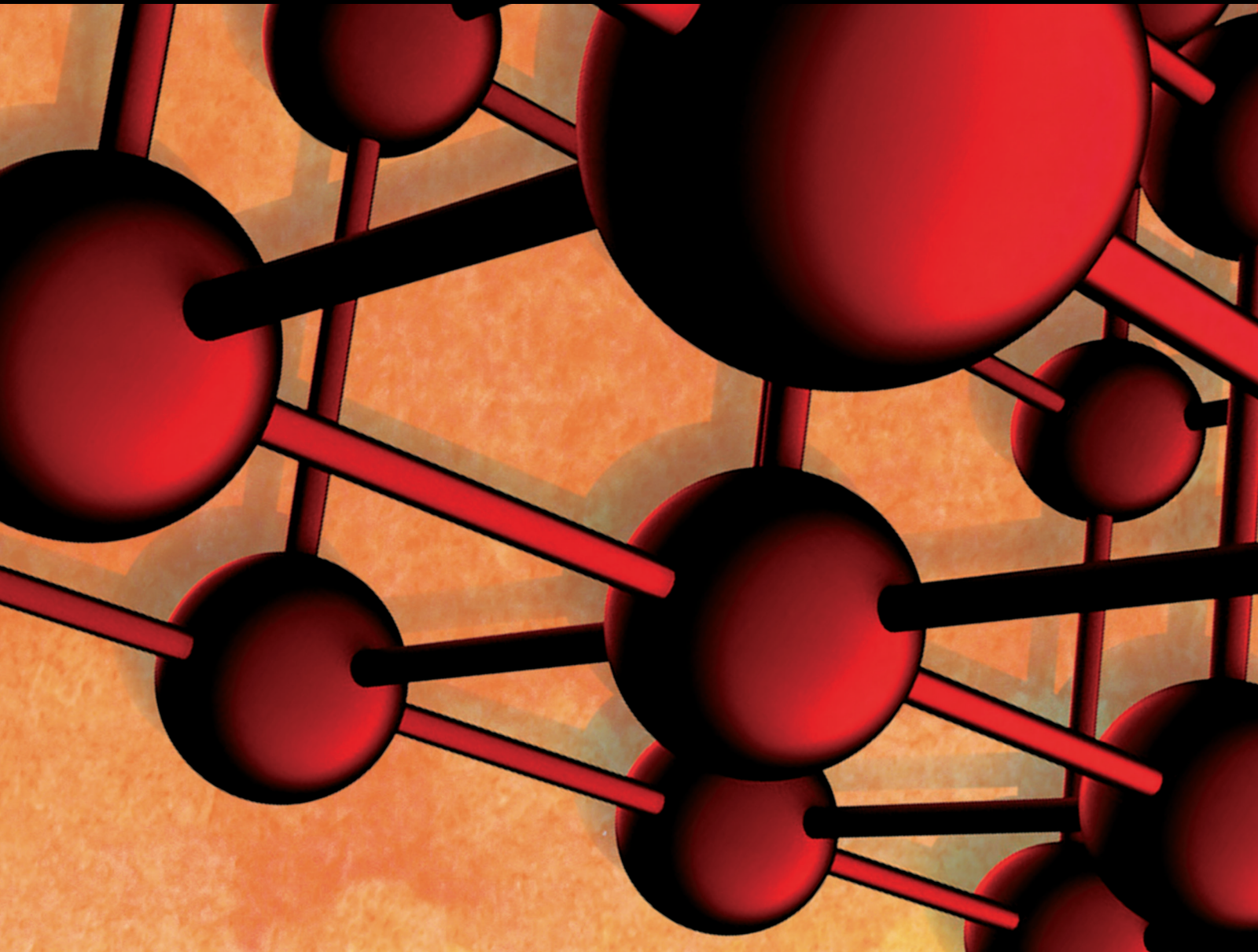


Advances in Materials Science and Engineering

Advanced Materials, Technologies and Testing for Structural Performance Improvement 2020

Lead Guest Editor: Stefano Sorace

Guest Editors: Stathis N. Bousias, Sreekanta Das, Norbert Randl, and
Gloria Terenzi





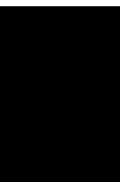
**Advanced Materials, Technologies and Testing
for Structural Performance Improvement 2020**

Advances in Materials Science and Engineering

**Advanced Materials, Technologies and
Testing for Structural Performance
Improvement 2020**

Lead Guest Editor: Stefano Sorace


Guest Editors: Stathis N. Bousias, Sreekanta Das,
Norbert Randl, and Gloria Terenzi



Copyright © 2020 Hindawi Limited. All rights reserved.

This is a special issue published in "Advances in Materials Science and Engineering." All articles are open access articles distributed under the Creative Commons Attribution License, which permits unrestricted use, distribution, and reproduction in any medium, provided the original work is properly cited.

Chief Editor
















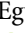

Amit Bandyopadhyay , USA

Associate Editors

Vamsi Balla , India
Mitun Das , USA
Sandip Harimkar, USA
Ravi Kumar , India
Peter Majewski , Australia
Enzo Martinelli , Italy
Luigi Nicolais , Italy
Carlos R. Rambo , Brazil
Michael J. Schütze , Germany
Kohji Tashiro , Japan
Zhonghua Yao , China
Dongdong Yuan , China
Wei Zhou , China

Academic Editors

Antonio Abate , Germany
Hany Abdo , Saudi Arabia
H.P.S. Abdul Khalil , Malaysia
Ismael Alejandro Aguayo Villarreal , Mexico
Sheraz Ahmad , Pakistan
Michael Aizenshtein, Israel
Jarir Aktaa, Germany
Bandar AlMangour, Saudi Arabia
Huaming An, China
Alicia Esther Ares , Argentina
Siva Avudaiappan , Chile
Habib Awais , Pakistan
NEERAJ KUMAR BHOI, India
Enrico Babilio , Italy
Renal Backov, France
M Bahubalendruni , India
Sudharsan Balasubramanian , India
Markus Bambach, Germany
Irene Bavasso , Italy
Stefano Bellucci , Italy
Brahim Benmokrane, Canada
Jean-Michel Bergheau , France
Guillaume Bernard-Granger, France
Giovanni Berselli, Italy
Patrice Berthod , France
Michele Bianchi , Italy
Hugo C. Biscaia , Portugal

Antonio Boccaccio, Italy
Mohamed Bououdina , Saudi Arabia
Gianlorenzo Bussetti , Italy
Antonio Caggiano , Germany
Marco Cannas , Italy
Qi Cao, China
Gianfranco Carotenuto , Italy
Paolo Andrea Carraro , Italy
Jose Cesar de Sa , Portugal
Wen-Shao Chang , United Kingdom
Qian Chen , China
Francisco Chinesta , France
Er-Yuan Chuang , Taiwan
Francesco Colangelo, Italy
María Criado , Spain
Enrique Cuan-Urquizo , Mexico
Lucas Da Silva , Portugal
Angela De Bonis , Italy
Abílio De Jesus , Portugal
José António Fonseca De Oliveira
Correia , Portugal
Ismail Demir , Turkey
Luigi Di Benedetto , Italy
Maria Laura Di Lorenzo, Italy
Marisa Di Sabatino, Norway
Luigi Di Sarno, Italy
Ana María Díez-Pascual , Spain
Guru P. Dinda , USA
Hongbiao Dong, China
Mingdong Dong , Denmark
Frederic Dumur , France
Stanislaw Dymek, Poland
Kaveh Edalati , Japan
Philip Eisenlohr , USA
Luis Evangelista , Norway
Michele Fedel , Italy
Francisco Javier Fernández Fernández , Spain
Spain
Isabel J. Ferrer , Spain
Massimo Fresta, Italy
Samia Gad , Egypt
Pasquale Gallo , Finland
Sharanabasava Ganachari, India
Santiago Garcia-Granda , Spain
Carlos Garcia-Mateo , Spain

Achraf Ghorbal , Tunisia
Georgios I. Giannopoulos , Greece
Ivan Giorgio , Italy
Andrea Grilli , Italy
Vincenzo Guarino , Italy
Daniel Guay, Canada
Jenő Gubicza , Hungary
Xuchun Gui , China
Benoit Guiffard , France
Zhixing Guo, China
Ivan Gutierrez-Urrutia , Japan
Weiwei Han , Republic of Korea
Simo-Pekka Hannula, Finland
A. M. Hassan , Egypt
Akbar Heidarzadeh, Iran
Yi Huang , United Kingdom
Joshua Ighalo, Nigeria
Saliha Ilican , Turkey
Md Mainul Islam , Australia
Ilia Ivanov , USA
Jijo James , India
Hafsa Jamshaid , Pakistan
Hom Kandel , USA
Kenji Kaneko, Japan
Rajesh Kannan A , Democratic People's
Republic of Korea
Mehran Khan , Hong Kong
Akihiko Kimura, Japan
Ling B. Kong , Singapore
Pramod Koshy, Australia
Hongchao Kou , China
Alexander Kromka, Czech Republic
Abhinay Kumar, India
Avvaru Praveen Kumar , Ethiopia
Sachin Kumar, India
Paweł Kłosowski , Poland
Wing-Fu Lai , Hong Kong
Luciano Lamberti, Italy
Fulvio Lavecchia , Italy
Laurent Lebrun , France
Joon-Hyung Lee , Republic of Korea
Cristina Leonelli, Italy
Chenggao Li , China
Rongrong Li , China
Yuanshi Li, Canada

Guang-xing Liang , China
Barbara Liguori , Italy
Jun Liu , China
Yunqi Liu, China
Rong Lu, China
Zhiping Luo , USA
Fernando Lusquiños , Spain
Himadri Majumder , India
Dimitrios E. Manolakos , Greece
Necmettin Maraşlı , Turkey
Alessandro Martucci , Italy
Roshan Mayadunne , Australia
Mamoun Medraj , Canada
Shazim A. Memon , Kazakhstan
Pratima Meshram , India
Mohsen Mhadhbi , Tunisia
Philippe Miele, France
Andrey E. Miroshnichenko, Australia
Ajay Kumar Mishra , South Africa
Hossein Moayedi , Vietnam
Dhanesh G. Mohan , United Kingdom
Sakar Mohan , India
Namdev More, USA
Tahir Muhmood , China
Faisal Mukhtar , Pakistan
Dr. Tauseef Munawar , Pakistan
Roger Narayan , USA
Saleem Nasir , Pakistan
Elango Natarajan, Malaysia
Rufino M. Navarro, Spain
Miguel Navarro-Cia , United Kingdom
Behzad Nematollahi , Australia
Peter Niemz, Switzerland
Hiroschi Noguchi, Japan
Dariusz Oleszak , Poland
Laurent Orgéas , France
Togay Ozbakkaloglu, United Kingdom
Marián Palcut , Slovakia
Davide Palumbo , Italy
Gianfranco Palumbo , Italy
Murlidhar Patel, India
Zbyšek Pavlík , Czech Republic
Alessandro Pegoretti , Italy
Gianluca Percoco , Italy
Andrea Petrella, Italy

Claudio Pettinari , Italy
Giorgio Pia , Italy
Candido Fabrizio Pirri, Italy
Marinos Pitsikalis , Greece
Alain Portavoce , France
Simon C. Potter, Canada
Ulrich Prah, Germany
Veena Ragupathi , India
Kawaljit Singh Randhawa , India
Baskaran Rangasamy , Zambia
Paulo Reis , Portugal
Hilda E. Reynel-Avila , Mexico
Yuri Ribakov , Israel
Aniello Riccio , Italy
Anna Richelli , Italy
Antonio Riveiro , Spain
Marco Rossi , Italy
Fernando Rubio-Marcos , Spain
Francesco Ruffino , Italy
Giuseppe Ruta , Italy
Sachin Salunkhe , India
P Sangeetha , India
Carlo Santulli, Italy
Fabrizio Sarasini , Italy
Senthil Kumaran Selvaraj , India
Raffaele Sepe , Italy
Aabid H Shalla, India
Poorva Sharma , China
Mercedes Solla, Spain
Tushar Sonar , Russia
Donato Sorgente , Italy
Charles C. Sorrell , Australia
Damien Soulat , France
Adolfo Speghini , Italy
Antonino Squillace , Italy
Koichi Sugimoto, Japan
Jirapornchai Suksaeree , Thailand
Baozhong Sun, China
Sam-Shajing Sun , USA
Xiaolong Sun, China
Yongding Tian , China
Hao Tong, China
Achim Trampert, Germany
Tomasz Trzepieciński , Poland
Kavimani V , India

Matjaz Valant , Slovenia
Mostafa Vamegh, Iran
Lijing Wang , Australia
Jörg M. K. Wiezorek , USA
Guosong Wu, China
Junhui Xiao , China
Guoqiang Xie , China
YASHPAL YASHPAL, India
Anil Singh Yadav , India
Yee-wen Yen, Taiwan
Hao Yi , China
Wenbin Yi, China
Tetsu Yonezawa, Japan
Hiroshi Yoshihara , Japan
Bin Yu , China
Rahadian Zainul , Indonesia
Lenka Zaji#c#kova# , Czech Republic
Zhigang Zang , China
Michele Zappalorto , Italy
Gang Zhang, Singapore
Jinghuai Zhang, China
Zengping Zhang, China
You Zhou , Japan
Robert Černý , Czech Republic

Contents

New Mortar Mixes with Chemically Depolymerized Waste PET Aggregates

Dora Foti  and Michela Lerna


Research Article (9 pages), Article ID 8424936, Volume 2020 (2020)

Influence of the Drive Plate with Different Surface Textures on the Property of Carbonyl Iron-Based Magnetorheological Fluid

He Lu , Lifeng Wang, Lili Dai, Hongxing Ding , Qiuxiang Zhang, and Xinhua Liu 


Research Article (10 pages), Article ID 8701908, Volume 2020 (2020)

Effect of Combining Fiber and Textile Reinforcement on the Flexural Behavior of UHPC Plates

Támás Mészöly , Sandra Ofner, and Norbert Randl



Research Article (8 pages), Article ID 9891619, Volume 2020 (2020)

A Study on the Wear Characteristics of Al7075 with Changes in Surface Roughness and Ti Thin Film Deposition Time

Jihye An, Sunghoon Im, Haneul Kang, Hyunji Kim, Yunyoong Yoo, Jungpil Noh, and Sunchul Huh 


Research Article (9 pages), Article ID 7934842, Volume 2020 (2020)

Study on Void Structure Reconstruction of Asphalt Mixture by X-Ray Computed Tomography and Otsu's Method

Jiantong Zhang , Jun Yang , Tiejun Liu, Rongxing Cai, and Rui Yang


Research Article (13 pages), Article ID 4546731, Volume 2020 (2020)

Optimal Design of the Sealing Structure of a Hydraulic Cylinder on the Basis of a Surrogate Model

Hong Zhang, Yu Sun , Chenchen Li, and Haoran Wang



Research Article (9 pages), Article ID 1753964, Volume 2020 (2020)

Influence of Red Mud Proportion on Circular Concrete-Filled Steel Tubular Short Columns

Wu Bin , Tan Zhuoying, Li Fan, and Wang Sun

Research Article (11 pages), Article ID 8578059, Volume 2020 (2020)

Characterization Methods for the Effect of Microbial Mineralization on the Microstructure of Hardened C₃S Paste

Yanqiang Chen , Chunxiang Qian , and Hengyi Zhou


Research Article (9 pages), Article ID 7869345, Volume 2020 (2020)

Prototype Steam Turbine for Solar Power Production

Kawira Millien 

Research Article (7 pages), Article ID 4589281, Volume 2020 (2020)

Magnetic Circuit Design and Magnetic Field Finite Element Analysis of Converging Stepped Magnetofluid Seal with Small Clearance

Xiaolong Yang , Guohong Wang, and Ruibo Zhang

Research Article (10 pages), Article ID 4201891, Volume 2020 (2020)

Research Article

New Mortar Mixes with Chemically Depolymerized Waste PET Aggregates

Dora Foti  and **Michela Lerna**

Department of Civil Engineering and Architecture, Polytechnic of Bari, Bari, Italy

Correspondence should be addressed to Dora Foti; d.foti@poliba.it

Received 28 May 2020; Revised 15 November 2020; Accepted 3 December 2020; Published 12 December 2020

Academic Editor: Norbert Randl

Copyright © 2020 Dora Foti and Michela Lerna. This is an open access article distributed under the Creative Commons Attribution License, which permits unrestricted use, distribution, and reproduction in any medium, provided the original work is properly cited.

Nanoparticles are used in innovative mortars in order to improve their engineering properties. In this paper, recycled PET (polyethylene terephthalate) nanoparticles were used as a substitute for sand in mortars. PET aggregates were obtained cutting water bottles wastes into many small sized pieces and the plastic fibres were treated through chemical depolymerization process. Mortars with different percentages of PET were tested to determine their physical and mechanical (flexural and compressive strength) properties. Specific attention is given to the heat-transfer capacity of the cement pastes investigated. The results of the mechanical tests showed a reduction of the flexural and compressive strength values when the amount of PET nanoparticles increase. The thermal conductivity tests showed that chemically depolymerized PET nanoparticles derived from plastic wastes reduced the heat conduction capacity of the mortar. Therefore, the innovative mortars here tested can be considered for thermal insulation applications in the construction field with the advantage of recycling waste PET.

1. Introduction

Polyethylene terephthalate or PET is defined as a polyester resin which results from the combination of terephthalic acid and ethylene glycol or dimethyl terephthalate and ethylene glycol [1]. Furthermore, it accounts for around (18%) of all polymers, which are produced worldwide; over 60% of its production can be used for synthetic fibres and bottles, which form approximately 30% of global PET demand [2]. It is generally used for various applications such as bottles, mouldings, fibres, and sheets due to its excellent tensile and impact strength, clarity, chemical resistance, thermal stability, and process ability. It is commonly agreed that PET, which differs from natural polymers, is a non-degradable polymer in the natural environment and becomes a pollutant when it is discarded after use. Therefore, it has been noticed that recycling the discarded PET polymer is one of the most important approaches to protect the

environment and reduce the consumption of resources at the same time [3].

Nowadays, in fact, the recycling rate of PET bottles is much lower than the sales of virgin PET production for common uses. This gap is dramatically increasing, pushing towards finding a solution to this problem and a higher recycle of PET. As a consequence, the reuse of waste PET bottles is stirring particular interest. With the aim to reduce the waste and take profit from this material in the last two decades, many authors investigated the uses of PET in concrete. This field has been investigated in several different ways, focusing on different possible utilization of this material [4].

In recent decades, with the aim of giving the conglomerate a better behavior in terms of mechanical characteristics, it was attempted to add in its mixture fibres and aggregates of various types [5, 6]. A possible application is to utilize waste PET fibres as reinforcement for concrete to

improve its tensile strength [7–12]. Concrete, as it is known, is a material with good compressive strength but low tensile strength. This reduced tensile strength is partly due to the presence of micro- and macrocracks caused by shrinkage of the concrete. These cracks, moreover, represent a factor in the aggression of steel bars in reinforced concrete elements provoking a fast oxidation of the bars and the degradation of the structure accompanied by a reduction of its tensile strength.

Some preliminary studies on the utilization of fibres obtained from PET bottles to improve the mechanical behaviour of concrete can be found in Silva et al. [13]. The good results of this experimental study pushed the research towards the utilization of this kind of fibres. However, what makes PET so important, among the plastics used as reinforcement for concrete, is its recyclability together with the great abundance of postconsumer waste in the form of bottles. The presence of fibres improves the tensile behaviour of concrete thanks to the sewing effect that they have on the cracks [14]. Their action, in fact, is more effective in the postcracking phase, preventing and reducing the propagation of cracks. Concretes with a higher ductility and a reduced shrinkage cracking are obtained. Ductility is evidenced by a large deformation associated with the fibre elongation at break.

From the point of view of recycling waste to be added in concrete the use of waste PET bottles in concretes is not as common as scrap rubbers since slitting, shredding, and retreating processes are relatively more complex and costly [15].

Mechanical recycling is a current industrial technique for the recovery of waste polymers, but another available pathway for recycling of polymers consists in the chemical processing. This type of recycling has a high potential for heterogeneous and contaminated plastic waste material if the separation is neither economical nor completely technically feasible [16, 17]. Chemical recycling routes can be roughly divided into thermochemical and catalytic conversion processes. Chemical recycling of PET can completely depolymerize it into its monomers terephthalic acid, dimethyl terephthalate, bis(hydroxyethylene) terephthalate, and ethylene glycol (EG). The depolymerization is the reverse reaction of the polymer formation route. There are different depolymerization routes such as methanolysis, glycolysis, hydrolysis, ammonolysis, aminolysis, and hydrogenation, depending on the chemical agent used for the PET chain scission. Glycolysis is the simplest and oldest method of PET depolymerization, converting the polymers into smaller molecules, which can be subsequently seen as sustainable through a closed system glycolysis process.

The plastic waste material can often be heterogeneous and contaminated so as to make the mechanical production of PET aggregates difficult. Furthermore, the separation process is not economical and in many cases not entirely technically feasible. Consequently, the chemical recycling process has a high potential in PET-waste recycling. In the chemical process, the PET bottles do not need to be purified as instead provided for the mechanical one. Chemical recycling by glycolysis is a suitable tool and this should

reduce the cost of the recycled pet base. The polymeric mortar applications thus helps to reduce costs and provides long-term disposal of PET waste, an important consideration in recycling applications.

In this paper, the authors have studied the possibility to adopt a chemical approach to depolymerize PET (DPET) in order to use it in the cement paste as a substitute for, or in addition to, sand. In particular, the effect of additive degraded PET on the properties of cement paste has been analysed. Consequently, the effect on the mechanical and thermal properties of modified paste has been studied, finding an improvement especially in terms of heat-transfer; finally, the optimum percentage of plastic waste (PET) by comparing the conventional and modified material has been determined.

2. Substitution of Aggregates

In the last decade, more attention has been paid, to the use of aggregates made from PET bottles as a partial replacement of the aggregate in the concrete mix. Choi et al. [18] published an in-depth research on the subject that analysed the substitution of fine aggregate with PET bottles lightweight aggregate. The tests, carried out on concrete specimens prepared with varying percentages of aggregate replacement (0%, 25%, 50%, and 75% by volume of inert), regarded numerous properties of the concrete such as the density, the failure, the workability, the compressive and tensile strengths, and the modulus of elasticity, thereby creating an almost complete framework on this subject. The results showed first a decrease of the specific weight of concrete as the content of PET increases. The influence of the substitution of aggregates on the workability of concrete was also studied; it was found to grow with the fraction of inert replaced, also thanks to the spherical shape of the aggregate in PET. With regard to the compressive and tensile strengths, instead, a reduction was pointed out in correspondence of the increased proportion of the replaced aggregate.

Further studies were carried out on this topic in the following years. Among these, it is worth citing the results obtained in 2007 by Marzouk [19], who showed that the partial or complete substitution of sand with PET in concrete composites does not affect either the compressive nor the tensile strengths of concrete if the level of substitution is below 50% of the volume. PET aggregates, however, should not have an equivalent diameter lower than 5 mm, as it does not significantly influence the compressive and tensile strength of the concrete. These results represent a significant incentive to the innovative use of PET, since they confirmed the undeniable economic benefits regarding the possibility of using waste material readily available and the environmental aspects, which involve the possibility to reduce the waste.

The same results are found in [20] where 5% by weight of siliceous sand was substituted with PET in the concrete mix. WPET aggregates were manufactured from waste PET bottles and, through a grinding process, these granules pass from a thickness of 1–1.5 mm to the size of 0.1–5 mm. Irrelevant differences were detected in the compressive and

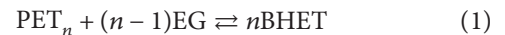
tensile strengths in case of mixes containing Waste PET (WPET) at low w/c ratio (0.45). The differences became slightly more significant by increasing the w/c ratio (up to 0.55) because the interface between WPET and the hydrated cement Portland presented a higher porosity. In this case, it was detected that small percentages of fine aggregates (PET) do not affect the water absorption. As a result of this study, when WPET is used as a partial substitute for fine aggregates in a reference concrete, there is an increase in the toughness and ductility, the same values of workability, and a shrinkage influenced by the higher ductility but still acceptable for the structural elements.

In other research studies, instead, (i.e., Hannawi et al. [21]) a decrease in compressive strength is observed with the use of PET (particle size ≤ 10 mm) and polycarbonate (particle size ≤ 5 mm) waste aggregates as replacement in volume of sand. Probably it can be attributed to the poor bond between the matrix and plastic aggregates, but the specimens tested were able to carry a load for a few minutes after failure without full disintegration, showing also a higher ductility. This trend seems to be more obvious as the percentage of plastic aggregates increases. Otherwise, the flexural strength values remain almost unchanged when the sand volume substituted with aggregates varies in a range of about 0–20%. Additionally, a significant improvement of the postpeak flexural behaviour is observed. The calculated flexural toughness factors increase significantly by increasing the volume fraction of PET and polycarbonate aggregates because also the energy absorbing capacity increases, a fundamental characteristic in case of dynamic or impact forces (in fact there is a decrease of the elastic modulus). In addition, the good sewing effect of PET and polycarbonate fibres has been experimentally demonstrated in the post-cracking phase of concrete when included in the concrete mix as aggregates.

Recently, a study similar to [21] has been developed in [22] where PET has been obtained from waste bottles subjected to a grinding process to obtain PET particles used as fine aggregates in the concrete. In this case, lower percentages of PET than in [21] have been utilized as a substitute for sand (5%, 10%, and 15%) but the results indicate a lower density. For these percentages of PET, a lower workability has been detected, together with a lower modulus of elasticity and splitting tensile strength with respect to a conventional concrete. The compressive and flexural strengths show an ascending trend at the initial stages; however, they tend to decrease in the second stage. Finally, to investigate the structure of the concrete containing PET particles, ultrasonic pulse tests have been performed and a porous structure has been observed. As demonstrated by experimental results in a further study, the mechanical properties of the concrete depend on the PET particle size and its concentration [23]. Lower sizes and concentrations of PET particles create less space in the concrete, and, consequently, the compressive strength and the compression strain increase, while Young's modulus decreases when the size of PET particles used is increased. This means that deformations tend to be higher, but the maximum stresses reduce in magnitude.

In order to use the recycled PET nanoparticles in addition to or a substitute for fine aggregates (i.e., sand) in the cement paste, the chemically polymerization process of PET can be a valuable tool to reuse the PET wastes. PET is considered as a polyester with functional ester groups that are cleaved by reagents, like acids, bases or water (hydrolysis), alcohols (alcoholysis), amines (aminolysis), ammonia (ammonolysis), and glycols (glycolysis). Previous studies have shown that it is possible to use plastic waste in concretes, mortars, or bituminous conglomerates as a binder with the aim to remove the PET waste by means of mixing it directly into the mixtures [24, 25]. Most of the studies carried out for the depolymerization of PET have discussed the role of various types of glycols and metal acetates to be used as catalyst in the process [26–28].

The main depolymerization processes that have reached commercial maturity up to now are glycolysis. Specifically, the glycolysis reaction is the molecular degradation of PET polymer by glycol, in the presence of trans-esterification catalysts, basically by using ethylene glycol as solvent. The ester linkages of PET polymer are broken and replaced by hydroxyls terminals to give bis (2-hydroxyethyl terephthalate) (BHET), which is the raw material for producing PET, according to the following reaction scheme [29]:



Glycolysis of PET is the most frequent process by using metal acetates (Zn, Co, Pb, and Mn) as catalysts [30].

Studies on the kinetics of PET glycolysis have revealed that glycolysis without using a catalyst seems to be very slow and a complete depolymerization of PET to BHET cannot be achieved. In addition, it yields an end-product which has a significant number of other oligomers in addition to the BHET monomer. These results face difficulty in recovering the BHET monomer when it is the aimed product. The current interest in the depolymerization of PET by glycolysis to recover bis-hydroxyethyl terephthalate (BHET) monomer has led to studies of glycolysis catalysts. Therefore, the efforts of recent research is directed towards duplicating the rate and BHET monomer yielded through the development of highly efficient catalysts and other techniques, in addition to optimizing the reaction conditions (such as time, temperature, PET/catalyst ratio, and PET/EG ratio) [31, 32]. It has been concluded that zinc acetate is the most suitable glycolysis catalyst of the four metal acetates (lead, zinc, cobalt, and manganese) under a pressure of 1 atm [33].

In the present paper, the influence of using processed PET waste particles as a part of fine aggregates on the mechanical and physical properties of cementitious paste is investigated. In particular, the amount to be substituted is determined as weight percentage of the sand. In the following, the process of PET particles production is described and illustrated.

3. Materials and Test Methods

3.1. Materials and Samples Preparation. In this study, the depolymerized PET obtained by chemical degradation of plastic water bottles is added as a modifier of cement paste to

evaluate the recycled effect on mechanical behaviour. Ordinary Portland cement type CEM I-52.5R was used throughout the current experimental campaign of preparation of the specimens. The chemical composition of the cement employed is presented in Table 1.

In the first phase, PET water bottles were cut into many small sized pieces. Such plastic particles with diameter equal to 2 mm were employed in the PET depolymerization process through the glycolysis reaction. The $C_2H_6O_2$ Ethylene Glycol (EG) solvent and the catalyst consists of TiO_2 zinc-dioxide particles were added to allow the reaction activation. In the mixture, the EG : PET molar ratio was equal to 4 : 1 with 0.5% catalyst based on the weight of PET. In PET chemical recycling phase, the mixture was heat-treated at $190^\circ C$ for five hours until the mixture came in the resin state [34]. Heat treatment was involved in the complete condensation in close system through the use of glass condenser using water as a cooler (Figure 1(a)). The unreacted (EG) solution was separated in the form of depolymerized polyethylene terephthalate (DPET) as shown in Figure 1(b). After a liquid separation, the solid component was ground and reduced to fine powder with diameter 30 nm.

In the second phase, different cement pastes were produced depending on the manufacturing of the specimens. The cement mixtures were obtained to replace a part of sand with DPET particles. The nanoparticles were mixed with cement in a dry condition, and the dry mixtures were sieved several times for a proper dispersion of the nanoparticles. The materials were mixed in a planetary mixer according to the UNI-EN 196 recommendations [35]. The water-cement ratio (W/C) used was set to 0.45.

Seven cement pastes were prepared using normalized sand (according to UNI-EN 196-1-2006 [35]) and unnormalized sand with particle size from values of 0.5 to 2 mm. The samples of the DPET mixtures were prepared to measure the additional effect of DPET to the mixture and to using six different amounts added to the content of cement (Table 2).

Three samples ($40\text{ mm} \times 40\text{ mm} \times 160\text{ mm}$) were prepared for each proportion to determine the unit weight, flow, mechanical characteristic (compressive and flexural strength), and thermic properties.

3.2. Test Methods

3.2.1. Thermal Conductivity. The thermal conductivity and the specific heat capacity were measured using the multifunctional commercial device, ISOMET 2104. Such instrument is equipped with various types of optional probes, for example, needle probes for porous, fibrous, or soft materials, and surface probes for hard materials. The measurement of the thermal properties of the material is based on the analysis of temperature response to heat flow impulses. The surface of sample to test is put in direct thermal contact with the heat flow induced by a resistor. The thermal data in this research were acquired measuring the moisture content constantly (Figure 2).

3.2.2. Flexural Strength. For each investigated mortar described in Table 2, three specimens were casted according to EN 196-1 [34]. All $40 \times 40 \times 160$ mm prismatic specimens

TABLE 1: Chemical composition of cement.

Oxides	Content (%)
SiO ₂	20.3
Al ₂ O ₃	4.4
Fe ₂ O ₃	2.6
CaO	62.5
MgO	2.5
SO ₃	2.1
LOI	1.0

(Figure 3) were stored at $20^\circ C$ (90% RH). As suggested by EN 196-1 https://www.sciencedirect.com/science/article/pii/S0950061816317111?casa_token=4vjs3FIZOn4AAAAA:n0EoE21cF3wBGXgIc5w5w8sQIA0bzi7Dmdq5Rp6utBk7l0KLPJeqPbKAUf28HaiFEoEZh337fg [35], three point bending tests were carried out after 28 days to assess the flexural strength. The external load P was applied through an Instron L.T.D. loading machine, having a loading capacity of 50 kN. Tests were performed by driving the displacement of the loading cell, whose stroke moved at a velocity of 0.5 mm/min. Both the applied load P and the midspan deflection δ of the beam were recorded during the tests, until the complete failure of the specimen (Figure 4).

The flexural strength was determined by the following according to [35]:

$$R_f = \frac{1.5 * P * l}{b^3}, \quad (2)$$

where R_f is the flexural strength (N/mm^2); P is the load applied to the middle of the prism at the first crack, in Newtons; b is the side of the square section of the prism, in millimetres; l is the distance between the supports, in millimetres.

3.2.3. Compressive Strength. Compressive strength tests of the cement paste samples were carried out at 28 days after casting. The cubic specimens were obtained by the prismatic samples after being tested for bending. The flat surfaces of the cubic specimens were polished and smoothed in order to eliminate the unevenness. Three samples were tested for each paste. The load was applied perpendicularly and continuously on the specimen by using a hydraulic testing compression machine with a maximum load of 150 kN. The compressive strength was determined according to [35] (Figure 5).

The compressive strength of the specimen was calculated by dividing the maximum load carried by the specimen during the test by the average cross-sectional area of the specimen as shown in the following in accordance with [35]:

$$R_c = \frac{F_c}{A}, \quad (3)$$

where R_c is the compressive strength, in N/mm^2 ; F_c is the maximum load at fracture in Newtons; A is the area of the prism face in millimetres (40×40).

4. Results and Discussion

4.1. Flow Value. To evaluate the fluidity of the cement pastes, a slump test was conducted on the cementitious mix prepared at the laboratory by using the slump cone or Abrams

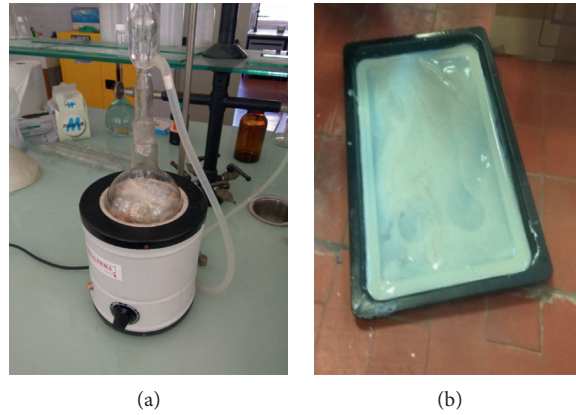


FIGURE 1: (a) Close system of chemical recycling step; (b) depolymerization of polyethylene terephthalate (DPET) after a liquid separation.

TABLE 2: Mixture typologies with the sand type used and the weight replacement of sand by DPET.

Cement paste	Sand type	Sand (g)	DPET (g)	Sand (%)	DPET (%)	Specific weight ρ (kg/m ³)
1	Normalized	500	—	100	—	2100
2	Normalized	350	150	70	30	1950
3	Unnormalized	500	—	100	—	1960
4	Unnormalized	400	100	80	20	1812
5	Unnormalized	300	200	60	40	1636
6	Unnormalized	200	300	40	60	1494
7	Unnormalized	100	400	20	80	1451



FIGURE 2: Conductivity test device.

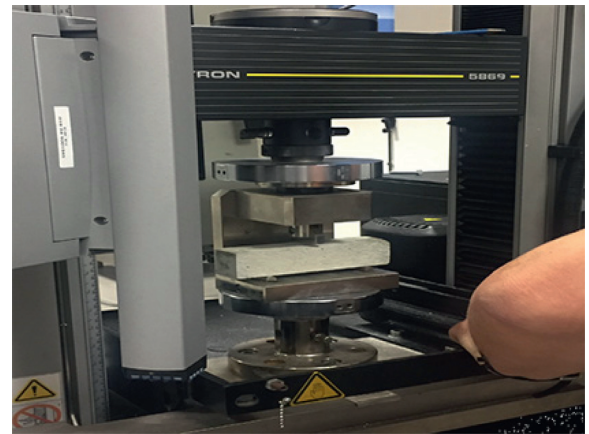


FIGURE 4: Flexural test on prismatic sample.



FIGURE 3: DPET-prismatic samples tested to flexural load.

cone, which was filled with the prepared mortar mix in three stages. The slump was thus determined by measuring the distance from the top of the subsided cement paste to the level of the top of the slump cone and was recorded in terms of millimetres. In Figure 6, the flow value of each cement paste normalized to the flow value of the conventional cement mixture (Paste 1 in Table 1) is represented. The results obtained from the slump test show that the mixture 3 and 4 were more fluid than mixture 1. The flow values decrease continuously for the DPET percentage greater than 20% (paste 4-5-6-7 in Table 1).



FIGURE 5: Compressive test on cubic sample.

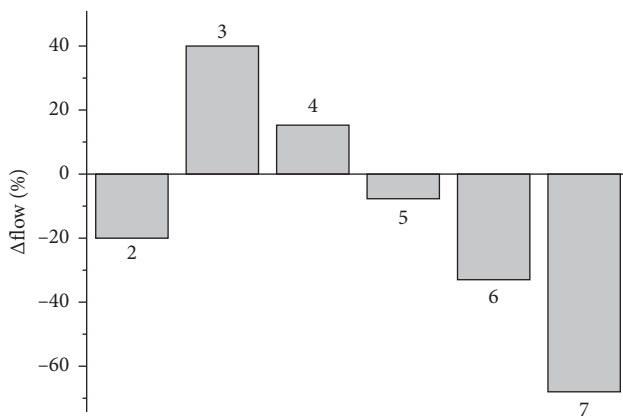


FIGURE 6: Flow values normalized to flow value of cement paste 1.

4.2. Thermal Conductivity. The results obtained from the thermal conductivity tests are reported in Table 3 and are represented in Figure 7(a). The thermal conductivity is substantially indicated as the attitude of a heat-transmitted material. The data relating to the conducted tests show that the experimental values regarding this characteristic decrease with the progressive increase of DPET amount in the cementitious paste.

In Table 3, the thermal diffusivity values of all tested specimens are reported. Such characteristic describes the propagation of the thermal field where the regime of the boundary conditions is not stationary and the capacity of the material to adapting to the changes in temperature imposed from the outside. Similarly to the thermal conductivity, the

thermal diffusivity decreases when the DPET percentage increases in the mixture. This trend is not observed for sample 6, which can be still counted among the measurement errors due to the smaller surface of the test sensor.

It is clear from the results represented in Figure 7(b) that the more DPET is added to the mixture, the more the diffusivity is lowered, and therefore the thermal inertia increases.

The minimum thermal conductivity value was 0.35 W/m K, observed at 80% aggregates replacement. From this result, it was concluded that waste PET aggregates replacement with conventional aggregate in the mixture showed better insulation properties (i.e., lower thermal coefficient). The low unit weight and high thermal conductivity values of DPET mortars make it possible to assess the use of such materials in construction applications.

In fact, the thermal conductivity values of produced mortars decreased with increasing weight fractions of depolymerized plastic, and their thermal conductivities were lower than the ordinary mortar by about 31–62%. Such reduction is in agreement with the experimental results in another preliminary research conducted on mortars with milled PET waste until reaching particles size similar to sand [36, 37]. In [37], the percentual improvement of thermal property has increased up to 57% in mortars with sand replacement by PET obtained by milling. As noted in the presented experimental results, the cement mortar containing a large part of polymeric material replacing sand preserves the high thermal performances of milled PET mortar with the added advantage of using non-depurated plastic waste. For this reason, it can prove to be a highly recommended material that can offer advantages in terms of thermal insulation.

4.3. Mechanical Strength. The flexural and compressive strengths of the different mixtures are collected in Table 4.

Specifically, Table 4 shows the variations in the flexural strength of the different mixtures as a function of the percentage of sand replaced by the same weight of plastic. Comparing with the control mixture, no significant changes are observed for mixtures containing up to 40% of DPET aggregates. However, a decrease of 46% and 51% for mixtures with, respectively, 60% and 80% of DPET content is observed. In Figure 8, the flexural strengths of the DPET mixture with respect to the specific weights are represented.

The experimental results show a decrease in compressive strength when the plastic content increases both the normalized and unnormalized sand mixtures. The drop in compressive strength seems not to be proportional to the weight fraction of sand replaced by plastic aggregates. In fact, a decrease of 20% for the mixture with 30% of DEPT aggregates and normalized sand (cement paste 2 in Table 4) is observed. For mixtures with, respectively, 20%, 40%, 60%, and 80% of DPET aggregates and un normalized sand (cement paste 4, 5, 6, and 7 in Table 4) a decrease equal to 25%, 47%, 60%, and 66% of compressive strength, respectively, is observed. The drop in compressive strengths due to the addition of plastic aggregates is closely related to the decrease of the specific weight of the DPET mixture (Figure 9).

TABLE 3: Thermal conductivity and thermal diffusivity values of the seven mixtures investigated.

Cement paste	Sand type	Sand (%)	DPET (%)	Specific weight ρ (kg/m ³)	Thermal conductivity (W/mK)	Thermal diffusivity (m ² /s) x 10 ⁻⁸
1	Normalized	100	—	2100	2.02 ± 0.05	1.10 ± 0.08
2	Normalized	70	30	1950	1.45 ± 0.10	0.892 ± 0.05
3	Unnormalized	100	—	1960	0.99 ± 0.06	0.608 ± 0.1
4	Unnormalized	80	20	1812	0.627 ± 0.02	0.426 ± 0.03
5	Unnormalized	60	40	1636	0.57 ± 0.02	0.38 ± 0.05
6	Unnormalized	40	60	1494	0.42 ± 0.09	0.518 ± 0.06
7	Unnormalized	20	80	1451	0.35 ± 0.01	0.35 ± 0.02

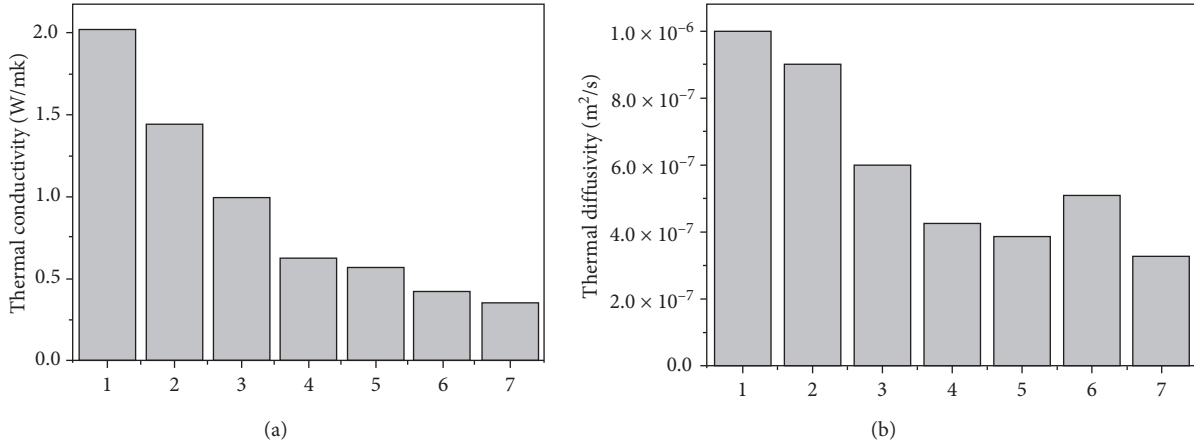


FIGURE 7: (a) Reduction of the thermal conductivity according to each mixture type; (b) reduction of the thermal diffusivity according to each mixture type.

TABLE 4: Results of flexural and compressive strength of cementitious pastes with different weight additions of DPET.

Cement paste	Sand type	DPET (%)	Flexural strength R_f (N/mm ²)	Compressive strength R_c (N/mm ²)
1	Normalized	—	10.02 ± 0.53	51.97 ± 1.32
2	Normalized	30	8.80 ± 0.25	42.06 ± 1.02
3	Unnormalized	—	6.87 ± 0.48	47.91 ± 0.89
4	Unnormalized	20	7.79 ± 0.50	35.82 ± 1.06
5	Unnormalized	40	6.77 ± 0.47	25.60 ± 0.89
6	Unnormalized	60	4.36 ± 0.31	18.78 ± 0.60
7	Unnormalized	80	3.32 ± 0.32	16.27 ± 0.95

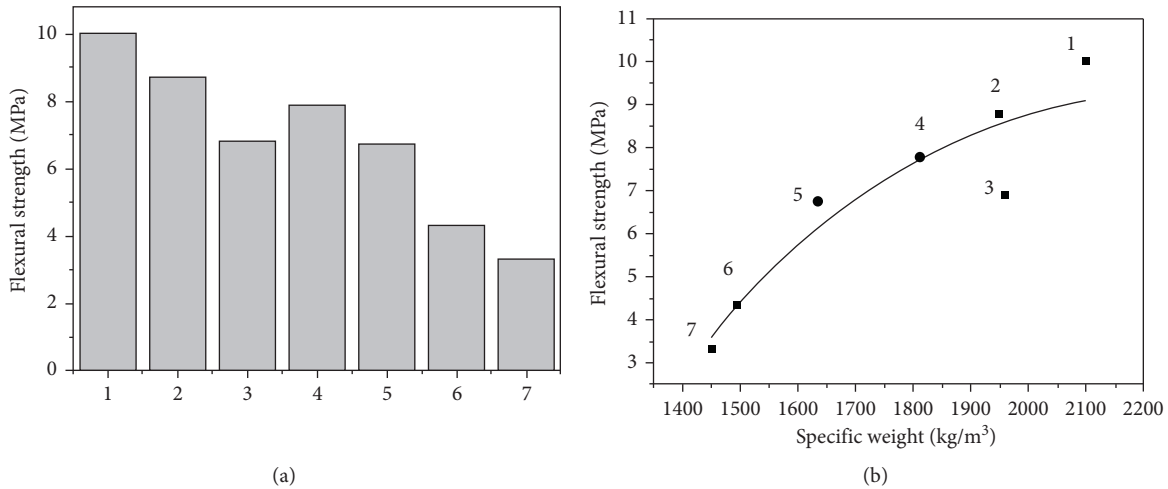


FIGURE 8: (a) Flexural strength according to tested mixture type; (b) relationship between the flexural strength and specific weight of the specimens.

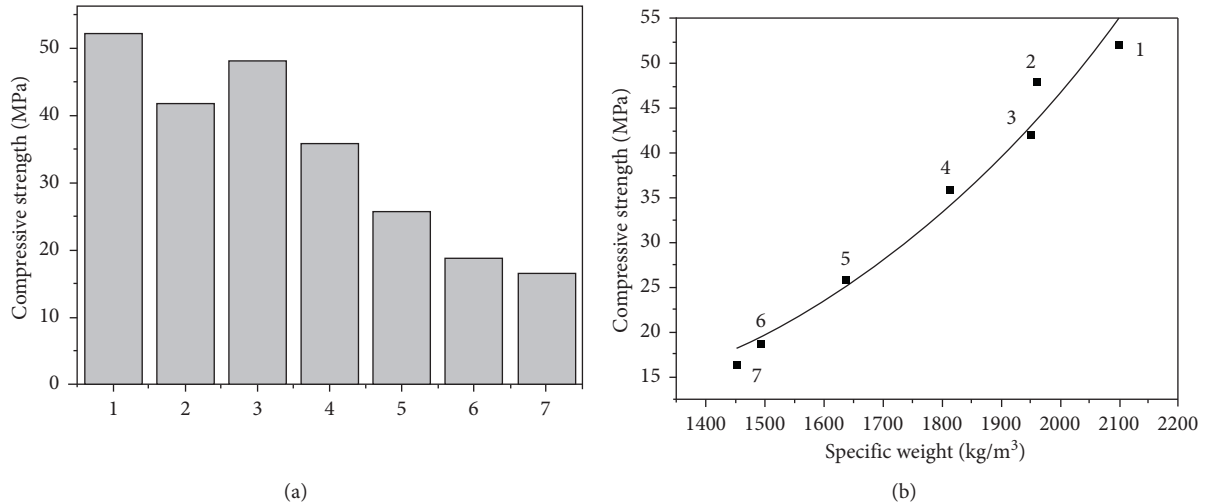


FIGURE 9: (a) Compressive strength according to tested mixture type; (b) relationship between the compressive strength and specific weight of the specimens.

The reduction of compressive and tensile strengths in correspondence of the increased proportion of the replaced aggregate results in agreement with the experimental evidence revealed by previous studies carried out on mortars containing milled PET particles [21, 22]. The mechanical behaviour DPET-mortar results were comparable to mortars with the incorporation of ground PET waste. Depolymerization of the PET thus allows obtaining a mortar with similar performance without include the needed steps for the mechanical recycling on (i.e., separation based on shape, density or chemical composition of waste, and washing to removal of impurity).

5. Conclusions

In recent years, the recycling of PET has received a great deal of attention for the heavy amount of plastic material destined to disposal treatment. The presented paper focused on the use of a postconsumer PET-bottles wastes as aggregates in a cement paste in order to evaluate its physical and mechanical characteristics. In the material research field, the postconsumer PET-bottles are mainly recycled into fibres through mechanical process. Nevertheless, mechanical processing can often lead to low-grade material due to the difficulty of obtaining fibres uniform throughout and free from defects. For this reason, the conducted research aimed to explore the possibility of using PET nanoparticles obtained by a chemical process as the depolymerization of plastic pieces through the glycolysis reaction using Ethylene Glycol as a solvent.

Different DPET percentages were added to the cement mixture in replacement of sand. The results of mechanical tests and thermal conductivity tests conducted on mortar mixed with chemically depolymerized PET have been compared with the performance of a traditional paste. The experimental data showed that the use of plastic nanoparticles decreases the mechanical performance in terms of flexural and compressive strength of the new mortars. The results showed that a higher percentage of DPET provides a lower heat-transfer capacity to the mortar. For this reason, the chemically DPET- mortars can

be considered a valuable material in the building field for all those cases where a good thermal insulation level is required. Finally, the high advantage obtained from recycling a waste material like PET that is very dangerous for the environment must be underlined.

The present research on PET waste chemically recycle to improve mortar performance can be considered preliminary. It showed interesting properties of DPET mortars such as thermal conductivity; however, further study remains to optimize the chemical process conditions with several reagents and to define the optimal DPET-additive amount. Additionally, this research can also be expanded analysing the microstructure of DPET mortars and evaluating a possible fire resistance difference according to DPET utilization.

Data Availability

The data used to support the findings of the study are included in the article.

Conflicts of Interest

The authors declare that there are no conflicts of interest regarding the publication of this paper.

References

- [1] S. Shahiron, "Concrete incorporated with optimum percentages of recycled polyethylene terephthalate (PET) bottle fiber," *International Journal of Integrated Engineering*, vol. 10, no. 1, 2018.
- [2] M. Sulyman, J. Haponiuk, J. Haponiuk, and K. Formela, "Utilization of recycled polyethylene terephthalate (PET) in engineering materials: a review," *International Journal of Environmental Science and Development*, vol. 7, no. 2, p. 100, 2016.
- [3] P. Sang Ho and K. Seong Hun, "Poly (ethylene terephthalate) recycling for high value added textiles," *Fashion and Textiles*, vol. 1, no. 1, pp. 1-17, 2014.

- [4] D. Foti, "Innovative techniques for concrete reinforcement with polymers," *Construction and Building Materials*, vol. 112, pp. 202–209, 2016.
- [5] D. Foti and D. Cavallo, "Mechanical behavior of concretes made with non-conventional organic origin calcareous aggregates," *Construction Build Mater*, vol. 179, pp. 100–106, 2018.
- [6] D. Foti, M. Lerna, M. Sabbà, and V. Vacca, "Mechanical characteristics and water absorption properties of blast-furnace slag concretes with fly ashes or microsilica additions," *Applied Sciences*, vol. 9, no. 7, p. 1279, 2019.
- [7] D. Foti, "Preliminary analysis of concrete reinforced with waste bottles PET fibers," *Construction and Building Materials*, vol. 25, no. 4, pp. 1906–1915, 2011.
- [8] L. A. Pereira de Oliveira and J. P. Castro-Gomes, "Physical and mechanical behaviour of recycled PET fibre reinforced mortar," *Construction and Building Materials*, vol. 25, no. 4, pp. 1712–1717, 2011.
- [9] E. Silva, J. Coelho, and J. Bordado, "Hybrid polyethylene/polypropylene blended fiber-reinforced cement composite," *Journal of Composite Materials*, vol. 47, no. 25, p. 3131, 2013.
- [10] D. Foti, "Use of recycled waste pet bottles fibers for the reinforcement of concrete," *Composite Structures*, vol. 96, pp. 396–404, 2013.
- [11] T. Ochi, S. Okubo, and K. Fukui, "Development of recycled PET fiber and its application as concrete-reinforcing fiber," *Cement and Concrete Composites*, vol. 29, no. 6, pp. 448–455, 2007.
- [12] D. Foti and F. Paparella, "Impact behavior of structural elements in concrete reinforced with PET grids," *Mechanics Research Communications*, vol. 57, pp. 57–66, 2014.
- [13] D. A. Silva, A. M. Betioli, P. J. P. Gleize, H. R. Roman, L. A. Gómez, and J. L. D. Ribeiro, "Degradation of recycled PET fibers in Portland cement-based materials," *Cement Concr. Res.* vol. 35, pp. 1741–1746, 2004.
- [14] S. De Silva and T. Prasanthan, "Application of recycled PET fibers for concrete floors," *Engineer: Journal of the Institution of Engineers, Sri Lanka*, vol. 52, no. 1, pp. 21–27, 2019.
- [15] B. Yesilata, Y. Isiker, and P. Turgut, "Thermal insulation enhancement in concretes by adding waste PET and rubber pieces," *Construction and Building Materials*, vol. 23, no. 5, pp. 1878–1882, 2009.
- [16] K. Ragaert, L. Delva, and K. Van Geem, "Mechanical and chemical recycling of solid plastic waste," *Waste Management*, vol. 69, pp. 24–58, 2017.
- [17] Z. Guo, K. Lindqvist, and H. de la Motte, "An efficient recycling process of glycolysis of PET in the presence of a sustainable nanocatalyst," *Journal of Applied Polymer Science*, vol. 135, no. 21, p. 46285, 2018.
- [18] Y.-W. Choi, D.-J. Moon, J.-S. Chung, and S.-K. Cho, "Effects of waste PET bottles aggregate on the properties of concrete," *Cement and Concrete Research*, vol. 35, no. 4, pp. 776–781, 2005.
- [19] O. Y. Marzouk, R. M. Dheilly, and M. Queneudec, "Valorization of post-consumer waste plastic in cementitious concrete composites," *Waste Management*, vol. 27, no. 2, pp. 310–318, 2007.
- [20] M. Frigione, "Recycling of PET bottles as fine aggregate in concrete," *Waste Management*, vol. 30, no. 6, pp. 1101–1106, 2010.
- [21] K. Hannawi, S. Kamali-Bernard, and W. Prince, "Physical and mechanical properties of mortars containing PET and PC waste aggregates," *Waste Management*, vol. 30, no. 11, pp. 2312–2320, 2010.
- [22] E. Rahmani, M. Dehestani, M. H. A. Beygi, H. Allahyari, and I. M. Nikbin, "On the mechanical properties of concrete containing waste PET particles," *Construction and Building Materials*, vol. 47, pp. 1302–1308, 2013.
- [23] L. Ávila Córdoba, G. Martínez-Barrera, C. Barrera Díaz, F. Ureña Nuñez, and A. Loza Yañez, "Effects on mechanical properties of recycled PET in cement-based composites," *International Journal of Polymer Science*, vol. 2013, pp. 1–6, Article ID 763276, 2013.
- [24] F. Mahdi, H. Abbas, and A. A. Khan, "Strength characteristics of polymer mortar and concrete using different compositions of resins derived from post-consumer PET bottles," *Construction and Building Materials*, vol. 24, no. 1, pp. 25–36, 2010.
- [25] F. Mahdi, H. Abbas, and A. A. Khan, "Flexural, shear and bond strength of polymer concrete utilizing recycled resin obtained from post consumer PET bottles," *Construction and Building Materials*, vol. 44, pp. 798–811, 2013.
- [26] S. Nica, A. Hanganu, A. Tanase et al., "Glycolytic depolymerization of polyethylene terephthalate (PET) wastes," *Revista de Chimie Bucharest*, vol. 66, no. 8, pp. 1105–1111, 2015.
- [27] A. M. Al-Sabagh, F. Z. Yehia, G. Eshaq, A. M. Rabie, and A. E. ElMetwally, "Greener routes for recycling of polyethylene terephthalate," *Egyptian Journal of Petroleum*, vol. 25, no. 1, pp. 53–64, 2016.
- [28] S. M. Cakić, I. S. Ristić, M. M. Cincović, N. Č. Nikolić, L. B. Nikolić, and M. J. Cvetinović, "Synthesis and properties biobased waterborne polyurethanes from glycolysis product of PET waste and poly (caprolactone) diol," *Progress in Organic Coatings*, vol. 105, pp. 111–122, 2017.
- [29] R. López-Fonseca, I. Duque-Ingunza, B. De Rivas, S. Arnaiz, and J. I. Gutiérrez-Ortiz, "Chemical recycling of post-consumer PET wastes by glycolysis in the presence of metal salts," *Polymer Degradation and Stability*, vol. 95, no. 6, pp. 1022–1028, 2010.
- [30] M. Zhu, S. Li, Z. Li, X. Lu, and S. Zhang, "Investigation of solid catalysts for glycolysis of polyethylene terephthalate," *Chemical Engineering Journal*, vol. 185–186, pp. 168–177, 2012.
- [31] J. R. Campanelli, M. R. Kamal, and D. G. Cooper, "Kinetics of glycolysis of poly(ethylene terephthalate) melts," *Journal of Applied Polymer Science*, vol. 54, no. 11, pp. 1731–1740, 1994.
- [32] M. Alzuhairi, A. Al-Ghaban, and S. N. Almutalabi, "Chemical recycling of polyethylene terephthalate (waste water bottles) for improving the properties of asphalt mixture," in *Proceedings of the MATEC Web of Conferences*, vol. 162, EDP Sciences, Bandung, Indonesia, April 2018.
- [33] J.-W. Chen, L.-W. Chen, and W.-H. Cheng, "Kinetics of glycolysis of polyethylene terephthalate with zinc catalyst," *Polymer International*, vol. 48, no. 9, pp. 885–888, 1999.
- [34] M. A. H. Alzuhairi, A. M. Al-Ghaban, and S. N. Almutalabi, "Chemical recycling of Polyethylene Terephthalate (PET) as additive for asphalt," *ZANCO Journal of Pure and Applied Sciences*, vol. 28, no. 2, pp. 675–679, 2016.
- [35] EN, TS. 196-1, *Methods of Testing Cement—Part 1: Determination of Strength*, Vol. 26, European Committee for standardization, Brussels, Belgium, 2005.
- [36] A. S. Benosman, M. Mouli, H. Taibi et al., "Chemical, mechanical and thermal properties of mortar composites containing waste pet," *Environmental Engineering and Management Journal*, vol. 16, no. 7, pp. 1489–1505, 2017.
- [37] M. R. Oliveira, M. da Luz Garcia, A. C. M. Castro, and T. N. Silva, "Mortar with pet-preliminary results," *Energy Reports*, vol. 6, pp. 800–803, 2020.

Research Article

Influence of the Drive Plate with Different Surface Textures on the Property of Carbonyl Iron-Based Magnetorheological Fluid

He Lu ^{1,2}, Lifeng Wang,³ Lili Dai,¹ Hongxing Ding ¹, Qiuxiang Zhang,²
and Xinhua Liu ²

¹Lianyungang Normal College, Lianyungang 222006, China

²School of Mechatronic Engineering, China University of Mining and Technology, Xuzhou 221116, China

³Chongqing Three Gorges University, Chongqing 404000, China

Correspondence should be addressed to He Lu; luhe119879@126.com and Hongxing Ding; dinghx@126.com

Received 31 May 2020; Revised 22 July 2020; Accepted 25 July 2020; Published 16 October 2020

Academic Editor: Gloria Terenzi

Copyright © 2020 He Lu et al. This is an open access article distributed under the Creative Commons Attribution License, which permits unrestricted use, distribution, and reproduction in any medium, provided the original work is properly cited.

Aiming to study the effect of drive plate with different surface topographies on the wear property of magnetorheological fluid (MRF), some specific experiments are carried out and analyzed in this paper. Firstly, experiment materials and test methods for MRF are elaborated, and four different surface topography drive plates are designed and manufactured. MRF test-bed is built up to test the rheological properties of MRF. Moreover, the surface morphology of particles is taken using a scanning electron microscope (SEM). Finally, experimental results show that there are remarkable influences on tribological properties of carbonyl iron-based MRF with different drive plates. Therefore, the drive plate with specific surface topography can meet the needs of different MRF transmission systems.

1. Introduction

As a kind of smart material that is sensitive to magnetic field, magnetorheological fluid (MRF) is a solid-liquid two-phase system formed by micron or submicron magnetic particles and additives disperse in a nonmagnetic carrier liquid [1, 2]. MRF changes into a solid-like structure from a liquid-like structure when exposed to an external magnetic field. When the external magnetic field is removed, the behavior of MRF reverts to the previous state within a few milliseconds. Such phenomenon is called magnetorheological effect [3, 4]. As magnetorheological effect is rapid, continuous, and reversible, MRF is widely applied in biological medicine [5], automobile industry [6], polishing technology [7, 8], aerospace [9], mechanical engineering, and other fields [10, 11].

In practical engineering applications, carbonyl iron-based magnetorheological fluid with different physical parameters has different application properties, which has received extensive research by scholars. The corrosion process of carbonyl iron particles on magnetorheological behavior was investigated by Plachy et al., indicating that

carbonyl iron particles were oxidized at fierce thermal oxidation at 500°C in the air and mild chemical oxidation in 0.05 M HCl [12]. Sedlacik and Pavlinek performed an experimental investigation to elucidate the effect of partial substitution on the overall MR performance as well as sedimentation stability; the sedimentation test showed positive role of dimorphic composition of dispersed phase on the sedimentation stability [13]. A systematical study of the overall influence of carbon allotrope additives on performance, stability, and redispersibility of magnetorheological fluids was carried out by Cvek et al., showing that carbon nanotubes had a better effect on stability and redispersibility of MRF [14]. In addition, the effect of acid additives on the stability and rheological properties of a suspension of carbonyl iron (CI) microparticles dispersed in silicone oil was studied by Ashtiani and Hashemabadi. Experimental results showed that, by increasing carbon chain length of acids, yield stress and stability increased up to 22 times (at $H = 362$ kA/m) and 7 times, respectively [15]. The relationship between shear stress and volume fraction and shear rate of MRFs was studied by Sun et al., and it was

found that the volume fraction had great effect on the yield stress of MRF [16].

Particle morphology also has great influence on the properties of magnetorheological fluids. The characterization, magnetic, and rheological properties of plate-like carbonyl iron particle (CIP) in comparison with conventional spherical CIP were studied by Shilan et al., and they indicated that the plate-like CIP obtained higher saturation magnetization (about 8%) than that of the spherical particles [17]. Moreover, a nonspherically shaped iron particle-based magnetorheological (MR) fluid, particularly flake-shaped, is synthesized to evaluate the performance of an MR brake by Patel et al., and it was shown that flake-shaped particle-based MR fluid with 70% weight fraction of iron particles exhibits 17% higher breaking torque at relatively low magnetic field strength compared to spherically shaped MR fluid with 72% particle weight fraction [18]. Effect of nanocelluloses on the magneto-responsive behavior and stability of MR fluids was studied by Wang et al., and they indicated that both CNC and CNF can stabilize MR fluids and improve their sensitivity to alterations of magnetic field strengths [19]. The effect of nanodiamond on the MRF was studied by Zhao et al., and they demonstrated that the physical properties and external working conditions of the nanodiamond could have a higher impact on MRF, which was of high significance to the preparation of MRF with excellent performance [20]. The iron nanoparticles and commercial carbonyl iron microsized particles were used in the dispersing phase to prepare MR fluids; magnetorheological effect and sedimentation stability were measured for comparison by Zhu et al., and they indicated that the iron nanoparticles-based MR fluids present a slightly lower MR effect but much better sedimentation stability with respect to the MR fluids with carbonyl iron microsized particles [21].

Furthermore, external working condition is also one of the key factors affecting the properties of MRF. The temperature effect on performance of compressible magnetorheological fluid suspension systems was studied by McKee et al. and it was found that the shear yield stress of the magnetorheological fluid remained unchanged within the testing range, while both the plastic viscosity, using the Bingham plastic model, and the bulk modulus of the magnetorheological fluid decreased as the temperature of the fluid increased [22]. The microscopic characteristics of a magnetorheological fluid (MRF) in a magnetic field was studied by Wang et al., and they indicated that the chain structure of the same MRF becomes more apparent as the magnetic field strength increases and, in the same external magnetic field, the chain structure also becomes more apparent with an increase in the particle volume fraction [23].

Bearing the above observations in mind, the research of MRF is greatly in the component parameters of MRF (magnetic particles, carrier fluid, and additives) and external conditions, such as magnetic field and temperature. However, few studies focus on surface texture of the drive plate on the property of MRF. In this paper, MRF test-bed is used to study the effects of different surface topography on properties of carbonyl iron-based magnetorheological fluid. Sedimentation stability, zero-field viscosity, maximum

transmittable torque, and shear yield stress of the samples have been studied and analyzed. Test results show that there are remarkable influences on tribological properties of carbonyl iron-based MRF with different surface texture.

The rest of this paper is organized as follows: experimental methods and preparation of the MRF are elaborated in Section 2. Results and discussion based on drive plate with different surface texture on MRF experiments are discussed in Section 3. Our conclusions and future work are summarized in Section 4.

2. Experiment

2.1. Preparation of MRF. Carbonyl iron particles and synthesized base oil are used as magnetic particles and carrier fluid for MRF, respectively. Carbonyl iron powders consisted of polydisperse spherical particles with diameter ranging between 1 and 2 μm . Due to its excellent high-temperature and low-temperature performance and wide range of working temperatures, PAO 6 (Poly-Alpha-Olefins 6) is chosen as carrier fluid. Firstly, the synthesized base oil is heated from normal temperature to 60°C by a digital magnetic agitator. Secondly, dispersant, thickener, and activator are added to the synthesized base oil with certain proportion successively. Thirdly, the mixture is magnetically stirred for about 2 hours until it is well blended and the speed is kept at 300 rpm; then we get compound liquid. Fourthly, a certain percentage of carbonyl iron powder is added to the compound liquid gradually. Fifthly, stirring is performed and mechanical stirring speed is kept at 1800 rpm for about 8 hours. Sixthly, the suspension liquid is stirred at 25°C for about 1 hour. MRF of 30% mass fraction is prepared by the above method. The preparation process of MRF is shown in Figure 1. Then we get the prepared carbonyl iron-based magnetorheological fluid sample that is marked as MRF-0.

2.2. Experimental Methods for Properties of MRF. As shown in Figure 2, there are three working modes of MRF device: flow mode, shear mode, and squeeze mode. MRF transmission device is based on the shear mode. According to the model of Newton fluid and Bingham fluid, the relation between total shear stress τ and shear strain rate $\dot{\gamma}$ is given by [24]

$$\tau = \tau_y(B) \text{sgn}(\dot{\gamma}) + \eta \dot{\gamma}, \quad \tau > \tau_y(B), \quad (1)$$

$$\dot{\gamma} = 0, \quad \tau \leq \tau_y(B), \quad (2)$$

where $\tau_y(B)$ is the yield stress in response to the applied magnetic field intensity B and η is the constant plastic viscosity, which is the apparent viscosity.

Before the magnetic particles are not magnetized to saturation, $\tau_y(B)$ increases with the increasing magnetic field intensity B and it is given by [24]

$$\tau_y(B) = \alpha B^n, \quad (3)$$

where B is the applied magnetic flux density and α and n are constant parameters that approximate the relationship

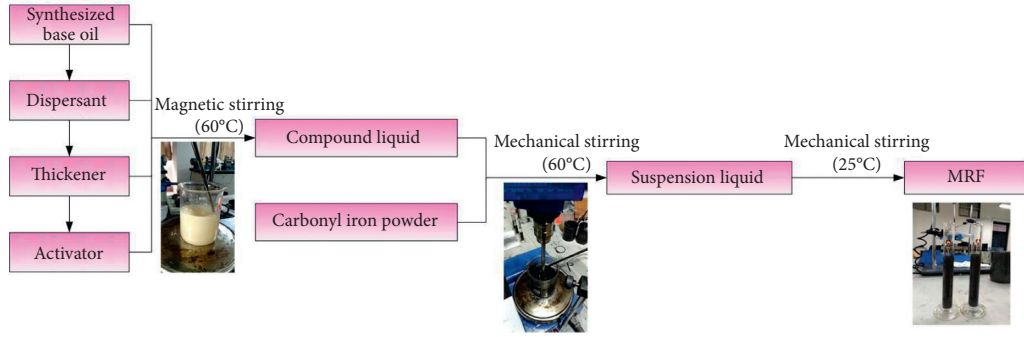


FIGURE 1: Preparation process of MRF.

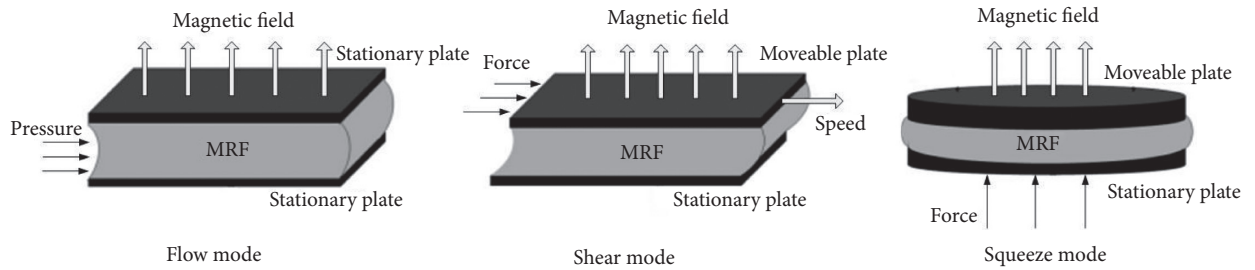


FIGURE 2: Working modes of MRF device.

between the magnetic field intensity and the yield stress for MRF, which is determined by the properties of MRF.

In this paper, a disc rotary shear test device is used to test the transferable torque and its working principle is shown in Figure 3, and the resistant torque can be written as [24]

$$T = 2\pi \int_{r_1}^{r_2} \tau r^2 dr. \quad (4)$$

The angular velocities of the rotating disks are ω_1 and ω_2 , and h is the thickness of the MR fluid gap; then

$$\dot{\gamma} = \frac{r(\omega_1 - \omega_2)}{h}. \quad (5)$$

Substituting equations (1)–(5), the resistant torque is given by

$$T = \int_{r_1}^{r_2} 2\pi r^2 dr = \frac{2\pi\tau_y}{3}(r_2^3 - r_1^3) + \frac{\pi\eta\Delta\omega}{2h}(r_2^4 - r_1^4). \quad (6)$$

It can be seen from the above equation that the resistant torque of MRF transmission device is mainly composed of two parts, $T_B = (2\pi\tau_y/3)(r_2^3 - r_1^3)$ and $T_\eta = (\pi\eta\Delta\omega/2h)(r_2^4 - r_1^4)$. T_B is produced by shearing chain columnar structure of MRF, and T_η is formed by the viscosity of MRF that is related to physical property of MRF.

In order to observe the dynamic evolution process of magnetorheological fluid with the applied magnetic field, MRF microstructure observation device is built up (Figure 4). As shown in Figure 5, magnetic particles are randomly distributed in carrier liquid without an applied magnetic field. The magnetic particles attract each other and line up into chains in the direction of an applied magnetic field and the chains are wider and longer with the intensity of magnetic field increasing.

A testing device is designed and its integral structure is shown in Figure 6. In order to study the effects of different surface topography on properties of carbonyl iron-based magnetorheological fluid, drive plate with smooth surface, ring groove, radial groove, and pitted surface are designed, where the depth of the grooves and pitted surface is 2 mm, as shown in Figure 7. MRF test-bed is designed and constructed, as shown in Figure 8. Firstly, four samples of MRF with the same composition are prepared as a reference sample before the experiment. Sedimentation stability, zero-field viscosity, and shear yield stress are tested, respectively. Secondly, the sample of MRF is injected into the MRF working gap of the testing device. Thirdly, loads of magnetic powder brake are kept at 20 N/m, regulating DC electrical source and delivering up to 3.5 A of continuous output current, running the system. Fourthly, the maximum load is recorded once an hour, which can be transferred by the test device when the systems stabilize. Fifthly, the system is stopped when the load remains constant, and samples are taken to test its dispersion stability, zero-field viscosity, and shear yield stress. Sixthly, drive plate is changed with four different surface topographies shown in Figure 2, and steps 2 through 5 are repeated.

3. Results and Discussion

MRF samples' index and the corresponding test drive plate in the wear experiments are given in Table 1.

3.1. SEM Images of Magnetic Particles Morphology. The surface morphology of magnetic particles is observed by scanning electron microscopy (SEM). Carbonyl iron particles are essentially spheroids, as shown in Figure 9(a). The

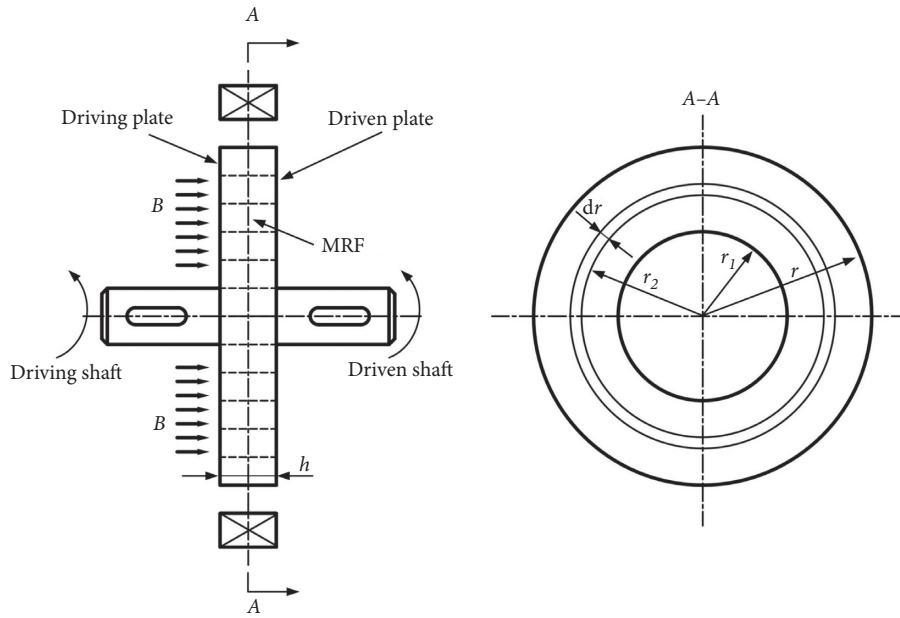


FIGURE 3: Working principle of MRF shear.

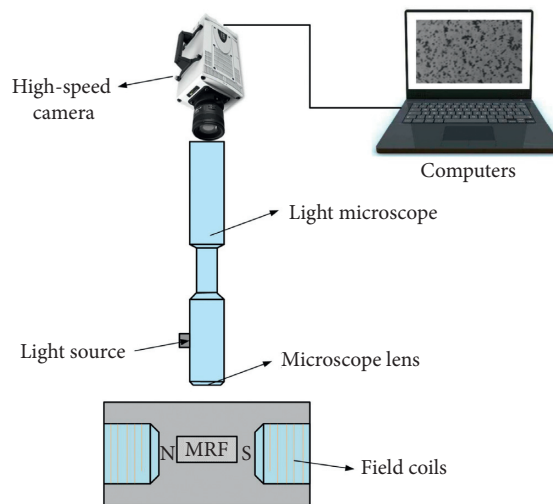


FIGURE 4: Diagram of MRF microstructure observation device.

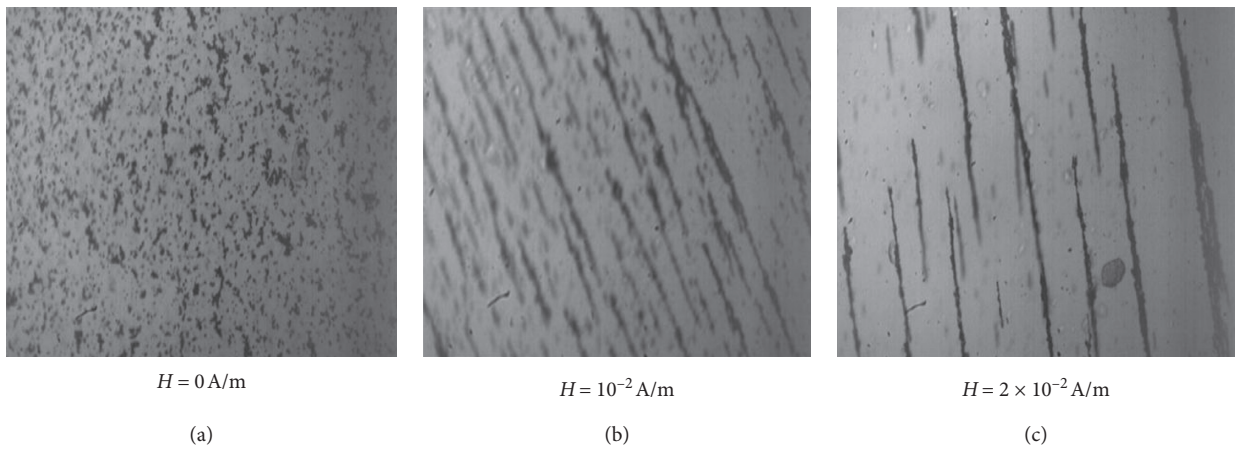


FIGURE 5: Microstructure of magnetorheological fluid under different magnetic intensity.

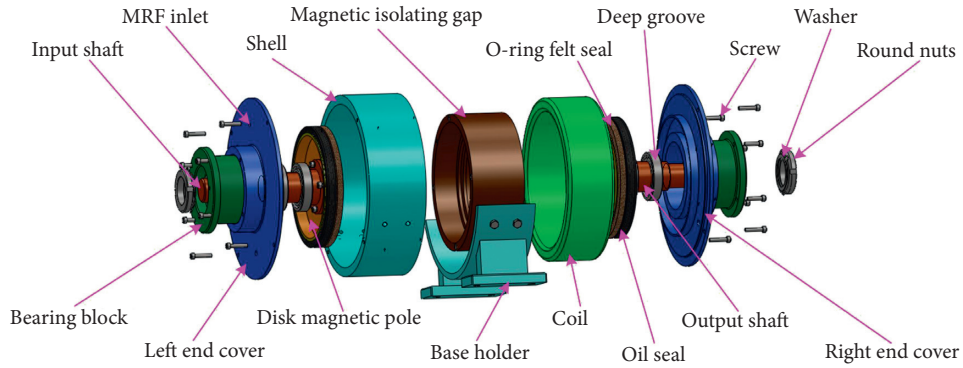


FIGURE 6: Explosive view of testing device.



FIGURE 7: Drive plate with different surface topography.

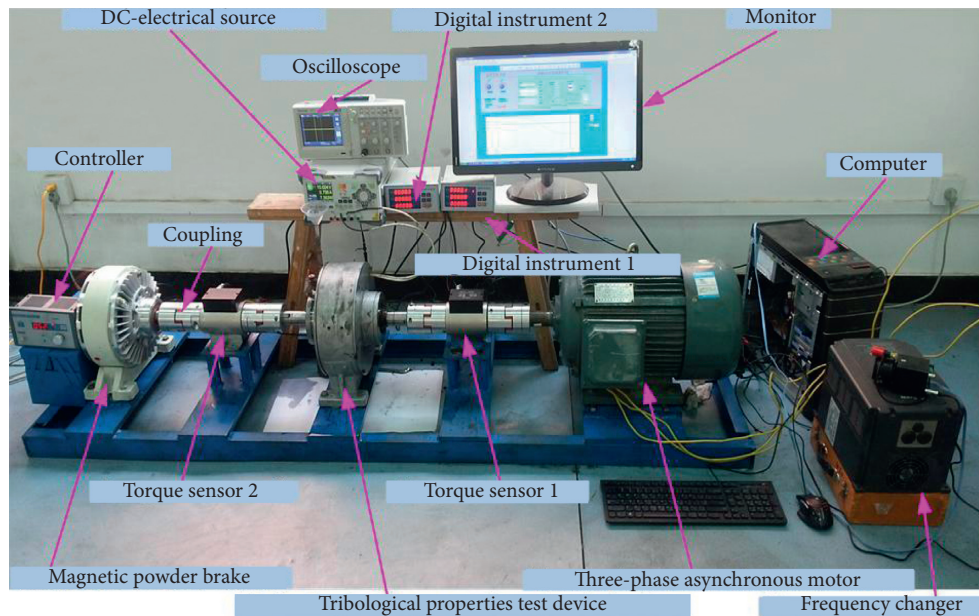


FIGURE 8: MRF test-bed.

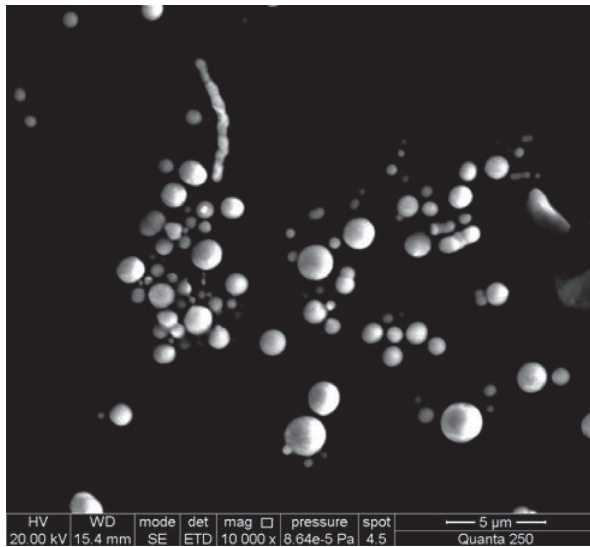
modified particles with floccule surface can improve the suspension stability of MRF shown in Figure 9(b). Figures 9(c) and 9(d) show that particles are worn after the wear test due to the interactions between the particles [25, 26].

3.2. *Sedimentation Test.* The sedimentation stability of the samples is investigated by visual observation method and can be expressed by sedimentation ratio V [27]:

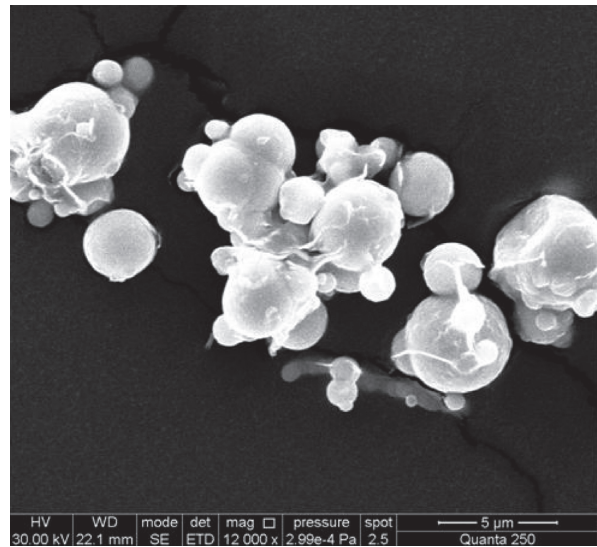
$$V = \frac{h}{H} \times 100\%. \quad (7)$$

TABLE 1: Index of MRF samples and the corresponding test drive plate.

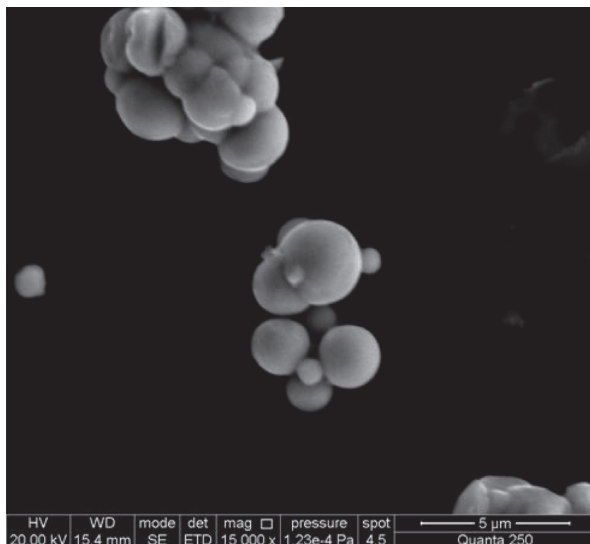
Index	Experimental projects	Surface morphology of test drive plate
MRF-0	—	—
MRF-1	Sedimentation stability	Ring groove surface
MRF-2		Pitted surface
MRF-3		Smooth surface
MRF-4		Radial groove surface
MRF-1	Zero-field viscosity	Ring groove surface
MRF-2		Pitted surface
MRF-3		Smooth surface
MRF-4		Radial groove surface
MRF-1	Maximum transmittable torque	Ring groove surface
MRF-2		Pitted surface
MRF-3		Smooth surface
MRF-4		Radial groove surface
MRF-1	Shear yield stress	Ring groove surface
MRF-2		Pitted surface
MRF-3		Smooth surface
MRF-4		Radial groove surface



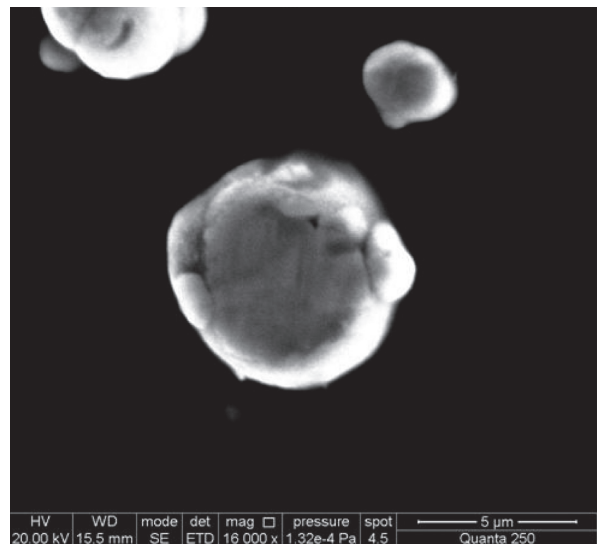
(a)



(b)



(c)



(d)

FIGURE 9: (a) SEM images of magnetic carbonyl iron particles. (b) Modified particles of MRF before experimental test. (c) Multiple particles of MRF after experimental test. (d) Particles of MRF after experimental test.

In this formula, h is the height of the particle-rich phase relative to H , which is the total MR fluid height.

The sedimentation stability curve is shown in Figure 10. It is illustrated that the sedimentation stability of all the samples decreases with time, and at last it remains stable. The sedimentation ratios of samples that experience test are lower than MRF-0, which indicates that the surface of modified particles is damaged by the interactions force between particles during the experiment. In addition, MRF-4 has the lowest sedimentation ratio of 73.8%, and it is followed by MRF-2, 74.5%, MRF-3, 76.1%, and MRF-1, 78.7%, respectively.

3.3. Zero-Field Viscosity. The experiments of zero-field viscosity are carried out at room temperature, 25°C, and the rheometer (version: Anton Paar MCR 302) is used in the test of zero-field viscosity. From Figure 11, the zero-field viscosity of all the samples decreases with the increment of shear rate and zero-field viscosity of MRF-0 is lower than that of the others. In addition, MRF-4 has the highest zero-field viscosity. Therefore, MRF subjected to wear experiment has higher zero-field viscosity.

3.4. Shear Yield Stress. The change of maximum transmittable torques of MRF samples with four different drive plates with working time is shown in Figure 12. The maximum transmittable torques of the samples are different. From the maximum to minimum are drive plates with radial groove, pitted surface, smooth surface, and ring groove. The corresponding maximum transmittable torques are 27.7 Nm, 25 Nm, 24.4 Nm, and 22.3 Nm. The rates of decline are 29%, 30.6%, 30.3%, and 31.2%, respectively. Drive plate with ring groove has the minimum transmit of torque; the reason may be the increase of the working gap of MR fluid as well as the same direction of ring groove and the shear direction of MR fluid, which reduces transmittable torque of MRF.

The relation curves of field current and shear yield stress are obtained in Figure 13. In the working gap between the drive plate and brake plate, the magnetic flux density in x -axis direction with different field current is shown in Figure 14. As shown in Figure 13, the shear yield stress of MRF becomes lower after the wear experiment. The curves of MRF-1 and MRF-3 are almost the same, and the shear yield stress reaches 39.7 kPa and 39.8 kPa, respectively, when the field current is 4 A. However, MRF-4 has minimum shear yield stress, which is 31.8 kPa, when the field current reaches 4 A. Through the above analysis, radial groove and pitted surface drive plates not only improve the transmittable torque of MRF but also increase the wear of MRF.

3.5. Discussion. There are remarkable influences on tribological properties of carbonyl iron-based MRF with different surface topography drive plates. Compared with smooth surface plate, drive plates with radial groove surface and pitted surface can improve transmittable torques of MRF, but drive plate with ring groove surface cannot. However,

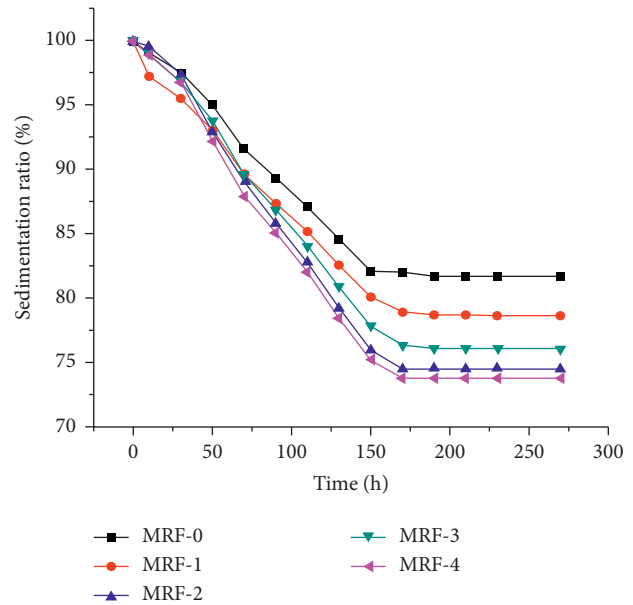


FIGURE 10: Sedimentation ratio of MRF before and after experiments.

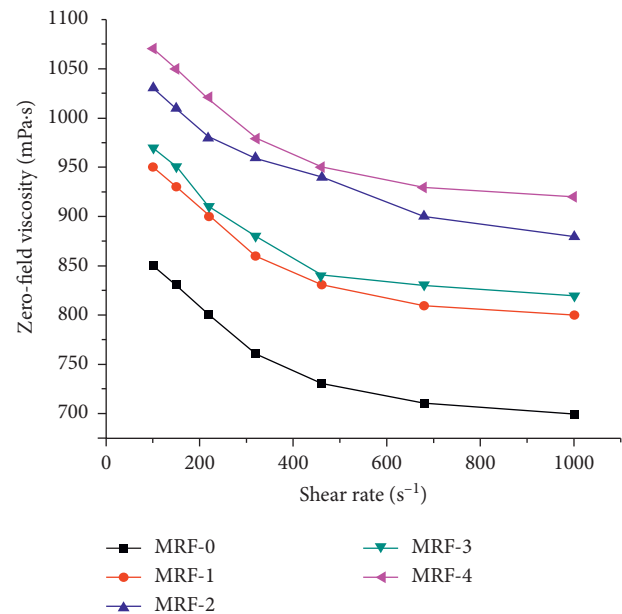


FIGURE 11: Zero-field viscosity of the samples.

radial groove surface plate and pitted surface plate can also exacerbate the wear of MRF, which will reduce shear yield stress of MRF. In addition, with intensification of the wear of MRF, there results an increase in worn particles, which leads to reduction of zero-field viscosity of MRF. Zero-field viscosity of MRF subjected to wear experiment is as follows in decreasing order: drive plate with radial groove surface, drive plate with pitted surface, drive plate with smooth surface, and drive plate with ring groove surface. Moreover, the sedimentation stability of MRF worsens due to the damage of additives after wear experiments. Therefore, the wear property of MRF needs to be considered in the choice

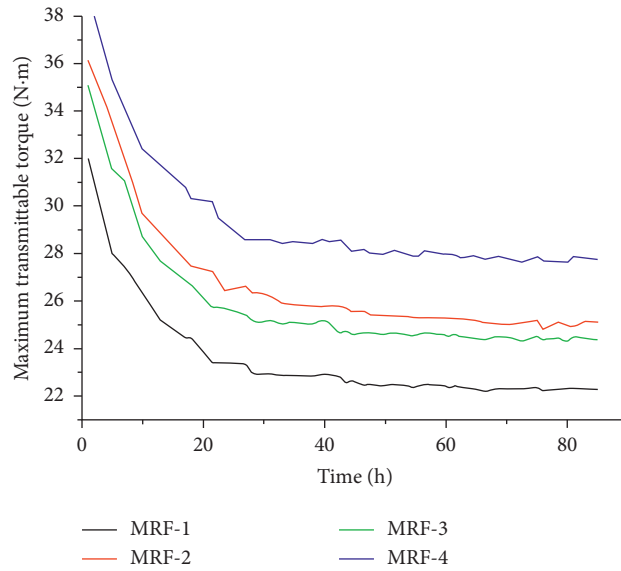


FIGURE 12: Relationship between maximum transmittable torque of MRF and working time.

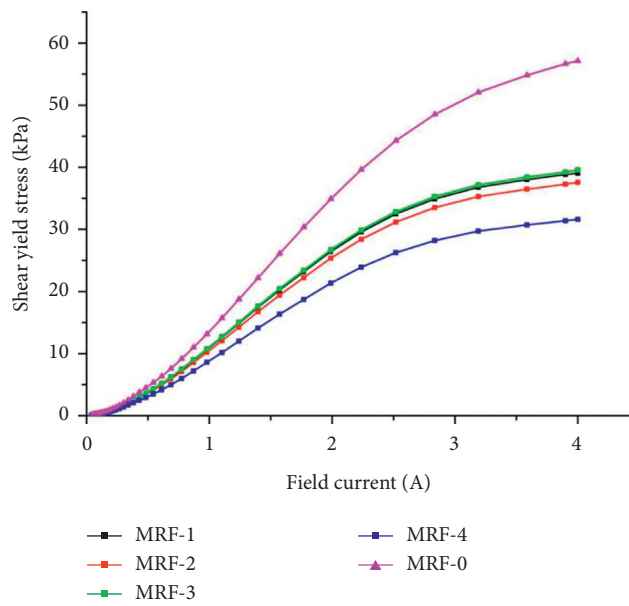


FIGURE 13: Shear yield stress curves before and after wear experiments.

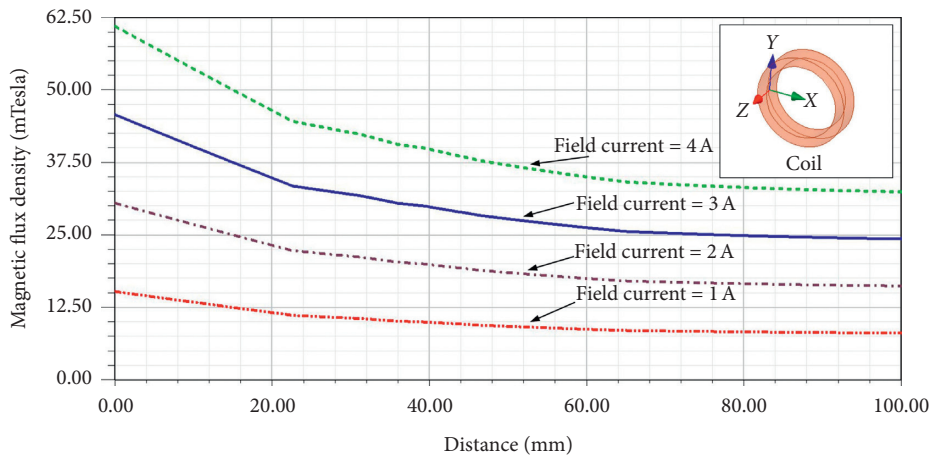


FIGURE 14: Magnetic flux density curves with different field current and position coordinate of coil.

of surface texture for drive plate applied to MRF transmission system.

4. Conclusions and Future Work

A manufacturing process method for MRF was described in detail, drive plates with four different surface topographies were designed, and an experiment table of MRF transmission test-bed was designed and constructed to study the wear property of carbonyl iron-based MRF.

The future work will focus on other factors on the properties of MRF, such as improving control algorithm of MRF transmission system to optimal property of carbonyl iron-based magnetorheological fluid, and the study of the mechanism of friction and wear of MRF is also our future work.

Data Availability

The data used to support the findings of this study are available from the corresponding author upon request.

Conflicts of Interest

The authors declare that there are no conflicts of interest regarding the publication of this article.

Acknowledgments

The support of Qing Lan Project of Colleges and Universities in Jiangsu Province of China, Technology Plan of Lianyungang (no. CG1615), Youth Talents Program (LSZQNXM202001), the National Natural Science Foundation of China (no. 51975568), and the Natural Science Foundation of Jiangsu Province (no. BK20191341) in carrying out this research is gratefully acknowledged.

References

- [1] Y. Gou, C. Sun, Z. Xu, and X. Jing, "Preparation and tests of MR fluids with CI particles coated with MWNTS," *Frontiers in Materials*, vol. 5, 2018.
- [2] F. Chen, H. Li, M. Han, and L. Aimin, "Preparation of magnetorheological fluid with excellent sedimentation stability," *Materials and Manufacturing Processes*, vol. 35, no. 10, pp. 1077–1083, 2020.
- [3] M. Cvek, R. Torres-Mendieta, O. Havelka, M. Urbanek, T. Plachy, and M. Cernik, "Laser-induced fragmentation of carbonyl iron as a clean method to enhance magnetorheological effect," *Journal of Cleaner Production*, vol. 254, p. 120182, 2020.
- [4] W. Zhu, X. Dong, H. Huang, and M. Qi, "Enhanced magnetorheological effect and sedimentation stability of bimodal magnetorheological fluids doped with iron nanoparticles," *Journal of Intelligent Material Systems and Structures*, 2020.
- [5] E. Shokrollahi, A. Goldenberg, J. Eastwood et al., "Application of a nonlinear hammerstein-wiener estimator in the development and control of a magnetorheological fluid haptic device for robotic bone biopsy," *Actuators*, vol. 7, no. 4, p. 83, 2018.
- [6] A. K. El Wahed, "A novel hydraulic actuation system utilizing magnetorheological fluids for single-port laparoscopic surgery applications," *Materials*, vol. 13, no. 6, p. 1380, 2020.
- [7] R. Desai, S. Acharya, M. Jamadar et al., "Synthesis of magnetorheological fluid and its application in a twin-tube valve mode automotive damper," *Proceedings of the Institution of Mechanical Engineers, Part L*, vol. 234, no. 7, pp. 1001–1016, 2020.
- [8] N. Mutalib, I. Ismail, S. Soffie, and S. N. Aqida, "Magnetorheological finishing on metal surface: a review," *IOP Conference Series-Materials Science and Engineering*, vol. 469, no. 1, p. 012092, 2019.
- [9] B. Kim, J. Chung, M. Cho, and G.-S. Yoon, "Magnetorheological fluid polishing using an electromagnet with straight pole-piece for improving material removal rate," *Journal of Mechanical Science and Technology*, vol. 32, no. 4, pp. 3345–3350, 2018.
- [10] X. Jiang, Y. Zhang, W. Lu, L. Ling, and L. Xiao, "Characteristics of shear stress based on magnetorheological fluid flexible fixture during milling of the thin-walled part," *The International Journal of Advanced Manufacturing Technology*, vol. 108, no. 7-8, pp. 2607–2619, 2020.
- [11] D. Güth and J. Maas, "Long-term stable magnetorheological fluid brake for application in wind turbines," *Journal of Intelligent Material Systems and Structures*, vol. 27, no. 15, pp. 2125–2142, 2016.
- [12] T. Plachy, E. Kutalkova, M. Sedlacik, A. Vesel, M. Masar, and I. Kuritka, "Impact of corrosion process of carbonyl iron particles on magnetorheological behavior of their suspensions," *Journal of Industrial and Engineering Chemistry*, vol. 66, pp. 362–369, 2018.
- [13] M. Sedlacik and V. Pavlinek, "Magnetorheology of dimorphic magnetorheological fluids based on iron nanorods," *Journal of Physics: Conference Series*, vol. 790, Article ID 012031, 2017.
- [14] M. Cvek, M. Mrlik, R. Moucka, and M. Sedlacik, "A systematic study of the overall influence of carbon allotrope additives on performance, stability and redispersibility of magnetorheological fluids," *Colloids and Surfaces A: Physicochemical and Engineering Aspects*, vol. 543, pp. 83–92, 2018.
- [15] M. Ashtiani and S. H. Hashemabadi, "An experimental study on the effect of fatty acid chain length on the magnetorheological fluid stabilization and rheological properties," *Colloids and Surfaces A: Physicochemical and Engineering Aspects*, vol. 469, pp. 29–35, 2015.
- [16] H. Sun, X. Zhu, N. Liu, L. Liang, and L. Shixu, "Effect of different volume fraction magnetorheological fluids on its shear properties," *Journal of Physics Conference Series*, vol. 1187, no. 3, p. 032078, 2019.
- [17] S. T. Shilan, S. A. Mazlan, M. H. A. Khairi, and Ubaidillah, "Properties of plate-like carbonyl iron particle for magnetorheological fluid," *Journal of Physics: Conference Series*, vol. 776, p. 012033, 2016.
- [18] S. Patel, D. Patel, and R. Upadhyay, "Performance enhancement of MR brake using flake-shaped iron-particle-based magnetorheological fluid," *Journal of Testing and Evaluation*, vol. 48, no. 3, pp. 2393–2411, 2020.
- [19] Y. Wang, W. Xie, and D. Wu, "Rheological properties of magnetorheological suspensions stabilized with nanocelluloses," *Carbohydrate Polymers*, vol. 231, p. 115776, 2020.
- [20] M. Zhao, J. Zhang, and J. Yao, "Effects of Nano-Diamond on Magnetorheological Fluid Properties," *Nano*, vol. 1210 pages, 2017.
- [21] W. Zhu, X. Dong, H. Huang, and M. Qi, "Iron nanoparticles-based magnetorheological fluids: a balance between MR effect

- and sedimentation stability,” *Journal of Magnetism and Magnetic Materials*, vol. 491, p. 165556, 2019.
- [22] M. McKee, F. Gordaninejad, and X. Wang, “Effects of temperature on performance of compressible magnetorheological fluid suspension systems,” *Journal of Intelligent Material Systems and Structures*, vol. 29, no. 1, pp. 41–51, 2018.
- [23] N. Wang, X. Liu, S. Sun, G. Królczyk, Z. Li, and W. Li, “Microscopic characteristics of magnetorheological fluids subjected to magnetic fields,” *Journal of Magnetism and Magnetic Materials*, vol. 501, p. 166443, 2020.
- [24] E. Park, L. da Luz, and A. Suleman, “Multidisciplinary design optimization of an automotive magnetorheological brake design,” *Computers and Structures*, vol. 86, no. 3–5, pp. 207–216, 2008.
- [25] N. Wang, D. H. Li, W. L. Song, S. C. Xiu, and X. Z. Meng, “Effect of surface texture and working gap on the braking performance of the magnetorheological fluid brake,” *Smart Materials and Structures*, vol. 25, no. 10, p. 105026, 2016.
- [26] Q. Zhang, X. Liu, Y. Ren, L. Wang, and Y. Hu, “Effect of particle size on the wear property of magnetorheological fluid,” *Advances in Materials Science and Engineering*, vol. 2016, Article ID 4740986, 7 pages, 2016.
- [27] M. Sedlacik, V. Pavlinek, R. Vyroubal, P. Peer, and P. Filip, “A dimorphic magnetorheological fluid with improved oxidation and chemical stability under oscillatory shear,” *Smart Materials and Structures*, vol. 22, no. 3, Article ID 035011, 2013.

Research Article

Effect of Combining Fiber and Textile Reinforcement on the Flexural Behavior of UHPC Plates

Tamás Mészöly , Sandra Ofner, and Norbert Randl

Department of Civil Engineering and Architecture, Carinthia University of Applied Sciences, Spittal an der Drau, Austria

Correspondence should be addressed to Tamás Mészöly; meszoely@cuas.at

Received 24 April 2020; Revised 28 August 2020; Accepted 14 September 2020; Published 29 September 2020

Academic Editor: Zhiping Luo

Copyright © 2020 Tamás Mészöly et al. This is an open access article distributed under the Creative Commons Attribution License, which permits unrestricted use, distribution, and reproduction in any medium, provided the original work is properly cited.

A series of flexural tests were performed in order to investigate the effect of steel fiber reinforcement (SFR) in textile-reinforced concrete (TRC) plates. Some of the specimens were reinforced only with textile, some of them only with fibers, and some of them were provided with both textile and fiber reinforcement. The concrete matrix was a self-developed ultrahigh performance concrete (UHPC) mixture with a compression strength over 160 MPa. The tensile strength of the used textiles was around 1500 MPa for glass fiber textile and over 3000 MPa for carbon fiber textile. In case of fiber reinforcement, the concrete was reinforced with 2 vol% of 15 mm long and 0.2 mm diameter plain high strength steel fibers. The dimensions of the rectangular plate test specimens were 700 × 150 × 30 mm. The plate specimens were tested in a symmetric four-point bending setup with a universal testing machine. The tests were monitored using a photogrammetric measurement system with digital image correlation (DIC). The paper presents and evaluates the test results, analyses the crack patterns and crack development, and compares the failure modes. The results showed a general advantageous mechanical behavior of specimens reinforced with the combination of fibers and textiles in comparison to the specimens reinforced with only fiber or textile reinforcement.

1. Introduction

Ultrahigh performance concrete has been developed since the 1990s and offers an outstanding compression strength of higher than 150 MPa, which is multiple times higher than in case of normal strength concrete (NSC) [1]. To reach the extraordinary kind of strength, a very fine and dense structure is needed, which contains a proper combination of finest compounds such as quartz powder, microsilica, and cement. Because of the high packing density, UHPC has a matrix almost free of capillary pores, which makes the material nearly resistant to chloride ingress, alkali, and deicing salt. With a partly substitution of cement in the mixture, for example, with fly ash or blast furnace slag, an almost identical compressive strength without any degradation of the mechanical properties and workability parameters can be reached [2–5]. Including these facts and the material-savings potential due to the high compressive strength and the smaller necessary concrete cover, UHPC can be rated as material-saving and durable building material with a lower ecological impact than NSC [5, 6].

Due to the high packing density, UHPC has a very brittle behavior under compression loading. Therefore, usually steel fibers are added in the mixture to avoid this negative behavior. By adding fibers, ultrahigh performance fiber-reinforced concrete (UHPRC) is able to resist notable tensile forces [7], and it provides a more ductile behavior. Moreover, fibers can significantly increase the shear resistance of UHPC beams [8], or prefabricated UHPRC units can be applied for local strengthening of highly compressed concrete zones [9]. When using fiber-reinforced concrete, the fiber orientation and distribution have a strong impact on the tensile behavior. These attributes are influenced not only by the production and the pouring of the concrete but also by depending on the shape and size of the specimens [10].

The demand of a more predictable structural response leads to the idea to combine UHPC with textile reinforcement. In addition to the other outstanding features of UHPC, a very high bond strength to reinforcing materials can be developed [11]. Typical materials for textile reinforcements are alkali-resistant (AR) glass or carbon. These

materials show besides their high tensile strength (up to 5 times the tensile strength of ordinary reinforcement steel) and sufficient ultimate strain, an adequate modulus of elasticity and a low relaxation and resistance to corrosion in alkaline environment and in concrete [12, 13]. Above all, it can be placed exactly in the direction and where it is needed, which beneficially affects the failure mechanism and the ductility of the concrete structure [13, 14].

Textile reinforcement is made of rovings, which are bundles of infinite filaments. These filaments are glued together with an impregnation made of epoxy (EP) or styrene-butadiene (SB). The impregnation leads to an activation of the inner core of filaments in the roving, which is important to get a uniform stress distribution over the whole cross-section of the bundle [15]. The rovings are connected by means of knitting threads at the crossing points, which has an essential effect on the composite bearing capacity of the fabrics [14].

Due to the small mesh sizes of the usually used plane textile reinforcement, only fine grain concrete mixes and mortars with a maximum grain size of 4 mm are used. For rigid EP impregnated textiles, the maximum grain size of the used concrete can go up to 8 mm. Therefore, UHPC with its grain size of usually less than 4 mm is an optimal material for this composition.

Regarding aspects of sustainability, it can be mentioned, that the high resistance to corrosion of textile reinforcement can lead to a reduced concrete cover, which means that the cross-section of structural components can be reduced as well. Several studies are dealing with the sustainability of the textile reinforcement [16, 17]. Furthermore, the recycling of textile-reinforced concrete, when comparing with ordinary steel-reinforced or fiber-reinforced concrete, with respect to separation of textile and surrounding concrete matrix, is relatively easy [18, 19].

2. Materials and Methods

The ongoing project investigates and compares the following types of material combinations:

- (i) UHPC with steel fibers
- (ii) UHPC with textile reinforcement
- (iii) UHPC with steel fibers and textile reinforcement

The paper presents and evaluates the test results, analyses the crack patterns and the crack development, and compares the failure modes.

2.1. Materials. The used textiles are epoxy-coated carbon and AR-glass textiles produced by the Solidian company. The distance of the rovings is the same 38 mm into the two horizontal directions, and the rovings have the same cross-sectional area into the two main directions. The main geometrical and mechanical properties of the textiles are summarized in Table 1.

The used fibers are commercial products manufactured from high strength steel wires. The fibers are straight by their product description but slightly curved in practice, with a

circular cross-section. They are coated with brass for corrosion protection. The main geometrical and mechanical properties of the fibers are summarized in Table 2.

The specimens were produced using a self-developed UHPC mixture either without fibers or with a fiber content of 2% by volume. Table 3 presents the mixture proportions of the applied UHPC and UHPFRC materials. The maximum grain size of the quartz sand was 0.4 mm. The mean compression strengths of the mixtures are in the range of 165 MPa and 180 MPa measured on cubes 28 days after casting. A summary of the main characteristics of the mixtures can be found in Table 4.

2.2. Methods. To determine the load bearing behavior of the different material combinations of UHPC with textile and fiber reinforcement, bending tests were performed following the recommendation of Kulas [12]. The test specimens were produced with the dimensions length \times width \times thickness equal to 700 \times 150 \times 30 mm. The textile reinforcement layer was placed 10 mm from the bottom surface and 20 mm from the top surface of the specimens, which was ensured with a two-part formwork. The warp direction of the textile was orientated in longitudinal direction to the axis of the specimen. Three specimens were produced, tested, and evaluated for each combination. The specimens were tested in a symmetric four-point bending test setup with a span of 600 mm. The test setup can be seen in Figure 1:

3. Results and Discussion

3.1. Load-Deflection Curves. Figure 2 depicts a comparison of the load-deflection curves derived from four-point bending tests. Figure 2(a) depicts a comparison of test results with carbon textile-reinforced UHPC, carbon textile-reinforced UHPFRC, and UHPFRC. The graphs show that the initial stiffness of the composites is very similar. After the first crack, carbon textile-reinforced UHPC plates exhibit strong drops in the load value at each new crack: after the crack appears, the specimen loses more than half of its load; then, the load level increases until the next crack appears at a slightly higher load level. This slow increase and sudden dropping behavior becomes less dominant later on, as more and more the textile reinforcement holds the load and drives the overall structural behavior.

In contrast, UHPFRC plates lose their initial stiffness gradually, without any pronounced load drop, and after the peak load, also the descending branch of the curve shows a gradual load decrease during the pull-out of the fiber reinforcement. The first crack at carbon textile-reinforced UHPFRC plates results in a significant stiffness change without a load drop. After that, the structural stiffness decreases gradually, but this change is not significant. Furthermore, the curves do not show any significant load dropping until the ultimate load.

Figure 2(b) depicts the comparison of the load versus deflection curves with glass textile-reinforced UHPC, UHPFRC, and UHPFRC without textile. The glass textile-

TABLE 1: Main properties of the used textiles (producer's data sheet).

Used textiles	Cross-sectional area of rovings (mm ²)	Axial distance (mm)	Cross-sectional area of reinforcement (mm ² /m)	Young's modulus (GPa)	Tensile strength (mean value) (MPa)
Solidian GRID Q95/95-CCE-38	3.62	38	95	220	3 200
Solidian GRID Q97/97-AAE-38	3.68	38	97	72	1 550

TABLE 2: Main properties of the used steel fibers (producer's data sheet).

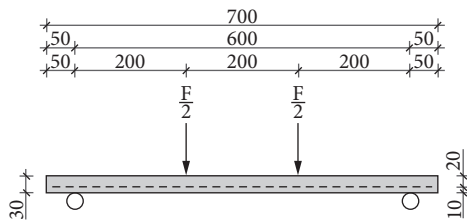
Used fibers	Length (mm)	Diameter (mm)	Length/diameter (-)	Young's modulus (GPa)	Tensile strength (mean value) (MPa)
Stratec Weidacon FM 0.20/15	15	0.2	75	200	>2000

TABLE 3: Mixture proportions of the applied UHPC and UHPFRC materials (in kg/m³).

Ingredient	UHPC	UHPFRC
Cement	867	850
Sand	883	865
Microsilica	146	143
Quartz powder	250	245
Water	199	195
Superplasticizer	20	20
Fiber	0	157

TABLE 4: Main properties of the used UHPC and UHPFRC mixtures 28 days after casting.

Used mixtures	Compression strength (MPa)	Splitting tensile strength (MPa)	Young's modulus (GPa)	Maximum grain size (mm)	Fiber content (vol %)
UHPC	166.3	7.9	44.7	0.4	0
UHPFRC	172.5	16.1	49.3	0.4	2



(a)



(b)

FIGURE 1: (a) Dimensions of the specimen and the test setup (mm). (b) The test setup during testing.

reinforced UHPC plates behave similar to the carbon textile-reinforced ones: they show pronounced repetitive load drops and increases during cracking. The increase of the peak load between these local maximums is, however, smaller, and the overall structural stiffness is lower, which is attributed to the significantly lower stiffness of the glass textile (Table 1). The characteristics of the load vs. deflection curves of glass textile-reinforced UHPFRC plates are similar to the carbon textile-reinforced UHPFRC: after the first crack, there are only few smaller load drops, while the structural stiffness

decreases gradually. The second part of the curves (considering deflections between 10 mm and 30–35 mm) is close to linear, and it is determined by the properties of the glass textile.

Comparing the three types of plates generally, the textile-reinforced UHPC has the lowest structural stiffness because of its repetitive load dropping behavior, the textile-reinforced UHPFRC shows significantly higher structural stiffness, and the UHPFRC shows the highest one, but that stiffness declines continuously because of the cracking

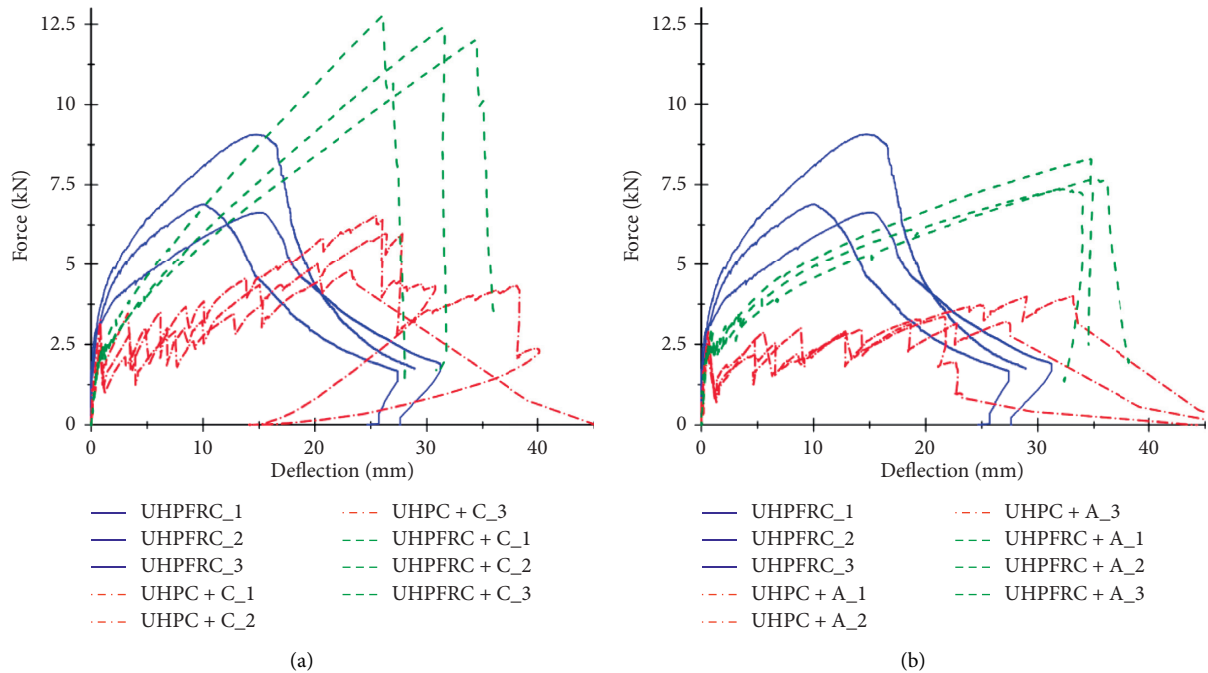


FIGURE 2: Comparison of load-deflection curves by using UHPC and UHPFRC with and without (a) carbon textile and (b) glass textile.

process. The tests approved that fiber reinforcement can effectively help textile-reinforced plates in the first part of the loading process (where the repetitive cracking of the concrete matrix drives the structural behavior) by bridging the cracks and limiting the crack opening, while the textile reinforcement can effectively hold larger loads, at a stage where the fiber reinforcement would reach its deformation capacity by pull-out without the textile.

Failure modes of the different plates are different as well. The UHPFRC plates have no well-defined failure point: after the ultimate load, the load slowly decreases with the increasing deflection, and the cracks open wider, but the specimens stay intact and can hold the residual load. The textile-reinforced UHPC plates split at maximum load in a way, that part of the concrete cover drops down (delamination), and then, later at even larger deformations, the textile breaks. In contrast, textile-reinforced UHPFRC plates do not show any sign of delamination. The load increases linearly with increasing deformation, the cracks open wider, until the textile reaches its failure and suddenly breaks.

While the scatter of the ultimate load is quite large in case of UHPFRC plates, it is relatively smaller with textile-reinforced UHPC plates and low with textile-reinforced UHPFRC plates. Similarly, the scatter of the deformation at the ultimate load is relatively large in the case of UHPFRC and textile-reinforced UHPC plates, but it is smaller at textile-reinforced UHPFRC plates.

Table 5 summarizes the main parameters of the load versus deflection curves: the mean ultimate load values, the mean deflection at the ultimate load, and the mean measured deflection just before final failure. Final failure of the specimen was reached when it collapsed or could not hold the load anymore, with the exception of UHPFRC plates,

where there is no definite loss of load bearing capacity. The numbers show, that the textile-reinforced UHPC fails at the lowest load: 3.5 kN at glass textile-reinforced plates and 5.8 kN at carbon textile-reinforced plates in the performed tests. The UHPFRC plates can hold higher loads around 7.5 kN on average. Combining textile and fiber reinforcement more than doubles the ultimate load compared with specimens only with textile reinforcement: 7.8 kN with glass textile (123% increase) and 12.4 kN with carbon textile (114% increase). Compared with only fiber-reinforced plates, the increase is only 4% in the case of glass textile and 65% in case of carbon textile. This means that the glass textile with its low load bearing capacity and stiffness cannot help effectively the UHPFRC plate, while interaction of carbon textile reinforcement with UHPFRC results in almost addition of the load bearing capacities of the two types of reinforcement (12.4 kN vs. 13.3 kN).

The deflection values in Table 5 show that UHPFRC plates reach their ultimate load at only 13.3 mm on average, while this value is almost doubling with textile-reinforced UHPC and almost two and a half times higher with textile-reinforced UHPFRC. Comparing the deflection values of textile-reinforced plates at the ultimate load, the presence of fibers increases this value by 48% for glass textile-reinforced plates and by 20% for carbon textile-reinforced plates. Mean deflection values before failure show that textile-reinforced UHPC plates fail at about 22% higher deflection compared to the deflection at the ultimate load, while textile-reinforced UHPFRC plates fail at only about 2% higher deflection. This means that textile-reinforced UHPFRC plates fail close to their peak load and behave less ductile than the same plates without fibers. On the other hand, this failure happens at least at two times higher load. In case of UHPFRC plates,

TABLE 5: Key values of the load-deflection curves.

Specimen types	Mean max load (kN)	Mean deflection at the ultimate load (mm)	Mean deflection before failure (mm)
UHPFRC	7.5	13.3	(28.8)
UHPC + glass textile	3.5	23.1	28.0
UHPC + carbon textile	5.8	25.6	31.5
UHPFRC + glass textile	7.8	34.1	35.1
UHPFRC + carbon textile	12.4	30.8	31.3

there is no well-defined failure point because at a slowly decreasing load level, it can reach three to five times higher deformations than observed at the ultimate load. The 28.8 mm deflection value in Table 5 is the point where the tests were stopped (on average), which is 2.2 times the deformation compared with its value at the ultimate load, but the specimens are not broken at that point. The measured values show that glass textile-reinforced UHPC plates fail at 12% lower deformation than carbon textile-reinforced UHPC plates, despite of the higher ultimate strain of the glass textile compared to carbon textile (around 2.0% vs. 1.5%), while the textiles do not reach their ultimate tensile strength neither. This observation fits to earlier experiences described in Mészöly et al. [20], and it is likely due to the transversal forces and damages in the textile caused by the cracked concrete. In comparison, glass textile-reinforced UHPFRC plates fail at 12% higher deformation than carbon textile-reinforced UHPFRC plates. The glass textile-reinforced plates can take the advantage of the fiber contribution (25% increase compared to the same plates without fibers), which results in a denser crack pattern, smaller crack opening values, and the consequently smaller transversal forces on the textile. In contrast, the carbon textile-reinforced UHPFRC plates fail at the same deflection level than the same plates without fibers.

3.2. Crack Distribution and Crack Widths. The tests were monitored using a photogrammetric measurement system with digital image correlation (DIC). With the DIC system, it is possible to observe and monitor the surface deformations, the crack pattern of the specimens, and measure the crack opening of every single crack with an accuracy of about one μm or the strain can be derived on the specified measurement range. Such type of measurement provides several advantages to traditional equipment: for example, the formation of cracks leads to a failure of attached strain gauges, whereas displacement transducers can only deliver information about a certain observation length and its total elongation; moreover, during abrupt rupture of a specimen, displacement transducers can be damaged. The DIC system allows on the other hand to monitor the full process from first loading to even after-peak behavior of a tested specimen. Table 6 summarizes some key values derived from the crack evaluation.

The first investigated value is the load where the first crack appears, which is defined where the largest crack mouth opening displacement (CMOD) reaches 0.01 mm. This parameter is the largest at UHPFRC plates, reaching 3.0 kN on average. The same parameter for textile-reinforced

UHPC plates is a little bit lower, 2.7 kN with glass textile, and 2.8 kN with carbon textile. Surprisingly, it is significantly lower for textile-reinforced UHPFRC plates, 2.1 kN with the glass textile and only 1.8 kN with the carbon textile. By back-calculating the tensile stress in the bottom surface of UHPC plates at the moment where the first crack appears, the tensile strength can be estimated. Based on the test results, it is 8.6 MPa on average, which is comparable with the measured splitting tensile strength of 7.9 MPa in Table 2.

The second investigated parameter is the load where the largest CMOD reaches 0.1 mm. Beside the load values summarized in Table 5, Figure 3 presents the crack pattern of the specimens when the largest crack reaches 0.1 mm. Figure 3(a) shows that the crack pattern is very dense at UHPFRC plates when the largest crack reaches 0.1 mm CMOD value: the plates depict 50–100 very small hairline cracks, which fill out the plate surface like a net. The UHPFRC plates hold 6.0 kN load at that phase. In case of UHPC plates (reinforced with glass or carbon textile, Figure 3(b) and 3(c)), the first crack opens wide abruptly (0.20 mm at 2.7 kN in case of glass textile and 0.15 mm at 2.8 kN in case of carbon textile-reinforced plates, in the moment when the first crack started to form). In comparison, fibers can effectively limit the opening of the cracks in case of plates reinforced with both fibers and textile: the cracks remain very small at the beginning, and then, they open wider at higher loads. As a result, when the largest crack reaches 0.1 mm at a significantly higher load level (3.4 kN for glass textile-reinforced UHPFRC and 3.8 kN for carbon textile-reinforced UHPFRC), there are already several similar cracks, Figures 3(d) and 3(e).

The third parameter is the CMOD value at a load level of 5 kN. Table 5 presents both the values of the largest crack width at 5 kN load and the typical, mean crack width value at 5 kN, and Figure 4 compares the crack patterns at 5.0 kN load level. The UHPFRC plates have 20–30 hairline cracks (Figure 4(a)). The largest crack opening values are measured between 30 μm and 60 μm , and the mean values are only between 10 μm and 30 μm . The shapes of the cracks are less regular and straight than observed at textile-reinforced plates. The glass textile-reinforced UHPC plates fail at a lower load level (3.5 kN in average); therefore, Table 5 gives no value, and there is no image of these plates in Figure 4. The carbon textile-reinforced UHPC plates have 6–7 cracks (Figure 4(b)) with a maximum crack opening of 1.1 mm and a mean crack opening value of 0.7 mm. These values are 20–50 times higher than the ones recorded with UHPFRC plates. When fibers are provided for textile-reinforced plates, the number of cracks roughly doubles (10–11 cracks for glass textile and 12–13 cracks for carbon textile-reinforced plates, Figures 4(c) and

TABLE 6: Key values from the crack evaluation.

Specimen types	First crack appears (kN)	Largest crack reaches 0.1 mm (kN)	Largest/mean crack width at 5 kN (mm)	Largest crack width at the ultimate load (mm)
UHPFRC	3.0	6.0	0.05/0.02	0.3
UHPC + glass textile	2.7	2.7	–	1.7
UHPC + carbon textile	2.8	2.8	1.1/0.70	1.3
UHPFRC + glass textile	2.1	3.4	0.34/0.20	1.3
UHPFRC + carbon	1.8	3.8	0.18/0.10	0.9
Textile				

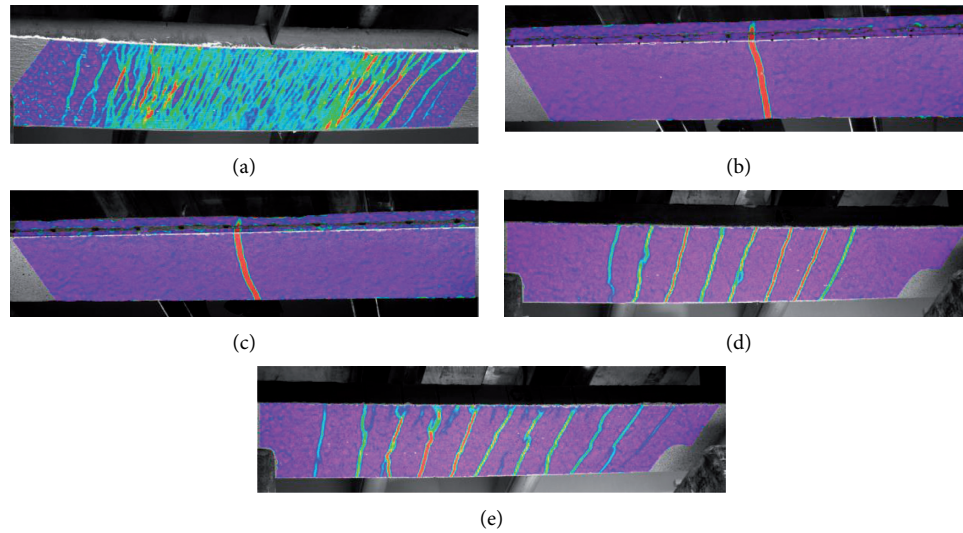


FIGURE 3: Crack pattern of the specimens at 0.1 mm crack opening. (a) UHPFRC, (b) UHPC + glass textile, (c) UHPC + carbon textile, (d) UHPFRC + glass textile, and (e) UHPFRC + carbon textile.

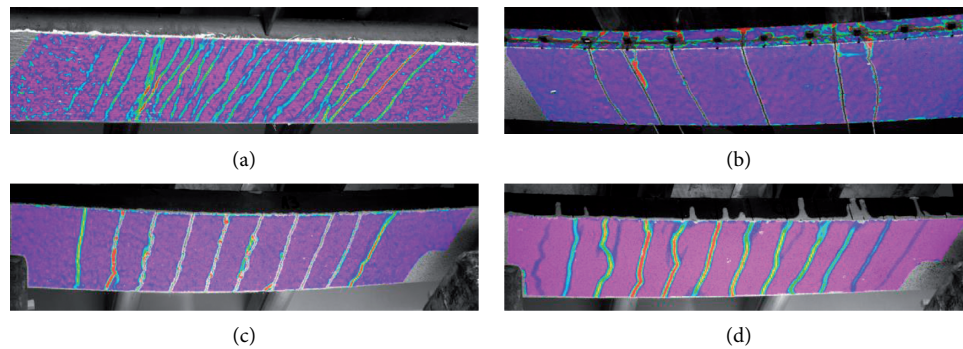


FIGURE 4: Crack pattern of the specimens at 5.0 kN load level. (a) UHPFRC, (b) UHPC + carbon textile, (c) UHPFRC + glass textile, and (d) UHPFRC + carbon textile.

4(d)) compared to the numbers observed for the same plates without fibers. With fibers, the plates reinforced with glass textile already reach a load level of 5.0 kN and show a largest crack opening value of 0.34 mm and a mean crack opening value of 0.20 mm. In comparison, the largest crack opening is 0.18 mm and the mean crack opening value is 0.10 mm for carbon textile-reinforced UHPFRC plates. These values are 85% (with other words 6.6 times) lower than without fibers.

The fourth investigated parameter is the largest CMOD value at the ultimate load level. Based on the test evaluation,

UHPFRC plates depict the smallest crack opening values again: the crack width reached only 0.3 mm at the maximum load. The largest crack opening was 4.4 times bigger (1.3 mm) at carbon textile-reinforced UHPC plates and 5.7 times bigger (1.7 mm) at the glass textile-reinforced UHPC plates. By adding fibers, the largest crack opening of textile-reinforced plates at the ultimate load decreases by 25–31% and reaches 1.3 mm in case of glass textile-reinforced UHPFRC and 0.9 mm in case of carbon textile-reinforced UHPFRC. Furthermore, it is worth mentioning that the load

values are 2–2.5 times higher for these specimens than for the ones without fibers.

4. Conclusions

The present paper compares the results of flexural tests on plates using UHPFRC, glass or carbon textile-reinforced UHPC, and glass or carbon textile-reinforced UHPFRC and investigates the effect of steel fiber reinforcement in case of textile-reinforced UHPFRC plates. The results back up the following most important conclusions when fibers are provided together with textile reinforcement:

- (i) The ultimate load is twice as high when comparing fiber-reinforced to nonfiber-reinforced TRC elements, and the scatter of the ultimate load values is smaller compared to both UHPFRC and TRC plates.
- (ii) The pronounced load dropping behavior that is typical for TRC elements can be avoided with the addition of steel fibers, and the load vs. deflection relation is more predictable and close to linear.
- (iii) The structural response during the cracking phase is significantly stiffer than the response for TRC elements without steel fibers.
- (iv) The deformation capacity and the deflection at the ultimate load are almost two and a half times higher than the respective values for UHPFRC without textile reinforcement.
- (v) The cracks remain very small at the beginning, and the further opening is delayed and observed only at higher load levels because the steel fibers are able to effectively limit the opening of the cracks. Furthermore, the number of (smaller) cracks increases, resulting in a more homogeneous stress distribution.
- (vi) Both steel fiber and textile-reinforced plates reach the 0.1 mm crack opening value at more than 30% higher load than TRC plates.
- (vii) At the chosen 5 kN load level, the crack opening values are 85% lower, and the number of cracks is double than in case of textile-reinforced UHPC plates, and the largest crack openings of TRC plates at the ultimate load decrease by 28% on average.

Concluding, the present test results verify a general advantageous mechanical behavior of specimens reinforced with the combination of fibers and textiles in comparison to the specimens reinforced with only fiber or textile reinforcement.

Data Availability

The data used to support this study are included within the article.

Conflicts of Interest

The authors declare that they have no conflicts of interest.

Acknowledgments

The authors would like to acknowledge the support of the Austrian Research Promotion Agency (CON_FIT project, grant number 866881). Likewise, the supply of material equipment by the companies Solidian and W&P is appreciated.

Supplementary Materials

Datasets of the load-deflection curves in the format of comma-separated values (CSV), are available in the Supplementary Materials. (*Supplementary Materials*)

References

- [1] P. Richard and M. Cheyrezy, "Composition of reactive powder concretes," *Cement and Concrete Research*, vol. 25, no. 7, pp. 1501–1511, 1995.
- [2] K. Droll, "Influence of additions on ultra high performance concretes—grain size optimisation," in *Proceedings of the International Symposium on Ultra High Performance Concrete, Schriftenreihe Baustoffe Und Massivbau*, no. 3, pp. 285–301, Kassel University Press, Kassel, Germany, September 2004.
- [3] H. Yazıcı, H. Yiğiter, A. Ş. Karabulut, and B. Baradan, "Utilization of fly ash and ground granulated blast furnace slag as an alternative silica source in reactive powder concrete," *Fuel*, vol. 87, no. 12, pp. 2401–2407, 2008.
- [4] E. Ghafari, H. Costa, E. Júlio, A. Portugal, and L. Durães, "Enhanced durability of ultra high performance concrete by incorporating supplementary cementitious materials," in *Proceedings of 2nd International conference on Microstructural-Related Durability of Cementitious Composites, RILEM Pro83*, pp. 1422–1430, Amsterdam, The Netherlands, April 2012.
- [5] N. Randl, T. Steiner, S. Ofner, E. Baumgartner, and T. Mészöly, "Development of UHPC mixtures from an ecological point of view," *Construction and Building Materials*, vol. 67, no. Part C, pp. 373–378, 2014.
- [6] A. Šajna, E. Denarié, and V. Bras, "Assessment of UHPFRC based bridge rehabilitation in Slovenia, two years after application," in *Proceedings of Hipermat 2012–3rd International Symposium on UHPC and Nanotechnology for High Performance Construction Materials, Schriftenreihe Baustoffe Und Massivbau*, no. 19, pp. 937–944, Kassel University Press, Kassel, Germany, March 2012.
- [7] E. Fehling, M. Schmidt, T. Teichmann, B. Kai, B. Roland, and M. Bernhard, "Entwicklung, dauerhaftigkeit und berechnung ultrahochfester betone (UHPC), DFG-forschungsbericht FE 497/1-1," in *Schriftenreihe Baustoffe Und Massivbau*, no. 1, Kassel University Press, Kassel, Germany, 2005.
- [8] T. Mészöly and N. Randl, "Shear behavior of fiber-reinforced ultra-high performance concrete beams," *Engineering Structures*, vol. 168, pp. 119–127, 2018.
- [9] M. Ricker, F. Häusler, and N. Randl, "Punching strength of flat plates reinforced with UHPC and double-headed studs," *Engineering Structures*, vol. 136, pp. 345–354, 2017.
- [10] NF P18-470, *Concrete–Ultra-high Performance Fibre-Reinforced Concrete–Specifications, Performance, Production and Conformity*, Association Française De Normalisation (AFNOR), Saint-Denis, France, 2016.
- [11] D. Čitek, P. Huňka, S. Řeháček, T. Mandlík, and J. Kolísko, "Testing of bond behavior of UHPC," *Advanced Materials Research*, vol. 1054, pp. 95–98, 2014.

- [12] O. Bruckermann, "Modelling the tensile behaviour of textile reinforced concrete," Ph.D. thesis, RWTH Aachen, Aachen, Germany, 2007.
- [13] M. Curbach and F. Jesse, "Eigenschaften und anwendungen von textilbeton," *Beton-Und Stahlbetonbau*, vol. 104, no. 1, pp. 9–16, 2009.
- [14] RILEM 201-TRC, "Textile reinforced concrete–state-of-the-art report of RILEM technical committee 201-TRC," in Report 36, W. Brameshuber, Ed., RILEM, Bagnoux, France, 2006.
- [15] C. H. Kulas, "Loadbearing behavior of impregnated textile reinforcements for concrete members," Ph.D. thesis, RWTH Aachen, Aachen, Germany, 2013.
- [16] P. Hájek, M. Novotná, A. Chira, C. Fiala, T. Vlach, and L. Laiblová, "Challenge of textile reinforced high performance concrete for sustainable construction," in *Proceedings of the Fib Symposium 2015*, Copenhagen, Denmark, May 2015.
- [17] N. W. Portal, K. Lundgren, H. Wallbaum, and K. Malaga, "Sustainable potential of textile-reinforced concrete," *Journal of Materials in Civil Engineering*, vol. 27, no. 7, pp. 1–12, 2014.
- [18] J. Kortmann, *Abbruch, Rückbau und Recycling Von C³-Bauteilen*, Carbon-Und Textilbetontage, Dresden, Germany, 2017.
- [19] S. Ofner, N. Randl, T. Mészöly, and B. Hofer, "Textile reinforcement in ultra high performance concrete—a sustainable material composition," in *Proceeding of the SGEM 2017–17th International Multidisciplinary Scientific Geo Conference*, pp. 683–694, Vienna, Austria, November 2017.
- [20] T. Mészöly, S. Ofner, and N. Randl, "Mechanical properties of glass and carbon textile reinforced UHPC," in *Proceedings of the Fib Symposium 2019*, pp. 289–296, Kraków, Poland, May 2019.

Research Article

A Study on the Wear Characteristics of Al7075 with Changes in Surface Roughness and Ti Thin Film Deposition Time

Jihye An,¹ Sunghoon Im,² Haneul Kang,¹ Hyunji Kim,¹ Yunyoong Yoo,³ Jungpil Noh,⁴ and Sunchul Huh⁴ 

¹Department of Energy and Mechanical Engineering Graduate School of Gyeongsang National University, Gyeongsang National University, Tongyeong 53064, Republic of Korea

²Department of Computer Applied Machinery, Changwon Campus of Korea Polytechnic, Changwon 51-88, Republic of Korea

³KP Aero Industries Co., Ltd., Gimhae 50875, Republic of Korea

⁴Department of Energy and Mechanical Engineering, Gyeongsang National University, Tongyeong 53064, Republic of Korea

Correspondence should be addressed to Sunchul Huh; schuh@gnu.ac.kr

Received 29 May 2020; Revised 8 September 2020; Accepted 15 September 2020; Published 25 September 2020

Academic Editor: Stefano Sorace

Copyright © 2020 Jihye An et al. This is an open access article distributed under the Creative Commons Attribution License, which permits unrestricted use, distribution, and reproduction in any medium, provided the original work is properly cited.

Mechanical parts have a problem of wear when used in extreme environments. Aluminum, most used in the industrial field, is a representative material of light weight, but its wear resistance is not good. To resolve the wear problem of such materials, research and development of surface thin film deposition technology has been increasing. Wear resistance was investigated after the Ti thin film was deposited by sputtering, one of the main methods of this technique. The smaller the surface roughness value and the thicker the thin film, the better the wear resistance. However, when a thin film is deposited for a predetermined time or less, the bonding strength with the base metal is lowered and the wear resistance is confirmed as low.

1. Introduction

Mechanical parts require light and high wear resistance. Aluminum alloys, which are representative materials of light weight, are widely used in manufacturing fields such as the automotive, aerospace, and defense industries because of their excellent mechanical properties and excellent ductility and high strength, toughness, and fatigue resistance [1–4]. However, when parts are used in the industrial field, there is a problem that wear occurs more than the basic properties of the material [5–7]. The resistance of the material can be increased by improving surface conditions such as hardness and roughness and reducing the coefficient of friction. For thin film deposition technology, techniques using hard materials such as chromium and titanium are best known. Therefore, in order to improve the wear problem, we intend to apply the surface thin film deposition technology [8].

Surface thin film deposition technology is a technique to improve the mechanical properties by forming a thin film on the surface of the material and is well known as one of the

main methods for improving the mechanical properties and wear behavior of the material [9–12]. In surface thin film deposition technology, properties of coating methods such as deposition rate, thin film thickness, and bonding of substrate and coating can greatly affect surface quality [13]. Various methods such as sputtering, PLD (pulsed laser deposition), and DLC (diamond-like carbon) have been studied for the manufacture of thin films [14], and among them, magnetron sputtering methods having high adhesion are most commonly used [15, 16]. Majzoobi et al. [8] studied the fatigue behavior of Al7075 alloy by applying surface treatment technology and Ti coating. As a result of the experiment, it was found that fatigue life can be greatly reduced at high working stress.

Metal surface roughness is an important factor in determining mechanical properties. The surface of the material looks smooth, but in reality, there is surface roughness depending on the type of machining. This is an important factor in determining the mechanical properties of the surface. Depending on the purpose of use, there should be no

roughness to prevent wear. Therefore, surface roughness is directly related to the life of the equipment. However, the Ti coating material, which has the advantage of wear resistance, is accompanied by tribological phenomena such as abrasion and fusion due to the extreme friction with the counterpart material and the harsh working environment [17]. Therefore, the selection of surface roughness is a very important factor.

In this paper, the wear characteristics were investigated by sputtering Ti thin films on Al7075-T6 with a different surface roughness. The surface roughness was measured by applying a surface roughness to the base metal, and a Ti thin film was deposited to perform the wear test. In addition, the surface of each specimen was observed using an indentation and a SEM (scanning electron microscope).

2. Materials and Methods

In this study, Al7075, which is widely used as an aircraft component, was selected as the base metal and the components of Al7075 are shown in Table 1. The base metal was processed into a cylindrical shape having a diameter of 32 mm and a thickness of 10 mm. To investigate the wear characteristics according to surface roughness and thin film deposition time, a total of 16 specimens were prepared by combining four types according to surface roughness and four types according to thin film deposition time. Roughness was measured by polishing the surface with sandpaper #400, #800, #1600, and #0.3 μm size alumina powder, and then, Ti thin films were deposited up to 90' at 30' intervals. The unit of surface roughness is Ra, which is the roughness value of arithmetic mean.

The equipment used for thin film deposition is the DC magnetron sputtering equipment. Sputtering is a process in which gas particles collide with the target, and the target particles are released and deposited on the surface. Target was made of Ti and sputtered at the same time by fabricating specimen holder to sputter four kinds of specimens with a different surface roughness at once under the same conditions. Table 2 shows the conditions used to deposit the thin films. The test conditions for all specimens were set identical except for the deposition time. In addition, the surface roughness and deposition time for each specimen are summarized in Table 3.

TRIBOSS PD-102 friction and wear tester was used to analyze the wear resistance of each specimen. The ball used in the experiment was a zirconia ball (ZrO_2) with a diameter of 12.7 mm. In addition, the rotation speed of the ball was set to 60 RPM and the experiment time 30 minutes; the load was 0.2 kg, and the ball on disk test sliding track diameter of the device was 11.5 mm.

The wear tracks produced after the experiments were observed using an SEM. In addition, the component analysis was carried out using EDS (energy dispersive spectroscopy), which can analyze the composition and content of the sample in a short time.

After the wear test, the AIS-3000 indentation equipment was used to measure the hardness of each specimen. Indentation is a device that can repeatedly measure the change

in indentation depth according to indentation load by using a small indenter and evaluate the hardness and tensile properties through the result. This method is a Vickers hardness measurement, and the unit is Hv. The test was measured 10 times for each specimen, and the average value was calculated.

3. Results and Discussion

3.1. Surface Roughness. Table 4 shows roughness values according to the polishing type, and data on the average values were measured five times for each specimen. As a result of the measurement, the higher the particle size, the lower the surface roughness value, and the #alumina polished specimen had a roughness of about Ra (roughness value of arithmetic mean) = 0.23.

3.2. Thin Film Thickness. Figure 1 is a SEM photograph of thin film thickness. The thickness of the 30' deposited specimen was 0.51 μm , the thickness of the 60' deposited specimen was 1.10 μm , and the thickness of the deposited specimen for 90' was measured to be 1.58 μm . Therefore, it can be seen that the thin film thickens by about 0.5 mm each time it is deposited for 30 minutes.

3.3. Surface Hardness. Table 5 shows the surface hardness values of each specimen. Both the specimen and the base metal on which the thin film was deposited showed hardness values between about 150 and 160 Hv regardless of surface roughness and thin film thickness. The standard deviation values for this data are shown in Figure 2. This result is considered because the indenter is pressed deeper than the thickness of the thin film during the hardness measurement.

3.4. Coefficient of Friction. Figure 3 shows the friction coefficient according to the surface roughness. According to Lee [18], the lower the surface roughness value, the lower the friction coefficient, and according to Song et al. [19], the higher the thickness is, the lower the friction coefficient is. In this paper, results similar to the above documents are also shown. Looking at the graphs in Figures 3(a)–3(c), it can be seen that, as the deposition time increases, the friction coefficient decreases. Thus, in general, Al materials belonging to roughness of approximately $R_a = 0.3\sim 0.45$ are considered to have improved wear resistance as the thin film becomes thicker.

On the contrary, in Figure 3(d), 16* of the graph, the friction coefficient is rather high. Therefore, wear resistance is considered to be inferior. It is thought that this is because the thin film is excessively thick and the base metal and the bonding strength are weakened. Also, the 30' sputtered specimen showed similar coefficient of friction as the base metal. Thus, it is judged that the wear resistance is not affected when the thin film is below a certain thickness.

Based on the above results, the best wear resistant specimen was 12* which was sputtered for 60' after polishing

TABLE 1: Chemical compositions of Al7075-T6.

Al7075	Chemical components									
	Al	Si	Fe	Cu	Mn	Mg	Zn	Cr	Ti	Etc.
	87.1~91.4	0.4	0.5	1.2~2.0	0.3	2.1~2.9	5.1~6.1	0.18~0.28	0.2	0.15

TABLE 2: Sputtering conditions for thin film deposition.

Film material	Ti
DT (deposition time)	30', 60', 90'
Base vacuum (torr)	5.0×10^{-6}
Working vacuum (torr)	2.0×10^{-3}
Plasma factor (w)	200
Temperature	RT

TABLE 3: Deposition time according to surface roughness.

	Surface roughness (sandpaper polishing number)				
	#400	#800	#1200	#Alumina (0.3 μ m)	
	0'	1*	2*	3*	4*
Deposition time (min)	30'	5*	6*	7*	8*
	60'	9*	10*	11*	12*
	90'	13*	14*	15*	16*

TABLE 4: Surface roughness value (average).

Type	#400	#800	#1200	#Alumina
Surface roughness (Ra)	0.45	0.35	0.31	0.23

with #alumina. In addition, quantitative analysis was performed through surface observation and wear comparison.

3.5. Surface Observation. Figure 4 shows a magnification 40x of the specimen surface after the wear test. In the specimen (Figure 4(a)) on which the thin film was deposited, the wear track was sharply narrowed relative to the base metal (Figure 4(b)) on which the thin film was not deposited. It is thought that this is from the increase in surface hardness of the specimen because of the thin film, resulting in less wear than the relatively soft base metal. In particular, this phenomenon was found in 90' sputtered specimens in which thick films were deposited, and 12 specimens polished with #alumina were the most frequent. It is thought that the thin film deposited on the smooth surface is relatively easily peeled off, and the debris dropped out is partially deposited on the ball during the wear test to accelerate the wear.

Figure 5 shows the component analysis of the specimen surface: Figure 5(a) is all detected as Ti because the thin film was deposited; Figure 5(b) is a graph of the component analysis of the track part subjected to the wear test. Looking at Figure 5(b), it can be seen that O, Na, Mg, and Zn components appeared in addition to Al and Ti. This is a component contained in Al7075, an aluminum alloy, and thus appears in the analysis results. It is also believed that Ti was measured on the peeled thin film.

Table 6 summarizes the wear track widths. Measurements were made at regular intervals and averaged. The wear tracks of the 30' and 60' sputtered specimens and the base metal became narrower as the roughness decreased, whereas the wear tracks of the 90' sputtered specimens became wider as the roughness decreased. It is considered that the specimens sputtered for 90' were relatively easily peeled off because the thin films were deposited at low roughness. In addition, the longer the thin film deposition time, the narrower the wear track width. Therefore, it is thought that the thin film deposition time affects the wear resistance.

3.6. Wear Loss. Figure 6 is a graph that calculates the amount of wear by measuring the weight before and after the wear test. In the 30' and 60' sputtered specimens and those without thin films, the lower the roughness, the lower wear loss. In particular, it was confirmed that all 60' sputtered specimens had lower wear loss than the base metal.

Conversely, in 90' sputtered specimens, the amount of wear increases as the roughness value decreases. The reason for this is considered that the relatively thick thin film reduces the bonding force with the base metal and easily peels off. According to Vega-Morón et al. [20], the adhesion of the thin film deposited for 60 minutes was superior to the thin film deposited for 90 minutes. In fact, when Ti was deposited on aluminum for more than 90 minutes, a phenomenon in which the thin film detached from the base material occurred. After the wear test, it was confirmed from the SEM observation that the adhesion was poor in the specimen deposited for 90 minutes. Figure 7 is a SEM image of a thin film separation phenomenon.

Therefore, the wear resistance of 60' sputtered (no. 12) specimens after polishing with #alumina was the best, and the surface roughness and the thickness of the thin film directly affect the wear resistance.

3.7. Graph Analysis of Average Wear Loss and Average Friction Coefficient. Figure 8 is a graph showing the average of the entire specimen according to the surface roughness and the deposition time of the thin film: Figure 8(a) is the average wear loss according to the surface roughness and thin film deposition time. According to Zuiker et al. [21], there are reports that the smaller the surface roughness, the lower the coefficient of friction, and in Figure 8, it can be seen that the friction coefficient value tends to decrease as the surface roughness value decreases. The curve according to the thin film deposition time in Figure 8(a) shows the smallest value when deposited for 60'. Figure 8(b) is a graph of the average

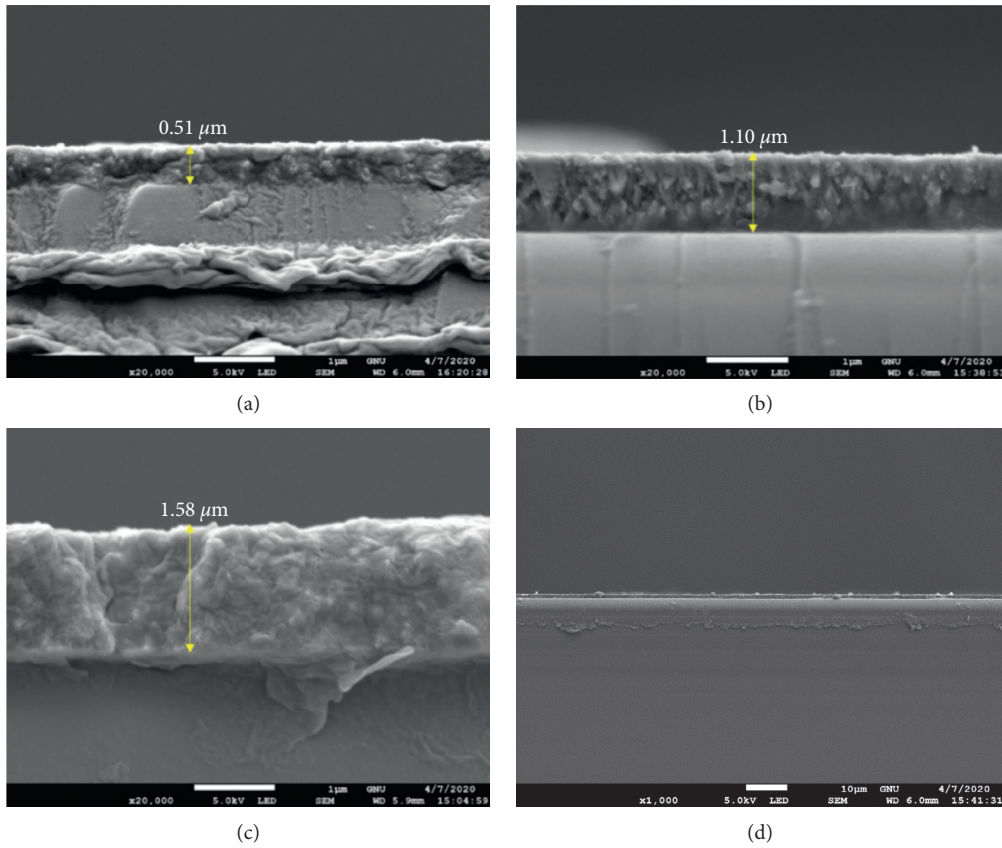


FIGURE 1: Photograph of thin film thickness using SEM equipment: (a) 30' sputtered specimen; (b) 60' sputtered specimen; (c) 90' sputtered specimen; (d) thin film low magnification photo.

TABLE 5: Surface hardness value (average).

Type	1*	2*	3*	4*	5*	6*	7*	8*
Surface hardness (Hv)	148	159	157	157	147	153	150	153
Type	9*	10*	11*	12*	13*	14*	15*	16*
Surface hardness (Hv)	154	158	149	153	153	159	148	153

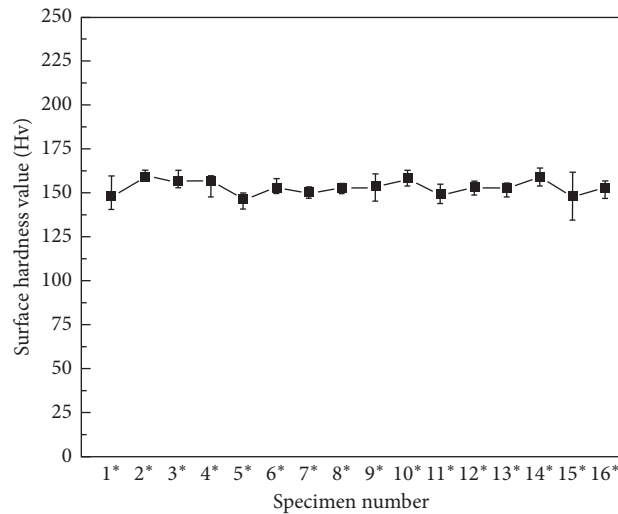


FIGURE 2: Standard deviation graph of surface hardness.

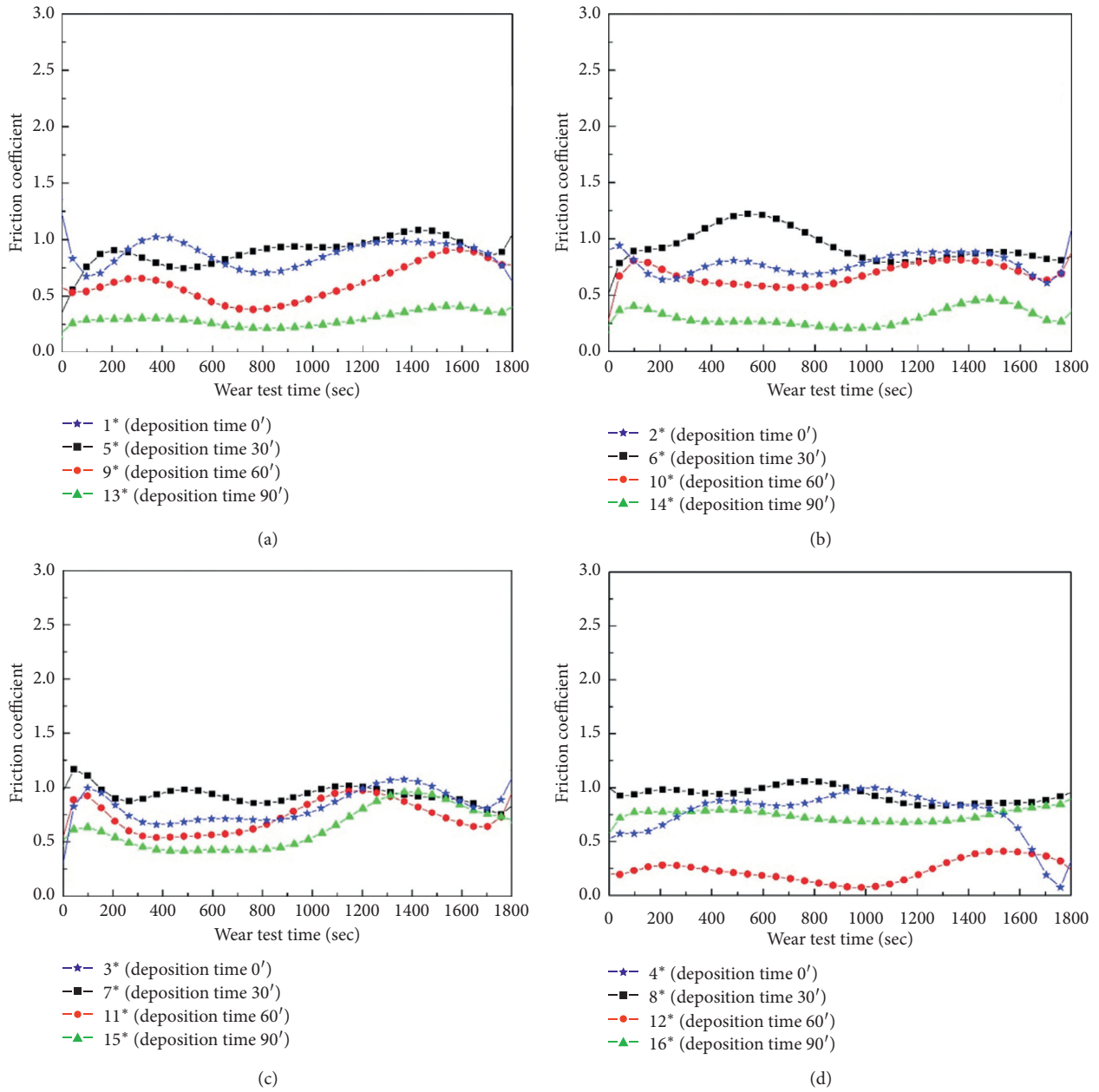


FIGURE 3: Friction coefficient graph by surface roughness: (a) polished with #400; (b) polished with #800; (c) polished with #1200; (d) polished with #alumina.

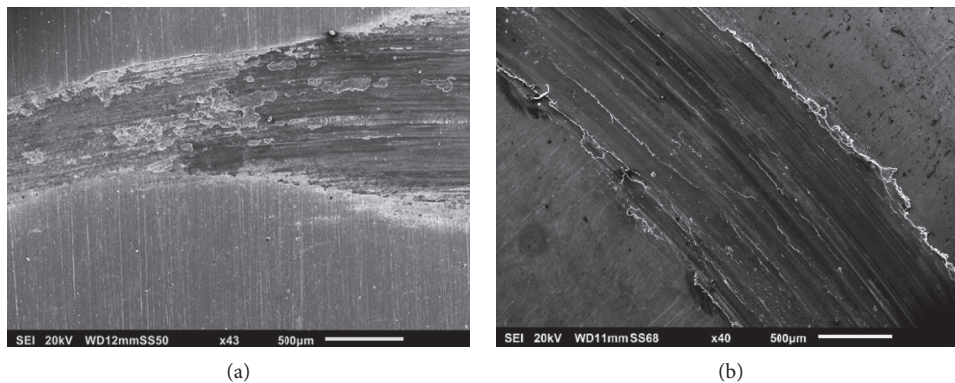


FIGURE 4: Photograph of SEM wear track: (a) thin film deposited specimen (15*); (b) specimen without thin films (4*).

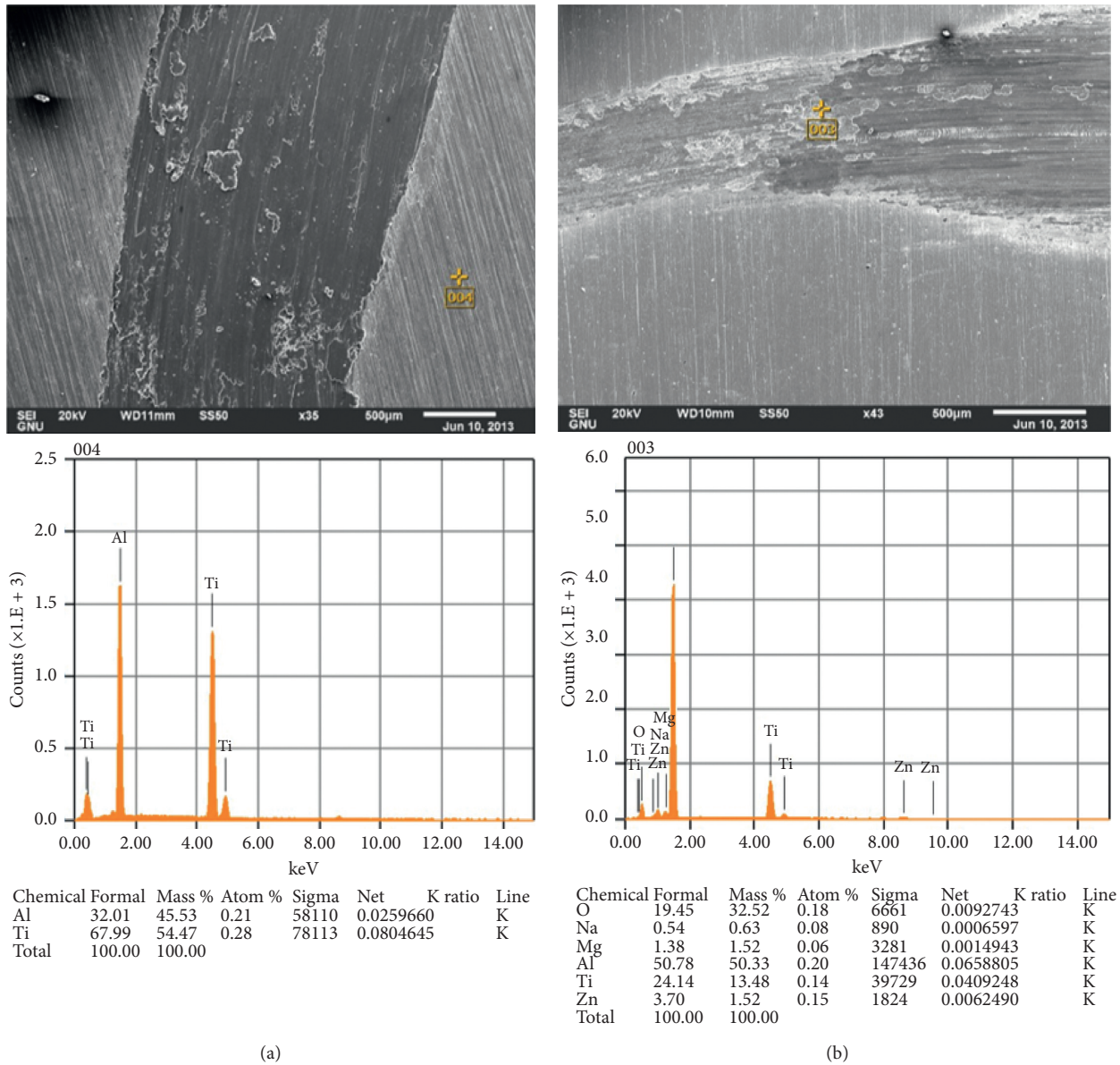


FIGURE 5: Photograph of EDS analysis: (a) EDS of thin film deposition part (6*); (b) EDS of track subjected to wear test (15*).

TABLE 6: Average of wear track width.

Type	1*	2*	3*	4*	5*	6*	7*	8*
Wear track width (mm)	1.39	1.40	1.40	1.32	1.60	1.50	1.38	1.47
Type	9*	10*	11*	12*	13*	14*	15*	16*
Wear track width (mm)	1.28	1.28	1.00	0.80	0.83	0.84	0.97	0.95

wear loss and the average friction coefficient according to the surface roughness. From the friction coefficient and wear loss curve, the average of specimens polished with alumina was the lowest. When combining the graphs of Figures 8(a) and 8(b), it can be seen that the 60' deposited specimen after

polishing with alumina has the best wear resistance. This means 12* specimens, and it can be seen that the abrasion resistance of 12* specimens is the best even when the results such as the wear loss and the width of the wear track mentioned in the previous contents of the paper are seen.

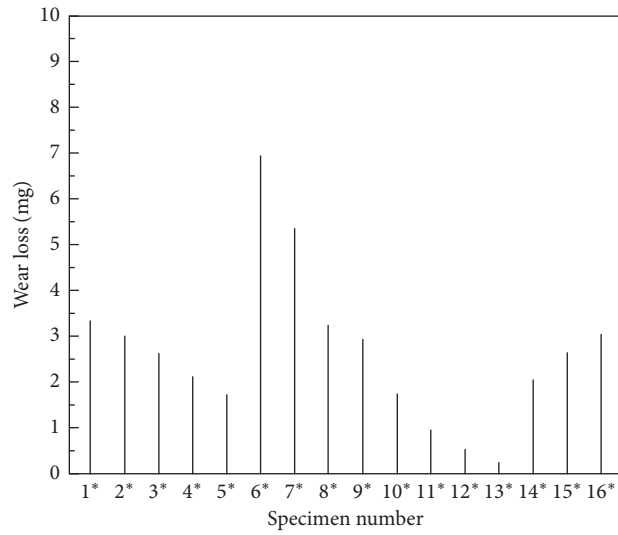


FIGURE 6: Wear loss graph by thin film deposition time.

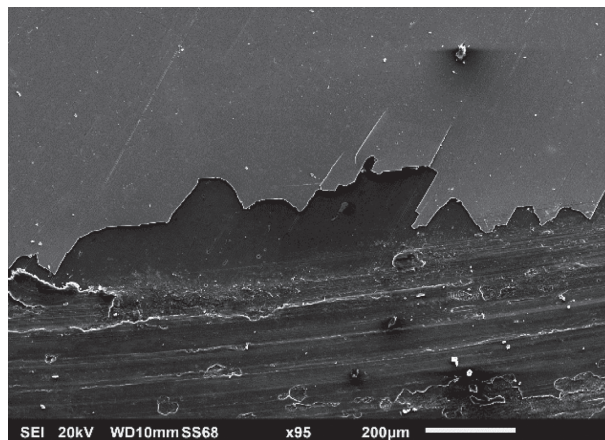


FIGURE 7: Photograph of thin film detachment around the abrasion test track (90' sputtered specimen, 16*).

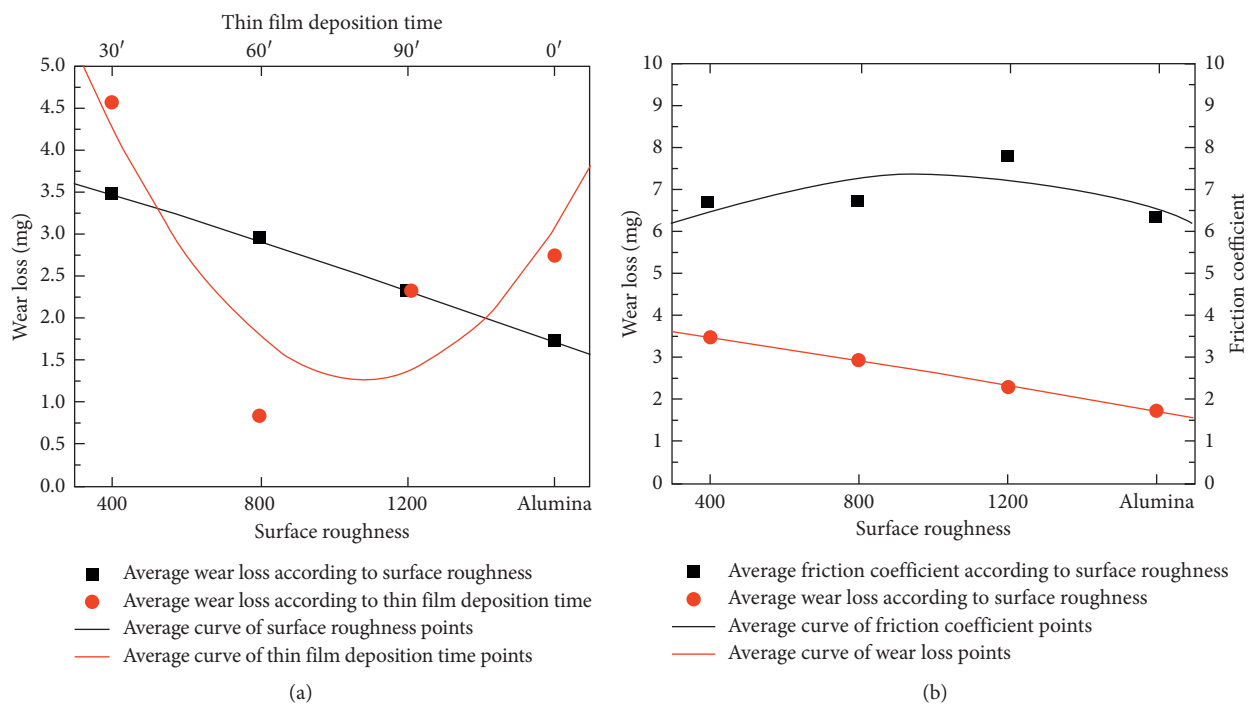


FIGURE 8: Graph organized according to average of wear loss and average of friction coefficient: (a) average of wear loss according to surface roughness and thin film deposition time; (b) the average of friction coefficient and the average of wear loss according to the surface roughness.

4. Conclusions

In this study, the wear test was conducted to investigate the effect of surface roughness and thin film thickness on wear characteristics. And the following conclusions were made:

- (1) As a result of the roughness measurement, the lower the particle size of the abrasive, the lower the roughness value, and the specimen polished with alumina has a roughness of about 0.23. As a result of measuring the thickness of the thin film, it is thickened by about $0.5\ \mu\text{m}$ each time the thin film is deposited for 30 minutes.
- (2) As a result of the friction coefficient analysis, the smaller the surface roughness value and the thicker the thin film, the lower the friction coefficient, but the 90' deposition resulted in a high friction coefficient when the surface was smooth. It is thought that the thin film detached from the base metal is transferred to the ball, which is the counterpart, and the transferred thin film debris accelerates the wear.
- (3) As a result of the surface observation, the wear tracks of the specimen (a) on which the thin film was deposited were sharply narrowed relative to the base metal (b) on which the thin film was not deposited. It is thought that the thin film deposited on the smooth surface is relatively easily peeled off, and the debris dropped out is partially deposited on the ball during the wear test to accelerate the wear. When the thin film was deposited for more than 90 minutes, it was confirmed that the adhesion of the thin film was poor.
- (4) As a result of analyzing the average wear and friction coefficients for the entire specimen, the lowest wear and friction coefficient values were obtained when 60 minutes of deposition after polishing with alumina. It can be seen that this corresponds to the 16* specimen.

In conclusion, the smaller the surface roughness value and the thicker the thin film, the better the abrasion resistance, but if the film becomes thicker than a certain level, $1.5\ \mu\text{m}$ (90' sputtering), it is considered that the adhesion between the thin film and the base metal is poor and it is easily peeled off so that it does not affect the wear resistance. Therefore, based on the above results, we have identified the most improved abrasion resistance of the 16* specimen with narrow track width and the lowest amount of abrasion, and the surface roughness and thickness of the thin film have a direct effect on abrasion resistance. Based on the results of this study, surface thin film deposition technology can be used in the mechanical and industrial fields, and further experiments on surface thin film deposition technology will be conducted based on the results of this study in the future.

Data Availability

All data used to support the findings of this study are included within the article.

Conflicts of Interest

The authors declare that they have no conflicts of interest.

Acknowledgments

This project was supported by the Basic Science Research Program through the National Research Foundation of Korea (NRF) funded by the Ministry of Science, ICT and Future Planning (no. 2018R1A5A5A05022883). And "Overseas order-linked aviation parts industry process technology development in 2019" of the Korea Institute for Advancement of Technology (KIAT) granted financial resource from the Ministry of Trade, Industry & Energy, Republic of Korea (P0010339).

References

- [1] E. S. Kim, "A study on the evaluation of wear-resistance in Al 7075 alloys," *Journal of the Korean Society of Mechanical Technology*, vol. 2016, pp. 102–105, 2016.
- [2] P. Rambabu, N. Eswara Prasad, V. Kutumbarao, and R. Wanhill, *Aerospace Materials and Material Technologies*, Springer, Berlin, Germany, 2017.
- [3] M. Ohring, *Engineering Materials Science*, Academic Press, Cambridge, MA, USA, 0-12-524995-0, 1995.
- [4] G. S. Was and R. M. Pelloux, "The effect of shot peening on the fatigue behavior of alloy 7075-T6," *Metallurgical Transactions*, vol. 10, no. 5, 1979.
- [5] M.-S. Kim, J.-H. Kho, and S.-H. Kim, "A study on the friction and wear characteristic of TiAlN and CrAlN coating on the SKD61 extrusion mold steel for 6xxx aluminum alloy," *Journal of the Korean Institute of Surface Engineering*, vol. 43, no. 6, pp. 278–282, 2010.
- [6] C. B. In and S. S. Chun, "Wear behavior of TiN coatings deposited by plasma assisted chemical vapor deposition," *KJMR*, vol. 3, no. 5, pp. 451–458, 1993.
- [7] H. Zhang, X. Qiu, X. Zhao, and D. Xu, "Effect of surface self-nanocrystallization on friction and wear behavior of Al7075-T6511 alloy," *Materials Research Express*, vol. 6, no. 11, Article ID 115031, 2019.
- [8] G. H. Majzoobi, J. Nemati, A. J. Novin Rooz, and G. H. Farrahi, "Modification of fretting fatigue behavior of AL7075-T6 alloy by the application of titanium coating using IBED technique and shot peening," *Tribology International*, vol. 42, no. 1, pp. 121–129, 2009.
- [9] J. H. Jang, S. H. Tak, Q. Jang, C. S. Huh, and S. K. Lyu, "Effect of the Ti-series coating on the friction and wear characteristics of SCM415 steel," *Journal of the KSTLE*, vol. 26, no. 3, pp. 162–166, 2010.
- [10] H.-S. Yu and H.-B. Park, "Study on the improvement of wear properties of automobile elements in titanium alloy coated," *The Journal of Korea Navigation Institute*, vol. 17, no. 5, pp. 574–580, 2013.
- [11] D. S. Kim, T. E. Fischer, and B. Gallois, "The effects of oxygen and humidity on friction and wear of diamond-like Carbon films," *Metallurgical Coatings and Thin Films 1991*, vol. 49, p. 537, 1991.
- [12] H. Renondeau, B. L. Papke, M. Pozebanckukz, and P. P. Parthasarathy, "Tribological properties of diamond-like Carbon coatings in lubricated automotive applications," *Proceedings of the Institution of Mechanical Engineers, Part J*:

- Journal of Engineering Tribology*, vol. 223, no. 3, pp. 405–412, 2009.
- [13] G. H. Majzoobi and M. Jaleh, “Duplex surface treatments on Al7075-T6 alloy against fretting fatigue behavior by application of titanium coating plus nitriding,” *Materials Science and Engineering: A*, vol. 452-453, pp. 673–681, 2007.
 - [14] J. I. Jung and J. S. Yang, “Trend and prospect of thin film processing technology,” *Journal of the Korean Magnetics Society*, vol. 21, no. 5, pp. 185–191, 2011.
 - [15] T. H. Kim, “Characteristic study on tribological characteristic of dlc film deposited on graphene layer thesis for a degree of psnu,” 2013.
 - [16] M. V. Kirichenko, R. V. Zaitsev, A. I. Dobrozhan, G. S. Khrypunov, and M. M. Kharchenko, “Adopting of DC magnetron sputtering method for preparing semiconductor films,” in *Proceedings of the 2017 IEEE International Young Scientists Forum on Applied Physics and Engineering (YSF)*, Lviv, Ukraine, October 2017.
 - [17] J. Y. Lee, “A study of corrosion resistance and adsorption property of calcareous deposit according to steel surface roughness,” Master thesis, Gyeongsang National University, Jinju, Republic of Korea, 2018.
 - [18] H. Y. Lee, “A study of sliding friction and wear properties for PTEE layer coated on steel,” *Journal of the KSTLE*, vol. 24, no. 2, pp. 96–103, 2008.
 - [19] M. H. Song, J. G. Lee, and Y. S. Kim, “Friction and wear behavior of ultra-thin TiN film during sliding wear against alumina and hardened steel,” *Korea Journal of Materials Research*, vol. 10, no. 1, pp. 62–68, 2000.
 - [20] R. C. Vega-Morón, G. A. Rodríguez Castro, D. V. Melo-Máximo, J. V. Méndez-Méndez, L. Melo-Máximo, and J. E. Oseguera-Peña, “Adhesion and mechanical properties of Ti films deposited by DC magnetron sputtering,” *Surface and Coatings Technology*, vol. 349, pp. 1137–1147, 2018.
 - [21] C. Zuiker, A. R. Krauss, D. M. Gruen et al., “Physical and tribological properties of diamond films grown in argon-carbon plasmas,” *Thin Solid Films*, vol. 270, no. 1-2, p. 154, 1995.

Research Article

Study on Void Structure Reconstruction of Asphalt Mixture by X-Ray Computed Tomography and Otsu's Method

Jiantong Zhang ^{1,2}, Jun Yang ³, Tiejun Liu,¹ Rongxing Cai,¹ and Rui Yang⁴

¹Shenzhen Municipal Engineering Corporation, Shenzhen 518109, China

²School of Civil and Transportation Engineering, Guangdong University of Technology, Guangzhou 510006, China

³School of Transportation, Southeast University, 2#Sipailou, Nanjing, Jiangsu 210096, China

⁴Department of Civil and Architecture Engineering, Tianhe College of Guangdong Polytechnic Normal University, Guangzhou 510540, China

Correspondence should be addressed to Jun Yang; yangjun@seu.edu.cn

Received 11 March 2020; Revised 24 April 2020; Accepted 13 July 2020; Published 31 August 2020

Academic Editor: Stefano Sorace

Copyright © 2020 Jiantong Zhang et al. This is an open access article distributed under the Creative Commons Attribution License, which permits unrestricted use, distribution, and reproduction in any medium, provided the original work is properly cited.

The purpose of this paper is to obtain the pore distribution of asphalt mixture accurately by nondestructive technology. Specimens prepared with four gradations of asphalt mixtures were scanned using X-ray computed tomography (CT) which was used to measure air void sizes at different depths within specimens. The air void distributions of obtained CT images were analyzed using ring blocking segmentation combining Otsu's method, which provided an accurate estimate of air voids in asphalt mixtures. The image processing results showed that air void distribution was not uniform in the specimens; higher air void concentrations were found at the top and bottom of the specimen, and lower, in the rest of the sample depth. The air void sizes of SUP13 and AC13 are mainly distributed between 0.15 to 0.2 mm, while PA13 and SMA13 are 0.4 to 0.65 mm and 0.4 to 0.7 mm, respectively. It is believed that the CT pictures processed by the ring blocking segmentation combining Otsu's method is feasible and rational to capture the air voids size and content of asphalt mixtures.+

1. Introduction

Performances of asphalt mixtures are dependent on the volume of aggregate, asphalt binder, as well as air voids. Specifically, the stiffness of the mixture is highly related to the air void content of the mixture. It is generally accepted that air voids play an important role in determining the resistance of asphalt mixtures to major pavement distresses including rutting, fatigue cracking, and low temperature cracking [1]. The research shows that stiffness and compressive strength increase with decreasing air void content, when the binder content is kept constant [2]. Air void content also influences the durability of asphalt mixes in terms of aging and stripping. For example, low air void content minimizes the aging of the asphalt binder films within the aggregate mass, the possibility of water penetrating into the mix, and stripping the asphalt binder off the

aggregates [3]. It is also found that low air void content can lead to asphalt bleeding [4], while high air voids may result in early aging processes of the mixture, which make it prone to moisture damage, cracking, and pavement deterioration [5].

Air void content is a common parameter used to characterize the void structure of compacted asphalt mixtures [6]. It should be noted that the level of homogeneity of the distribution of air voids inside the asphalt course has significant impacts on the response of the material [7–11]. It is necessary to further study the characterization of air voids such as void's size including radius and area of air void, distribution, and content. However, it is difficult to obtain the air void characterization by using traditional techniques. Therefore, the computer imaging technology and nondestructive techniques which can solve the problem described above and have the ability to characterize internal structure

of materials [12–14] were applied in this study. First of all, CT technology is used to scan asphalt mixture specimens. The microstructure characteristics of asphalt mixture, such as voids and coarse aggregate, are studied using Otsu image processing method, MATLAB software, and image processing software, and then the virtual asphalt mixture specimen is reconstructed.

2. Objectives

The objective of this study is to investigate the air void distribution (i.e., air void content and air void size) using X-ray CT, Otsu image processing method, and MATLAB software. Image analysis software and computer algorithms were used to analyze the X-ray CT images and quantify the air void content, size distribution, and connectivity.

3. Test Materials and Sample Preparation

Specimens with 150 mm in diameter and 165 mm in height were fabricated using the superpave gyratory compactor (SGC). In order to obtain high definition CT picture, the specimens were further cored into 50 mm in diameter and 75 mm in height for test purposes. Four types of asphalt mixtures known as AC13, SMA13, PA13, and SUP13 were studied in details. The aggregate gradations for the four mixtures are shown in Table 1.

SBS-modified asphalt was used in AC13, SUP13, and SMA13, and high-viscosity asphalt was used in PA13. The properties of SBS-modified asphalt and high-viscosity asphalt are shown in the Table 2. The optimum binder content is 5.36%, 5%, 5.9%, and 4.85% for AC13, SUP13, SMA13, and PA13, respectively. The air void content is 4.7%, 4.1%, 4.0%, and 18.5% for AC13, SUP13, SMA13, and PA13.

4. X-Ray CT Scanning and Image Analysis Techniques

4.1. Image Scanning Analysis Study. The specimens were nondestructively scanned using an X-ray CT machine to generate a map representing the density at every point in the microstructure with the resolution of approximately 0.083 mm/pixel. Horizontal two-dimensional image slices were captured relative to the specimen's height from bottom to top at every 0.1 mm interval. 750 CT images were obtained using X-ray CT scanning for each specimen. The 8-bit grayscale images have a range of pixel intensities from 0 (pure black) to 255 (pure white). The geometry of the cylindrical specimen and an example of a captured X-ray CT image are shown in Figure 1. Two imaging software packages, MATLAB, and Image-Pro Plus, were used to process and analyze the CT images.

4.2. Otsu's Method. In image segmentation, threshold segmentation is common and effective method especially when the objective and background grayscale are distinctively different. Otsu [16] presented the maximum class square error method (that is, Otsu's method) which was simple,

TABLE 1: Compositions and aggregate gradations of asphalt mixtures.

Sieve size (mm)	% passing by weight			
	AC13	SUP13	SMA13	PA13
16	100	100	100	100
13.2	95.9	97.1	96.7	97.7
9.5	76.8	78.8	59.1	70.2
4.75	50.7	53.0	25.5	21.2
2.36	34.4	32.5	22.0	16.4
1.18	25.2	19.9	18.3	12.6
0.6	18.3	15.3	14.9	9.1
0.3	13.5	9.4	12.8	6.9
0.15	10.6	7.2	11.7	5.8
0.075	7.2	5.5	10.5	5.1

Note: the number of each mix represents the nominal maximum aggregate size.

adaptive, and widely used in threshold segmentation. Otsu's method was used to characterize the microstructure of asphalt mixtures [17].

In Otsu's algorithm, supposing the image has L gray levels (the gray value ranges from $[1, 2 \dots L]$) and considers the pixel of which gray value is i , so the total pixel numbers n_i are obtained by

$$N = \sum_{i=0}^{L-1} n_i. \quad (1)$$

Assuming the entire image is divided by gray value t into regions A (background) and region B (destination), the gray level of region A ranges from 1 to t , the gray level of region B ranges from $t+1$ to $L-1$, the class probabilities of A and B are estimated as equations (2) and (3), respectively.

$$p_A = \sum_{i=0}^t p_i, \quad (2)$$

$$p_B = \sum_{i=t+1}^{L-1} p_i = 1 - p_A. \quad (3)$$

Thus, the gray level of A and B can be calculated using the following equations:

$$w_A = \sum_{i=0}^t \frac{i p_i}{p_A}, \quad (4)$$

$$w_B = \sum_{i=t+1}^{L-1} \frac{i p_i}{p_B}$$

and the total gray value of image is expressed as

$$w_0 = p_A w_A + p_B w_B = \sum_{i=t+1}^{L-1} p_i. \quad (5)$$

The class variance expression between regions A and B is calculated as follows:

$$\sigma^2 = p_A (w_A - w_0)^2 + p_B (w_B - w_0)^2. \quad (6)$$

TABLE 2: Properties of SBS-modified asphalt and high-viscosity asphalt.

Properties	Value		Testing method [11]
	SBS-modified asphalt	High-viscosity asphalt	
Penetration (25°C, 0.1 mm)	54	53	T0604
Ductility (5°C, 5 cm/min)	39	46	T0605
Softening point (°C)	77	120	T0606
Density (15°C, g/cm ³)	1.03	1.04	T0662
TFOT residue (163°C, 5 h)			
Mass loss (%)	-0.3	-1.6	T0610
Residue penetration (°C)	92	182	T0604
Ductility (5°C, 5 cm/min)	10.3	10.6	T0605

Note: the testing method is conducted according to the Standard Test Methods of Bitumen and Bituminous Mixtures for Highway Engineering (JTG E20-2011) [15].

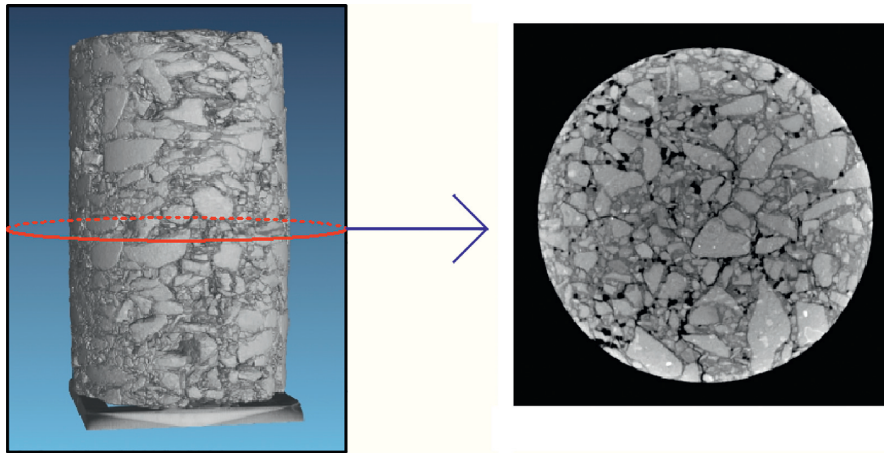


FIGURE 1: Images of asphalt mixtures specimen scanned using CT X-ray.

According to equation (6), the largest t value is the optimum value needed for complete image segmentation. The optimized threshold t^* is given by

$$\sigma(t^*) = \text{Max}_{0 \leq t \leq L-1} \{\sigma(t)\}. \quad (7)$$

In a recursion algorithm, the class probabilities and class means are given in equations (8)(10), respectively.

$$p_A(t+1) = p_A(t) + P_{(t+1)}, \quad (8)$$

$$w_A(t+1) = \frac{p_A(t)w_A(t) + (t+1)P_{(t+1)}}{p_A(t+1)}, \quad (9)$$

$$w_B(t+1) = \frac{w_0 - p_A(t+1)w_A(t+1)}{1 - p_A(t+1)}. \quad (10)$$

4.3. Image Processing and Analysis Using Ring Blocking Method and Otsu's Method. Image threshold processing plays an important role in image segmentation. According to the characterization of the grayscale which is increasing from the center to the edge of CT pictures for the same phase (there are three phases in asphalt mixtures, that is, aggregate,

air void, and asphalt mastic), the CT pictures are segmented using ring block (shown in Figure 2) combining Otsu's method to characterize the microstructure of asphalt mixtures [18]. The CT pictures are segmented with 5 rings as shown in Figure 2.

Image processing is explained in following steps. Firstly, the image analysis process includes the image format, noise reduction, image enhancement, and a hole filling algorithm to recognize the hole region. Secondly, the preprocessed image is segmented using the ring blocking method. And there are 50% overlaps among the adjacent rings. Thirdly, the ring segmentation regions are processed using Otsu's method to calculate the threshold of air voids and the background. Finally, the ring segmentation regions are combined to obtain the whole segmentation image (Figure 3). The aggregate, air void, and asphalt mastic of each segmentation image are captured using Otsu's method as shown in Figure 3(c).

In order to illustrate the validity and accuracy of ring blocking segmentation combining Otsu's method, Bernsen's method [19] and traditional Otsu's method are also used to process the CT pictures. Otsu's method is the global threshold technique, and Bernsen's method is the local threshold technique. Figure 4 shows comparisons among the

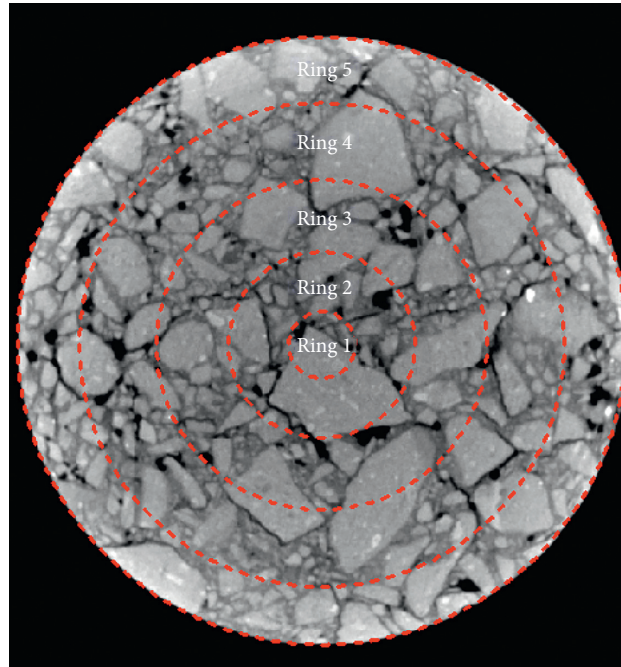


FIGURE 2: Segmentation of CT picture.

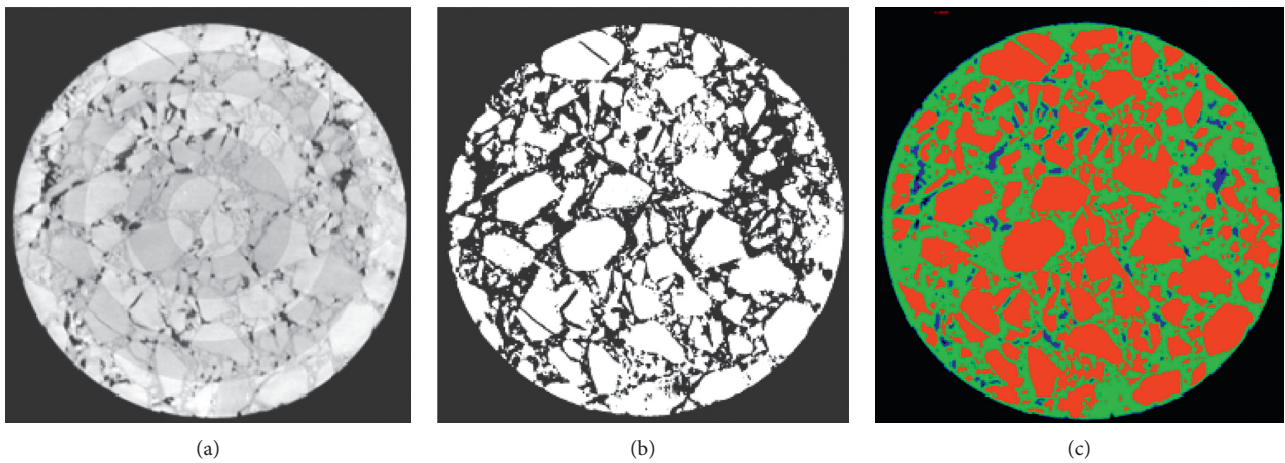


FIGURE 3: Segmentation image processed by 5-ring blocking [18]. (a) Segmentation with 5 rings (b) After segmentation with 5 rings. (c) After processed with segmentation and Otsu's method.

original CT picture processed by Bernsen's method, conventional Otsu's method, and ring segmentation using Otsu's method, respectively.

The variation in gray intensity of the CT image depends on the density of each material in the composite. Brighter regions correspond to denser objects, such as aggregates, and dark regions correspond to lower density objects, for instance, air voids. Figure 4(b) shows that Bernsen's method is hard to distinguish the fine aggregate and mastic inside the specimen. The conventional Otsu's method shown in Figure 4(c) can be used to capture fine aggregate structures. However, it cannot distinguish the denser structure of the fine aggregate and mastic. Therefore, it can be seen that the

ring segmentation combining Otsu's method is the most effective, compared with other two methods to process the CT picture.

5. Air Void of Asphalt Mixtures Analysis

5.1. Air Void Distribution. The Image-Pro® Plus software and MATLAB software are used to visualize the air void structure of the asphalt mixture samples. The air void structure includes the radii, areas, and air void content. The percent air voids for an image ($\%AV_j$) and the total percent air voids of the sample ($\%AV$) are computed as follows:

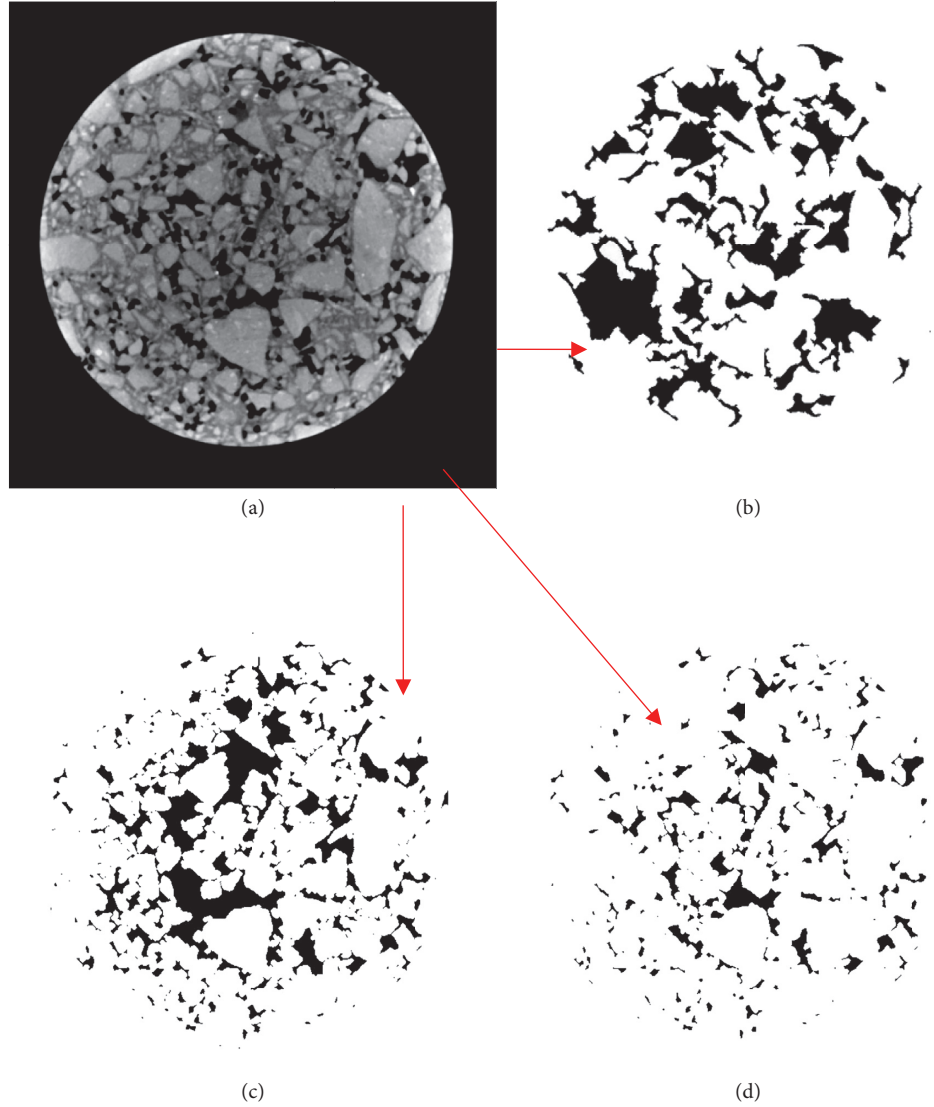


FIGURE 4: Comparisons among Bernsen, conventional Otsu, and ring blocking using Otsu's method. (a) Original CT picture. (b) Processed using Bernsen method. (c) Processed using conventional Otsu's method. (d) Processed using ring blocking using Otsu's method.

$$\%AV_j = \frac{A_{vj}}{A_j}, \quad (11)$$

$$\%AV = \frac{\sum_{j=1}^N \%AV_j}{N}, \quad (12)$$

where A_{vj} is the area of air voids in image j , A_j is the cross-sectional area of image j , and N is the total number of images. The air void radii in image j , also called air void size in this study, are computed as follows:

$$\bar{r}_j = \sqrt{\frac{A_{vj}}{\pi M_j}}, \quad (13)$$

where M_j is the number of air voids in each image. Several threshold values are used as input to the macro until the total

percent air voids of the sample (equation (12)) matches the laboratory measurements.

Based on the aforementioned information, the air void content and air void size in terms of air void radius and area can be calculated. Figure 5 shows that the air void distributes along with the height of the specimen based on the CT picture. Each CT picture's air voids content can be calculated according to the modified Otsu's method. Figure 6 shows that the air void size plotted against the void number in SUP13, AC13, SMA13, and PA13 specimens. The air void size is represented by the air void radius which can be obtained from the air void area. The air void radius is used to evaluate the magnitude of air voids. The air void sizes of SUP13 and AC13 mainly are distributed from 0.15 to 0.2 mm in radius, following by 0.1 to 0.15 mm and 0.2 to 0.25 mm. In terms of air void size greater than 0.3 mm, the number is 9 and 2 for SUP13 and AC13, respectively. For PA13 specimen, the air void sizes mainly are distributed between 0.4

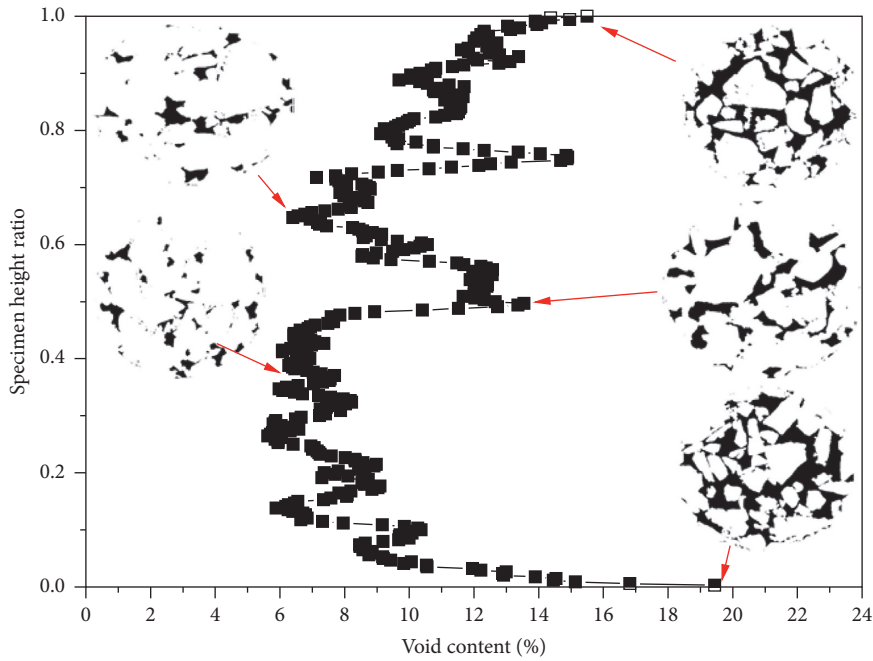


FIGURE 5: Air void distribution along with the height of specimen.

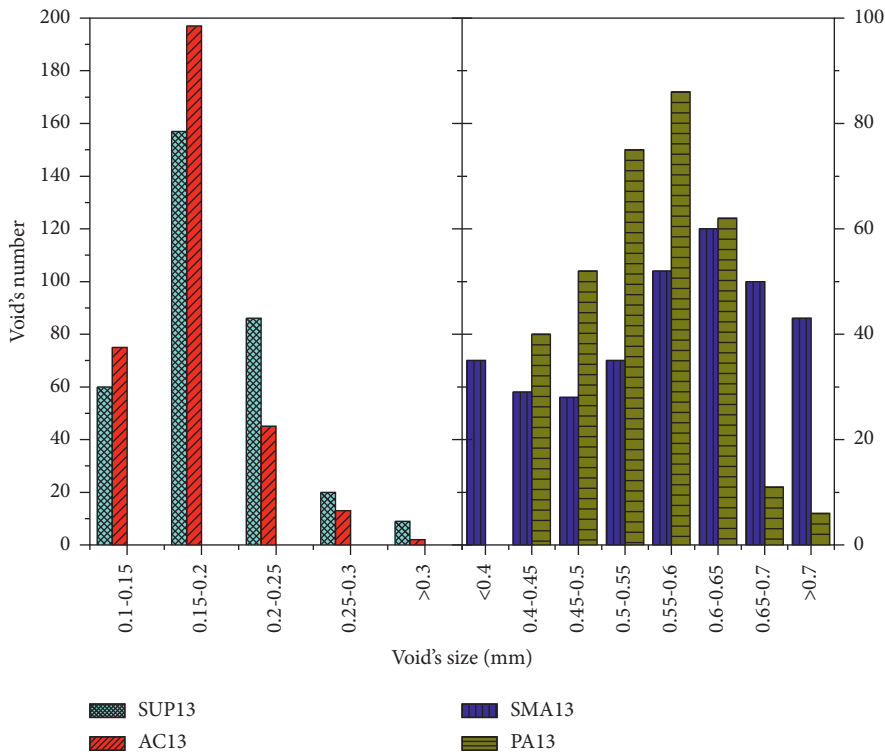


FIGURE 6: Air void size plotted against void number in SUP13, AC13, SMA13, and PA13 specimen.

and 0.65 mm, especially from 0.5 to 0.65 mm. For SMA13 specimen, the air void sizes have uniform distribution mainly ranging from 0.4 to 0.7 mm.

Figures 7–10 depict air void size distributions along with the AC13, SUP13, PA13, and SMA13 specimens' height

ratio. The height ratio along the y -axis is defined as the ratio of the vertical distance of a slice from the bottom of the specimen to the total height of the specimen. The air void radius, air void area, and air void content are plotted according to the analysis of processed CT pictures and air

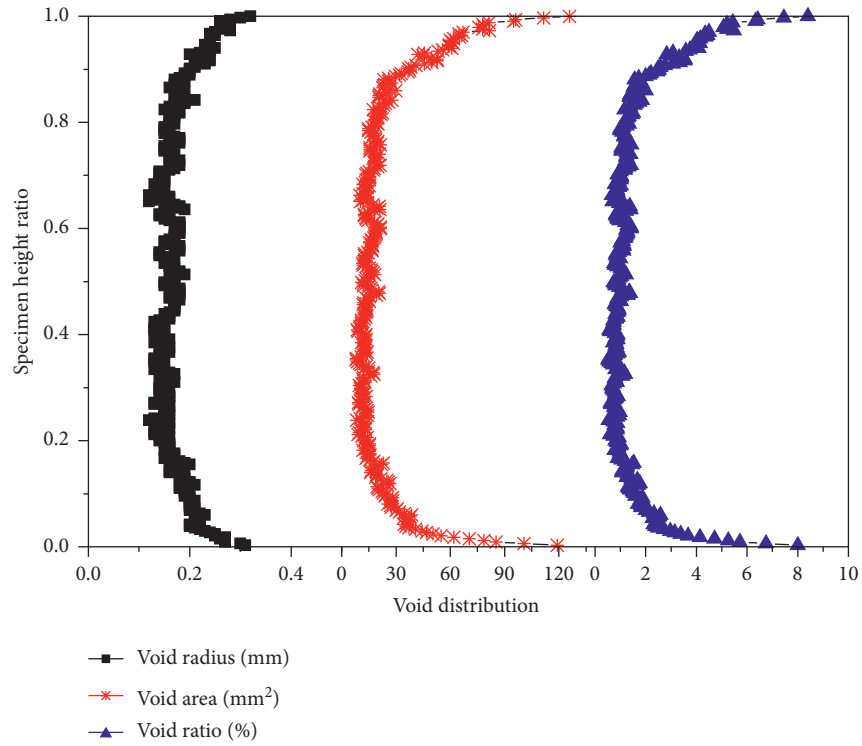


FIGURE 7: Air size distributions along with the AC13 specimen height ratio.

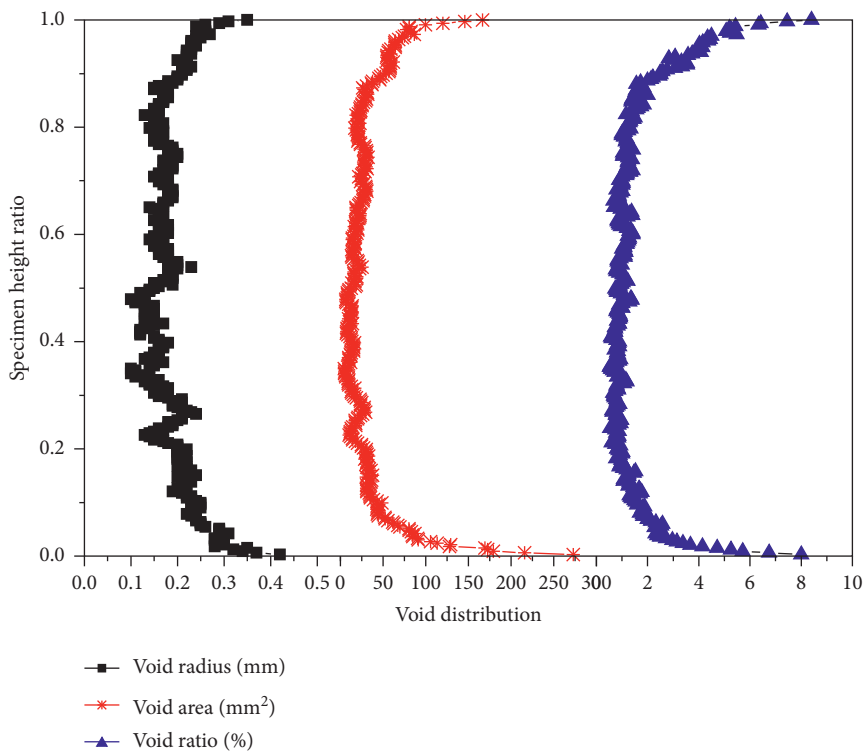


FIGURE 8: Air size distributions along with the SUP13 specimen height ratio.

void's distribution algorithm. For SUP13 and AC13 samples, the relationship between void content and depth is bathtub-

shaped like. The porosity at the top and bottom of the sample is higher, and the porosity in the middle is lower and more

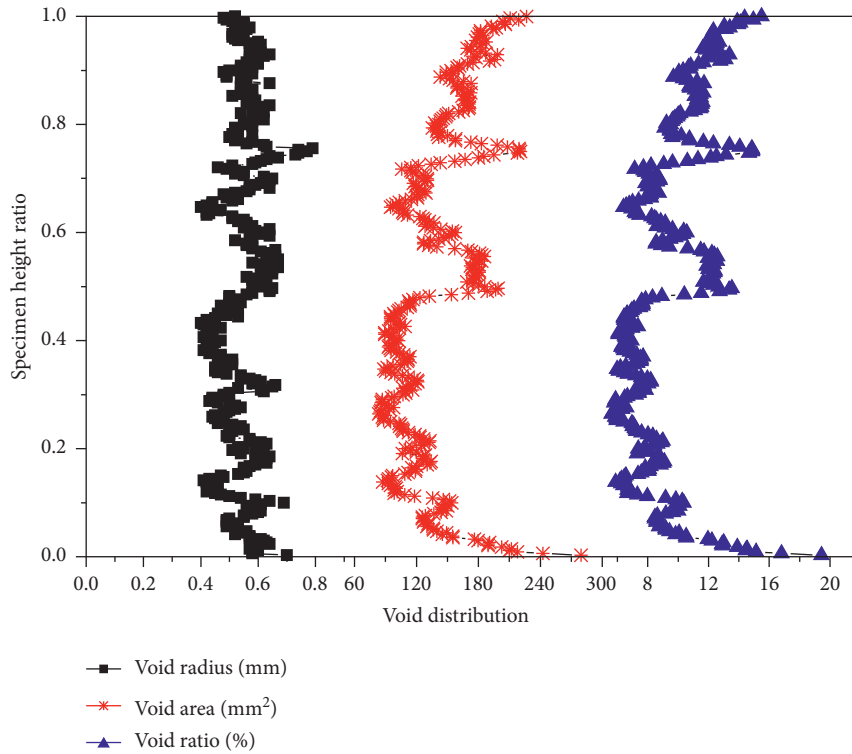


FIGURE 9: Air size distributions along with the PA13 specimen height ratio.

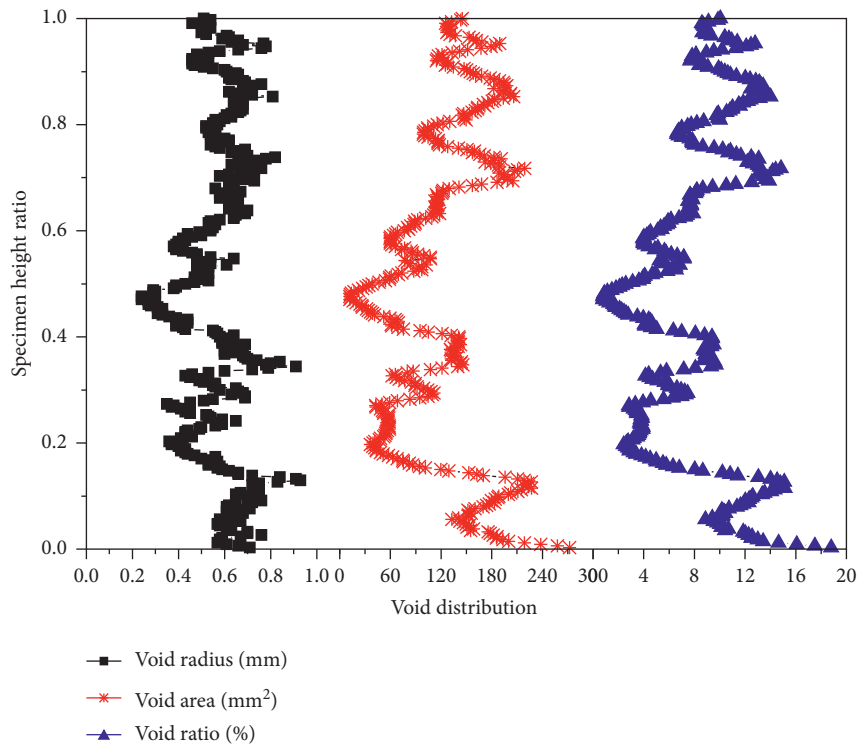


FIGURE 10: Air size distributions along with the SMA13 specimen height ratio.

uniform. The results for the SMA13 and PA13 samples show different trends, but in general, the air void content is higher at the top of the sample and lower in the rest of the sample

depth. The results are comparable to the field cores, that is, the air void content is higher at the top of the sample and lower in the rest of the sample depth [20]. An internal trend

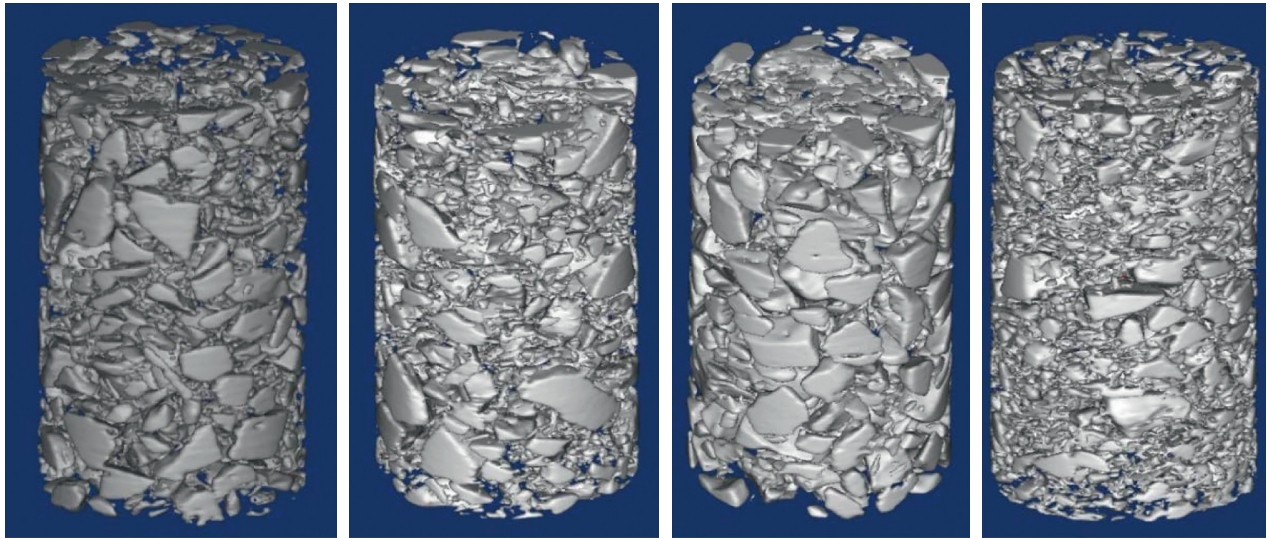


FIGURE 11: Reconstructed virtual specimens (PA13, AC13, SMA13, and SUP13, from left to right).

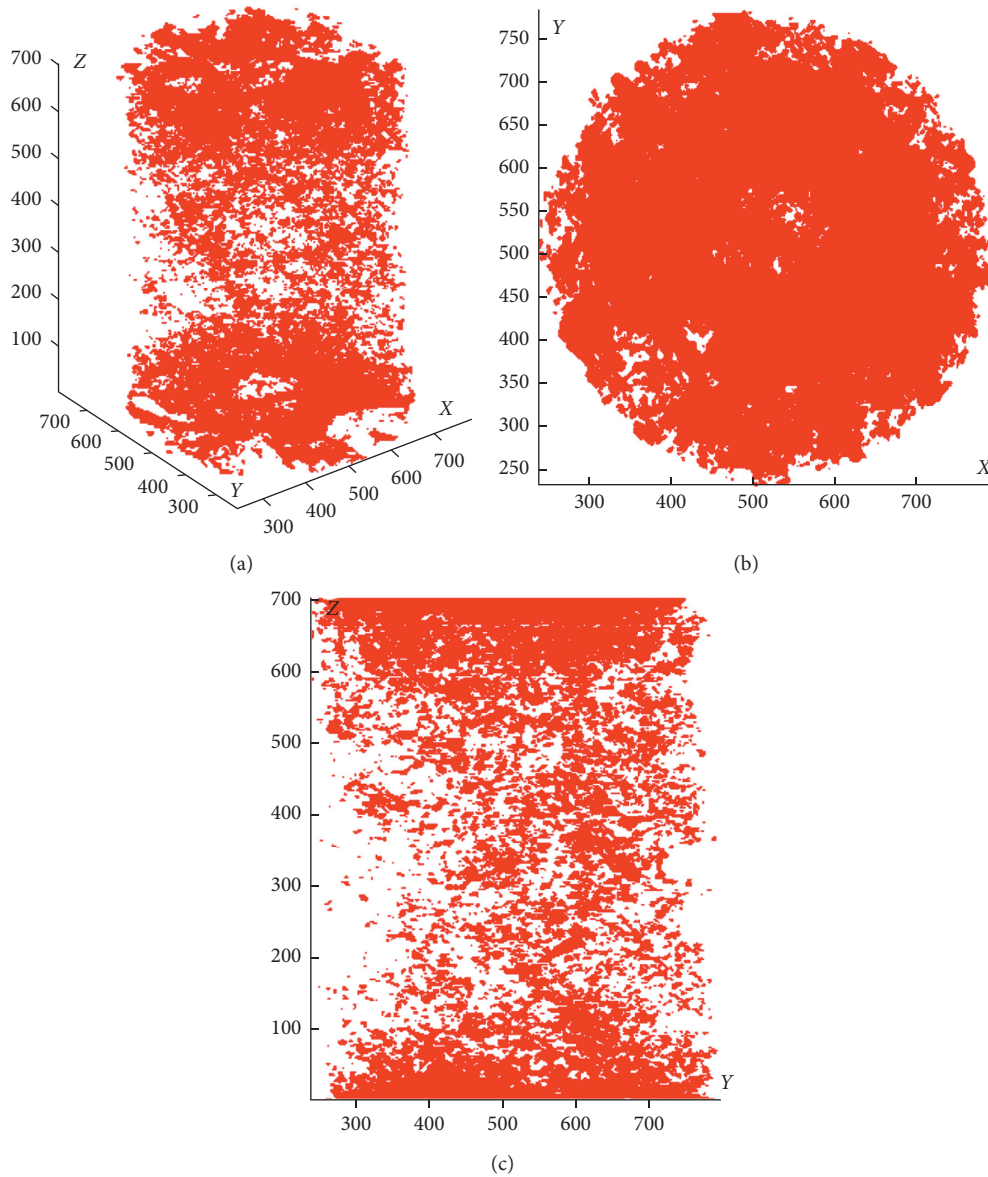


FIGURE 12: Air void distribution of AC13 specimen. (a) Three dimensions. (b) Projection in transverse section. (c) Projection in vertical section.

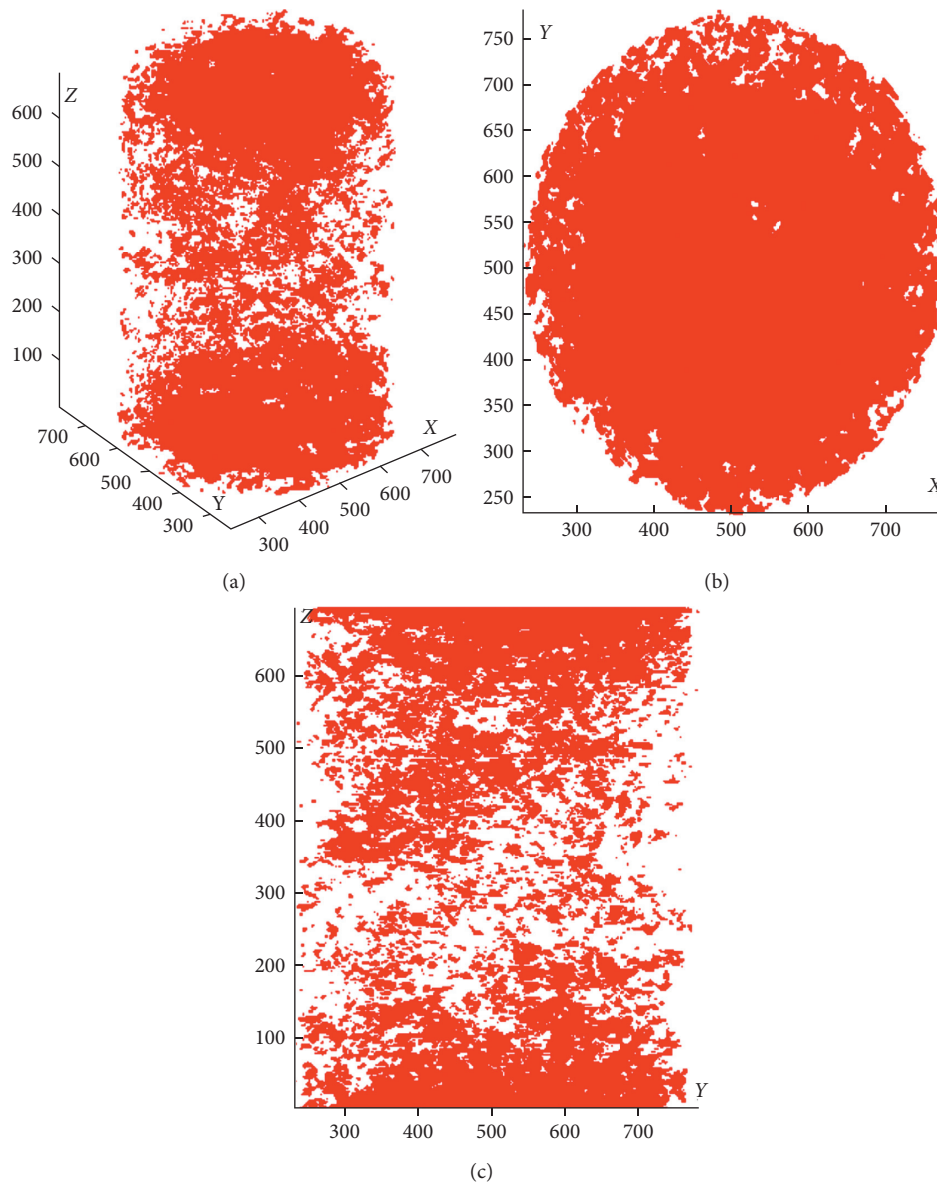


FIGURE 13: Air void distribution of SUP13 specimen. (a) Three dimensions. (b) Projection in transverse section. (c) Projection in vertical section.

in field sample air voids is roughly two times higher near the surface of the asphalt course than on the middle and bottom of the layer [21, 22]. Figures 7–10 indicate that the air void content is depend on the air void areas which relate to the air void size (that is, air void radius).

The graphs in Figures 7 and 8 are distinctively different than those in Figures 9 and 10. The reason for this is that the used large stones and SBS-modified binder in Figure 9 and high-viscosity binder in Figure 10. Both of these produce a more uniform distribution of air voids vertically, even though there is more variability in the air void content than is the case with Figures 7 and 8.

5.2. Air Void Distribution Reconstruction. In order to construct the three-dimension distribution of air voids, the

commercially available software, MATLAB program, is used to reconstruct the processed CT pictures. Remove the particles with the particle size less than 1.18 mm, and then reconstruct the four grading specimen model, as shown in Figure 11. The three-dimension air voids microstructure of asphalt mixtures are shown in Figures 12–15 for AC13, SUP13, PA13, and SMA13, respectively. The two-dimension CT images processed by ring blocking and Otsu's method are collected and converted into three-dimension image of the original sample. The images are thresholded to identify mixture constituents. Thresholding is the technique applied to characterize the components of the mixture. It converts the representative gray scale of a component into a value. This value is the only value associated with an element, and so it can be identified in the mixture. The gray value is assigned to air voids. The reconstruction of air voids of

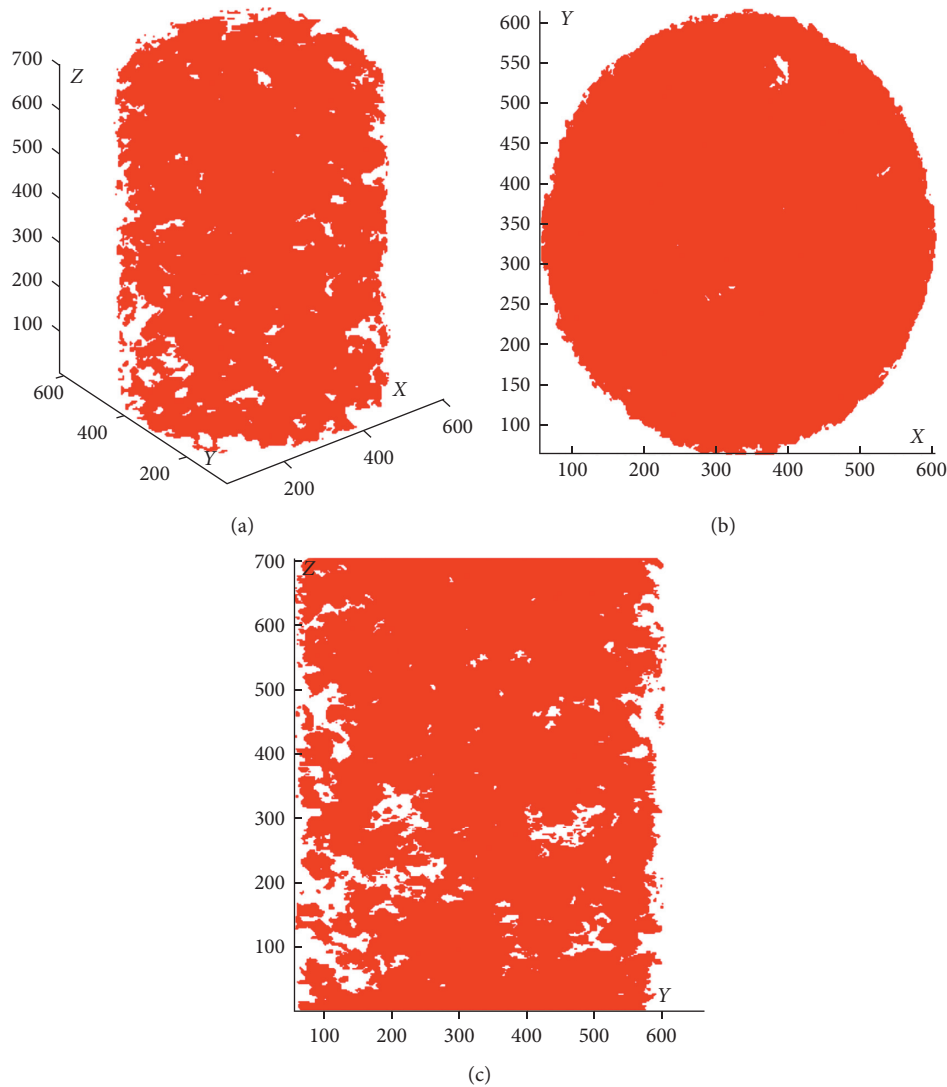


FIGURE 14: Air void distribution of PA13 specimen. (a) Three dimensions. (b) Projection in transverse section. (c) Projection in vertical section.

asphalt mixtures can be simply carried out as in the following steps. Firstly, the horizontal slices of 1.0 mm thickness with an overlap of 0.2 mm were captured. Secondly, these slices were stacked together in the computer to form the actual three-dimension porous microstructure. Thirdly, the three-dimension structure of air voids is rotated to project in transverse section and vertical section.

It appears in Figures 12 and 13 that the distributions of the air void content of SUP13 and AC13 with respect to depth coincide with those in Figures 7 and 8; a higher air void content was observed at the sample top and bottom, while lower and more uniform air void content were observed in the middle section. Figures 14 and 15 show different trends compared with SUP13 and AC13, and in general, the air void content is higher at the top of the sample and lower in the rest of the sample depth. And

the air void's distribution seen from Figures 14 and 15 are in line with Figures 9 and 10, respectively. It indicates that the CT pictures processed by the ring blocking segmentation and Otsu's method are feasible and rational to capture the air voids size and content of asphalt mixtures.

6. Conclusions and Discussion

The X-ray CT was used to scan the specimens of AC13, SUP13, PA13, and SMA13. The CT pictures were processed by ring blocking segmentation and calculated by Otsu's method. Based on preprocesses, segmentation, and identification, the air voids of asphalt mixtures were calculated and reconstructed with Image-Pro® Plus software and MATLAB program. The key findings are summarized as follows:

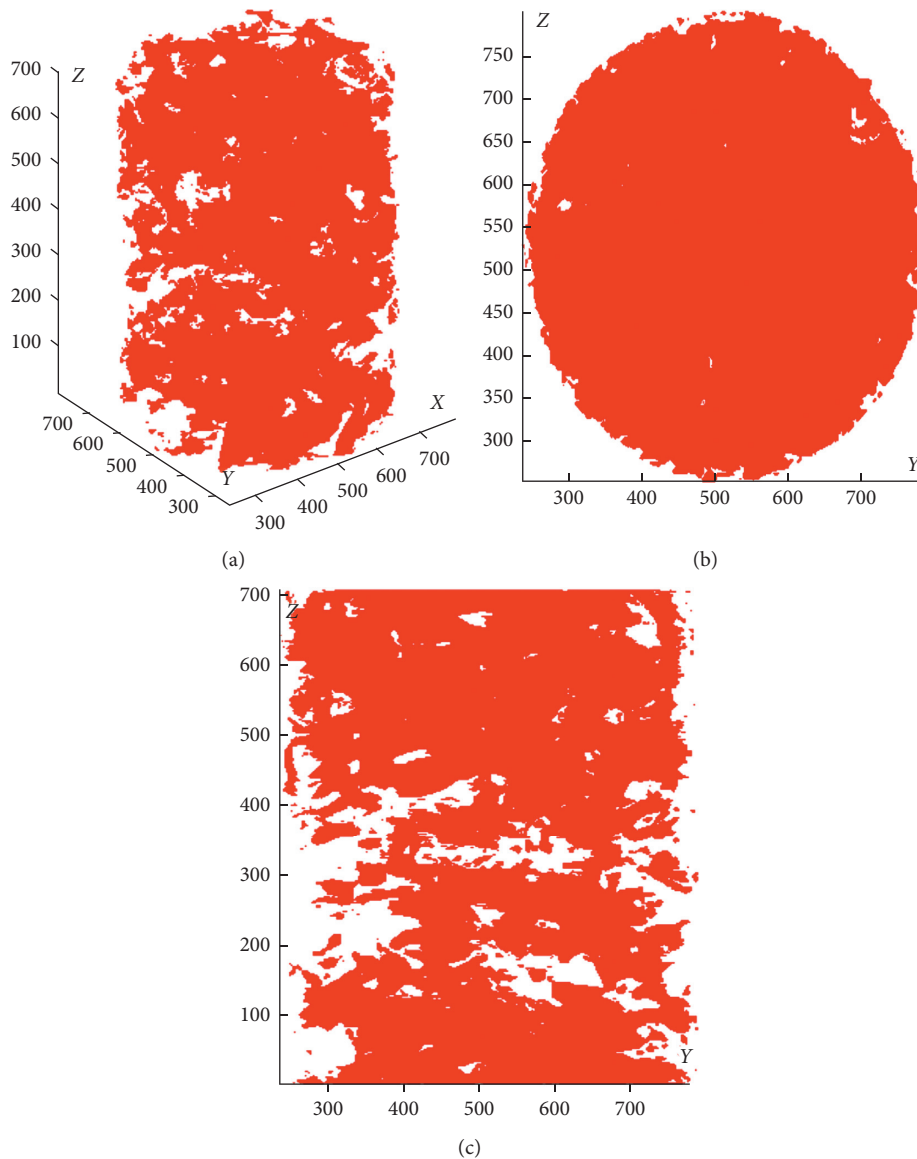


FIGURE 15: Air void distribution of SMA13 specimen. (a) Three dimensions. (b) Projection in transverse section. (c) Projection in vertical section.

- (1) The air voids of AC13, SUP13, PA13, and SMA13 specimens can be distinct to capture using the ring blocking segmentation combining Otsu's method to process the CT pictures.
- (2) According to the analysis of method processed, it is believed that the ring blocking segmentation combining Otsu's method is feasible and rational to identify the air voids of asphalt mixtures in comparison with Bernsen's method and the conventional Otsu's method.
- (3) The air void sizes of SUP13 and AC13 are mainly distributed between 0.15 to 0.2 mm, while it is mainly distributed between 0.4 and 0.65 mm for PA13. For SMA13 specimen, the air void sizes have uniform distribution mainly ranging from 0.4 to 0.7 mm.
- (4) Image analysis reveals that air void's distribution is not uniform through the specimens, namely, higher air voids concentrations were found at the specimen's top and bottom and lower air voids in between.
- (5) It is a significant progress of asphalt mixtures' research to conduct three-dimensional reconstruction of the air voids. The air voids of SUP13, AC13, SMA13, and PA13 were reconstructed and displayed. The three-dimensional air voids distribution of AC13, SUP13, PA13, and SMA13 are in accordance with the analysis of air void size distribution along with the height ratio of specimen.
- (6) The used large stones and SBS-modified binder in SMA13 and high-viscosity binder in PA13 produce a more uniform distribution of air voids vertically,

even though there is more variability in the air void content than is the case with AC13 and SUP13.

Data Availability

The Fish code data and Excel data of experiment used to support the findings of this study were supplied by the National Natural Science Foundation of China and China Postdoctoral Science Foundation under license and so cannot be made freely available. Requests for access to these data should be made to Jiantong Zhang, tongtong01@126.com.

Conflicts of Interest

The authors declare that they have no conflicts of interest.

Acknowledgments

The authors gratefully acknowledge the financial assistance provided by the National Natural Science Foundation of China (No. 51078089) and China Postdoctoral Science Foundation (No. 2016M590717).

References

- [1] C. L. Monismith, "Analytically based asphalt pavement design and rehabilitation," vol. 1354, pp. 5–26, Transportation Research Record, 1992.
- [2] T. K. Pellinen, J. Song, and S. Xiao, "Characterization of hot mix asphalt with varying air voids content using triaxial shear strength test," in *Proceedings of the 8th Conference on Asphalt Pavements for Southern Africa (CAPSA'04)*, Sun City, South Africa, September 2004.
- [3] E. Masad, V. K. Jandhyala, N. Dasgupta, N. Somadevan, and N. Shashidhar, "Characterization of air void distribution in asphalt mixes using X-ray computed tomography," *Journal of Materials in Civil Engineering*, vol. 14, no. 2, pp. 122–129, 2002.
- [4] F. Beainy, S. Commuri, and M. Zaman, "Quality assurance of hot mix asphalt pavements using the intelligent asphalt compaction analyzer," *Journal of Construction Engineering and Management*, vol. 138, no. 2, pp. 178–187, 2012.
- [5] S. Caro, E. Masad, and M. Sánchez-Silva, "Stochastic micromechanical model of the deterioration of asphalt mixtures subject to moisture diffusion processes," *International Journal for Numerical and Analytical Methods in Geomechanics*, vol. 35, no. 10, pp. 1079–1097, 2011.
- [6] E. Little, *Compaction Effects on Uniformity, Moisture Diffusion, and Mechanical Properties of Asphalt Pavements*, Thesis (PhD), Texas A&M University, Fort Worth, TX, USA, 2008.
- [7] Q. Xu, K. C. George, L. G. Victor, and D. H. Robert, "Influences of intelligent compaction uniformity on pavement performances of hot mix asphalt," *Construction and Building Materials*, vol. 30, pp. 746–752, 2011.
- [8] D. Caro and C. Silvia, "Effects of air voids variability on the thermo-mechanical response of asphalt mixtures," *International Journal of Pavement Engineering*, vol. 15, no. 2, pp. 110–121, 2014.
- [9] L. F. Walubita, B. Jamison, A. E. Alvarez, X. Hu, and C. Mushota, "Air void characterisation of HMA gyratory laboratory-moulded samples and field cores using X-ray computed tomography (X-ray CT)," *Journal of The South African Institution of Civil Engineering*, vol. 54, no. 1, pp. 22–30, 2012.
- [10] L. F. Walubita and S. Scullion, "Perpetual pavements in Texas: the fort worth sh 114 perpetual pavement in wise county," Technical Report No. FHWA/TX-05/0-4822-2), Texas A&M University, Fort Worth, TX, USA, 2007.
- [11] L. F. Walubita and S. Scullion, *Texas Perpetual Pavements: Experience Overview and the Way Forward*, FHWA/TX-10/0-4822-3, TTI, College Station, TX, USA, 2010.
- [12] C. Denison, W. D. Carlson, and R. A. Ketcham, "Three-dimensional quantitative textural analysis of metamorphic rocks using high-resolution computed X-ray tomography: Part I. Methods and techniques," *Journal of Metamorphic Geology*, vol. 15, no. 1, pp. 29–44, 1997.
- [13] E. Masad, B. Muhunthan, N. Shashidhar, and T. Harman, "Internal structure characterization of asphalt concrete using image analysis," *Journal of Computing in Civil Engineering*, vol. 13, no. 2, pp. 88–95, 1999.
- [14] L. F. Walubita, T. Scullion, J. Leidy, and W. Liu, "Non-destructive testing technologies application of the ground penetrating radar (GPR) to perpetual pavements," *Road Materials and Pavement Design*, vol. 10, no. 2, pp. 259–286, 2009.
- [15] Ministry of Transport, *Standard Test Methods of Bitumen and Bituminous Mixtures for Highway Engineering. JTG E20-2011*, Ministry of Transport, Beijing, China, 2011.
- [16] N. Otsu, "A threshold selection method from gray-level histograms," *IEEE Transactions on Systems, Man, and Cybernetics*, vol. 9, no. 1, pp. 62–66, 1979.
- [17] X.-ning Zhang, DuanYue-hua, and Li Zhi, "Classification of asphalt mixture materials based on X-ray computed tomography," *Journal of South China University of Technology (Nature Science Edition)*, vol. 39, no. 03, pp. 120–123, 2011, in Chinese.
- [18] Li Zhi and J. Liu, "Segmentation of asphalt mixtures using X-ray computed tomography images based on ring block and OTSU method," *Journal of Wuhan University of Technology*, vol. 33, no. 6, pp. 50–53, 2011.
- [19] P. K. Sahoo, A. K. C. Wong, and Y. C. Chen, "A survey of thresholding techniques," *Computer Graphics, Vision and Image Processing*, vol. 41, no. 3, pp. 233–260, 1988.
- [20] L. Tashman, E. Masad, J. D'Angelo, J. Bukowski, and T. Harman, "X-ray tomography to characterize air void distribution in superpave gyratory compacted specimens," *International Journal of Pavement Engineering*, vol. 3, no. 1, pp. 19–28, 2002.
- [21] L. Tashman, M. Eyad, B. Peterson, and H. Saleh, "Internal structure analysis of asphalt mixes to improve the simulation of superpave gyratory compaction to field conditions," *Asphalt Paving Technology*, vol. 70, pp. 605–645, 2001.
- [22] E. Masad, K. Emad, and C. Arif, *Application of Imaging Technology to Improve the Laboratory and Field Compaction of HMA*, Texas Transportation Institute (TTI), The Texas A&M University System, College Station, TX, USA, 2009.

Research Article

Optimal Design of the Sealing Structure of a Hydraulic Cylinder on the Basis of a Surrogate Model

Hong Zhang, Yu Sun , Chenchen Li, and Haoran Wang

School of Mechanical Engineering, Dalian University of Technology, Dalian 116024, China

Correspondence should be addressed to Yu Sun; 284274494@qq.com

Received 20 April 2020; Revised 22 June 2020; Accepted 24 July 2020; Published 26 August 2020

Academic Editor: Gloria Terenzi

Copyright © 2020 Hong Zhang et al. This is an open access article distributed under the Creative Commons Attribution License, which permits unrestricted use, distribution, and reproduction in any medium, provided the original work is properly cited.

In this study, a finite-element simulation model was established for a two-dimensional hydraulic cylinder seal structure with highly nonlinear materials and contacts for achieving the optimal sealing effect with the structure. The effects of gaps as well as single and double O-rings on the sealing effect were examined. On the basis of this examination, a parametric model was developed for double-O-rings without gaps, which are suitable for hydraulic cylinder sealing. Suitable design variables, objective functions, and constraint conditions were determined for the parametric model. Then, a surrogate model was fitted and optimised through a constrained Latin hypercube method, an interpolating reemultiquadric radial basis function method, and the genetic algorithm. The results indicate that the seal and seal groove structures obtained through optimisation with the surrogate model provide a superior sealing effect to unoptimised structures. Therefore, the combination of the developed surrogate model and finite-element method can provide a theoretical reference for the design of the sealing structure of hydraulic cylinders.

1. Introduction

Hydraulic transmission has attracted considerable attention for transportation vehicles, such as automobiles, ships, and aircraft, due to the development of manufacturing with the advancement of technology. In a hydraulic system, structures such as valves, pumps, and cylinders are connected to hydraulic pipe joints through a piping system. Hydraulic pipe joints, pumps, valves, and cylinders are the most basic hydraulic system components that play a vital role in the circulation of gas, water, and oil in the system [1–5]. Because the hydraulic pipeline is in a high-risk environment in the circulation and power system, the pipeline seal requires further analysis [6]. In aircraft, ships, automobiles, and other transportation vehicles, when the hydraulic seal system fails, internal oil, gas, pollutants, and waste are leaked. Such failure may also cause fatalities and major accidents. Thus, the sealing performance of the hydraulic pipeline sealing structure in vehicles considerably influences the safety and reliability of the equipment [7, 8].

Currently, the research on and production capacity of seals in China is relatively low, and manufacturers blindly

increase the compression amount of seals in most cases to solve the problem of hydraulic seal failure [9]. Although the sealing purpose is temporarily achieved when using the aforementioned approach, the seal duration and reliability decrease, which may cause problems such as seal damage. Therefore, research on the sealing performance of hydraulic cylinder sealing structures is critical [10].

In general, the functional components of a sealing device are the upper and lower flanges and the middle sealing rubber. Therefore, a study of the sealing performance should begin from the analysis of these three components. The amount of compression of the sealing rubber directly affects the sealing performance of the hydraulic cylinder sealing structure. Moreover, large compression reduces the service life of the sealing rubber. The cross-sectional shape of the sealing rubber directly affects the contact area between the sealing material and the upper and lower flanges on the application of the pretightening force and thus affects the sealing efficiency. The structures of the upper and lower flanges also affect the tightness of the hydraulic cylinder sealing structure. The size of the gap in the groove of the seal ring affects the amount of deformation of the seal rubber,

which affects the sealing ability of the device. Chen et al. obtained an O-type seal with a higher reliability than the contact pressure distribution between the rectangular seal and the O-ring [11]. On the basis of the finite-element method, Zhou et al. proposed that reducing the height of the lower flange close to that of the measuring cavity of the oil cavity can reduce the loss of oil pressure and thus improve the sealing efficiency [12]. Lan et al. proposed a method of using finite sample points to establish a proxy model to conduct intradomain structural analysis and dimensional optimisation [13]; Wang et al. used genetic algorithm to optimise the size of the structure to improve the performance of the whole structure [14].

This study mainly used Ansys Workbench to perform finite-element analysis on the seals of hydraulic cylinders, compare the seal ring section shape, flange groove width, and groove depth, and optimise the groove structure through a surrogate model in MATLAB for obtaining a set of optimal structural parameters for the sealing rubber and flange and for achieving the best sealing effect for the hydraulic cylinder sealing structure.

2. Model Description

2.1. Geometric Model. The seal of a hydraulic cylinder has a typical symmetric structure. Considering the symmetry of the structures of the seal ring and hydraulic cylinder, this study simplified the three-dimensional plane strain problem for a hydraulic cylinder into a two-dimensional problem for simulation calculation. The two-dimensional axial seal models of the four seals considered in this study, which are based on the Chinese standard GB/T-3452.3-2005 [15], are displayed in Figure 1.

Figures 1(a) and 1(b) display single O-ring seal structures, and Figures 1(c) and 1(d) represent double O-ring seal structures ($A = \pi r^2$). Figure 1(a) displays a schematic of a two-dimensional model of a seal groove with a gap, and Figure 1(b) displays a schematic of a two-dimensional model of a seal groove without a gap. Figure 1(c) depicts a schematic of a seal model with a gap, and Figure 1(d) depicts a schematic of a gapless seal model. In nonlinear finite-element simulation calculations, the following assumptions must be made to reduce the number of calculations and the calculation time:

- (a) The rubber material is an isotropic and uniform material.
- (b) The creep properties of rubber materials are uniform during elongation and compression, and the volume change is negligible when creep occurs.
- (c) Compared with hydraulic cylinders, the quality of O-type rubber seals is negligible. The overall model of the hydraulic cylinder can be simplified into two dimensions.

2.2. Selection of Material Parameters. Because the sealing ring is usually made of rubber material and has a high degree of nonlinearity in the finite-element simulation, this study adopted the Mooney–Rivlin model with two parameters to

represent the constitutive relationship of the material with large deformation [16]. The strain energy and compression constant in the aforementioned model can be expressed as follows:

$$W = C_1(I_1 - 3) + C_2(I_2 - 3), \quad (1)$$

$$D = \frac{(1 - 2\nu)}{(C_1 + C_2)}, \quad (2)$$

where W is the strain energy; D is the compression constant; C_1 and C_2 are the mechanical property constants of the nonlinear material; I_1 and I_2 are the first and second strain tensor invariants, respectively; and ν is Poisson's ratio of the material [17]. Theoretically, the mechanical property constant should be determined through tensile and compression experiments [18]; however, in practice, the constant is determined from the hardness value (Hs) of the material [19, 20]:

$$6C_1 \left(1 + \frac{C_1}{C_2} \right) = \frac{15.75 + 2.15 HS}{100 - HS}. \quad (3)$$

The aforementioned formula indicates that the mechanical property constant of a material can be obtained from the Hs value and (C_1/C_2) . According to the literature [21], the recommended value of (C_1/C_2) is generally 0.25.

Considering the oil and water resistance, NBR is selected for analysing many rubber materials. The hardness of the seal under high pressure in this study was 85. According to the aforementioned formula, $C_1 = 1.84$ MPa, $C_2 = 0.47$ MPa, $\nu = 0.499$, and $D = 0.00087$ MPa⁻¹. The upper and lower flanges are made of standard structural steel, whose elastic modulus is 200 GPa and Poisson's ratio is 0.3.

Network segmentation is a critical step when a model is used for numerical simulation analysis. They must be as regular as possible in addition to the number of units that need to be controlled. Therefore, element independence analysis is usually required before determining the element size. As displayed in Figure 2, the maximum value of the contact pressure was stabilised at 4.38 MPa. Finally, the grid sizes of the upper and lower flanges and the sealing rubber were controlled to be less than 0.07 mm. The grid of the hydraulic cylinder sealing system was divided into a combination of tetrahedrons and hexahedrons. The number of grids was 14,932, and the number of nodes was controlled at approximately 45,000.

2.3. Contact Settings. Due to the large friction forces between the sealing rubber and the upper and lower flanges, the contact method was set to frictional contact, and the friction coefficient was 2×10^{-2} . The contact algorithm uses the augmented Lagrange multiplier method to adapt to large-deformation contact problems. Moreover, the finite-element control method uses the integration point detection method (Gauss Point) to analyse the friction contact problem [22, 23].

2.4. Boundary Condition Settings. In the finite-element analysis of the seal in this study, a 5.3 mm-diameter nitrile rubber was used as the seal ring. The width B of the seal groove with a gap was 6.3 mm, and the width B of the seal

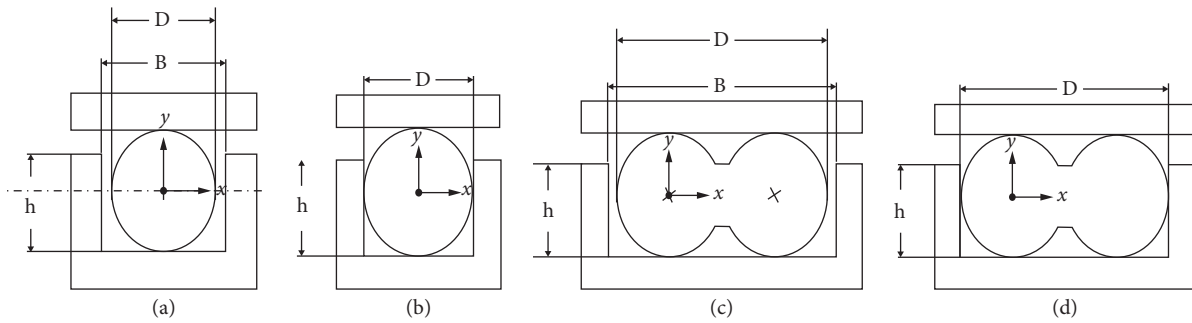


FIGURE 1: Two-dimensional models of the four seals considered in this study.

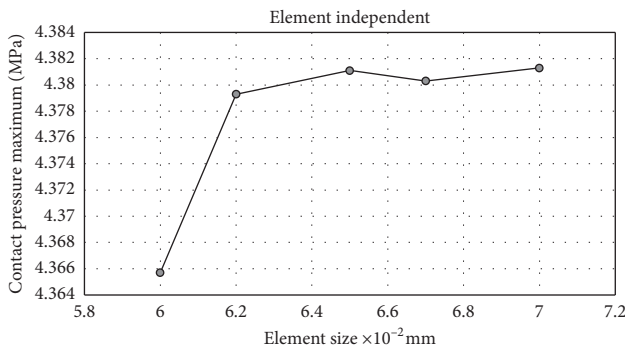


FIGURE 2: Element independence verification.

groove without a gap was 5.3 mm. The seal groove depth of the single groove was 4.13 mm. The first force causes large deformation, and second force constrains all the displacements of the lower flange. Three load steps were set. The first load step was the initial situation without any force; the second load step involved the application of a pretightening load, and the compression was 20% of the seal ring (i.e., 1.06 mm); and the third load step involved setting the internal pressure of the hydraulic cylinder to 2 MPa. In the simulation, the left side was assumed as the inside of the hydraulic cylinder and the right side was assumed as the external side. Therefore, a pressure load of 2 MPa was applied to the left side of the seal.

2.5. Simulation Results and Analysis. A comparison of the results obtained for a single-groove seal with and without gaps is displayed in Figure 3.

Figures 3(a) and 3(b) depict the equivalent stress cloud diagram of a single-groove seal with a gap and the cloud diagram of the contact pressure between this seal and the upper flange, respectively. Figures 3(c) and 3(d) depict the equivalent stress cloud diagram of the single-groove gapless seal and the cloud diagram of the contact pressure between this seal and the upper flange, respectively. Figures 3(e) and 3(f) illustrate the equivalent stress cloud diagram of a double-groove seal with a gap and the cloud diagram of the contact pressure between this seal and the upper flange, respectively. Figures 3(g) and 3(h) display the equivalent stress cloud diagram of the double-groove gapless seal and the cloud diagram of the contact pressure between this seal and the upper flange, respectively.

The mean average pressure and maximum contact pressure results are presented in Table 1. The mean equivalent stress was 2.66 MPa for the single-groove seals with and without a gap. Moreover, the difference in the maximum contact pressures of the aforementioned two seals was only 0.001 MPa. For the double-groove seal, the equivalent stresses with and without a gap were 2.65 and 2.64 MPa, respectively. Therefore, in the case of large compression, the presence or absence of gaps has almost no effect on the equivalent stress on the seal ring.

The contact pressure is the major factor affecting the sealing effect. When the contact pressures are greater than the pressures in the hydraulic cylinder, the sealing is successful and the sealing effect is proportional to the contact pressures. A comparison of Figures 3(b), 3(d), 3(f), and 3(h) indicates that the maximum contact pressures between the single-groove seal with a gap and the upper flange and between the double-groove seal with a gap and the upper flange were 4.3808 and 4.3876 MPa, respectively. The maximum contact pressures between the gapless single-groove seal and the upper flange and between the gapless double-seal groove and the upper flange were 4.3813 and 4.3888 MPa, respectively. For single-groove seals, the maximum contact pressure without a gap was 0.011% higher than that with a gap. For double-groove seals, the maximum contact pressure without a gap was 0.17% higher than that with a gap. The maximum contact pressure was greater without a gap than with a gap because the horizontal deformation of gapless seal grooves was constrained. The aforementioned data indicate that the number of seal ring layers considerably influences the sealing effect of the hydraulic cylinder for the adopted two sets of variables. Therefore, structure optimisation was performed for the seal groove and seal ring of the double-layer seal without a gap.

3. Structural Optimisation Design Based on a Surrogate Model

Structural optimisation design involves determining a set of optimal solutions from design variables under the proposed constraints. The general optimisation solution process involves mathematically modelling the optimisation problem, proposing constraints according to the mathematical model, and selecting an appropriate method to optimise the established model for a certain goal. In general, the following parameters are considered in the process of optimal design [24]:

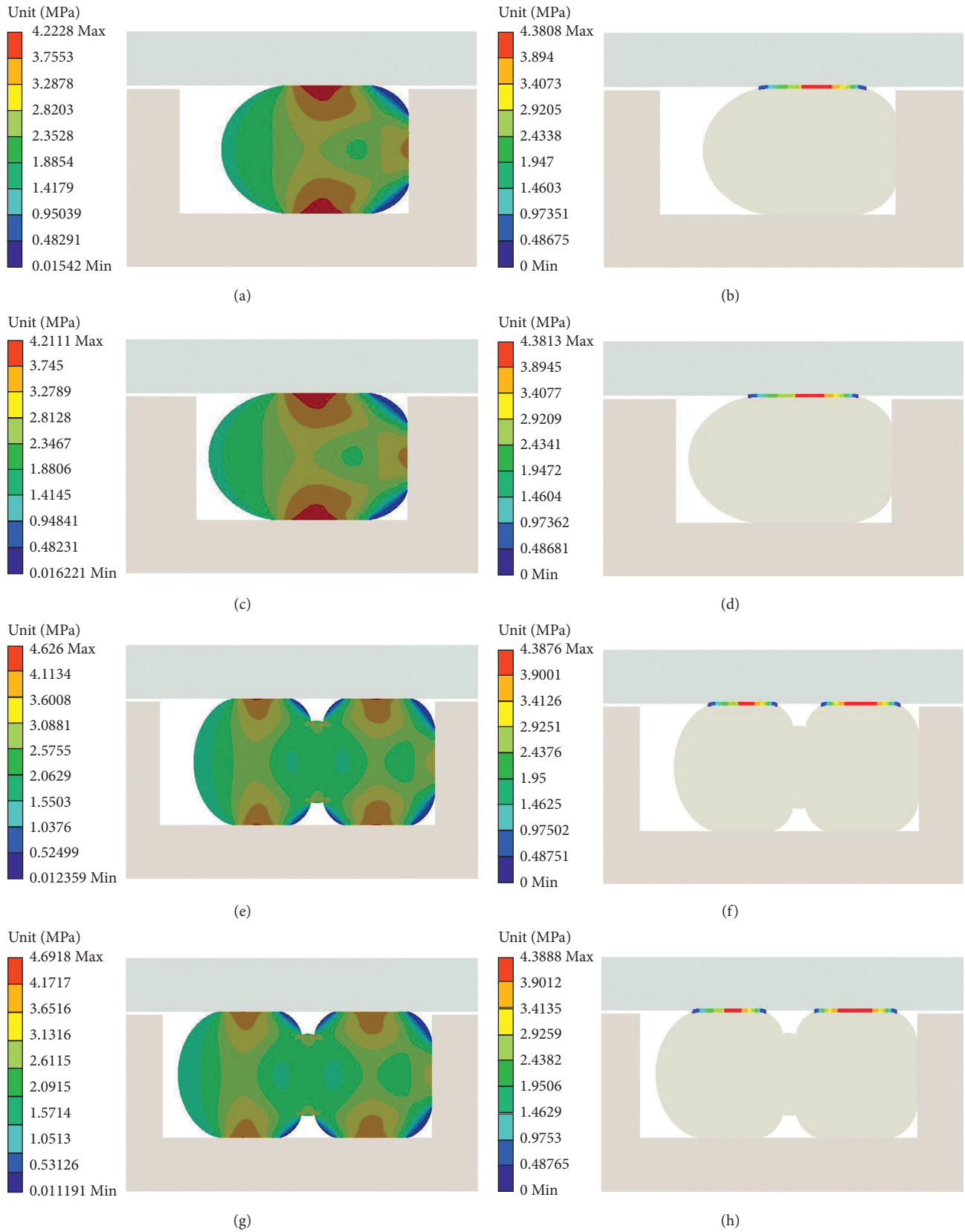


FIGURE 3: Equivalent stress and contact pressure cloud diagrams of the single-groove seal.

TABLE 1: Mean average pressure and maximum contact pressure for different sealing methods.

	Single seal with gap (MPa)	Single seal with gapless (MPa)	Double seal with gap (MPa)	Double seal with gapless (MPa)
Mean equivalent stress	2.66	2.66	2.65	2.65
Maximum contact pressure	4.3808	4.3818	4.3876	4.3888

- (a) Design variables: design variables are parameters that have a major influence on the model (design variables are generally denoted by x).
- (b) Objective function: the objective function is the optimisation objective (optimisation object), which is generally denoted as $f(x)$.
- (c) Constraints: constraints refer to the ranges of design variables. The types of constraints in the optimisation process include stress and volume constraints.

3.1. Determination of Design Variables. According to the simulation results presented in Section 2.5, the double-layer seal without a gap exhibits a superior sealing effect to the other seal structures. Therefore, the double-layer seal structure was parameterised and modelled, as depicted in Figure 1(d). Two parameters, namely, the diameter of the seal ring (D) and the depth of the seal groove (h), were calculated due to their high influence on the sealing effect in parametric modelling. In addition, the chamfer of the upper and lower flanges affects the equivalent stress on the seal ring. However, in currently used structures, the seal ring does not contact the chamfer of the flange under a compression of 20% and working pressure of 2 MPa. Therefore, the chamfer was not considered as a design variable in the study [25].

3.2. Determination of the Objective Function. In this study, the maximum value of the contact pressure between the seal ring and the upper flange was used to evaluate the sealing effect [26].

3.3. Determination of Constraints. The current diameter of the seal ring was 5.3 mm, and the diameter of the seal ring (D) was set to 4–7 mm according to the sealing conditions considered in this study. The depth of the seal groove (h) must not be less than the radius of the seal ring. Moreover, sufficient displacement must be caused by the upper flange due to the pretightening force [27]. Therefore, the mathematical model of the seal structure is expressed as follows:

$$\begin{aligned}
 &\text{Find} && X = [D, h]^T, \\
 &\text{max} && f(x) = f(D, h), \\
 &\text{Subject to} && 4 \text{ mm} \leq D \leq 7 \text{ mm}, \\
 &&& \frac{D}{2} \leq h \leq D - 1.2 \text{ mm}.
 \end{aligned} \tag{4}$$

3.4. Test Design. The Latin hypercube method [28, 29] was used to obtain the test points in the experiment. The points selected using this method can evenly cover the entire design space. Considerable space information can be accurately obtained with only a small number of test points. Because the upper and lower limits of the design variables in this study changed with a change in any parameter, a constrained Latin hypercube was used to select the test point [30].

The number of test points was selected according to the following principle: the number of test points must be 10 times higher than the number of variables. Two design variables were used in this study; therefore, 20 points were selected to build the surrogate model. The plane distribution of the design variables is displayed in Figure 4, in which the value ranges of the design variables are indicated by the coordinate axes.

3.5. Parametric Modelling. After the selection of the test points, the maximum contact pressure between the sealing ring and the upper flange was calculated for all the training and test points through finite-element simulation. Ansys Workbench was directly used for parametric modelling and finite-element calculation. The corresponding results are presented in Table 2.

3.6. Surrogate Model. The interpolating recombiquadric radial basis function method [31–33] was used for data fitting after obtaining the design and response points. A total of 20% of the data points (five points) were used as test points. The response surface and residuals of the training points are displayed in Figure 5.

The residual error of the training points was 10^{-7} (Figure 5), which is considerably lower than 10^{-4} ; thus, the surrogate model had a high degree of fit for the training points. The root mean square error of the aforementioned model was 0.48 for the five test points. The difference between the maximum stress values obtained with the surrogate model and in the experiment (7.3 MPa) was less than 10%, which is within the acceptable error range.

3.7. Optimisation of the End Plate Structure by Using the Genetic Algorithm. The genetic algorithm [34, 35] was used to optimise the design of the seal structure. The final iteration results are presented in Table 3. The maximum contact pressure was 7.28 MPa [36].

3.8. Reliability of the Sealing Structure. Let X_1, X_2, \dots, X_n be n random variables that affect the structural function, the function of which can be expressed as the following equation:

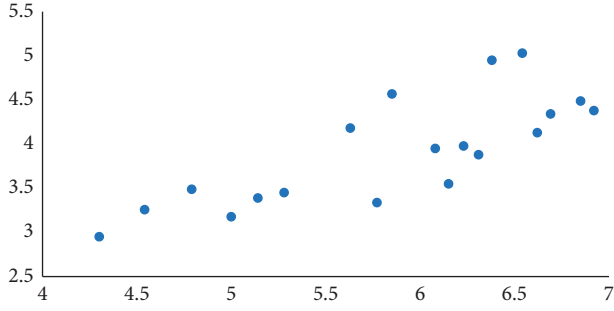


FIGURE 4: Plane distribution of design variables.

TABLE 2: Data points and response values.

D (mm)	h (mm)	P_{max} (MPa)
5.14	3.39	6.528
6.23	3.98	4.1881
4.54	3.26	4.8721
5.28	3.45	6.4509
6.31	3.88	4.1706
6.85	4.49	4.027
5.77	3.34	4.3518
5.85	4.57	4.302
5.63	4.18	4.3994
6.92	4.38	4.015
5.00	3.18	6.3237
6.62	4.13	4.0882
6.15	3.55	4.2387
6.69	4.34	4.0658
6.08	3.95	4.234
7.00	5.79	3.992574
4.30	2.95	5.0262
6.54	5.03	4.1055
6.38	4.95	4.1484
4.79	3.49	6.5858

$$Z = g(X_1, X_2, \dots, X_n), \quad (5)$$

where X_1, X_2, \dots, X_n could be the structural dimension parameter, the physical property of the material, or the loading on the structure. When $Z > 0$, the structure could perform the objective functions and work in a reliable state; when $Z < 0$, the structure could fail to perform the objective function and become unstable; when $Z = 0$, the structure is in the limit state or critical state. In this paper, p_f denoted the probability of failure, i.e., the probability of the structural function $Z < 0$. We used $f(z)$ to represent the probability density function. Therefore, the probability of $Z < 0$ is

$$p_f = \int_{-\infty}^0 f(z) dz. \quad (6)$$

However, the structure function should be standardized in the actual calculations:

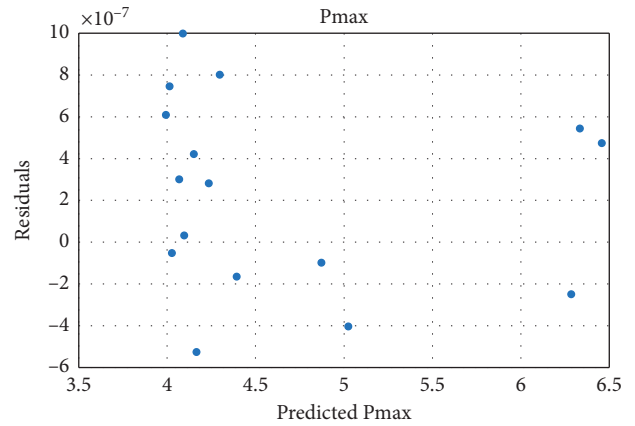
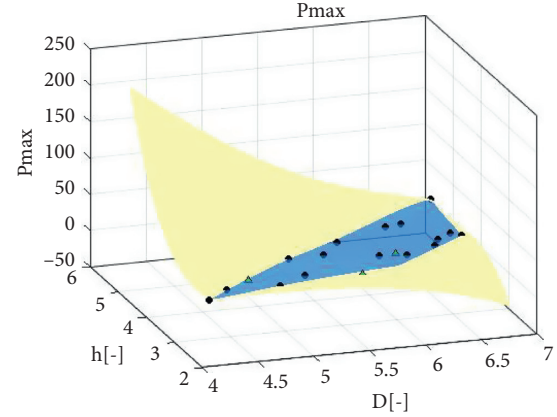


FIGURE 5: Response surface and residuals of the training points.

TABLE 3: Optimal design variables and optimal solutions.

D (mm)	h (mm)	P_{max} (MPa)
4.23	2.8	7.2778

$$Z' = \frac{C - \mu_z}{\sigma_z}. \quad (7)$$

The probability of failure after standardization can be expressed as

$$p_f = \int_{-\infty}^{(-\mu_z/\sigma_z)} f(z') dz'. \quad (8)$$

The reliability of the structure can be expressed as

$$P_r = 1 - p_f. \quad (9)$$

In this paper, the Gram-Charlier series was used to decompose and fit the distribution of the function, which could be expressed as

$$f(X) = \Phi'(X) = \sum_{n=3}^{\infty} \frac{(-1)^n C_n}{\sqrt{n!}} \Phi^{(n+1)}(X), \quad (10)$$

TABLE 4: The mean values and the mean square error in case of the maximum contact pressure after storage and aging of the sealed structure.

Time of usage	Shortly after sealing	10 years	20 years	25 years	30 years
Mean of response (MPa)	4.59	4.57	4.38	3.72	3.64
Mean square error of response (MPa)	0.94	0.88	0.84	0.72	0.72

TABLE 5: Reliability of 5 sealed structure joints.

Serial number	Shortly after sealing	10 years	20 years	25 years	30 years
1	0.976	0.921	0.851	0.827	0.796
2	0.983	0.926	0.846	0.821	0.793
3	0.984	0.927	0.859	0.835	0.794
4	0.987	0.931	0.861	0.845	0.807
5	0.994	0.938	0.881	0.848	0.813

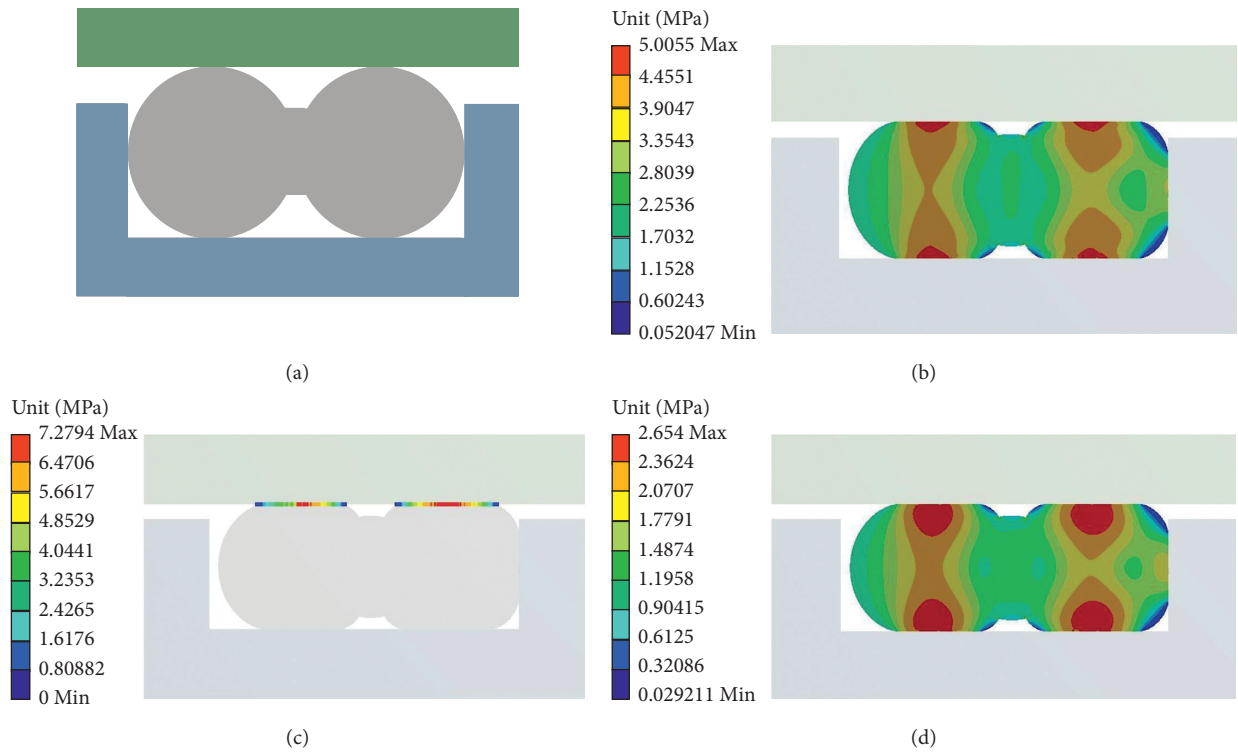


FIGURE 6: Model and simulation results.

where $\Phi(X) = (1/\sqrt{2\pi}) \int_0^x e^{-(t^2/2)} dt$ and C_n is the moment coefficient of each order. In this paper, in order to improve the calculation accuracy, the order of six was selected for calculation, which revealed the following equations:

$$C_0 = 1, \quad (11)$$

$$C_1 = C_2 = 1,$$

$$C_3 = \frac{1}{\sqrt{3!}} \frac{\mu_3}{\sigma^3}, \quad (12)$$

$$C_4 = \frac{1}{\sqrt{4!}} \left(\frac{\mu_4}{\sigma^4} - 3 \right),$$

$$C_5 = \frac{1}{\sqrt{5!}} \left(\frac{\mu_5}{\sigma^5} - 10 \frac{\mu_3}{\sigma^3} \right), \quad (13)$$

$$C_6 = \frac{1}{\sqrt{6!}} \left(\frac{\mu_6}{\sigma^6} - 15 \frac{\mu_4}{\sigma^4} + 30 \right), \quad (14)$$

where μ_k is the k th central moment of Z , and σ^k is the k th power of the mean square error of Z .

According to the finite-element analysis results above, the mean values and the mean square error in case of the maximum contact pressure after storage and aging of the sealed structure can be calculated. The results are shown in Table 4.

According to the finite-element simulation and the surrogate model, the limit state equation of the sealing structure was established, and the corresponding moments of the structure under the maximum contact pressure in each aging period can be obtained, and the reliability of the sealing structure can be calculated according to the above equations. In this paper, five nodes in the middle of the

TABLE 6: Comparison of the optimised and unoptimised results.

	Unoptimized seal structure (MPa)	Optimized sealing structure (MPa)	Lift percentage (%)
Mean equivalent stress	2.65	5.01	89.06
Maximum contact pressure	4.39	7.28	65.83
Maximum shear stress	2.67	2.65	-0.75

O-ring were selected for calculation. The results of reliability for the sealing structure joints are shown in Table 5.

The average value of the five nodes was used to represent the reliability of the sealing structure; it can be seen that the reliability of the sealing structure after 10 years, 20 years, 25 years, and 30 years was 0.985, 0.929, 0.859, and 0.801, respectively. A failure rate less than 10% is acceptable for ordinary hydraulic cylinder sealing structures. Therefore, the sealing structure could still be effective after 10 years.

4. Comparison of the Results Obtained before and after Optimisation

The parameters obtained after design variable optimisation were substituted into the model, and simulation was performed using Ansys Workbench. The maximum contact pressure was obtained as 7.2794 MPa. The error between the aforementioned value and the corresponding result obtained using the surrogate model was 0.027%. The model and simulation results are presented in Figure 6.

Figure 6(a) displays a schematic of the optimised seal model, and Figure 6(b) displays the equivalent stress cloud diagram. Figure 6(c) illustrates the cloud diagram of contact pressure between the seal ring and the upper flange, and Figure 6(d) displays the maximum shear stress cloud diagram. A comparison of the optimised and unoptimised structural design results are presented in Table 6.

According to the aforementioned simulation results, all the structures, the O-ring seal did not contact the chamfers of the seal grooves under a preload of 1.06 mm and working pressure of 2 MPa. The equivalent stress had a spindle-shaped distribution and was larger at the contact area than at other areas. The average equivalent stress of the optimised structure was 89.06% higher than that of the unoptimised structure. Moreover, the maximum contact pressure for the optimised structure was 65.83% higher than that for the unoptimised structure. The maximum shear stress indicates the service life of the seal ring. The maximum shear stress of the optimised seal structure was 0.75% lower than that of the unoptimised structure; thus, the shear stress was only marginally reduced after optimisation. The aforementioned results indicate that the optimised structure has a considerably stronger sealing effect and only marginally smaller service life than the original structure.

5. Conclusions

- (a) The obtained qualitative finite-element simulation results indicate that, during the operation of hydraulic cylinders, the peak values of the equivalent stress and contact pressure are always located at the contact between the seal ring and the upper flange in

the prestressed state. Thus, the sealing effect of a hydraulic cylinder seal can be assessed according to the maximum contact pressure at the contact between the seal and the upper flange.

- (b) The finite-element analysis results obtained for the four sealing structures considered in this study indicated that the sealing effect of the gapless double O-ring was stronger than those of the double O-ring with a gap, the gapless single O-ring, and the single O-ring with a gap.
- (c) According to the surrogate model and finite-element simulation calculations, the contact pressure of the optimised seal structure is 65.83% higher than that of the original gapless double O-ring. The combination of the developed surrogate model and finite-element method can provide ideas for the optimal design of seal structures without sacrificing the service life.

Data Availability

The datasets supporting the conclusions of this study are included within the article.

Conflicts of Interest

The authors declare that there are no conflicts of interest regarding the publication of this paper.

Acknowledgments

This project was supported by National Natural Science Foundation of China (Grant no. 51975092)

References

- [1] Y.-F. Gu, Y. Zhao, R.-Q. Lv, and Y. Yang, "A practical FBG sensor based on a thin-walled cylinder for hydraulic pressure measurement," *IEEE Photonics Technology Letters*, vol. 28, no. 22, pp. 2569–2572, 2016.
- [2] L. Solazzi and A. Buffoli, "Telescopic hydraulic cylinder made of composite material," *Applied Composite Materials*, vol. 26, no. 4, pp. 1189–1206, 2019.
- [3] C. Zhan, "Research on low-friction and high-response hydraulic cylinder with variable clearance," *Journal of Mechanical Engineering*, vol. 51, no. 24, p. 161, 2015.
- [4] G. H. Han and Y. L. Fu, "A study on the accelerated life test for hydraulic cylinders," *Advanced Materials Research*, vol. 199–200, pp. 630–637, 2011.
- [5] R. Lin, Y. Guo, S. Wei et al., "Critical load and optimum design for hydraulic cylinders," *China Mechanical Engineering*, vol. 22, no. 4, pp. 389–393, 2011.
- [6] C. H. Chen, C. T. Zhong, J. B. Wan et al., "Simulation and design for the hydraulic synchronization control system of clamping cylinders of tensioner on deep water cable-laying

- vessel,” *Ocean Engineering*, vol. 30, no. 4, pp. 137–143, 2012.
- [7] M. Kamezaki, H. Iwata, and S. Shigeki, “A practical approach to detecting external force applied to hydraulic cylinder for construction manipulator,” in *SICE Annual Conference*, IEEE, Taipei, Taiwan, August 2010.
- [8] X. Sheng, G. Si, and X. Li, “Reconfigurable hydraulic-mechanical combined drive devices based on multi-functional piston-rod built-in hydraulic cylinder,” in *Proceedings of 2010 International Conference on Digital Manufacturing & Automation*, IEEE, Changsha, China, December 2010.
- [9] E. Kassfeldt, “Analysis and design of hydraulic cylinder seals,” 2016.
- [10] F. Zhang, “The innovative design of reciprocating seal for hydraulic cylinder based on triz evolution theory,” in *Proceedings of International Conference on Programming Languages for Manufacturing*, pp. 440–449, Tianjin, China, 2006.
- [11] R. Chen, “The sealing problem of solid engine,” *Strength and Environment*, vol. 4, pp. 1–5, 1995.
- [12] Y. Zhou, B. Sun, S. Wang et al., “Finite element analysis of hydraulic cylinder sealing performance and friction force,” *Coal Mining Machinery*, vol. 39, no. 03, pp. 50–53, 2018.
- [13] H. Lan, L. Yang, F. Zhang, C. Zong, S. Wi, and X. Song, “Analysis and optimization of high temperature proton exchange membrane (HT-PEM) fuel cell based on surrogate model,” *International Journal of Hydrogen Energy*, vol. 45, no. 22, pp. 12501–12513, 2020.
- [14] H.-R Wang, S Wu, L.-L Yang et al., “Topology optimization of high temperature proton exchange membrane fuel cell reactor end plate,” *Journal of Dalian University of Technology*, vol. 60, no. 02, pp. 142–148, 2020.
- [15] X. Chen, *Finite Element Analysis and Optimization Design of High-Pressure Vessel Sealing Structure*, Lanzhou University, Lanzhou, China, 2015.
- [16] M. Yamamoto, S. Minewaki, H. Yoneda et al., “Nonlinear behavior of high-damping rubber bearings under horizontal bidirectional loading: full-scale tests and analytical modeling,” *Earthquake Engineering & Structural Dynamics*, vol. 41, no. 13, pp. 1845–1860, 2012.
- [17] Y. Ma, F. Scarpa, D. Zhang et al., “A nonlinear auxetic structural vibration damper with metal rubber particles,” *Smart Materials and Structures*, vol. 22, no. 8, Article ID 084012, 2013.
- [18] L. G. Maqueda, A. N. A. Mohamed, and A. A. Shabana, “Use of general nonlinear material models in beam problems: application to belts and rubber chains,” *Journal of Computational and Nonlinear Dynamics*, vol. 5, no. 2, 2010.
- [19] H. Wang, J. A. Rongong, G. R. Tomlinson et al., “Nonlinear static and dynamic properties of metal rubber dampers,” *Energy*, vol. 10, no. 1, 2010.
- [20] N. Koprowski-Theiß, M. Johlitz, and S. Diebels, “Modelling of a cellular rubber with nonlinear viscosity functions,” *Experimental Mechanics*, vol. 51, no. 5, pp. 749–765, 2011.
- [21] Z. Liang and B. Xiao, “A method for determining the material coefficient of the rubber,” *Mooney-Rivlin Model*, vol. 46, no. 527, pp. 38–40, 2008.
- [22] R. A. Hawileh, A. Rahman, and H. Tabatabai, “Nonlinear finite element analysis and modeling of a precast hybrid beam-column connection subjected to cyclic loads,” *Applied Mathematical Modelling*, vol. 34, no. 9, pp. 2562–2583, 2010.
- [23] S. R. Wu and L. Gu, *Introduction to the Explicit Finite Element Method for Nonlinear Transient dynamics*, John Wiley & Sons, Hoboken, NJ, USA, 2012.
- [24] M. C. H. Wu, D. Kamensky, C. Wang et al., “Optimizing fluid–structure interaction systems with immersogeometric analysis and surrogate modeling: application to a hydraulic arresting gear,” *Computer Methods in Applied Mechanics and Engineering*, vol. 316, pp. 668–693, 2017.
- [25] F. Sanchez, M. Budinger, and I. Hazyuk, “Dimensional analysis and surrogate models for the thermal modeling of Multiphysics systems,” *Applied Thermal Engineering*, vol. 110, pp. 758–771, 2017.
- [26] R. Mallipeddi and M. Lee, “An evolving surrogate model-based differential evolution algorithm,” *Applied Soft Computing*, vol. 34, pp. 770–787, 2015.
- [27] W. Yamazaki, M. Rumpfkeil, and D. Mavriplis, “Design optimization utilizing gradient/hessian enhanced surrogate model,” in *Proceedings of 28th AIAA Applied Aerodynamics Conference*, p. 4363, January 2010.
- [28] H. Dette and A. Pepelyshev, “Generalized Latin hypercube design for computer experiments,” *Technometrics*, vol. 52, no. 4, pp. 421–429, 2010.
- [29] F. Zhang, L. Cheng, Y. Gao et al., “Fault tree analysis of a hydraulic system based on the interval model using latin hypercube sampling,” *Journal of Intelligent & Fuzzy Systems*, pp. 1–11, 2019.
- [30] P. Z. G. Qian, “Sliced Latin hypercube designs,” *Journal of the American Statistical Association*, vol. 107, no. 497, pp. 393–399, 2012.
- [31] B. Sarler, N. Massarotti, P. Nithiarasu et al., “Local radial basis function collocation method for linear thermoelasticity in two dimensions,” *International Journal of Numerical Methods for Heat & Fluid Flow*, vol. 25, no. 6, pp. 1488–1510, 2015.
- [32] O. Estruch, O. Lehmkuhl, R. Borrell et al., “A parallel radial basis function interpolation method for unstructured dynamic meshes,” *Computers & Fluids*, vol. 80, pp. 44–54, 2013.
- [33] X. Yang, B. Xue, L. Jia et al., “Quantitative analysis of pit defects in an automobile engine cylinder cavity using the radial basis function neural network–genetic algorithm model,” *Structural Health Monitoring*, vol. 16, no. 6, pp. 696–710, 2017.
- [34] B. Mhamdi, K. Grayaa, and T. Aguil, “Hybrid of genetic algorithm with particle swarm optimization to shape reconstruction of perfect conducting cylinders,” *AEU-International Journal of Electronics and Communications*, vol. 65, no. 12, pp. 1032–1039, 2011.
- [35] B. Mhamdi, K. Grayaa, and T. Aguil, “Microwave imaging of dielectric cylinders from experimental scattering data based on the genetic algorithms, neural networks and a hybrid micro genetic algorithm with conjugate gradient,” *AEU-International Journal of Electronics and Communications*, vol. 65, no. 2, pp. 140–147, 2011.
- [36] G. Raju, B. Panitapu, and S. Naidu, “Optimal design of an IC engine cylinder fin arrays using a binary coded genetic algorithms,” *International Journal of Modern Engineering Research*, vol. 2, no. 6, pp. 4516–4520, 2012.

Research Article

Influence of Red Mud Proportion on Circular Concrete-Filled Steel Tubular Short Columns

Wu Bin ^{1,2}, Tan Zhuoying,¹ Li Fan,³ and Wang Sun⁴

¹School of Civil and Resource Engineering, University of Science and Technology Beijing, Beijing 100083, China

²Department of Construction Engineering, Liaoning Provincial College of Communications, Shenyang, Liaoning 110122, China

³Hannover Greenland Venue Management Co., Ltd., Shanghai 100083, China

⁴Architectural and Civil Engineering College, Shenyang University, Shenyang, Liaoning 110044, China

Correspondence should be addressed to Wu Bin; 66084537@qq.com

Received 30 March 2020; Revised 22 June 2020; Accepted 30 July 2020; Published 24 August 2020

Guest Editor: Norbert Randl

Copyright © 2020 Wu Bin et al. This is an open access article distributed under the Creative Commons Attribution License, which permits unrestricted use, distribution, and reproduction in any medium, provided the original work is properly cited.

Tests on twelve circular concrete-filled steel tube stub columns with mixed red mud and three circular concrete-filled steel tube stub columns to investigate the influence of the mixed proportion of red mud on the mechanical behavior of axial compressive circular concrete-filled steel tube stub columns are reported. It is found that with the increase of red mud content, the ultimate load increases first and then decreases; on the contrary, the ultimate displacement decreases first and then increases; the specimen stress reaches the proportion limitation as the steel tube longitudinal strain is around $160 \mu\epsilon$ and reaches the yield limitation as the steel tubes' longitudinal strain is around $4400\sim 5000 \mu\epsilon$. The axial compressive bearing capacity empirical formulation of concrete-filled steel tubes stub columns mixed with red mud is proposed. The theoretical calculation results agree well with those experimental data.

1. Introduction

Circular concrete-filled steel tube (CCFST) can provide excellent structural properties, such as high bearing capacity and high ductility, and the steel tube of CCFST can be used as permanent formwork to reduce the construction schedule without any effect by seasonal climate. Therefore a considerable amount of studies on CCFST have been carried out in recent decades [1–9], which make this kind of structure more and more widely used in subways, tunnels, bridges, high-rise, and super high-rise buildings.

Various studies of the utilization of solid waste in the construction industry have been conducted in recent years [10–13]. Most of the solid wastes generally produce certain radiation and corrosiveness, and the poured concrete with mixing those solid wastes normally engenders attribute of high dispersion. However, the steel tube has the characteristics of radiation protection and corrosion resistance, and it has a behavior to constrain the dispersion of concrete. Therefore, the solid wastes utilized in the CCFST would

greatly improve the utilization rate of solid wastes in the world. Nowadays, the research works of solid wastes in CCFST [14–16] have already been conducted and achieved some research results.

As a result, this paper takes red mud as a research object to study its effective utilization. Red mud, as a solid waste produced in the process of bauxite extraction, occupies a large amount of land. Its high alkali content causes serious pollution in the surroundings, which makes the red mud disposal and utilization increasingly prominent [17]. At present, the main field of red mud treatment is in the construction industry, and some achievements have been made. It was found that red mud had good cementations' activity and could be well utilized [18]. Liu and Poon [19] used bauxite residue-red mud instead of part of fly ash to make self-compacting concrete in order to test its mechanical behavior. It was found that the compressive strength, the splitting tensile strength, and the elastic modulus of the specimens were increased, respectively. Wu et al. [20] put forward the concept of the CCFST mixed with

red mud first and conducted experimental research on pushing core concrete out of steel tube. The research result indicated that the bond slip behavior of the CCFST mixed with red mud was improved; it was proved that the cement of core concrete could be partly replaced by the red mud.

In order to investigate the influence of mixing proportion of the red mud on the mechanical behaviors of CCFST stub columns under axial compressive load, the tests on a total of fifteen specimens under axial compressive bearing load including twelve specimens of CCFST stub columns mixing with the red mud and three specimens of CCFST stub columns are reported in this paper. The main objective of these tests was twofold: firstly, to derive the empirical formulation of axial compressive bearing capacity by the discussion on the influence of mixing proportion of the red mud in CCFST stub columns; and secondly, to verify the correctness of the formulation by comparing and analyzing the calculation results and the test data.

2. Experimental Study

2.1. Specimen Material

- (1) Steel tube: a seamless circular steel tube was applied. According to Chinese Code GB/T228-2002, the tensile test method of metal material at the status of room temperature, the yield strength f_y , tensile strength f_u , elastic modulus E_s , yield strain ε_{sy} , and Poisson's ratio ν_s will be determined, shown in Table 1.
- (2) Concrete: Yatai brand 42.5R normal cement mixed with 5~15 mm aggregates, the river sand, and the tap water; the superplasticizer was applied from Liaoning Jianfeng Industrial Co., Ltd; Bauxite residue-red mud generated in Beihai Alumina Plant, Weiqiao, Shandong Province. The chemical composition of the red mud is shown in Table 2. The quality substitution rate of the red mud in the concrete was applied for 0%, 5%, 10%, 15%, and 20%, respectively. The mixture ratio of the red mud concrete was in accordance with the Chinese standard JGJ55-2001 mix design of normal concrete, as can be seen in Table 3.

2.2. Specimen Labels and Parameters. A total of fifteen specimens were constructed including twelve CCFST stub columns mixed with the red mud and three CCFST stub columns. A summary of the specimen information is given in Table 4. The specimens labeled as CSC are for Circular Stub Column; the fourth letter labeled as A, B, or C is for the external diameter of the specimens of 108 mm, 133 mm, or 159 mm, and the last Arabic numeral labeled 1, 2, 3, 4, or 5 is for the quality substitution rate of the red mud of 0%, 5%, 10%, 15%, or 20%. L is the length of the stub column; D is the external diameter of the circular steel tube; t_s stands for the wall thickness of the steel tube; $r\%$ means the quality substitution rate of the red mud; f_{cu} means the cubic compressive strength of concrete; α means the steel content; ξ_s ,

TABLE 1: Mechanic properties of the steel tube.

Label	$D \times t$ (mm)	f_y (MPa)	f_u (MPa)	E_s (GPa)	ε_{sy} ($\mu\varepsilon$)	ν_s
CSCA	108 × 4.5	323.3	490.0	205	1650	0.27
CSCB	133 × 4.5	298.9	462.7	203	1600	0.27
CSCC	159 × 4.5	292.3	463.6	203	1550	0.27

stands for the confining factor; N_u^e is the ultimate bearing capacity of stub column.

2.3. Specimens Fabrication. A circular steel tube was cut into fifteen steel tubes according to the length shown in Table 4 on the automatic cutting machine. All the specimens were three times the diameter in length to reduce the end effects and to ensure that the specimens would be stub columns with minimum effect from slenderness. Each tube was welded to a 200mm × 200mm × 10 mm steel base plate at the bottom of the steel tube. Fifteen same size steel plates were milled with a 3 mm deep concentric round groove which diameter was 0.2 mm bigger than the external diameter of the steel tubes and was used as the movable cover plates on the top of the steel tubes. The red mud concrete was poured from the top of the steel tube and compacted with vibration until the red mud concrete was higher than the top surface of the steel tube. All the specimens were cured for 2 weeks, then the top surface of the red mud concrete-filled steel tube was ground smooth and flushed with the steel tube by using an angle polishing machine. The steel cover plate covered on the top surface of the steel tube. This was done to ensure that the load was applied evenly across the cross-section and simultaneously to the steel tube and concrete core. See Figures 1 and 2 for the fabricated test specimens.

2.4. Test Arrangement and Measurement. The loading device and measuring equipment are shown in Figures 3 and 4. All the specimens were tested with a universal testing machine with a 2000 kN capacity in the structural engineering laboratory of Liaoning Construction Sciences Academy. The longitudinal displacement of each specimen was measured by two transducers with a measurement range of 50 mm. The arrangement of strain gauges is shown in Figure 5. There were 8 strain gauges in total, including 4 longitudinal strain gauges and 4 circumferential strain gauges (points 1–4). The type of strain gauge was BX120-5AA, and the size was 50 × 3. TDS602 was used for collecting relative strain and displacement.

2.5. Loading System. According to Chinese Code GB/T 50152-2012 Standard for test method of concrete structures, the test adopted method of load increment, as shown in Figure 6. The estimated ultimate loads of the 3 series A, B, C specimens were about 900 kN, 1300 kN, and 1700 kN, respectively. The preloading value was applied 10% of the estimated ultimate load in order to make a concentric adjustment imposing on specimens. Then, the loads were applied in increments of 1/10 of the estimated ultimate load

TABLE 2: Red mud chemical composition.

	Al ₂ O ₃	Na ₂ O _k	Fe ₂ O ₃	SiO ₂	TiO ₂	CaO	CO ₂	H ₂ O	H ₂ O	Loss	PH	Density (g.cm ⁻³)
%	23.73	7.39	28.79	24.63	2.22	2.69	0.97	8.59	1	14.94	11.3	3.2

TABLE 3: The proportion of red mud concrete Kg/m³.

SN	Red mud	Cement	Sand	Aggregate I	Aggregate II	Water	Superplasticize
RMC-0	0	360	780	216	862	162	3.6
RMC-5	18	342	780	216	862	162	3.9
RMC-10	36	324	780	216	862	162	4.2
RMC-15	54	306	780	216	862	162	4.5
RMC-20	72	288	780	216	862	162	4.8

Note: RMC labeled for red mud concrete; 0, 5, 10, 15, and 20 are for quality substitution rate of red mud 0%, 5%, 10%, 15%, and 20%, respectively.

TABLE 4: Parameters of the specimens.

SN	Specimen	L (mm)	D (mm)	ts (mm)	r (%)	f _y (MPa)	f _{cu} (MPa)	D (ts)	α	ξs	N _u ^e (kN)
1	CSCA-1	324	108	4.5	0	323.3	36.9	24	0.19	2.488	885.6
2	CSCA-2	324	108	4.5	5	323.3	50.5	24	0.19	1.815	1003.4
3	CSCA-3	324	108	4.5	10	323.3	46.6	24	0.19	1.968	971.8
4	CSCA-4	324	108	4.5	15	323.3	44.0	24	0.19	2.083	948.6
5	CSCA-5	324	108	4.5	20	323.3	34.0	24	0.19	2.700	860.5
6	CSCB-1	400	133	4.5	0	298.9	36.9	29.6	0.15	1.821	1289.6
7	CSCB-2	400	133	4.5	5	298.9	50.5	29.6	0.15	1.328	1403.6
8	CSCB-3	400	133	4.5	10	298.9	46.6	29.6	0.15	1.440	1369.4
9	CSCB-4	400	133	4.5	15	298.9	44.0	29.6	0.15	1.524	1349.2
10	CSCB-5	400	133	4.5	20	298.9	34.0	29.6	0.15	1.976	1265.6
11	CSCC-1	477	159	4.5	0	292.3	36.9	35.3	0.124	1.463	1630.1
12	CSCC-2	477	159	4.5	5	292.3	50.5	35.3	0.124	1.067	1884.5
13	CSCC-3	477	159	4.5	10	292.3	46.6	35.3	0.124	1.157	1812.5
14	CSCC-4	477	159	4.5	15	292.3	44.0	35.3	0.124	1.225	1766.5
15	CSCC-5	477	159	4.5	20	292.3	34.0	35.3	0.124	1.587	1600.0



FIGURE 1: Specimens.

in the elastic range. When the target loads were reached, each target load was maintained for 2 mins on the specimen. As the load reached 60% of the estimated ultimate load (540 kN, 780 kN, and 1020 kN, respectively), the loads were

applied in an increment of 1/20 of the estimated ultimate load. When the target loads were reached, each target load was maintained for 2 mins as well. As the specimen was under destruction, the load continued to increase slowly. After reaching the ultimate load value, the loads were applied continuously until the deformation of the specimen was too big, then the test stopped. Each test took approximately one hour to complete. In the whole process of the test, the load readings and deformation measurements were recorded automatically by the pressure servo machine, which provided enough data points to complete the drawing of load displacement curve.

3. Experimental Results and Discussion

3.1. Analysis of Experimental Phenomena. At the beginning, the specimens were loaded in the elastic stage without obvious change. When the load reached 60% ~ 70% of the ultimate load, the shear slip line appeared on the steel tube wall. As the load reached 80% ~ 90% of the ultimate load, the rust on the steel tube wall started falling down, the local buckling of the steel tube happened, and the cross shear slip line emerged. Then, the specimens were in the failure stage. Because the confining factor was relatively big, the

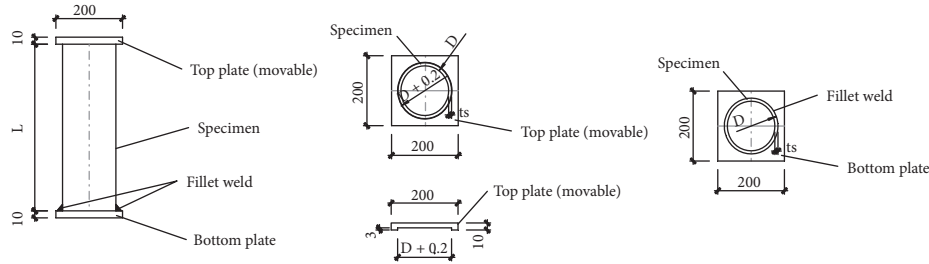


FIGURE 2: The specimens geometry.



FIGURE 3: The loading device.

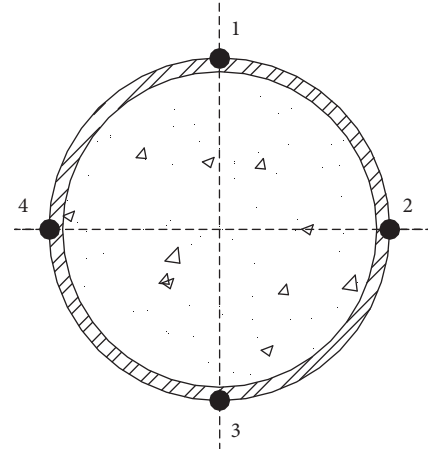


FIGURE 5: Arrangement of the strain gauges measuring equipment.

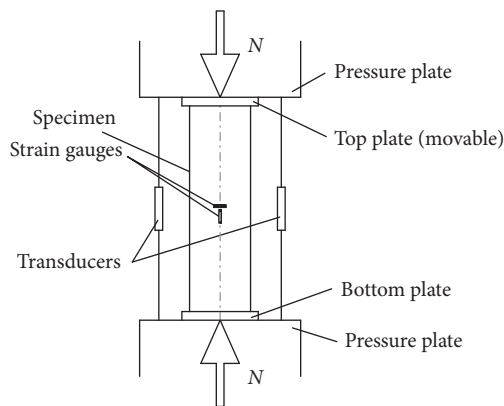


FIGURE 4: Column test layout.

drum-shaped failure occurred (Figure 7), while the specimens showed good ductility. After the ultimate load was reached, the bearing capacity of the specimens was different according to the different confining factor. For the specimens with big confining factor, the bearing capacity was slightly increased. For the specimens with small confining factor, the bearing capacity was slightly decreased. For the specimen with a moderate confining factor, the bearing capacity kept the same. The deformation of the specimens in those 3 situations was continuously increasing until the specimens were loaded to failure. The failure modality of the

CCFST with the red mud specimen was similar to the failure modality of the CCFST specimen. Figure 8 shows all the specimens with failure mode.

3.2. Influence of Mixed Red Mud. The load (kN) versus displacement (mm) curves for the 3 groups specimens (A, B, C) are presented in Figure 9.

As shown in Figure 9, the load (kN) versus axial displacement (mm) curves for the 3 series of specimens are little different. It was found that with the increase of the quality substitution rate of the red mud (r) in the CCFST stub column, the ultimate load of specimens increased first and then decreased. The ultimate load was the maximum, as $r = 5\%$, the ultimate load on the CCFST with the red mud specimens for groups A, B, and C were 1003.4 kN, 1403.6 kN, and 1884.5 kN, respectively, which increased 13.30%, 8.84%, and 15.61% compared with those 3 CCFST specimens. As $r = 20\%$, the ultimate load on the CCFST with the red mud specimens for groups A, B, and C were 860.5 kN, 1265.6 kN, and 1600 kN, respectively, which decreased 2.83%, 1.86%, and 1.85% than the ultimate load on the 3 CCFST specimens. It illustrates that when the quality substitution rate of the red mud is between 0%~20%, the ultimate load on the CCFST with the red mud increases, the reasons of which are twofold: firstly, the red mud has the characteristics of pozzolanic. During the hydration of concrete, $\text{Ca}(\text{OH})_2$ was produced. It reacted with active SiO_2 , Fe_2O_3 , and Al_2O_3 produced from the red mud in the second time hydration and generated the hydrate calcium

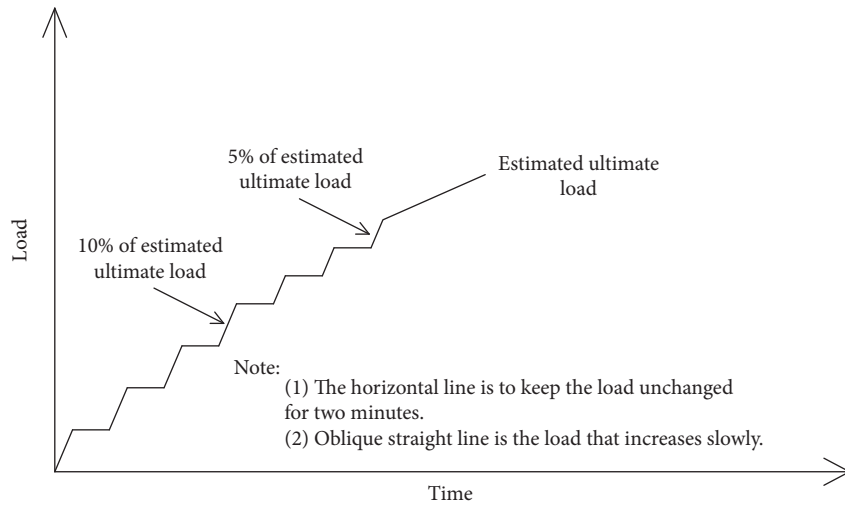


FIGURE 6: Simplified diagram of the method of load increment.



FIGURE 7: Local buckling of the steel tube.

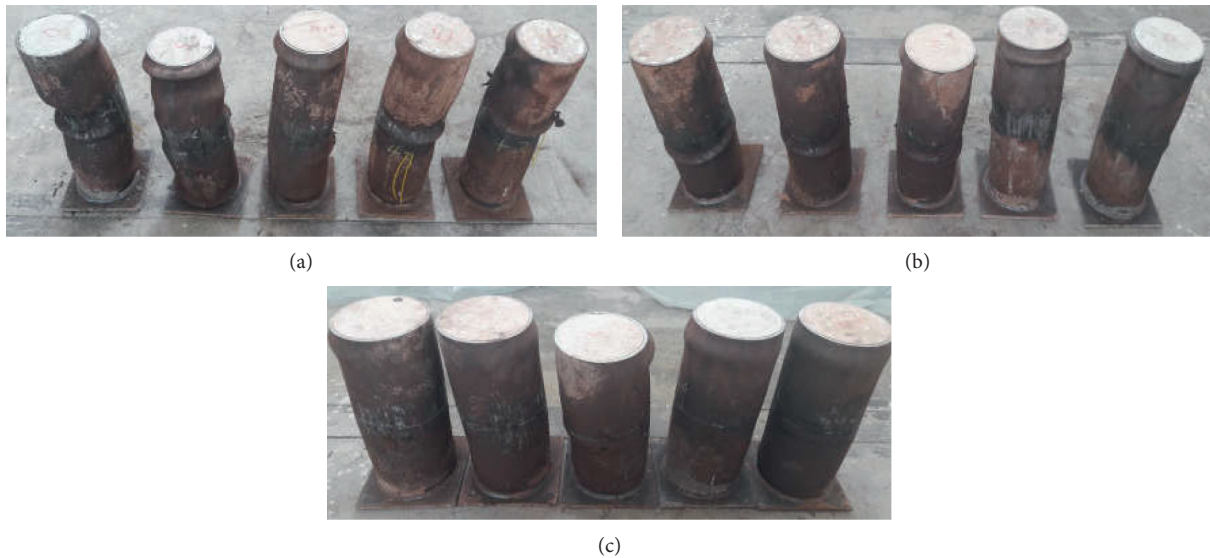


FIGURE 8: Failure mode of specimens. (a) CSCA. (b) CSCB. (c) CSCC.

silicate and the hydrate calcium acuminate. In the process of the reaction, $\text{Ca}(\text{OH})_2$ generated was being consumed, which caused further hydration reaction promoted. The structure of the interface between the internal medium of concrete was improved. The compressive strength of concrete was enhanced; and secondly, the red mud particles were finer after processing, its specific surface area was bigger than $400 \text{ m}^2/\text{kg}$, while the specific surface area of

Portland cement was only bigger than $300 \text{ m}^2/\text{kg}$. Therefore, the red mud played a physical filling role in the concrete. The concrete mixing with the red mud would have smaller pores and lower porosity, which caused the compactness of the concrete was raised. As a result, the compressive strength of the concrete would be improved.

As seen in Figure 9, with the increase of the quality substitution rate of the red mud (r) in the CCFST stub

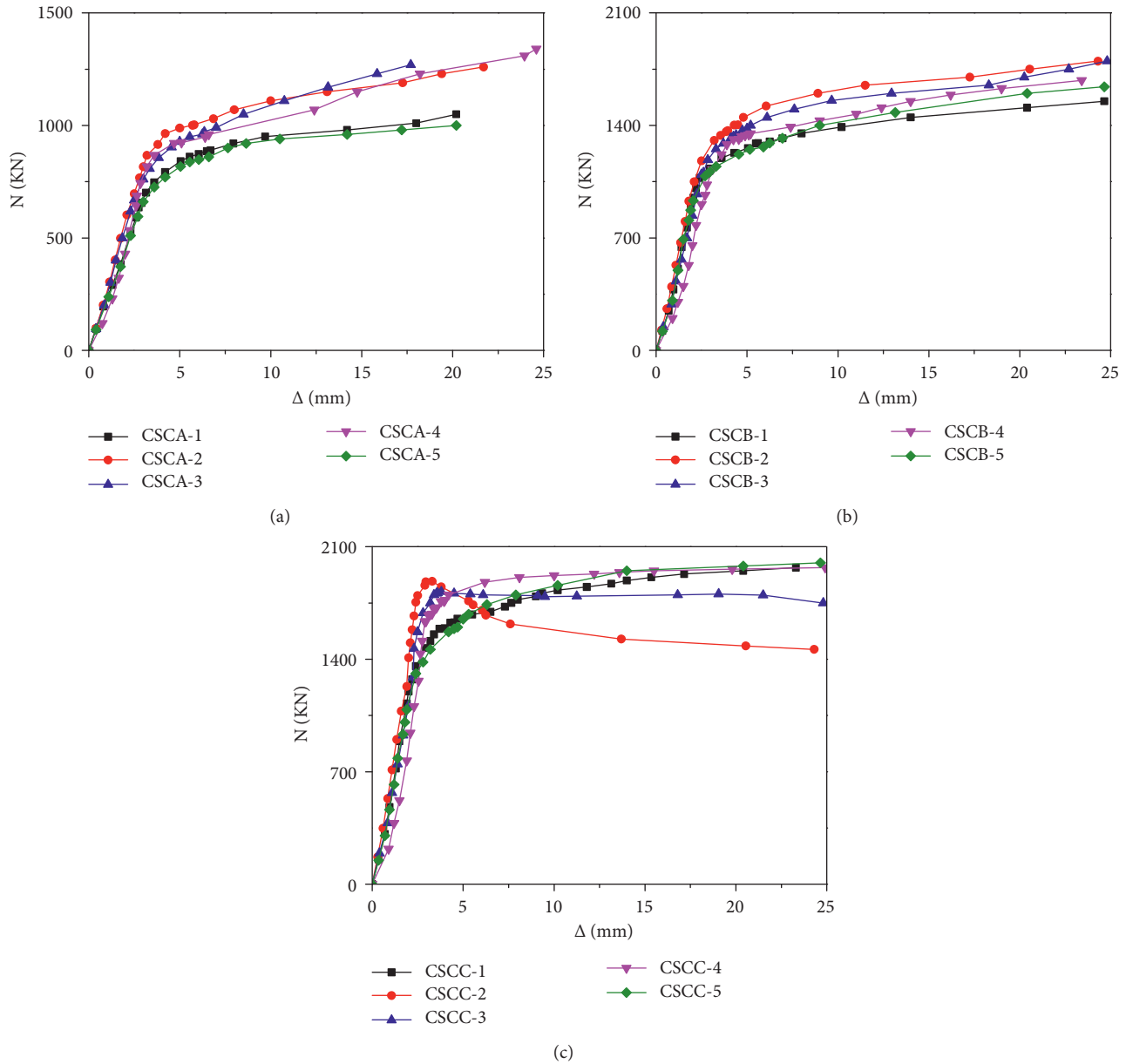


FIGURE 9: The load versus displacement curves. (a) Group A. (b) Group B. (c) Group C.

column, the ultimate displacement of the specimens decreased first and then increased, the ultimate displacement was minimum, as $r=5\%$, the ultimate displacement of the CCFST with the red mud specimens for groups A, B, and C were 5.8 mm, 4.5 mm, and 3.3 mm, respectively, decreased 10.77%, 19.64%, and 26.67% than those 3 CCFST specimens. As $r=20\%$, the ultimate displacement of the CCFST with the red mud specimens for groups A, B, and C was 6.6 mm, 5.9 mm, and 4.7 mm, respectively, increased 1.54%, 5.36%, and 4.44% than the ultimate displacement of the 3 CCFST specimens. Obviously, when the quality substitution rate of the red mud was between 0%~20%, the ultimate displacement of the CCFST with the red mud specimens decreased and the ductility became weaker compared with the CCFST specimens, the main reason of which was that the strength of

the CCFST mixing the red mud was improved and the stiffness was enhanced.

3.3. *Analysis of the Whole Process of Stress Strain.* The nominal compressive stress of the specimen is $\sigma_{sc} = N/A_{sc}$:

σ_{sc} is the nominal compressive stress of the specimen

N is the axial pressure,

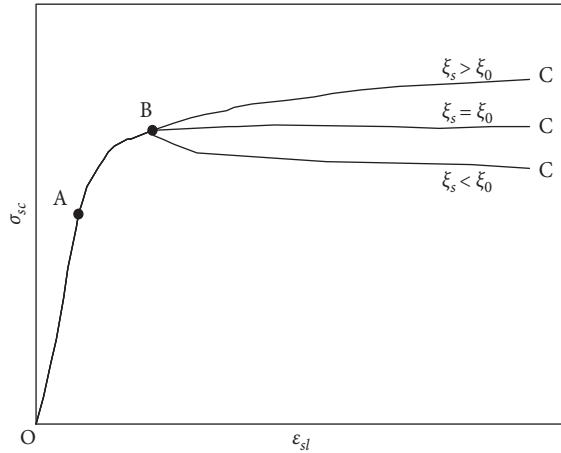
A_{sc} is the cross-sectional area of the specimen

The axial compressive strain of the specimen is $\varepsilon_{sl} = \Delta/L$:

ε_{sl} is the compressive strain of the specimen

Δ is the axial deformation

L is the height of the specimen


 FIGURE 10: The $\sigma_{sc} - \varepsilon_{sl}$ relations of the specimens.

According to Figure 8, the typical $\sigma_{sc} - \varepsilon_{sl}$ curves of the specimens were obtained, as shown in Figure 10.

As can be seen from Figure 10, the curve mainly undergoes three stages: elastic stage (OA), elastic-plastic stage (AB), and ascending/descending/horizontal stage (BC).

OA stage: the curve is linear. It indicates that the quality substitution rate of the red mud has little effect on the stiffness when the specimen is in the elastic stage. The steel tube and the red mud concrete have not been working well together. When reaching point A, the steel tube is in a compressive yield state, the longitudinal strain is about $1600 \mu\epsilon$, the circumferential strain is around $450 \mu\epsilon$, and the specimen reaches the proportional limitation.

AB stage: the specimen is in the elastic-plastic stage, and the steel tube and the red mud concrete bear the load simultaneously. With the development of the red mud concrete cracks in the steel tube, the transverse deformation exceeds the Poisson's ratio of the steel tube. Mutual extrusion produced between these two materials causes the steel tube to produce the confinement effect on the red mud concrete core. At the same time, the red mud concrete core is in a three-dimensional compressive state. Therefore, the bearing capacity of the specimen is enhanced. As reaching point B, the longitudinal strain of the steel tube is about $4400 \sim 5000 \mu\epsilon$, and the specimen reaches the yield limitation.

BC stage: when it exceeds point B, the curve is divided into three situations according to the different confining factor. As $\xi_s = \xi_0$, the curve is basically horizontal; as $\xi_s > \xi_0$, it becomes a slowly rising curve, the bigger the confining factor is, the larger the rise range is, and vice versa; as $\xi_s < \xi_0$, it is a gradually falling curve, the smaller the confining factor is, the larger the decline range is, and vice versa. According to Table 4 and Figure 9, $\xi_0 = 1.1$.

4. Simplified Calculation of Axial Compressive Bearing Capacity

4.1. *The Proposed Empirical Formulation of Axial Compressive Bearing Capacity of Stub Column.* According to Figure 9, when the specimens reach the peak load, the deformation is

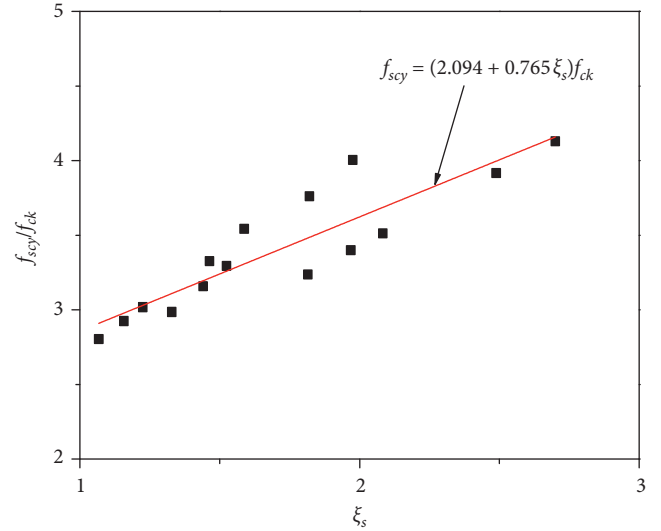


FIGURE 11: The relationship between ultimate yield strength and confining factor.

too big. The components would have lost their usage function if they were applied in the real projects. Therefore, the ultimate yield strength f_{scy} of the specimen (longitudinal strain is about $4400 \sim 5000 \mu\epsilon$) determined by the stress-strain relations shown in Figure 10 is defined as the ultimate strength of the axial compressive bearing capacity of the specimen. In the range of quality substitution rate of the red mud $r = 0\% \sim 20\%$, regression analysis of test data is carried out, as shown in Figures 11 and 12.

The formulation of f_{scy} proposed by regression analysis is as follows:

$$f_{scy} = \varphi_r (2.094 + 0.765\xi_s) f_{ck}. \quad (1)$$

Then, the axial compressive bearing capacity formulation of the CCFST stub column with the red mud is proposed as follows:

$$N_u = f_{scy} A_{sc}, \quad (2)$$

$$\varphi_r = 0.993 - 1.480r + 8.261r^2, \quad (3)$$

$$A_{sc} = A_s + A_c. \quad (4)$$

f_{scy} is the ultimate strength of axial compressive bearing capacity; f_{ck} is the standard value of compressive strength of concrete; $f_{ck} = 0.67 f_{cu}$. ξ_s is the confining factor of steel tube; $\xi_s = (f_y A_s / f_{ck} A_c)$. N_u is the axial compressive bearing capacity of stub column; A_{sc} is the composite section area of CCFST stub column with red mud; A_s is the section area of steel tube of CCFST stub column with red mud; A_c is the section area of concrete of CCFST stub column with red mud; φ_r is the influence coefficient of quality substitution rate of the red mud; r is the quality substitution rate of the red mud

When $r = 0\%$, it can be seen as the formulation of the axial compressive bearing capacity of the CCFST stub column.

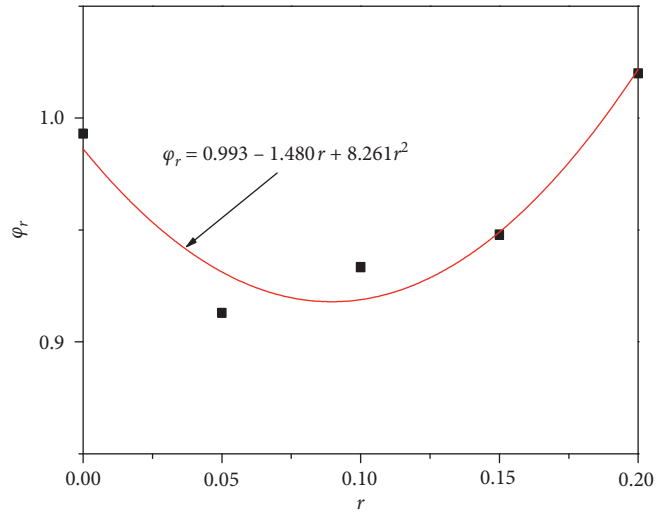
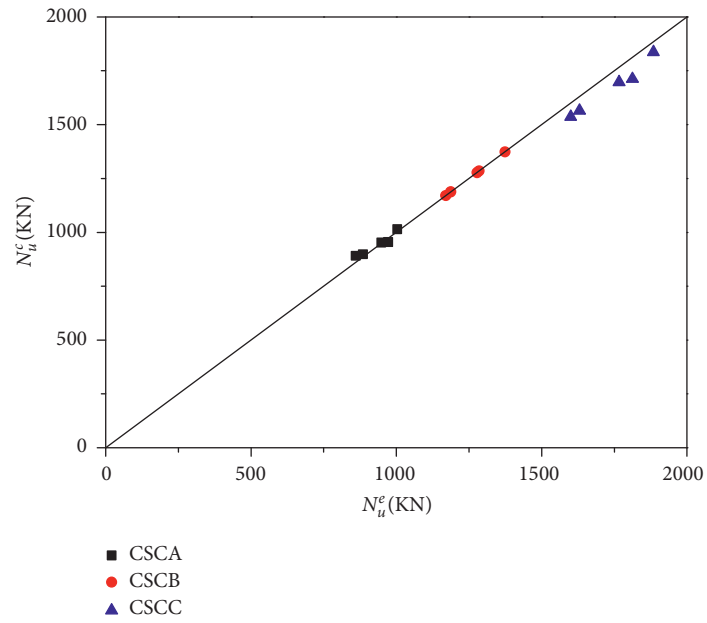


FIGURE 12: The relationship between ultimate yield strength and quality substitution rate of the red mud.



(a)

FIGURE 13: Continued.

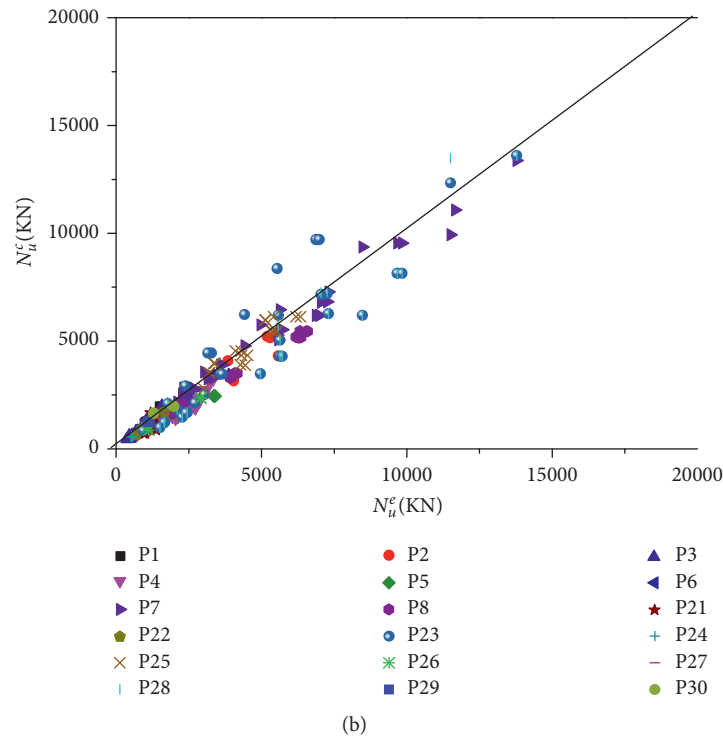


FIGURE 13: The comparison of calculated result and experiment result of axial compressive bearing capacity.

4.2. Validation of the Proposed Empirical Formulation. In order to verify the correctness of the proposed empirical formulation, the calculated results from formula (2) shown above were compared with test data of fifteen specimens, as can be seen in Figure 13(a). It was found that the mean value, the standard deviation, and the variation coefficient of the CCFST stub columns with the red mud N_u^c/N_u^e were 0.989, 0.024, and 0.024, respectively. The result indicates that, in general, the theoretical values of the axial compressive bearing capacity of stub columns agree well with the experimental data.

Due to the limited experimental data of 15 CCFST stub columns with the red mud, the additional experimental data of a total of 325 CCFST stub columns specimens ($r=0\%$) from references [1–8, 21–29] were introduced in order to further validate the proposed formulation and were compared with the calculated value from formula (2), as can be seen in Figure 13(b). It was found that the mean value, the standard deviation, and the variation coefficient of CCFST stub columns N_u^c/N_u^e were 0.938, 0.141, and 0.150, respectively. In the same way, the theoretical value of the axial compressive bearing capacity of the stub column agrees well with the experimental data as well.

Therefore, formula (2) is applicable to the calculation of axial compressive bearing capacity for the CCFST stub columns with the red mud (as $r=0\%$ for the CCFST stub columns). Formula calculation value is generally safe and suitable for engineering application.

5. Conclusions

Based on the results of this study, the following conclusions can be drawn:

- (1) with the increase of the quality substitution rate of the red mud ($r=0\%\sim 20\%$) in the CCFST stub column with the red mud, the ultimate load increases first and then decreases; on the contrary, the ultimate displacement decreases first then increases; the ultimate load is maximum, as $r=5\%$, while the ultimate displacement is minimum; as $r=20\%$, the ultimate load and the ultimate displacement are both nearly the same, respectively, as $r=0\%$.
- (2) As the longitudinal strain of the steel tube is about $1600\mu\epsilon$, the specimen reaches the proportional limitation; as the longitudinal strain of steel tube is about $4400\sim 5000\mu\epsilon$, the specimen reaches the yield limitation. When it exceeds yield limitation, as $\xi_s = \xi_0$, the curve is basically horizontal; as $\xi_s > \xi_0$, it becomes a slowly rising curve; as $\xi_s < \xi_0$, it is a gradually falling curve, $\xi_0 = 1.1$.
- (3) Empirical formulation of axial compressive bearing capacity of the CCFST stub columns with the red mud is proposed with clear expression, and it is suitable for engineering application.
- (4) The experimental data of total 340 specimens, including 15 specimens shown in this paper, were

compared with calculated results from formula (2). The calculated results agree well with the experimental data, which approve the correctness of the empirical formulation.

Data Availability

The literature data used to support the findings of this study have been deposited in the CNKI and Duxiu Academic Search repositories (ISBN7-03-012871-0; ISBN 978-7-114-06393-0; ISBN7-5611-1071-5; 10.14006/j.jzjgxb.2002.02.006; 10.14006/j.jzjgxb.1999.01.00210.15951/j.tmgxcb.2004.09.001; 10.14006/j.jzjgxb.2017.S1.034; doi:10.1016/j.jcsr.2003.10.001; ISSN 0733-9445/00/0011-1295-1303; ISSN:1708-5284; 10.1061/(ASCE)ST.1943-541X.0002474; doi.org/10.1016/j.jcsr.2003.10.001; doi.org/10.1061/(ASCE)0733-9445(2004)130:2(180); doi.org/10.1016/j.tws.2007.10.001; doi.org/10.1016/j.tws.2016.04.004). The test data used to support the findings of this study are included within the article. Previously reported literature data were used to support this study and are available at (ISBN7-03-012871-0; ISBN978-7-114-06393-0; ISBN7-5611-1071-5; 10.14006/j.jzjgxb.2002.02.006; 10.14006/j.jzjgxb.1999.01.00210.15951/j.tmgxcb.2004.09.001; 10.14006/j.jzjgxb.2017.S1.034; doi:10.1016/j.jcsr.2003.10.001; ISSN0733-9445/00/0011-1295-1303;ISSN:1708-5284;10.1061/(ASCE)ST.1943-541X.0002474;doi.org/10.1016/j.jcsr.2003.10.001;doi.org/10.1061/(ASCE)0733-9445(2004)130:2(180);doi.org/10.1016/j.tws.2007.10.001;doi.org/10.1016/j.tws.2016.04.004). These prior studies (and datasets) are cited at relevant places within the text as references [1~8] and [21~30].

Conflicts of Interest

The authors declare that they have no conflicts of interest.

Acknowledgments

This work was financially supported by the National Natural Science Foundation of China (51574015), Liaoning Province PHD Startup Fund (20170520139), Liaoning Province "Xingliao Talent Program" Project (XLYC1906010), and Liaoning Provincial Communications Technical College 2019 Technology Applied Research Funding Project (LNCCjyky201918).

References

- [1] L. H. Han, *Concrete Filled Steel Tubular structures*, Science Press, Beijing, China, 2nd edition, 2007.
- [2] S. H. Cai, *Modern Steel Tube Confined Concrete structures*, China Communications Press, Beijing, China, 2nd edition, 2007.
- [3] L. H. Han and S. T. Zhong, *Concrete Filled Steel Tube Mechanics*, Dalian University of Technology Press, Dalian, China, 2nd edition, 1996.
- [4] Z. Yu, F. Ding, and L. Song, "Researches on behavior of high-performance concrete filled tubular steel short columns," *Journal of Building Structures*, vol. 23, no. 2, pp. 41-47, 2002.
- [5] K. Tan, X. Pu, and S. Cai, "Study on the mechanical properties of steel extra-high strength concrete encased in steel tubes," *Journal of Building Structures*, vol. 20, no. 1, pp. 10-15, 1999.
- [6] S. Zhang and Y. Wang, "Failure mode of short columns of high-strength concrete-filled steel tubes," *China Civil Engineering Journal*, vol. 37, no. 9, pp. 1-10, 2004.
- [7] K. Sakino, H. Nakahara, and S. Morino, "Behavior of centrally loaded concrete-filled steel-tube short columns," *Journal of Structural Engineering*, vol. 130, no. 2, pp. 180-188, 2004.
- [8] P. Nishiyama, Y. Wang, C. Liu et al., "Experimental study on size effect of circular concrete-filled steel tubular columns subjected to axial compression," *Journal of Building Structures*, vol. 38, no. S1, pp. 249-257, 2017.
- [9] J. Xiao, Q. Zhang, J. Yu et al., "A novel development of concrete structures: Composite concrete structures," *Journal of Tongji University (Natural Science)*, vol. 46, no. 2, pp. 147-155, 2018.
- [10] J. Xiao, Z. Lin, and J. Zhu, "Effects of recycled aggregates' gradation on compressive strength of concrete," *Journal of Sichuan University (Engineering Science Edition)*, vol. 46, no. 4, pp. 154-160, 2014.
- [11] S. Omary, E. Ghorbel, and W. George, "Relationships between recycled concrete aggregates characteristics and recycled aggregates concretes properties," *Construction and Building Materials*, vol. 108, pp. 163-174, 2016.
- [12] M. Zhou, S. Tian, T. Guo et al., "Experimental research on the concrete using spontaneous combustion gangue as full active material," *Bulletin of the Chinese Ceramic Society*, vol. 30, no. 5, pp. 1221-1226, 2011.
- [13] L. Yan-hua, Li Liang, and Q.-xin Ren, "Mechanical properties of rubber concrete-filled square steel tubular stub columns subjected to axial loading," *Journal of Northeastern University (Natural Science)*, vol. 32, no. 8, pp. 1198-1209, 2011.
- [14] J. Chen, Y. Wang, C. W. Roeder, and J. Ma, "Behavior of normal-strength recycled aggregate concrete filled steel tubes under combined loading," *Engineering Structures*, vol. 130, pp. 23-40, 2017.
- [15] L. Ma and Z. Shan-tong, "Strength and lateral deformation coefficient of gangue concrete restrained by steel tube," *Journal of Harbin University of C. E.&Architecture*, vol. 35, no. 3, pp. 20-23, 2002.
- [16] A. Silva, Y. Jiang, J. M. Castro, N. Silvestre, and R. Monteiro, "Monotonic and cyclic flexural behaviour of square/rectangular rubberized concrete-filled steel tubes," *Journal of Constructional Steel Research*, vol. 139, pp. 385-396, 2017.
- [17] W. Liu, J. Yang, and B. Xiao, "Review on treatment and utilization of bauxite residues in China," *International Journal of Mineral Processing*, vol. 93, no. 3-4, pp. 220-231, 2009.
- [18] X. Liu, N. Zhang, and H. Sun, "Structural investigation relating to the cementitious activity of bauxite residue-Red mud," *Cement and Concrete Research*, vol. 41, no. 8, pp. 847-853, 2011.
- [19] R.-X. Liu and C.-S. Poon, "Utilization of red mud derived from bauxite in self-compacting concrete," *Journal of Cleaner Production*, vol. 112, pp. 384-391, 2016.
- [20] B. Wu, Z. Tan, Y. Zhang, Z. Zhao, C. Liu, and Q. Wang, "Experiment research on the bond-slip behavior of red mud concrete filled square steel tubes," *Journal of Henan Polytechnic University (Natural Science)*, vol. 38, no. 4, pp. 148-153, 2019.
- [21] G. Giakoumelis and D. Lam, "Axial capacity of circular concrete-filled tube columns," *Journal of Constructional Steel research*, vol. 60, pp. 1049-1068, 2004.
- [22] D. Lam and C. Roach, "Axial capacity of concrete filled stainless steel circular columns," *Welding in the World*, vol. 50, pp. 448-454, 2007.
- [23] M. D. O'Shea and R. Q. Bridge, "Design of circular thin-walled concrete filled steel tubes," *Journal of Structural Engineering*, vol. 126, no. 11, pp. 1295-1303, 2000.

- [24] M. Mimoune, F. Z. Mimoune, and M. Ait Youcef, "Axial capacity of circular concrete-filled steel tube columns," *World Journal of Engineering*, vol. 8, no. 3, pp. 237–244, 2011.
- [25] J. Wei, X. Luo, Z. Lai, and A. H. Varma, "Experimental behavior and design of high-strength circular concrete-filled steel tube short columns," *Journal of Structural Engineering*, vol. 146, no. 1, pp. 1–16, Article ID 04019184, 2020.
- [26] N. J. Gardner and R. Jacobson, "Structural behavior of concrete filled steel tubes," *ACI Journal*, vol. 64, no. 7, pp. 404–413, 1967.
- [27] G. Giakoumelis and D. Lam, "Axial capacity of circular concrete-filled tube columns," *Journal of Constructional Steel Research*, vol. 60, no. 7, pp. 1049–1068, 2004.
- [28] Q. Yu, Z. Tao, and Y.-X. Wu, "Experimental behaviour of high performance concrete-filled steel tubular columns," *Thin Walled Structures*, vol. 46, no. 4, pp. 362–370, 2008.
- [29] T. Ekmekyapar and B. J. M. Al-Eliwi, "Experimental behaviour of circular concrete filled steel tube columns and design specifications," *Thin Walled Structures*, vol. 105, no. 8, pp. 220–330, 2016.

Research Article

Characterization Methods for the Effect of Microbial Mineralization on the Microstructure of Hardened C₃S Paste

Yanqiang Chen ^{1,2,3,4}, Chunxiang Qian ^{1,2,3,4} and Hengyi Zhou^{1,2,3,4}

¹School of Materials Science and Engineering, Southeast University, Nanjing 211189, China

²Research Center of Green Building & Construction Materials, Southeast University, Nanjing 211189, China

³Key Laboratory of Materials Microbiology, Southeast University, Nanjing 211189, China

⁴Jiangsu Key Laboratory of Construction Materials, Southeast University, Nanjing 211189, China

Correspondence should be addressed to Yanqiang Chen; 230169462@seu.edu.cn and Chunxiang Qian; cxqian@seu.edu.cn

Received 3 May 2020; Accepted 14 July 2020; Published 18 August 2020

Guest Editor: Sreekanta Das

Copyright © 2020 Yanqiang Chen et al. This is an open access article distributed under the Creative Commons Attribution License, which permits unrestricted use, distribution, and reproduction in any medium, provided the original work is properly cited.

Microbial mineralization has a significant effect on the hydration process of cement-based materials. This paper mainly studied the characterization methods for hydration degree and hydration product of C₃S in hardened paste under microbial mineralization. Quantitative X-ray diffraction (QXRD), thermogravimetric analysis (TG), Fourier transform infrared spectroscopy (FT-IR), and electron backscatter diffraction (EBSD) were used and compared. The results showed that microbial mineralization increased the hydration degree of T-C₃S. QXRD and EBSD could be used to characterize the content of C₃S, and there were few differences between the two methods. TG could accurately characterize the content of Ca(OH)₂ and CaCO₃ at different depths of the sample, and FT-IR could qualitatively characterize the presence of Ca(OH)₂ and CaCO₃.

1. Introduction

In recent years, microbial mineralization in cement-based materials has become a research focus. Microbial-induced calcium carbonate precipitation (MICCP) [1, 2] is a typical biomineralization process which could be used to heal cracks in concrete and enhance the durability of cement-based materials [3]. In addition, new microbial cement-based materials have also been developed [4]. However, the effect of microbial mineralization on cement-based materials was caused by the effect on hydration process. Therefore, it was necessary to study the hydration and its characterization methods.

Many traditional methods for characterizing the hydration process of cement-based materials, such as heat evolution method, quantitative XRD (QXRD), differential thermal analysis (TGA), BSE, and so on, were used frequently. However, each method had its limitations.

Peiming et al. [5] compared the advantages and disadvantages of hydration heat method, chemically combined

water method, Ca(OH)₂ quantitative test method, and BSE method; the results showed that the BSE method had a better promising application for the characterization of hydration degree. Kocaba et al. [6] studied the degree of hydration of cement-based materials mixed with blast furnace slag and showed that it was poor to characterize the degree of hydration by the dissolution method and TGA method, while the results of image analysis and isothermal calorimetry were highly consistent. Alexander [7] compared the XRD and BSE methods to characterize the phase composition of the hardened paste, and the results showed that the two characterization methods were also highly consistent.

Microbial mineralization consumes Ca(OH)₂ in the hardened paste; therefore, the mineralization of microorganisms was closely related to the hydration process of the paste. Basaran Bundur [8] studied the effect of *S. pasteurii* bacteria on the hydration process of cement-based materials by hydration heat method and showed that there was a great effect of *S. pasteurii* bacteria on the hydration heat of mortar. Lee [9] also used hydration heat method and XRD method to

characterize the effect of bacteria on the hydration of cement-based materials. The results showed that the former method could clearly characterize the early-phase change of the hydration process caused by bacteria, and the latter could characterize the composition change of the phase during the whole hydration process. But for the intermediate products, the limitations were obvious.

Microbial mineralization could affect the hydration process and microstructure of cement-based materials by promoting the transformation of $\text{Ca}(\text{OH})_2$ to CaCO_3 . However, the characterization methods of cement hydration under mineralization lacked systematic research. Therefore, in order to systematically characterize the effects of mineralization on cement hydration, this paper mainly discussed the changes in the degree of hydration and products of hardened C_3S paste caused by mineralization through different characterization methods and compared the advantages and disadvantages of different characterization methods. The combination of different characterization methods could more accurately characterize the mineralization and hydration processes. In addition, the results of the study will provide a better understanding of mineralization and guide engineering practice.

2. Materials and Experimental Design

2.1. Raw Materials

2.1.1. Tricalcium Silicate. Before the test of C_3S sample, the C_3S powder was grinded to below 200 mesh in a dry environment for testing. The XRD pattern of C_3S which was collected using a D8-Discover diffractometer (Brook, Germany) is shown in Figure 1. The phases of the samples were mainly C_3S and CaO . By comparing C_3S crystal standard cards, it was concluded that the crystal form was T- C_3S . Fitting was calculated by TOPAS software [10]; the purity of C_3S was about 99.05%. The C_3S particle size distribution is shown in Figure 2. The particle size of the sample ranged between 3.62 and 70.4 μm , and the average particle size was 13.68 μm . Before the XRF test, the C_3S powder and boric acid were added to the pressure equipment and compressed into a tablet, and the element of C_3S by XRF (ARL Perform X 4200, Thermo Fisher) is shown in Table 1. In addition to CaO and SiO_2 , it also contained a small amount of MgO , Al_2O_3 , etc., and the ratio of CaO to SiO_2 was 3.04. The specific surface area was 388.29 m^2/kg .

2.1.2. Microbial Culture. *Paenibacillus* was selected and used in the study. Before experiment, *Bacillus* were domesticated for half a year in an alkaline environment. Medium for culture of the microorganisms is shown in Table 2, and the pH of the medium was adjusted by $\text{Ca}(\text{OH})_2$. After the medium was autoclaved at 121°C for 25 min, the bacteria were inoculated into it, and then the inoculated medium was placed in a shaking incubator with an oscillation frequency of 170 r/min and cultured at 30°C for 24 hours. The bacterial growth curve is shown in Figure 3, and the pH of the medium was 12. After 24 hours of culture, the number of

bacteria measured by flow cytometry (ACEA D2040R, China) was 2.0×10^8 cells/mL.

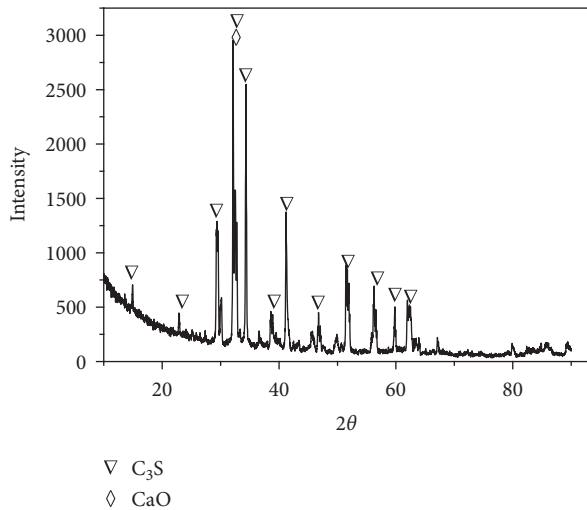
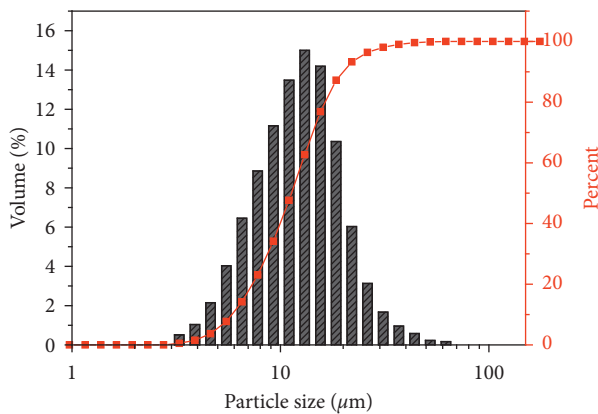
2.2. Biomineralization Experiment Design. In order to characterize the effects of biomineralization on the hydration degree and products of cement-based materials, a set of comparative experiments of mineralization and carbonization was designed. The microbes in the form of a suspension were mixed with C_3S powder. The number of microbes added was calculated based on the volume of the suspension. The amount of microorganism suspension added was equal to mixing water. The water-cement ratio was 0.45, the curing temperature was $20 \pm 0.5^\circ\text{C}$, relative humidity was $65 \pm 5\%$, the CO_2 concentration was 0.012 mol/L, and the curing time was 7 d. The schematic diagram of the test process is shown in Figure 4.

2.3. Characterization Methods

2.3.1. Characterization of Crystal Form and Phase Content by QXRD. QXRD was used to quantitatively analyze the crystal form and phase content of cement components. In the XRD quantitative analysis process, in order to reduce the data error, obtaining a higher-quality XRD map was necessary. During fitting the map, the number of the phases selected was gradually increased, so that the error was reduced. In addition, the preferred orientation of the phase was adjusted until the fitting map was similar to the one tested. The QXRD pattern was collected using a D8-Discover diffractometer (Brook, Germany) with a target source of $\text{Cu K}\alpha$, voltage and current of 40 kV and 30 mA, scan range of 10° – 90° , and step size of 0.002°, 0.35 seconds per step. Quantitative analysis was performed by Bruker's Topas Version 4.2 software [10], and a monoclinic structure of C_3S described by Nishi [11] was used. In the process of quantitative analysis, Rwp was used as an indicator of the degree of software fitting and was also the standard of accuracy of the results. In this study, the values of Rwp were between 8.11 and 11.04, which was less than 15. Therefore, the results of Topas 4.2 calculations were credible [10].

When preparing test samples, the C_3S hardened paste was measured and sized the upper layer of the test piece within 7 mm by using a caliper. The label was marked every 1 mm, and then the sample was polished with a file. Multiple measurements were taken to ensure the evenness of the hardened paste and the accuracy of the sampling depth. During samples preparation, all errors did not exceed 0.1 mm. The schematic diagram is shown in Figure 5. The powder sample obtained was further ground and then immersed in absolute ethanol solution for 3 days to arrest hydration and then dried in a vacuum oven at 60°C for 3 days. Before the test, α - Al_2O_3 with a mass fraction of 10% was added as an internal standard and uniformly mixed.

2.3.2. Quantitative Analysis of the Content of CaCO_3 and $\text{Ca}(\text{OH})_2$ at Different Depths. TG was used to determine the $\text{Ca}(\text{OH})_2$ and CaCO_3 content in the samples. The equipment used was Netzsch STA 449 F3. 5–10 mg of sample powder was placed in a Pt/Rh crucible and heated to 1000°C at 10 K/

FIGURE 1: XRD pattern of C₃S.FIGURE 2: Particle size of C₃S.TABLE 1: Chemical composition of C₃S samples by XRF analysis.

Oxide	CaO	SiO ₂	MgO	Al ₂ O ₃
Content (%)	75.07	24.60	0.15	0.07
Total (%)	99.89			

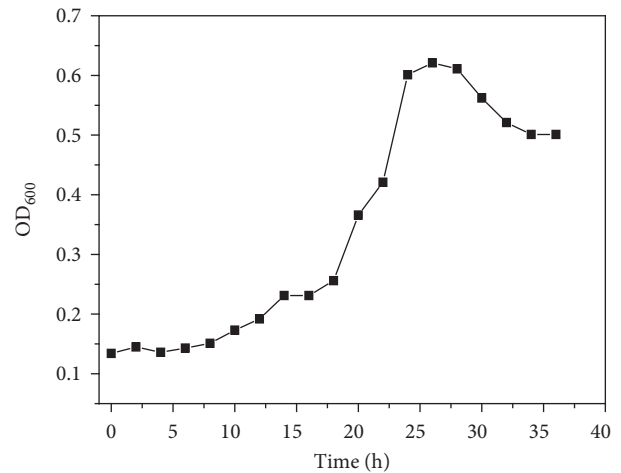
min in an N₂ atmosphere. The mass percentages of Ca(OH)₂ and CaCO₃ were calculated from the weight loss rate in the thermogravimetric curve. The analysis methods of TG curve mainly included “tangent method” and DTG. Younsi [12] pointed out that the Ca(OH)₂ content measured by the “tangent method” was about 20% lower than the actual value, so the analysis method used in this study was DTG.

The sample preparation for TG test was similar to that for XRD test, besides that no α-Al₂O₃ was added in TG.

2.3.3. EBSD-EDS Characterizing Phase Content. For EBSD imaging, the reaction of C₃S with water during hydration made the average number of atoms much lower than that of the unhydrated C₃S particles, so a strong difference of grayscale was obtained between unreacted (anhydrous) and reaction products (hydrates). Based on the entropy

TABLE 2: *Paenibacillus* medium.

Nutrients	Liquid medium (g/L)
Sucrose	10.0
Na ₂ HPO ₄ ·12H ₂ O	2.50
MgSO ₄	0.50
CaCO ₃	1.00
KCl	0.15
(NH ₄) ₂ SO ₄	0.50
Yeast extract	0.30

FIGURE 3: The growth curve of *Paenibacillus* (pH = 12).

maximization of the GLH curve, image processing was performed by image processing software (Image-Pro Plus 6.0) to extract the area fraction of the gray value. Regarding the processing of the image: first, the threshold of the entropy maximization of the GLH curve was obtained from plurality of images, and then a binary grayscale range image was obtained corresponding to the C₃S hardened paste. In addition, the microscope was operated at an acceleration voltage of 15 kV. Images of each sample were collected at magnifications of 250× (20 fields), 500× (30 fields), and 1000× (50 fields).

Before the test, the samples were impregnated with epoxy resin and polished, and then the equipment was sprayed with carbon 360 nm using the equipment LEICA ACE600 and then photographed by using a backscattered scanning electron microscope.

2.3.4. FT-IR Qualitative Characterizing Phase. FT-IR was frequently used to characterize functional groups in samples. The principle was that when the sample was irradiated with infrared light with a continuously changing frequency, the molecules absorbed radiation at certain frequencies, so that the intensity of the transmitted light in the absorption region was weakened. The infrared spectrum was obtained by recording the relationship between the percentage transmittance of infrared light and the wave number or wavelength. The device model used during the test was Nicolet iS10, with a spectral range of 500 cm⁻¹–4000 cm⁻¹ and the resolution better than 0.4 cm⁻¹. This method was mainly used for the characterization of Ca(OH)₂ and CaCO₃.

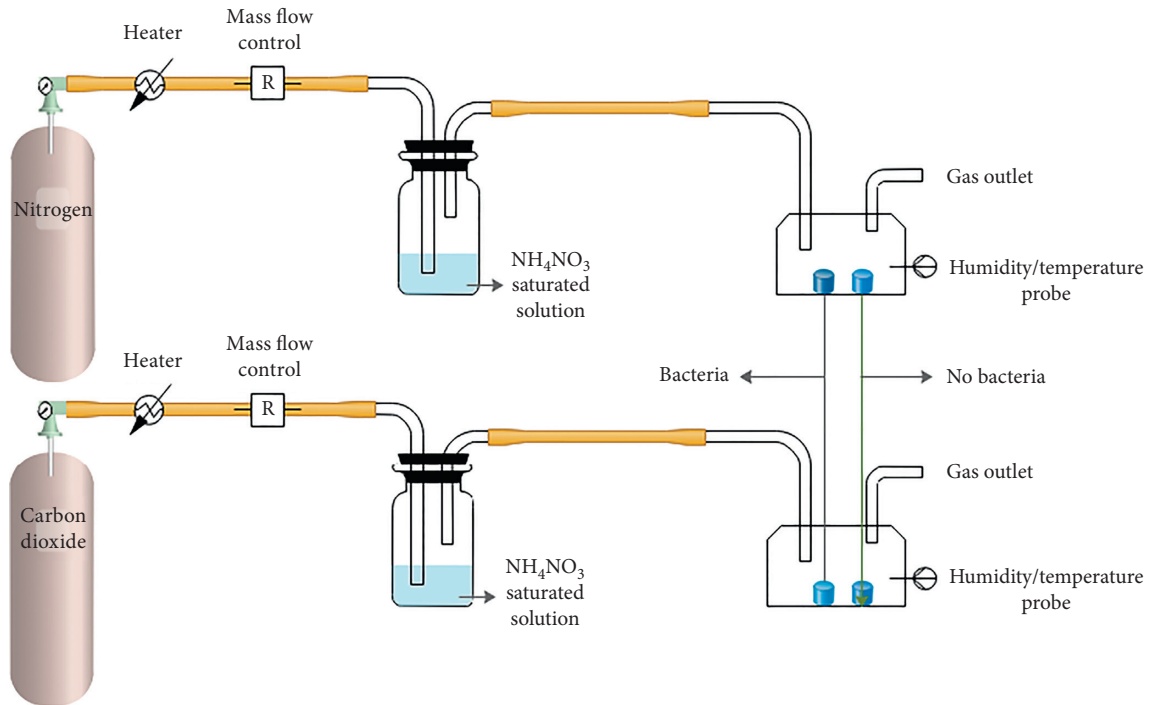


FIGURE 4: Schematic diagram of mineralization/carbonization setup.

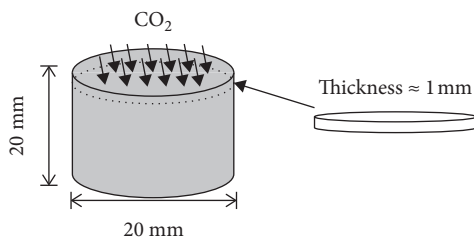


FIGURE 5: Schematic diagram of sample processing.

3. Results and Discussion

3.1. Characterization of Crystal Form and Phase Content by QXRD. XRD test was performed on mineralized and carbonized samples at different depths. The results within about 1 mm of the surface layer are shown in Figure 6. Among them, B was the mineralization group and C was the carbonization group (the same applies hereinafter). From the figure, there was a significant difference in the peak intensity near 29.4° , and by comparing the crystal forms, it was analyzed as calcite, indicating that the crystallinity of CaCO_3 within 1 mm of the surface layer of the mineralized group was better than that of the carbonized group. In addition, it could be seen from the figure that there was no peak at 18.4° within 0-1 mm of the surface layer, indicating that the Ca(OH)_2 was completely mineralized or carbonized in the previous period.

Through Topas software, quantitative analysis of XRD patterns of T- C_3S hardened paste at different depths is shown in Figure 7. As shown in Figure 7, the residual amount of C_3S in the mineralization group samples was lower than that of the carbonization group at different

depths, indicating that the addition of microorganisms promoted the hydration of C_3S . It was known from the literature that the decrease in C_3S content in mineralized samples might be related to bacteria as nucleation sites and then promote hydration. The above tests showed that QXRD could be used to characterize the degree of hydration of cement-based materials and perform phase analysis.

3.2. Quantitative Analysis of the Content of CaCO_3 and Ca(OH)_2 . TG test was performed at different depths within surface layer of the mineralization group and the carbonization group, and the curve is shown in Figure 8. By analyzing and calculating the TG curve in Figure 8, the content of Ca(OH)_2 and CaCO_3 at different depths was obtained, as shown in Figure 9. It could be seen that CaCO_3 in the mineralized group was higher than that in the carbonized group, which indicated that the mineralization promoted the formation of CaCO_3 . From the curve of Ca(OH)_2 in Figure 9, it was concluded that within 4 mm of the surface layer, the content of Ca(OH)_2 was lower than the carbonization group. This was due to Ca(OH)_2 mineralized to CaCO_3 . In 4-7 mm, the content of Ca(OH)_2 in the mineralized group was higher than that in the carbonized group, that is, the mineralization promoted the hydration of C_3S , and more Ca(OH)_2 was produced, which was consistent with the results of QXRD. In addition, from Figure 8, the weight loss of the mineralized group and the carbonized group at 1000°C was slightly different within the range of 0-2 mm, the weight loss of the mineralized group was slightly higher than that of the carbonized group. The reason was that mineralization promoted the reaction between CO_2 and Ca(OH)_2 , so the weight loss rate of the mineralized group was high.

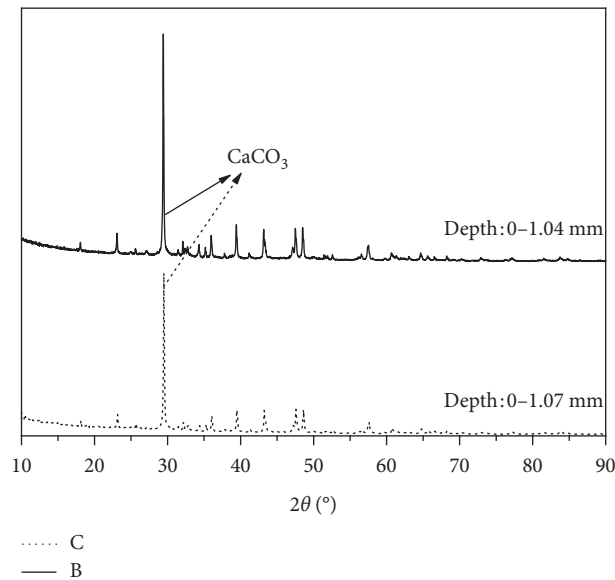


FIGURE 6: Comparison of CaCO_3 peak intensity within about 1 mm of the surface layer.

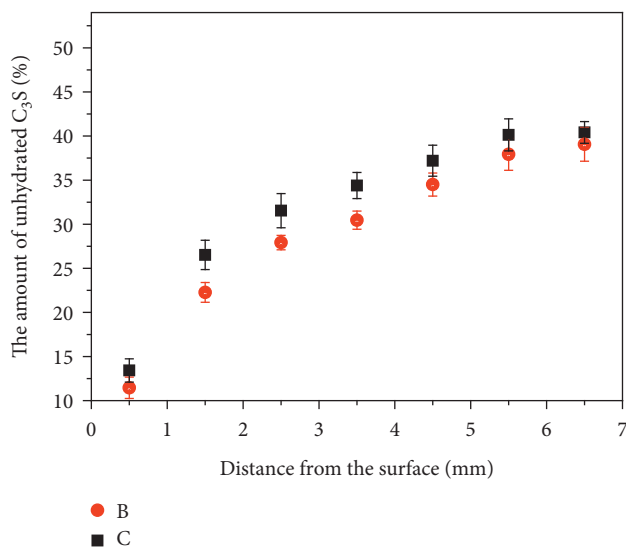


FIGURE 7: Remaining amount of C_3S at different depths in the surface layer.

3.3. EBSD-EDS Characterization of the Content of the Phases.

By cutting the samples longitudinally and then performing BSE shooting at different magnifications, as shown in Figure 10. The magnification used in this test was $\times 250$ for statistics and $\times 1000$ for analysis.

At a magnification of $\times 250$, more than three photos were taken. The software Image-Pro Plus 6.0 was used to analyze the grayscale of photos. Figure 11 shows the grayscale distribution of BSE images under this test conditions. Combining the energy spectrum and the literature, it could be seen that the first peak corresponds to the pore, the second peak corresponds to the phase C-S-H, the third peak corresponds to the phase of $\text{Ca}(\text{OH})_2$ and CaCO_3 , and the fourth peak corresponds to the unhydrated particles. The threshold was further determined according to Figure 12.

From Figure 12, it was concluded that the Ca/Si in region I was about 3, which was unhydrated C_3S ; in region II, the Si content was close to 0, which was $\text{Ca}(\text{OH})_2$ and CaCO_3 . From Figure (c), it could be concluded that the grayscale values at I, II, and III were greatly different when passing through different grayscale areas at the line scanning, and the grayscale values changed greatly at the connection points. Combining the gray distribution of the whole picture, area I was unhydrated C_3S , area II was $\text{Ca}(\text{OH})_2$ and CaCO_3 , and area III was C-S-H and some pores.

Combining the above methods, rendering was performed at different gray values, as shown in Figure 13.

Combined with the literature, it was calculated that the C_3S content of the surface layer of the mineralization group within the range of 0-1 mm was $11.30 \pm 1.64\%$, and the content of $\text{Ca}(\text{OH})_2$ and CaCO_3 was $67.34 \pm 1.49\%$. The porosity was $21.36 \pm 2.19\%$; the C_3S content in the 0-1 mm surface layer of the carbonization group was $14.1 \pm 1.24\%$, and the content of $\text{Ca}(\text{OH})_2$ and CaCO_3 was $60.17 \pm 1.19\%$. The porosity was $25.73 \pm 1.98\%$. The above data showed that microbial mineralization promoted the hydration of T- C_3S , which was consistent with the QXRD test results. In addition, the mineralization of microorganisms reduced the porosity of the surface layer.

3.4. FT-IR. In the T- C_3S hardened paste of the mineralization group and the carbonization group, a small amount of samples was taken at different depths for FT-IR testing. The results are shown in Figure 14.

In Figure 14, the vibrational peak at a wavelength of 3443 cm^{-1} represents $-\text{OH}$, and the vibrational peak at a wavelength of 713 cm^{-1} , 874 cm^{-1} , and 1797 cm^{-1} represents CO_3^{2-} . It could be seen that within 0-3 mm, the peak value of the sample in the mineralization group at 874 cm^{-1} was more obvious than that of the carbonization group. It reflects

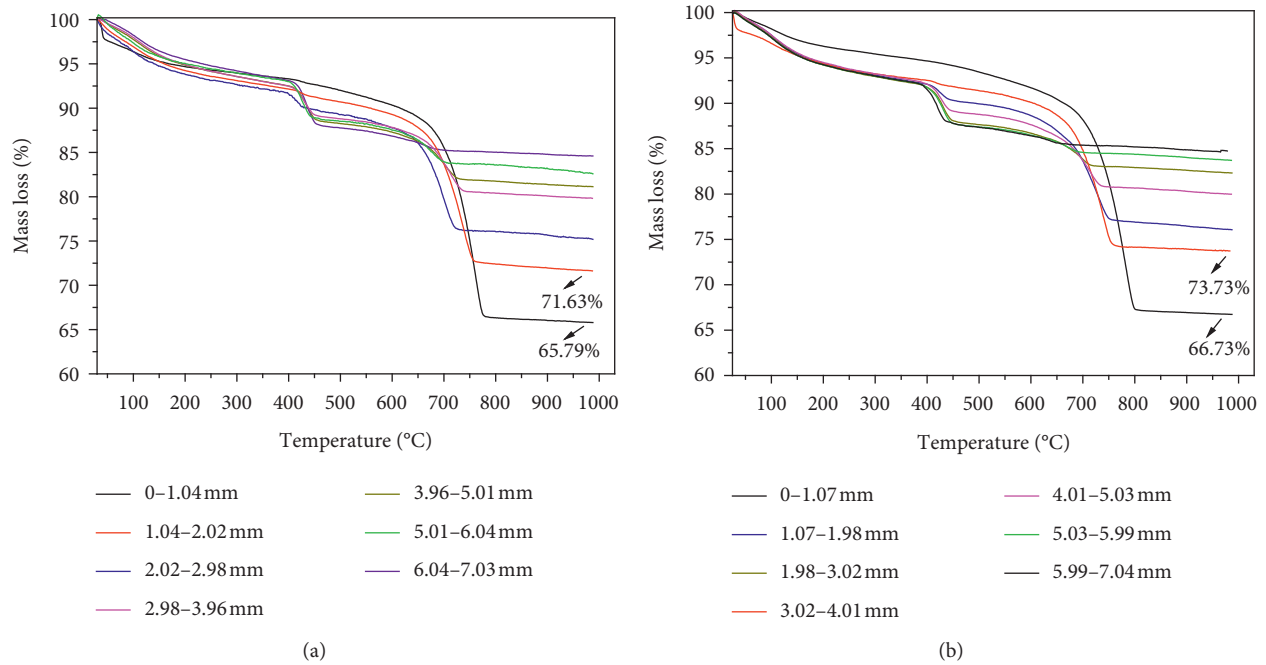


FIGURE 8: Mass loss curves at different depths of samples in the mineralization group (a) and the carbonization group (b).

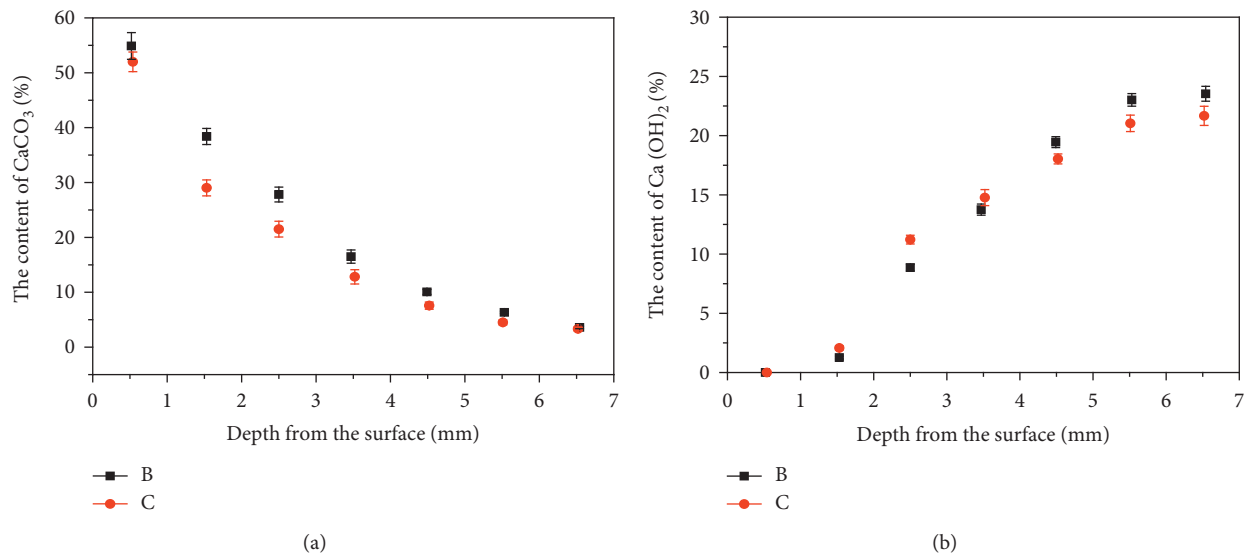


FIGURE 9: Content of CaCO₃ (a) and Ca(OH)₂ (b) at different depths of samples.

that the addition of microorganisms promoted the formation of CaCO₃ to some extent.

3.5. Comparisons. By combining the four characterization methods of QXRD, TG, EBSD, and FT-IR, the morphology, phase content, porosity, and main functional groups of cement-based materials with microbial mineralization could be obtained. QXRD, TG, and EBSD could quantitatively characterize the phases, while the results of FT-IR were qualitative. Because of the good fitting effect of QXRD results on crystal, it could be used to

quantify the content of C₃S. However, the fitting results of Ca(OH)₂ were lower which actually were due to its amorphous phase. TG could accurately determine the contents of Ca(OH)₂ and CaCO₃ according to the loss of combustion.

Different phases could be distinguished according to the gray value by EBSD. The quantitative results of C₃S content in the mineralized surface obtained by comparing EBSD and QXRD are shown in Table 3. It could be seen that for the C₃S content within 0-1 mm of the surface layer of the mineralization group and the carbonization group, the results obtained by the two characterization methods were relatively

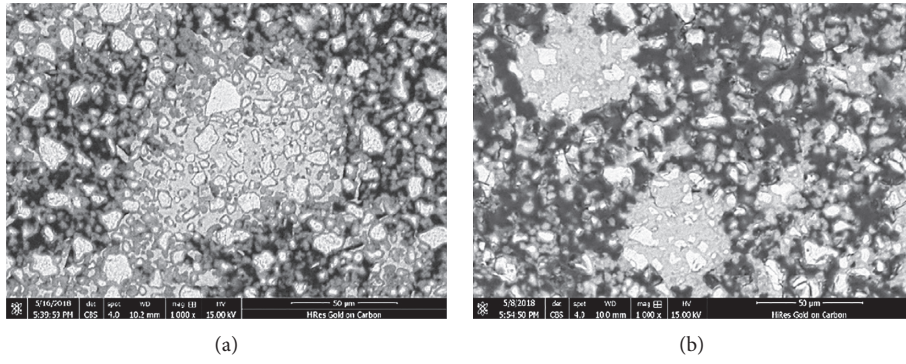


FIGURE 10: BSE image of the surface layer of the mineralization group (a) and carbonization group (b) ($0 \sim 1 \pm 0.3$ mm).

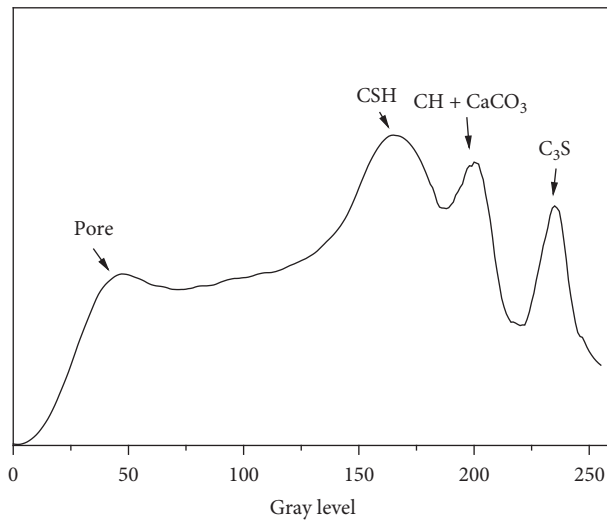


FIGURE 11: Gray distribution of BSE images of the BSE images.

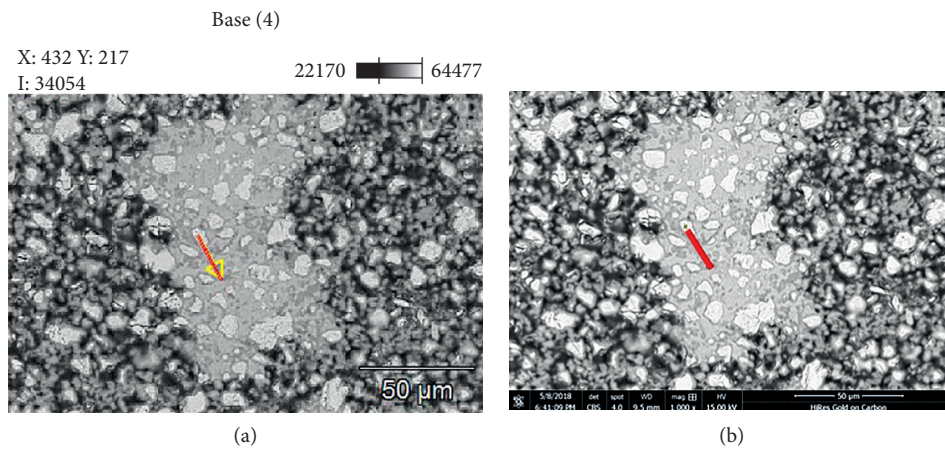
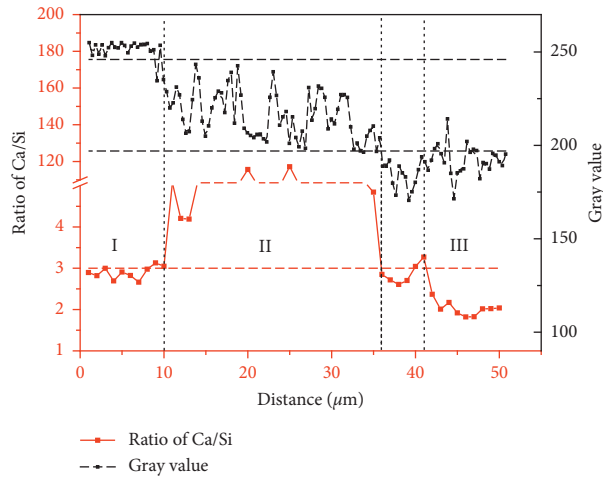
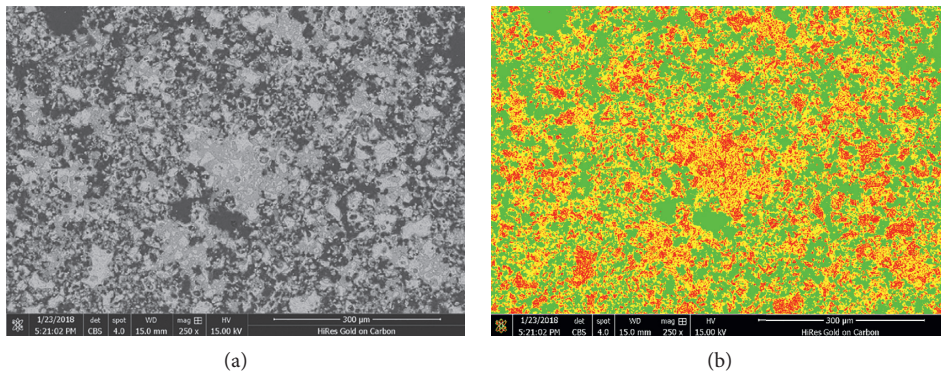


FIGURE 12: Continued.



(c)

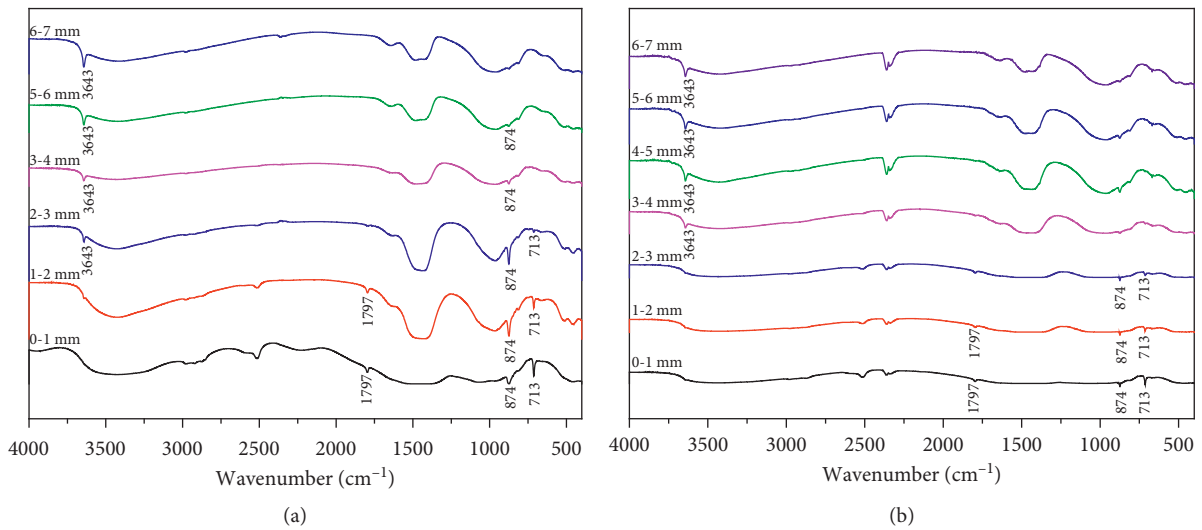
FIGURE 12: Corresponding map of BSE gray distribution and EDS. (a) The original line scan. (b) Postproduction, in order to facilitate observation and analysis. (c) The map of Ca/Si and gray value.



(a)

(b)

FIGURE 13: Color rendering of the EBSD picture based on the gray value.



(a)

(b)

FIGURE 14: Infrared curves of samples in the mineralization group (a) and carbonization group (b).

TABLE 3: Comparison of quantitative results of C_3S content between EBSD and QXRD.

	Remaining amount of C_3S -B (%)	Remaining amount of C_3S -C (%)
QXRD	11.46 ± 1.21	13.42 ± 1.32
EBSD	11.30 ± 1.64	14.10 ± 1.24

consistent, indicating that the data obtained by both characterization methods were reliable.

4. Conclusions

QXRD, TG/DSC, BSE, and FT-IR were used to study the effect of microbial mineralization on the hydration process of C_3S and microstructure of hardened C_3S pastes. The results showed that microbial mineralization promoted the hydration of T- C_3S . QXRD and EBSD/ESD could accurately characterize the content of C_3S , and the differences between the two characterization methods were minute. The content of $Ca(OH)_2$ and $CaCO_3$ at different depths of the sample could be exhaustively analyzed by TG/DSC, and FT-IR could qualitatively characterize the content of $CaCO_3$.

Data Availability

Some or all data, models, or codes that support the findings of this study are available from the corresponding author upon reasonable request.

Conflicts of Interest

The authors declare that they have no conflicts of interest regarding the publication of this paper.

Acknowledgments

The authors appreciate the financial support from the National Natural Science Foundation of China (Grant no.51738003) and the International Cooperation Project supported by Southeast University-Sika Technology AG (8512000478).

References

- [1] M. Li, C. Fang, S. Kawasaki et al., "Bio-consolidation of cracks in masonry cement mortars by *Acinetobacter* sp. SC4 isolated from a karst cave," *International Biodeterioration & Biodegradation*, vol. 141, pp. 94–100, 2019.
- [2] J. Zhang, D. Kumari, and V. Achal, "Combining the microbial calcite precipitation process with biochar in order to improve nickel remediation," *Applied Geochemistry*, vol. 103, pp. 68–71, 2019.
- [3] D. Kumari, A. Mukherjee, V. Achal, and Q. Zhang, "Bio-mineralization for sustainable construction - a review of processes and applications," *Earth Science Reviews*, vol. 148, pp. 1–17, 2015.
- [4] H. Rong, *Preparation and Binding Mechanism of Microbe Cement*, pp. 44–91, Southeast University, Nanjing, China, 2014.
- [5] W. Peiming, F. Shuxia, and L. Xianping, "Research methods and progress of cement hydration," *Journal of Building Materials*, vol. 8, no. 6, pp. 646–652, 2005.
- [6] V. Kocaba, E. Gallucci, and K. L. Scrivener, "Methods for determination of degree of reaction of slag in blended cement pastes," *Cement and Concrete Research*, vol. 42, no. 3, pp. 511–525, 2012.
- [7] A. V. Soin, L. J. J. Catalan, and S. D. Kinrade, "A combined QXRD/TG method to quantify the phase composition of hydrated Portland cements," *Cement and Concrete Research*, vol. 48, pp. 17–24, 2013.
- [8] Z. Basaran Bundur, M. J. Kirisits, and R. D. Ferron, "Bio-mineralized cement-based materials: impact of inoculating vegetative bacterial cells on hydration and strength," *Cement and Concrete Research*, vol. 67, pp. 237–245, 2015.
- [9] J. C. Lee, C. J. Lee, W. Y. Chun, W. J. Kim, and C.-W. Chung, "Effect of microorganism *sporosarcina pasteurii* on the hydration of cement paste," *Journal of Microbiology and Biotechnology*, vol. 25, no. 8, pp. 1328–1338, 2015.
- [10] A. X. S. Bruker, *TOPAS V4: General Profile and Structure Analysis Software for Powder Diffraction data: User's Manual*, Bruker AXS, Karlsruhe, Germany, 2008.
- [11] F. Nish, Y. Takeuchi, and I. Maki, "Tricalcium silicate Ca_3O [SiO_4]: the monoclinic superstructure," *Zeitschrift für Kristallographie*, vol. 172, pp. 297–314, 1985.
- [12] A. Younsi, S. Staquet, and A. A. T-Mokhtar, "Accelerated carbonation of concrete with high content of mineral additions: effect of interactions between hydration and drying," *Cement and Concrete Research*, vol. 43, pp. 25–33, 2013.

Research Article

Prototype Steam Turbine for Solar Power Production

Kawira Millien 

Department of Physical Sciences, University of Embu, P.O. Box 6–60100, Embu, Kenya

Correspondence should be addressed to Kawira Millien; kawira.millien@gmail.com

Received 13 April 2020; Revised 23 June 2020; Accepted 25 June 2020; Published 20 July 2020

Academic Editor: Stefano Sorace

Copyright © 2020 Kawira Millien. This is an open access article distributed under the Creative Commons Attribution License, which permits unrestricted use, distribution, and reproduction in any medium, provided the original work is properly cited.

Fabrication of a prototype direct drive steam turbine using locally available materials provides a means to supply power and process heat for off-grid areas, which are not accessible due to rugged terrain. The use of solar power technologies to provide clean power and heat will mitigate environmental pollution and global warming that are caused by combustion of fossil fuels and other carbon-based power sources. The energy density of fossil fuels is higher than that of nonconcentrated solar power, which makes them a better option compared to nonconcentrated solar power sources. The high cost of steam thermal turbines and the limited technical skills on utilization of local materials for steam turbine construction have hampered the realization of potential of producing both small- and large-scale power in Africa. The design of the single-stage blade wheel system solar thermal turbine was done using AutoCAD 2010. The blades were made from encapsulated rice husk particle boards, and the steam casing was made from 0.0015 galvanized black iron sheet. Compensation for more stages was done by sending the fluid exiting from the turbine into the solar collector for reheating. It was coupled to a single-phase generator and gearbox. The rotor was made of galvanized iron tube. The turbine's average efficiency was obtained as 61.6% and average isentropic efficiency was 55.3%. The combined gearbox and generator approximate efficiency was 54.7%. Locally available heat transfer fluids were used for solar thermal collection. The prototype turbine was designed to produce 500 W of power. It had a heat rate ratio of 0.08. The turbine inlet conditions were as follows: average temperature of 112.8°C, average pressure of $2.7 \times 10^5 \text{ Nm}^{-2}$, average enthalpy of 3156 kJ/kg, and average steam flow rate of 243.3 kg/hr. Outlet conditions were as follows: outlet average temperature of 97.3°C, average steam flow rate of 102.0 kg/hr, average pressure of $1.20 \times 10^5 \text{ Nm}^{-2}$, and enthalpy of 2103 kJ/kg. With use of 6 M sodium chloride solution, the turbine inlet conditions were as follows: enthalpy of 3789.1 kJ/kg at a pressure of $3.0 \times 10^5 \text{ Nm}^{-2}$ and its enthalpy at exit was 2346.3 kJ/kg at a pressure of $1.05 \times 10^5 \text{ m}^{-2}$ which can provide process heat and power for off-grid areas.

1. Introduction

Adverse climatic change and environmental pollution are among the key issues of international interest due to the products of combustion from fossil energy resources and biomass-based materials, which cause global warming and pollution. Renewable energy technologies hold the solutions in mitigation of environmental pollution and climatic change, since they are of great significance in alleviating the pollution and climate change crisis.

Due to concerted industrialization endeavors, especially by developing countries, the demand for power in the world, in fact, is overwhelming. The energy demand, which has been increasing continuously throughout the years, is making development of renewable power technologies to be

a necessity rather than an option, which indeed has been pushing towards depletion of the fossil fuels. Presently, renewable energy accounts for 18.2% of global energy consumption while the remaining 79.5% is obtained from oil, gas, and coal and 2.2% being produced from nuclear energy [1]. Specifically, in comparison with typical SEGS, solar plants that employ PTCs are well recognized and the technology is promising [2]. The greenhouse gases such as carbon (IV) oxide and carbon (II) oxide produced during combustion of the said materials increase the global temperature, making development of concentrated solar power and the paradigm change from conventional carbon-based fuels to renewable energy sources a stringent necessity. In addition to combustion, Jackson et al. [3] found that fossil fuel burning together with cement manufacturing release

about 90% of all carbon (IV) oxide emissions from human activities. Decarbonization via solar energy was predicted as the only major way to deal with the environmental and economic challenges caused by climate change [4]. The energy demand increases with increasing world population, and nowadays, the renewable energy technologies can provide process heat besides providing power. The enhanced demand for clean power and decarbonization has further exacerbated the energy security problem [5]. The economic, environmental, and safety factors are considered in deciding the type of energy source for utilization to produce power and process heat, considering the diverse needs of policy direction, which depends on whether a country has prioritized manufacturing industries and products processing or not. According to Kalogirou [6], among alternative energy sources, solar energy investment needs to be prioritized even though the initial cost of installation is higher. In terms of economic viability, established that solar energy systems provide electricity that is much cheaper than conventional energy supplied from fossil fuels and biomass besides the solar energy not emitting pollutants which are produced by the latter. In ordinary circumstances, carbon-based energy sources such as coal are preferred and more appealing, compared to nonconcentrated solar sources due to their higher energy densities, making them to be used more often for power production using boilers. However, research on renewable energy reveals that solar power is the most favorable resource [7] where an analytic hierarchy process model was studied. Besides, recent research has established that power production by use of screw expander technology can produce good efficiency at low to medium heat source temperatures [2]. In this study, 12.6% and 17.8% of maximum solar thermal power efficiency and exergetic efficiencies, respectively, were obtained. The screw expander technology consists of a rotary type positive displacement device which is characterized by absence of high-velocity working fluids, yet it is efficient enough to meet power demand. Back pressure steam turbines can be used for producing process heat in addition to power generation. Mechanical energy from steam was used for moving a rotor which was coupled to stator in a magnetic field. Use of the back pressure steam turbines has an advantage of being upgradable to cogenerate power and process heat in industries with high process heat demand such as tea processing industries while on the other hand, they can produce power for extraction of minerals such as copper. In an effort to produce cost-effective energy, 900 MW steam turbine cycle for off-design operation, using flue gases, was used to produce steam that increased the efficiency of the power plant by a large margin [8]. Multiple stage steam turbines, which operate on the principle of Rankine cycle, ensures that the steam discharge releases most of the thermal power before exiting the turbine. A convectional, ideal Rankine cycle operates between pressure of 30 kPa and 6 MPa at inlet temperatures of about 550°C. During design of steam turbine, if the interblade phase angle is between -45° and $+90^\circ$, stall flutter was recorded to have a probability of occurrence [9]. The ratio of actual power generated by a turbine to the power which would be generated by an ideal turbine

corresponds to the thermodynamic efficiency. An increase in efficiency of a steam turbine by 1% for 500 MW capacity led to minimal carbon (IV) oxide gas emissions to the environment [10]. To generate industrial power, multistage steam turbines are used to meet the demand, since the steam expansion takes place at all the stages, resulting in large energy conversion. However, steam turbines are not as competitive as screw expanders when the net power demand is smaller than 2 MW and for low grade heat sources [11]. A study showed that steam turbines produce about 90% of all electrical power used in United States of America [12]. In a study of solar systems, the input to any solar system was established to comprise of exergy [13]. The solar power intensity, which varies with time of day, determines the power output from solar power conversion technology device, and nowadays, renewable energy sources are characterized by low temperatures and low heat values, which have attracted increasing interest owing to their high accessibility amounts for exploitation. Process heat has much demand in industries such as agricultural produce processing, where materials produced are processed. In India, 70% of energy in form of thermal energy is used for applications below 250°C. A study on determination of environmental pollution from sea vessels traffic, by assessment of production and scattering of exhaust emitted by ships, when in manoeuvring mode and when in switching mode from heavy sulphur residual fuel to low sulphur distillate fuel oil, in the interest of mitigating sea environment pollution, creates interest in reducing pollution in the sea [14]. In this study, the fraction of sulphur (IV) oxide gas pollutant emission due to port activities of Naples city is nearly 40% which is substantial. In this regard, renewable energy technologies become necessary for pollution and climate change mitigation.

2. Materials and Methods

2.1. Turbine Fabrication. The means of fabrication of turbine was carried out by use of design guidelines by Jawad [15]. In this study, a single casing unit was fabricated using 2 mm thick galvanized black sheets. The rotor was coupled to a generator and gear box. It was fabricated using 1.5 mm thick galvanized iron tube. The solar thermal collector and heat exchanger were designed, fabricated, and tested [16,17].

The following factors were used in blade design: blade material, centrifugal bending stress, and load and dynamic pressure. The blade strength and vibration characteristics were tested using the blade trip timing process [18]. The fabricated turbine was a direct drive turbine with a single-stage blade wheel system as shown in Figure 1. The turbine blades were synthesized from rice husks and cassava adhesive particle board which were encapsulated with 2 mm aluminium casing [19]. The particle boards were synthesized in a study on synthesis of particle boards without use of harmful formaldehyde chemical [20]. The blades produced from the particle board had the following dimensions: 0.015 m thickness, radius of 0.02 m, 0.8 kg weight, and 0.7 m length. The steam was expanded in a nozzle inside the

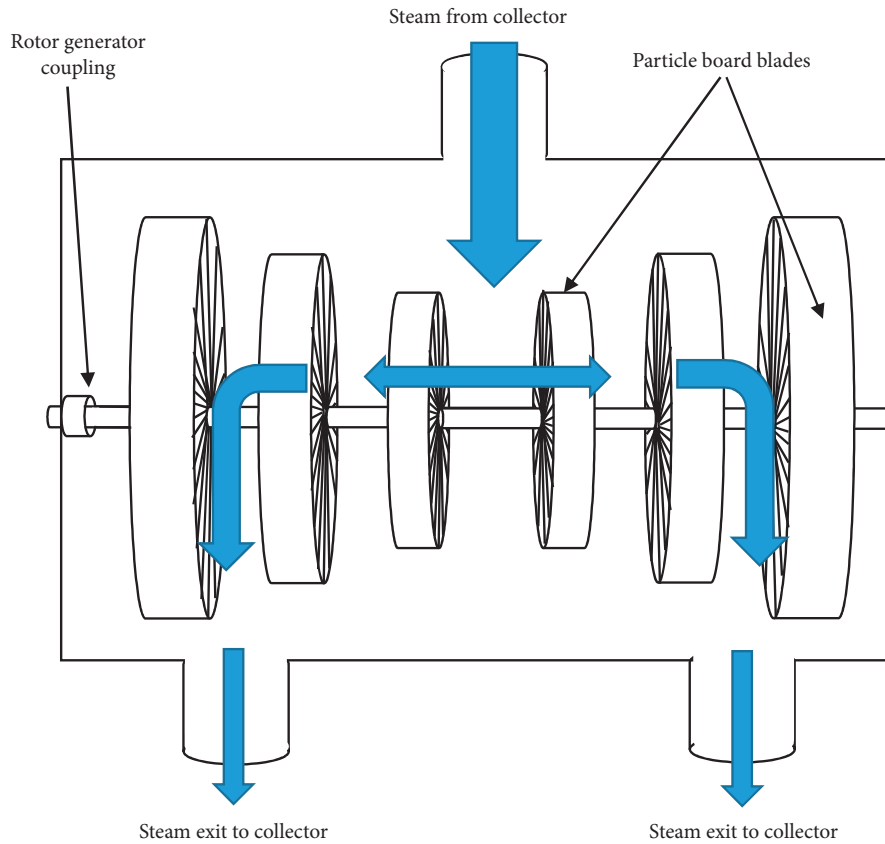


FIGURE 1: Single-stage blade system of the back pressure steam turbine.

turbine. Euler's turbine equation which is shown in equation (1) was used in the blade design [21].

$$V = h_{1+} + \frac{V_1^2}{2g} - h_2 - \frac{V_2^2}{2g} - \frac{U}{g} (W_{\theta 1} - W_{\theta 2}), \quad (1)$$

where h_1 and h_2 are the enthalpies of steam at entrance and exit, respectively, V_1 and V_2 are tangential absolute velocity components of fluid at inlet and exit, respectively, W is relative velocity, U is internal energy, and g denotes the state of the fluid. The design layout was made by using AutoCAD 2010. The turbine bearings were of diameter of up to 340 mm with L/D ratios of 0.4 to 0.21. Thrush bearings were used for shaft bearings. The turbine was designed to produce a rotor speed of 2800 rpm. It was machined to make provisions for contours and connection parts. Each end had a bearing, seal for gland, and a coupling area. Machining of axial grooves for the blades was made on the rotor. The steam turbine was connected to a single gear box coupled to a single-phase generator. In the study conducted by Zachos et al. [22], the finite element method was used for the structural design of the blade. Static analysis and thermal analysis were used during the blade design. The blades were fabricated individually and attached to the wheel disc. The moving blade tips were connected to a cover band which acted as a labyrinth that was fabricated, and it braced the moving blades to reduce the vibrations. The radial clearance was 0.3 m. The rotor was balanced both statically and dynamically after assembly of the blades. The rotor balancing was done at a low

speed of 500 rpm with weight adjustments made in two planes, one at each end of the rotor. Provision was made to vary screwed plugs in tapped holes. Four pedestals were fabricated from galvanized iron rods of 1 mm diameter and 0.3 m length. They supported the turbine via the bearings in a fixed axial relationship.

Each blade was balanced individually before assembly. In the static balancing, the weight was displaced parallel to rotor axis until the blade balanced. In this study, the mass axis did not coincide with the rotational axis during the dynamic balancing. The balance was achieved by cutting away or addition of material from the rotor. Drilling, milling, and addition of material were done by bolting and welding of the balance weights at various points to achieve balance. The rotor was tested at speeds ranging from 500 rpm to 3000 rpm.

The galvanized iron tube rotor was of good creep resistance and withstood high temperature and had high fracture toughness. The bores of bearings were elliptical to provide geometry for hydrodynamic lubrication. Circular bores were machined with shims in horizontal split. Only one shaft bearing was used on the shaft line. During operation, oil was poured manually into the bearing via lead-in ports at two diametrically opposite points on the horizontal center line.

The rotating component consisted of a solid single-piece integrally forged rotor with hydrodynamic tilting pad bearings and flexible element couplings. The rotor had an

overlay welding of the batter passes and the final overlay welds were done using the SAW process [23]. The nozzle end diameter was 0.001 m such that the flow of steam through the nozzle was an adiabatic expansion. A control valve was threaded to the nozzle to control steam flow into the turbine. The nozzles were fabricated such that the cross section varied from 0.008 m to 0.001 m, and they were put at an angle of 30° to the blade. The angle used compared well with US Patent number US 3452132 [24].

Instead of using stages, the fluid exiting from the turbine was fed back into the turbine after reheating through the solar heat collector. The rotor design depended on the flow path and the size of inlet which was 0.001 m. The half pieces were bolted together, and rubber seals were put in between the half cases to prevent leakage of steam from the steam chamber. The generator bearings had L/D ratios of 0.45 to 1.82.

The turbine efficiency η was tested using different heat transfer fluids and was determined using equation (3) [25].

2.2. Turbine Performance Characteristics. The following performance characteristics of the turbine were determined: turbine isentropic efficiency (using equation (4)), steam flow rate (kg/hr), inlet pressure (Nm^{-2}), outlet pressure (Nm^{-2}), inlet temperature ($^{\circ}\text{C}$), outlet temperature ($^{\circ}\text{C}$), and net heat rate (J/W). The generator/gear box used had an efficiency of 54.7%.

The proportion of flash steam, S_f , was determined by setting the charging pressure by use of pressure control valve, and the discharge pressure was measured using the pressure gauge. Equation (2) was used to calculate the proportion of flash steam (S_f) with use of steam tables [26].

$$S_f = \frac{(h_{f1}(P_1)) - (h_{f2}(P_2))}{h_{fg2}(P_2)}, \quad (2)$$

where h_{f1} is the specific enthalpy of saturated water at inlet, h_{f2} is the specific enthalpy of saturated water at outlet, and h_{fg2} is the latent heat of saturated steam at outlet at respective pressures and temperatures. Steam tables (superheated and saturated) were used in the determination of the proportion of flash steam. The heat coefficients of steam at various temperatures were obtained from steam tables [27].

The efficiency, η_{th} in equation 3, with respect to enthalpy of the heat transfer fluids, is each at a time and at different conditions of pressure and temperature, where H_{out} is the output enthalpy of the heat transfer fluid and H_{in} is the input enthalpy of the heat transfer fluid expressed as a percentage:

$$\eta_{\text{th}} = 1 - \frac{|H_{\text{out}}|}{|H_{\text{in}}|}, \quad (3)$$

where H_{in} and H_{out} are the enthalpy input and output, respectively.

The isentropic efficiency of the steam turbine was obtained using

$$\eta_T = \frac{H_1 - H_2}{H_1 - H_2^*}, \quad (4)$$

where H_1 is the enthalpy of high pressure inlet steam, H_2 is the actual enthalpy of exhaust low pressure steam, and H_2^* is the pressure of the exhaust low pressure steam assuming isentropic expansion. The magnitudes of enthalpy were obtained by use of saturated and superheated steam tables with respect to pressures and temperatures of operation.

Energy input \dot{E}_i was determined using equation (5) which is a product of mass flow rate of steam, \dot{m}_i , and the enthalpy at entry, \dot{h}_i , of the steam [28]:

$$\dot{E}_i = \dot{m}_i \times \dot{h}_i. \quad (5)$$

The energy output \dot{E}_o was determined by use of the product of mass flow rate of steam at exit, \dot{m}_o , and the enthalpy at exit, \dot{h}_o , as shown in the following equation [28]:

$$\dot{E}_o = \dot{m}_o \times \dot{h}_o. \quad (6)$$

The heat rate of the steam turbine was determined as a ratio of the net heat input and the turbine power as shown in the following equation:

$$\text{heat rate} = \frac{\text{heat input}}{\text{turbine power}}. \quad (7)$$

2.3. Heat Transfer Fluid Performance. The heat transfer fluids, namely, 6 M sodium chloride solution, 4 m sodium chloride solution, 2 M sodium chloride solution, unused engine oil, used engine oil, vegetable oil 2, and vegetable oil 1, were passed through a parabolic trough solar concentrator and then into heat exchanger with water as the secondary fluid [16,17]. The fabricated back pressure steam turbine was used for producing process steam and power. The steam from the collector via the heat exchanger was fed into the turbine input pipe where it expanded at the blades and exited at the outlet pipe. The temperature was measured using thermocouple sensors fixed at the inlet and the output of the steam turbine. Pressure was measured using steam pressure gauges with probes inside the inlet and outlet pipes of the steam turbine. The steam flow rate was measured using digital mass flow rate meters fixed at the inlet and outlet of the steam turbine. The enthalpy of the steam entering and leaving the steam turbine was determined using the superheated and saturated steam tables. The solar power intensity was measured using the solar power meter. The temperature of the heat transfer fluids was measured before and after exiting the solar collector. The secondary fluid which was water conducted solar thermal heat from heat transfer fluids. The heat exchanger was used to produce the steam which was fed into the turbine.

3. Results and Discussion

3.1. Steam Turbine Characteristics. The performance characteristics of the fabricated turbine were as follows: average isentropic efficiency of 55.3%, average cycle power output of 450.8 W, maximum power output of 498.2 W, generator/gear box efficiency of 54.7%, power/heat ratio of 0.08, inlet pressure of $3.60 \times 10^5 \text{ Nm}^{-2}$ to $2.5 \times 10^5 \text{ Nm}^{-2}$, average inlet temperature of 112.8°C , average outlet temperature of

TABLE 1: Average turbine efficiency for respective heat transfer fluids.

Heat transfer fluid	Average turbine efficiency (%)
6 M sodium chloride solution	61.5
4 M sodium chloride solution	61.05
2 M sodium chloride solution	58.6
Water	54.8
Unused engine oil	53.5
Used engine oil	49.6
Vegetable oil 2	47.5
Vegetable oil 1	41.15

TABLE 2: Inlet and outlet enthalpies of heat transfer fluids.

Heat transfer fluid	Enthalpy at inlet (kJ/kg)	Enthalpy at exit (kJ/kg)
4 M sodium chloride solution	3527.6	2211.3
2 M sodium chloride solution	3456.3	2176.1
Unused engine oil	3377.4	2099.7
Used engine oil	30301.7	1812.4
Vegetable oil 2	27548.2	16921.3
Vegetable oil 1	2404.6	13,875.6

98.8°C, average inlet steam flow rate of 239.6 kg/hr, average outlet pressure of $1.20 \times 10^5 \text{ Nm}^{-2}$ to $1.087 \times 10^5 \text{ Nm}^{-2}$, and average outlet steam flow rate of 102 kg/hr.

In a study of AC generators, the torque was converted to power with efficiency higher than 90% [29]. The efficiency was higher than the one recorded in this study due to the better conductivity nature of the heat transfer fluid used. In addition, the efficiency in this study was lower due to the variations in the solar power intensity during the solar thermal collection.

The screw expander device achieved a high efficiency of 75%, where a couple of twin helical screw rotors, male and female rotors, are fixed on the parallel axis and bound to the case [2], compared to other steam conversion devices. This was also the case in this study, where the efficiency was lower due to the difference in the technologies used.

Table 1 shows the average efficiencies of the turbine with respect to the heat transfer fluids. The differences observed on the efficiencies tabulated are due to the variances of the solar thermal heat conducted by the fluids as they, respectively, flowed through the solar collector [17]. The salt solutions conducted more solar thermal heat compared to vegetable oil fluids and the engine oils lay in between. The unused engine oil conducted more heat compared to the used engine oil. Hence, the efficiencies of the heat transfer fluids ranged from 61.5% to 41.15%.

In US patent number US 3452132 A, 300°C of superheated steam and a manifold pressure of magnitude of $1.0 \times 10^{10} \text{ Nm}^{-2}$ were impinged asymmetrically on the yarn at an angle of 30°C, which was the angle that produced the highest power [30]; this was in order to produce industrial heat. In the endeavor to improve performance of steam turbine, it was established that to meet industrial power demand, a high speed turbine of 45000 rpm and a small blade span of length $200 \times 10^{-6} \text{ m}$ would be required for

optimum efficiency [31]. In this study, process heat and power were cogenerated.

3.2. Turbine Performance with Heat Transfer Fluids. The average enthalpy at inlet of the 6 M sodium chloride solution was 3789.1 kJ/kg at a pressure of $3.01 \times 10^5 \text{ Nm}^{-2}$, and the enthalpy at exit was 2346.3 kJ/kg at a pressure of $1.05 \times 10^5 \text{ Nm}^{-2}$. Table 2 shows the inlet and outlet enthalpies of the other heat transfer fluids under the same conditions as the 6 M sodium chloride solution.

Turbine efficiency was found to range from 65% for small turbines to 90% for bigger commercial ones [32]. In this study, the highest temperature of steam entering the turbine was an average of 120°C and the temperature of the fluid leaving the turbine was 98.0°C for an average output of 487 W.

Figure 2 shows the variation of steam flow rate and power output for the heat transfer fluids at an average solar power intensity of 1103.8 Wm^{-2} . At 479 W, 6 M sodium chloride solution produced 298 kg/hr of steam at a temperature of 112 C and at a pressure of $1.24 \times 10^5 \text{ Nm}^{-2}$. Vegetable oil 1 produced power of 336.3 W which produced steam flow rate of 68.9 kg/hr at a temperature of 97.5°C and a pressure of $1.04 \times 10^5 \text{ Nm}^{-2}$. The steam flow rate was higher for the sodium chloride solutions while it was lower for vegetable oils as shown in Figure 2. This was because the vegetable oils absorbed less solar heat as they passed through the collector compared to the inorganic salt solutions and the engine oils. The unused engine oil produced higher steam flow rate compared to the used engine oil. This was because the used engine contained impurities, hence the lower steam flow rate. The performance of the engine oils lay in between the performance of the salt solutions and the vegetable oils. The mass flow rate of the secondary heat transfer fluid increased with the intensity of solar power

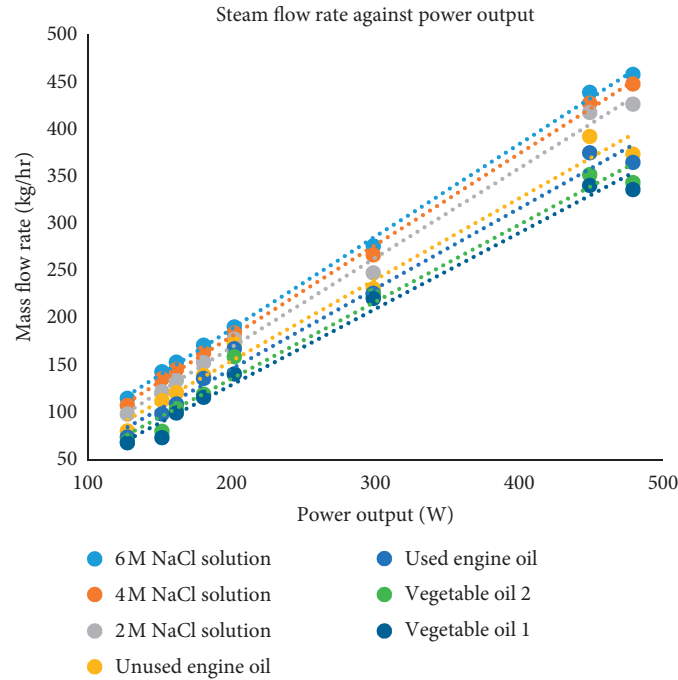


FIGURE 2: Steam turbine steam flow rate against power output for heat transfer fluids.

intensity. The measurement of power output and respective average steam flow rates were determined at an average solar power intensity of 1103.8 Wm^{-2} . In this study, the rotor was rotating at 2800 rpm which compared well with a rotor in a study which was carried out by Misek and Kubin [33] which rotated at 3000 rpm.

It was found that the generator must rotate at constant synchronous speed which is in tandem with the frequency of the power source [34] which was in tandem with the findings in this study.

4. Conclusion

Steam turbines, utilizing the power from the sun, can provide process heat and electrical power in off-grid areas, which are inaccessible due to rugged terrain. Local technology and materials have the potential of sustainability and in fact can be utilized for improving the energy demand locally. However, the heat transfer fluids need to be fortified against degradation to reduce the cost of production of the process heat and power. The steam that was exiting from the turbine at temperatures of an average of 109.0°C was used to heat the feed water, flowing into the absorber in the collector, and it was reheated by the collector before reentry into the turbine. The highest efficiency of the turbine was 61.6%, with respect to the 6M sodium chloride solution, which achieved the highest enthalpy. The turbine operation conditions show that the turbine in this study can be upgraded to produce small scale industrial power and process heat. Improvement of temperatures of operation of the heat transfers fluids so that they degrade at higher temperatures and can lead to higher process heat and power production. In addition, increasing the thermal conductivity of the heat transfer

fluids would increase the inlet steam enthalpy leading to increased process heat and power available for various industrial uses. The stepped up output can be used to run a medium industrial plant such as a fruits processing factory and mineral extraction industry.

Nomenclature

- \dot{m} : Mass flow rate (kg/h)
- η_{th} : Efficiency with respect to enthalpy, %
- η_T : Isentropic efficiency, %
- \dot{E} : Energy flow rate (J/s)
- h_i : Enthalpy flow rate (J/kg)

Abbreviations

- rpm: Rotations per minute
- L/D : Length to diameter ratio
- SAW: Submerged arch welding
- US: United States of America
- NaCl: Sodium chloride solution
- W : Relative velocity in velocity triangle
- SEGSs: Solar thermal electricity generating systems

Subscripts

- 1 and 2: Inlet and outlet streams
- θ_1 and θ_2 : Inlet and outlet velocity triangle angles
- g : Gas
- h : Enthalpy
- in: Inlet
- out: Outlet
- f : Flash
- U : Internal energy
- V : Tangential absolute velocity components.

Data Availability

The data used to support the findings of the study are available from the corresponding author upon request.

Conflicts of Interest

The author declares that there are no conflicts of interest.

References

- [1] G. Dolf, B. Francisco, S. Deger, D. Morgan, W. Nicholas, and G. Ricardo, "The role of renewable energy in the global energy," *Energy Strategy Reviews*, vol. 24, pp. 38–50, 2019.
- [2] P. Iodice, G. Langella, and A. Amoresano, "Modeling and energetic-exergetic evaluation of a novel screw expander-based direct steam generation solar system," *Applied Thermal Engineering*, vol. 155, pp. 82–95, 2019.
- [3] R. Jackson, C. LeQuere, M. Andrew et al., "Global energy growth is outpacing decarbonization," *Environmental Research Letters*, vol. 13, no. 12, Article ID 120401, 2018.
- [4] M. Mohsin, A. Rasheed, H. Sun et al., "Developing low carbon economies: an aggregated composite index based on carbon emissions," *Sustainable Energy Technologies and Assessments*, vol. 35, pp. 365–374, 2019.
- [5] A. A. M. H. Ai Asbahi, F. Gang, W. Iqbal, Q. Abass, M. Mohsin, and R. Iram, "Novel approach of principal component analysis method to assess the national energy performance via energy trilemma index," *Energy Reports*, vol. 5, pp. 704–713, 2019.
- [6] S. A. Kalogirou, "Solar thermal collectors and applications," *Progress in Energy and Combustion Science*, vol. 30, pp. 231–295, 2019.
- [7] A. Salman and M. Razman, "Selection of renewable energy sources for sustainable development of electricity generation system using hierarchy process: a case study of Malaysia," *Journal of Renewable Energy*, vol. 63, pp. 458–466, 2014.
- [8] M. Jaroslaw, B. Wojciech, W. Maran, F. Kamil, and K. Jan, "Off design operation of a 900 MW class power plant with utilization of low temperature of flue gases," 2015.
- [9] Y. Zhang, K. Li, and D. Tao, "Effect of inter blade phase Angle on blade flutter of steam turbine," *Journal of Aerospace Power*, vol. 9, no. 3, p. 277, 1994.
- [10] P. Subramanyam and K. Siva, "Experimental investigation on design of high pressure steam turbine blade," *International Journal of Innovative Research in Science, Engineering and Technology*, vol. 2, no. 5, 2013.
- [11] P. Iodice, G. Langella, and A. Amoresano, "Energy performance and numerical optimization of a screw expander—based solar thermal electricity system in a wide range of fluctuating operating conditions," *International Journal of Energy Research*, vol. 44, no. 3, pp. 1858–1874, 2020.
- [12] A. Chenduran, S. Tharani, G. Chenthooran, and S. Johnson, "Design of the steam turbine for small scale power plant," in *Proceedings of the Fifth Conference Proceedings, Department of Mechanical Engineering* University of Peradeniya, Sri Lanka, 2004.
- [13] S. A. Kalogirou, S. Karellas, K. Braimakis, C. Stanciu, and V. Badescu, "Exergy analysis of solar thermal collectors and processes," *Progress in Energy and Combustion Science*, vol. 56, pp. 106–137, 2016.
- [14] P. Iodice, G. Langella, and A. Amoresano, "A numerical approach to assess air pollution by ship engines in manoeuvring mode and fuel switch conditions," *Energy & Environment*, vol. 28, no. 8, pp. 827–845, 2017.
- [15] M. H. Jawad, *Theory and Design of Plate and Shell Structures*, Chapman and Hall Publishing Ltd, New York, NY, USA, 1994.
- [16] M. Kawira, R. Kinyua, and J. Kamau, "A prototype steam storage system for power production," *International Journal of Scientific Engineering and Technology (IJSET)*, vol. 3, no. 8, pp. 1012–1015, 2014.
- [17] M. Kawira, R. Kinyua, and J. Kamau, "A prototype parabolic trough solar concentrator for steam production," *Journal of Agriculture Science and Technology (JAGST)*, vol. 14, no. 2, 2012.
- [18] G. Janick and M. Byron, "Turbine blade vibration measurement methods for turbocharges," *American Journal of Sensor Technology*, vol. 2, no. 2, pp. 13–19, 2014.
- [19] S. W. Kariuki, J. Wachira, M. Kawira, and G. M. Leonard, "Characterization of prototype formulated particleboards from agro industrial lignocellulose biomass bonded with chemically modified cassava peel starch," *Advances in Materials Science and Engineering*, vol. 2019, Article ID 1615629, 15 pages, 2019.
- [20] S. W. Kariuki, J. Wachira, M. Kawira, and G. M. Murithi, "Formaldehyde use and alternative biobased binders for particleboard formulation: a Review," *Journal of Chemistry*, vol. 2019, Article ID 5256897, 12 pages, 2019.
- [21] W. B. Jechens, "Steam turbines—their construction, selection and operation," in *Proceedings of the South African Sugar Technologies Association*, Durban, South Africa, March 1966.
- [22] P. K. Zachos, M. Pappa, and A. I. Kalfas, "Turbine blading performance evaluation using geometry scanning and flow prediction tools," *Journal of Power and Energy Systems*, vol. 2, no. 6, pp. 1345–1358, 2008.
- [23] K. Weman, *Welding Process Handbook*, Elsevier, Science Direct, Amsterdam, Netherlands, 2nd edition, 2012.
- [24] G. Pitzl: Process of steam drawing and annealing polyester yarn, US Patent US3452132A, 1969.
- [25] M. Eck, E. Zarza, M. Eickhoff, J. Rheinländer, and L. Valenzuela, "Applied research concerning the direct steam generation in parabolic troughs," *Solar Energy*, vol. 74, no. 4, pp. 341–351, 2003.
- [26] E. F. Church, *Steam Turbines*, Mc Graw Hill Publishers Ltd., London, UK, 1987.
- [27] C. H. Peabody, *Thermodynamics of the Steam Engine and Other Heat Engines*, Wiley and Sons Publishers Ltd., New York, NY, USA, 2011.
- [28] A. H. Ranah and J. R. Mehta, "Energy and exergy analysis of extraction cum back pressure steam turbine," *Journal of Modern Engineering Research*, vol. 3, no. 2, pp. 626–632, 2013.
- [29] C. Whitaker, *AC Power Systems Handbook*, Taylor and Francis, Boca Raton, FL, USA, 2006.
- [30] P. Gilbert, "Process of Steam drawing and annealing," Assigned to Du Point, US Patent No. US 3452132 A, Assigned to Du Point, pp. 1593–1658, Atlanta, Georgia, 1969.
- [31] S. Satos, S. Jovanovic, J. Lang, and Z. Spakovscky, "Demonstration of a palm sized 30 W air-to-power turbine generator," *Journal of Engineering for Gas Turbines and Power*, vol. 133, no. 10, pp. 1–10, 2011.
- [32] A. Schetz and A. E. Fuhs, *Hand Book of Fluid Dynamics and Fluid Machinery*, Oxford Press, New York, NY, USA, 1996.
- [33] T. Misek and Z. Kubin, "Static and dynamic analysis Of 1220 mm steel last stage blade for steam turbine," in *Proceedings of the Applied and Computational Mechanics Symposium*, pp. 133–140, Honolulu, Hawaii, March 2009.
- [34] A. Leyzerovich, *Wet Steam Turbines for Nuclear Power Plants*, Pen Well Books, Tusla, Oklahoma, 2005.

Research Article

Magnetic Circuit Design and Magnetic Field Finite Element Analysis of Converging Stepped Magnetofluid Seal with Small Clearance

Xiaolong Yang , Guohong Wang, and Ruibo Zhang

School of Mechanical Engineering, Guangxi University of Science and Technology, Liuzhou 545006, China

Correspondence should be addressed to Xiaolong Yang; 09116324@bjtu.edu.cn

Received 13 May 2020; Revised 1 June 2020; Accepted 16 June 2020; Published 17 July 2020

Academic Editor: Stefano Sorace

Copyright © 2020 Xiaolong Yang et al. This is an open access article distributed under the Creative Commons Attribution License, which permits unrestricted use, distribution, and reproduction in any medium, provided the original work is properly cited.

The stepped magnetofluid seal is an effective method for improving the pressure ability of ordinary magnetofluid seals (OMS) with large clearance. At present, the research on stepped magnetofluid seal with less than 0.4 mm small clearance has not been carried out yet. The equivalent magnetic circuit design of converging stepped magnetofluid seal (CSMS) with small clearance has been carried out and verified by magnetic field finite element method based on the CSMS theory and magnetic circuit theory. The effects of the width of the axial seal position, the height of the radial seal position, the number of the pole tooth in the axial seal position, and the number of the pole tooth in the radial seal position on the theoretical pressure ability of the CSMS are investigated by numerical simulation. The calculation results are analyzed and discussed. The results show that the magnetic flux leakage at the junction of the permanent magnet and pole piece causes the higher pressure ability of the CSMS structure designed by the equivalent magnetic circuit method than that calculated by the magnetic field finite element method. When the width of the axial seal position is greater than the height of the radial seal position and the number of pole teeth in the axial seal position is less than the number of pole teeth in the radial seal position, the CSMS has the best effect. Compared with OMS with small clearance, CSMS has greater advantages.

1. Introduction

Magnetofluid is a kind of advanced intelligent material, which has become the research object of many researchers because of its stable and special properties [1]. Magnetofluid seals technique is a new kind of sealing method. In contrast to ordinary sealing, magnetofluid sealing has many strength points such as no wear, no leakage, no contamination, and lasting service life [2]. Therefore, magnetofluid seals are widely used in dynamic seals, isolation seal, and environmental seal [3–5].

At present, lots of research studies focus on OMS with less than 0.4 mm small clearance. Urreta and Mkubik et al. analyzed the sealing effect of two kinds of magnetofluid with different particle sizes to improve the pressure ability and to reduce friction torque and apply them to the spindle of high-precision machine tool [6, 7]. Zhang et al.

studied and analyzed the influence of volume fraction of magnetofluid, magnetic field parameters, geometrical parameters, and different ester magnetofluids on the sealing ability of OMS [8]. Wang and Zhao et al. studied the mechanism of OMS and obtained the influence of temperature on the sealing performance of magnetofluid [9, 10]. Szczech et al. carried out numerical simulation and experimental verification on the influence of magnetofluid volume, permanent magnet volume, polar tooth shape, and temperature on the sealing pressure performance [11, 12]. But it is difficult for OMS to work in large clearance environment. Parmar designed static and dynamic seal tests with large radial clearance (0.7 mm) and verified its performance. Yang et al. proposed a new type of stepped magnetofluid seal used for large clearance condition [13]. The pressure capabilities of converging and diverging stepped magnetofluid seals were researched

by numerical and experimental method, respectively, and were compared to that of the OMS. The results show that pressure ability of the stepped magnetofluid seal is better than that of the OMS [14, 15]. However, the existing stepped magnetofluid seals are aimed at the working environment of large clearance, and the study on CSMS under small clearance working condition has not been carried out yet.

This paper studied the CSMS with small clearance based on the CSMS with big clearance. The sealing structure of CSMS with small clearance and two magnetic sources is designed by the equality magnetic circuit way, and the pressure ability reliability of its structure designed by the equality magnetic circuit way is verified by the magnetic field finite element method. The effects of the axial seal position width, the radial seal position height, and the numbers of the pole teeth in the axial and radial seal position on the theoretical pressure capabilities of CSMS with small clearance have been investigated which can provide a theoretical basis for designing CSMS with small clearance and higher sealing performance.

2. Materials and Methods

Figure 1 is a schematic diagram of CSMS structure with small clearance and two magnetic origins. Its equivalent magnetic circuit is shown in Figure 2.

The magnetic field generated by the permanent magnet limits the magnetofluid to the seal position, and the magnetic field force acting on the magnetofluid is used to resist the pressure difference between two ends of the structure, so as to achieve the purpose of blocking the leakage channel.

As usual, the Bernoulli equation of magnetofluids can be shown (S. Parmar et al., 2018):

$$P + \frac{1}{2}\rho_f V^2 + \rho_f gh - \mu_0 \int_0^H M dH = C, \quad (1)$$

where g is the gravitational acceleration; h is the reference height; V is the density; M is the magnetization of magnetofluids; P is the total pressure of magnetofluids; ρ_f is the velocity; μ_0 is the vacuum permeability; H is the external magnetic field strength; and C is the constant. In general, the composite pressure ability of magnetofluid static seal is easier to understand in the following equation [14]:

$$\Delta P = \mu_0 M_s \sum_{i=1}^N (H_{\max}^i - H_{\min}^i) = M_s \sum_{i=1}^N (B_{\max}^i - B_{\min}^i). \quad (2)$$

In (2), M_s and N are the saturation magnetization of the magnetofluid and the number of pole teeth; H_{\min}^i , H_{\max}^i , B_{\min}^i , and B_{\max}^i are the minimum and maximum magnetic field strengths and the minimum and maximum magnetic inductions in the sealing position formed between the i th pole tooth and the stepped shaft, respectively.

The formula for theoretical pressure ability of CSMS is as follows:

$$\Delta P_{c \max} = \sum_i^N (P_{ia} + \lambda P_{ir}), \quad (3)$$

where P_{ia} and P_{ir} are the pressure abilities of the magnetofluid seal in the axial and in the radial seal positions formed by the stepped shaft and the i th pole piece. If P_{ia} is less than P_{ir} , then λ is 1, otherwise 0. The value of P_{ia} and P_{ir} can be calculated by equation (2).

The magnetic circuit devise of parallel CSMS includes two assumptions: first, ignoring magnetic leakage; second, ignoring edge effect. According to Kirchhoff's first law of magnetic circuit, it can be concluded that

$$\sum \phi_i = 0. \quad (4)$$

And it can be obtained that

$$\phi_2 = \phi_1 + \phi_3, \quad (5)$$

where ϕ_1 , ϕ_2 , and ϕ_3 , respectively, are the magnetic flux passing through pole piece at high pressure side, middle pole pieces, and pole piece at the atmospheric side.

$$\phi_1 = 3B_{g1}^1 S_{g1}^1 + 5B_{g2}^1 S_{g2}^1, \quad (6)$$

where B_{g1}^1 and B_{g2}^1 , respectively, are the magnetic flux densities in the first axial seal position and radial seal position formed by stepped shaft and pole teeth of the first pile piece. S_{g1}^1 and S_{g2}^1 are, respectively, the magnetic flux densities in the first axial seal position and radial seal position formed by stepped shaft and pole teeth of the first pile piece.

$$\phi_2 = 3B_{g1}^4 S_{g1}^4 + 5B_{g2}^6 S_{g2}^6, \quad (7)$$

where B_{g1}^4 and B_{g2}^6 , respectively, are the magnetic flux densities in the first axial seal position and radial seal position formed by stepped shaft and pole teeth of the first pile piece. S_{g1}^4 and S_{g2}^6 are, respectively, the magnetic flux densities in the first axial seal position and radial seal position formed by stepped shaft and pole teeth of the first pile piece.

$$\phi_3 = 3B_{g1}^7 S_{g1}^7 + 5B_{g2}^{11} S_{g2}^{11}, \quad (8)$$

where B_{g1}^7 and B_{g2}^{11} , respectively, are the magnetic flux densities in the first axial seal position and radial seal position formed by stepped shaft and pole teeth of the first pile piece. S_{g1}^7 and S_{g2}^{11} are, respectively, the magnetic flux densities in the first axial seal position and radial seal position formed by stepped shaft and pole teeth of the first pile piece.

$$\phi_{m2} = B_{m2} S_{m2} = \phi_3 = 3B_{g1}^7 S_{g1}^7 + 5B_{g2}^{11} S_{g2}^{11}, \quad (9)$$

where ϕ_{m2} , B_{m2} , and S_{m2} , respectively, are the flux, flux density, and annular area of the second permanent magnet at the atmospheric side.

According to Kirchhoff's second law, the magnetic potential of the permanent magnet at the atmospheric pressure side can be expressed as follows:

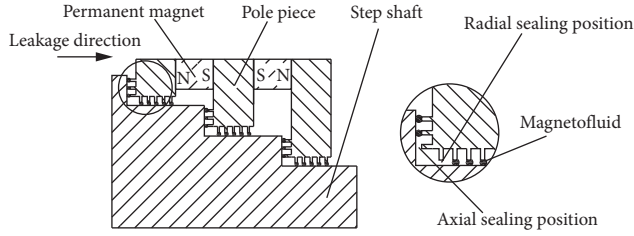


FIGURE 1: CSMS with small clearance. The enlarged area on the right side of the sketch shows the terms axial and radial seal positions used in the article.

$$\begin{aligned}
 F_2 = H_{m2}L_{m2} &= (3B_{g1}^4S_{g1}^4 + 5B_{g2}^6S_{g2}^6) \\
 &\cdot \left[R_{p2} + \frac{(R_{t1}^4 + R_{g1}^4)(R_{t2}^6 + R_{g2}^6)}{3(R_{t2}^6 + R_{g2}^6) + 5(R_{t1}^4 + R_{g1}^4)} \right] \\
 &+ (3B_{g1}^7S_{g1}^7 + 5B_{g2}^{11}S_{g2}^{11}) \\
 &\cdot \left[R_{p3} + R_{a2} + R_{m2} + \frac{(R_{t1}^7 + R_{g1}^7)(R_{t2}^{11} + R_{g2}^{11})}{3(R_{t2}^{11} + R_{g2}^{11}) + 5(R_{t1}^7 + R_{g1}^7)} \right], \quad (10)
 \end{aligned}$$

where H_{m2} and L_{m2} , respectively, are the magnetic field strength and the length of the second permanent magnet. R_{p3} , R_{a2} , and R_{m2} , respectively, are the magnetic resistances of the third pole piece, the second step, and the second permanent magnet. R_{t1}^4 and R_{g1}^4 , respectively, are the reluctance of the fourth polar tooth in the axial seal position and the fourth seal position in the axial seal position. R_{t2}^6 and R_{g2}^6 , respectively, are the reluctance of the sixth polar tooth in the axial seal position and the sixth seal position.

When (9) is multiplied by (10), the volume of permanent magnet can be calculated as follows:

$$V_{m2} = S_{m2}L_{m2} = \frac{F_2\phi_{m2}}{B_{m2}H_{m2}}. \quad (11)$$

In order to increase the utilization rate of permanent magnet, permanent magnet should work at their maximum magnetic energy product:

$$V_{m2} = S_{m2}L_{m2} = \frac{F_2\phi_{m2}}{(BH)_{\max}}. \quad (12)$$

When (9) is divided by (10), the following formula can be obtained:

$$\frac{S_{m2}}{L_{m2}} = \frac{(3B_{g1}^7S_{g1}^7 + 5B_{g2}^{11}S_{g2}^{11})H_{m2}}{F_2B_{m2}}. \quad (13)$$

When (12) is multiplied by (13), the cross-sectional area of the permanent magnet can be calculated as follows:

$$S_{m2} = (3B_{g1}^7S_{g1}^7 + 5B_{g2}^{11}S_{g2}^{11}) \sqrt{\frac{H_{m2}}{(BH)_{\max}B_{m2}}}. \quad (14)$$

When (12) is divided by (13), the length of the permanent magnet can be calculated as follows:

$$L_{m2} = F_2 \sqrt{\frac{B_{m2}}{(BH)_{\max}H_{m2}}}. \quad (15)$$

Because the magnetic permeability of pole pieces and shaft is much greater than that of air and permanent magnet, the magnetic resistance of pole piece and shaft can be neglected in calculating the length of permanent magnet. The length of the permanent magnet can be calculated by the following expression:

$$\begin{aligned}
 L_{m2} &= \left\{ (3B_{g1}^4S_{g1}^4 + 5B_{g2}^6S_{g2}^6) \left[\frac{R_{g1}^4R_{g2}^6}{3R_{g2}^6 + 5R_{g1}^4} \right] + (3B_{g1}^7S_{g1}^7 + 5B_{g2}^{11}S_{g2}^{11}) \right. \\
 &\quad \cdot \left. \left[R_{m2} + \frac{R_{g1}^7R_{g2}^{11}}{3R_{g2}^{11} + 5R_{g1}^7} \right] \right\} \sqrt{\frac{H_{m2}}{(BH)_{\max}B_{m2}}}. \quad (16)
 \end{aligned}$$

According to the known demagnetizing curve and magnetic circuit parameters of permanent magnet, the length and cross-sectional area of permanent magnet can be calculated, so as to ensure the maximum magnetic energy product in the sealing position and improve the utilization rate of permanent magnet.

If the sealing pressure resistance is required to be not less than 7.5×10^5 Pa, the total magnetic induction intensity difference is 16.6 T according to the theory of polymerized magnetic fluid seal. According to Table 1 and (13) and (15), the length and cross section of the permanent magnet can be calculated. The length is 4 mm, and the cross section of the permanent magnet 703.716 mm^2 . The structure parameters of CSMS designed by magnetic circuit theory are shown in Table 1.

To verify the reliability of CSMS with small clearance devised by magnetic circuit theory and research, the effects of the radial and axial seal positions and pole teeth numbers on its pressure capabilities, the magnetic field finite element method has been employed. Because of the symmetry of the seal structure, the three-dimensional axisymmetric problem of the CSMS is simplified to be a two-dimensional plane model. In numerical simulation method, the program ANSYS 15 was used. In the numerical simulations, an axially symmetric model was adopted, as was the Dirichlet boundary condition. The physical environment of the magnetofluid seal is created in the preprocessor of ANSYS finite element analysis software. And because the magnetic field strength in the sealing position produced by the permanent magnet is much more than that required by the saturated magnetized magnetofluid, magnetization of the magnetofluid will reach its maximum value. The magnetic permeability difference between the saturated magnetized magnetofluid and the air is very small, so the magnetofluid can be treated as air approximately. The coercivity of Nd-Fe-B permanent magnet is $1.356 \times 10^6 \text{ A/m}$. The magnetofluid is an oil-based fluid and the saturation magnetization is 30.7 kA/m . The corresponding material attributes are given to each component. The magnetic field computation was performed by use of intelligent mesh with precision 1. The Dirichlet boundary condition is applied, and the magnetic

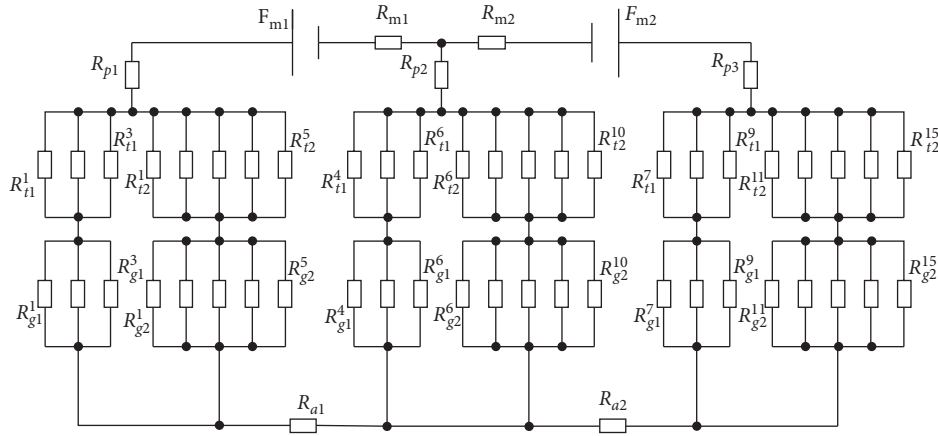


FIGURE 2: The equivalent magnetic circuit.

TABLE 1: The parameters of converging stepped magnetofluid seal with small clearance.

Item	Value
Inner radius of the 1/2/3 pole piece (mm)	21/17/13
Outer radius of the 1/2/3 pole piece (mm)	30
Length of the 1/2/3 pole piece (mm)	5.3
Pole tooth number of the 1/2/3 pole piece in the axial seal position	3
Pole tooth number of the 1/2/3 pole piece in the radial seal position	5
Axial seal position width (mm)	0.1
Radial seal position width (mm)	0.1
Width of pole tooth (mm)	0.3
Slot depth (mm)	0.8
Slot width (mm)	0.7

flux density distributions in the radial and axial seal positions could be gained by the ANSYS solver.

3. Results and Discussion

3.1. Reliability of CSMS Designed by Magnetic Circuit Method.

Through the above numerical analysis, magnetic flux density distribution in the sealing position of CSMS is shown in Figure 3 and the distribution of the magnetic force line is shown in Figure 4.

It can be seen from Figure 3 that the maximum magnetic flux density passing through the pole teeth of the middle pole piece is obviously greater than that passing through the pole teeth of the other two pole pieces because of the magnetic field strength in the middle pole piece generated by two magnetic sources.

According to (2) and (3) and magnetic flux density distribution as shown in Figure 3, the theoretical pressure ability of the CSMS should be $6.9 * 10^5$ Pa which is smaller than the required value of the magnetic circuit design and the error is 8%. This proves the reliability of CSMS designed by the magnetic circuit. The main reason of error is that the magnetic flux leakages occur at the junctions of permanent magnets and pole piece as shown in Figure 4.

3.2. Effect of Sealing Position Height and Width on CSMS.

When the size of the axial seal position is 0.1 mm, the magnetic field distribution in the small sealing position of

CSMS with different radial seal position heights is shown in Figure 5.

It can be seen from Figure 5 that the magnetic flux density in the axial seal position enlarges slowly and the magnetic flux density in the radial seal position reduces with the increase of the radial seal position height. The reason for this change is that the increase of the radial seal position height will enlarge the magnetic resistance of the radial seal position which causes the increase of the magnetic resistance of the whole magnetic circuit and the decrease of the magnetic flux of the whole magnetic circuit. According to the magnetic circuit theory, the increase of the magnetic potential of the radial seal position is far less than the increase of its magnetic resistance. Hence, magnetic flux density in the radial seal position reduces as the radial seal position height enlarges. On the other hand, the magnetic resistance of the axial seal position remains unchanged when the axial seal position width remains unchanged. The magnetic potential of the axial seal position enlarges with the increasing height of the radial seal position. Therefore, the magnetic flux density in the axial seal position enlarges slowly with the increasing height of the radial seal position.

When the size of the radial seal position is 0.1 mm, the magnetic field distribution in the small sealing position of CSMS with different axial seal position weight is shown in Figure 6.

It can be seen from Figure 6 that the magnetic flux density in the radial seal position enlarges slowly and the

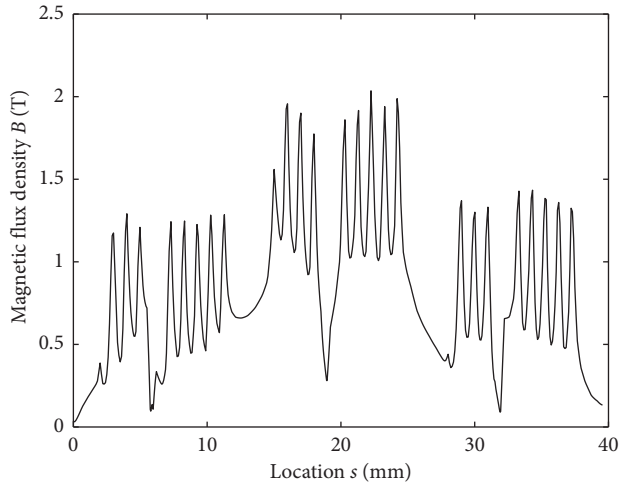


FIGURE 3: Magnetic field distribution.

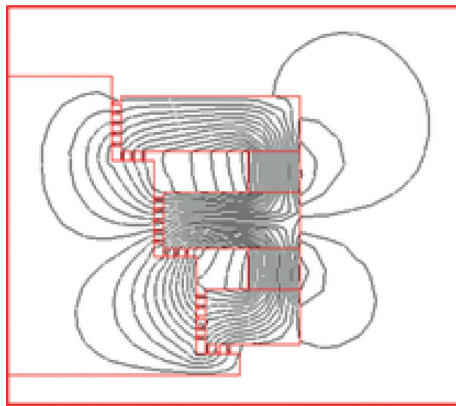


FIGURE 4: Distribution of the magnetic force line.

magnetic flux density in the axial seal position reduces with the increase of the axial seal position height. The reason for this change is that the increase of the axial seal position height will increase the magnetic resistance of the axial seal position which causes the increase of the magnetic resistance of the whole magnetic circuit and the decrease of the magnetic flux of the whole magnetic circuit. According to the magnetic circuit theory, the increase of the magnetic potential of the axial seal position is far less than the increase of its magnetic resistance. Hence, the magnetic flux density in the axial seal position reduces as the axial seal position height enlarges. On the other hand, magnetic resistance of the radial seal position remains unchanged when the radial seal position width remains unchanged. The magnetic potential of the radial seal position enlarges with the increasing height of the axial seal position. Therefore, the magnetic flux density in the radial seal position enlarges slowly with the increasing height of the axial seal position.

According to (2) and (3) and the magnetic field distributions as shown in Figures 5 and 6, the effects of the radial and axial seal positions on the pressure capabilities of CSMS and the comparison of the pressure capabilities between the CSMS and the OMS under different seal positions can be obtained as shown in Figures 7 and 8.

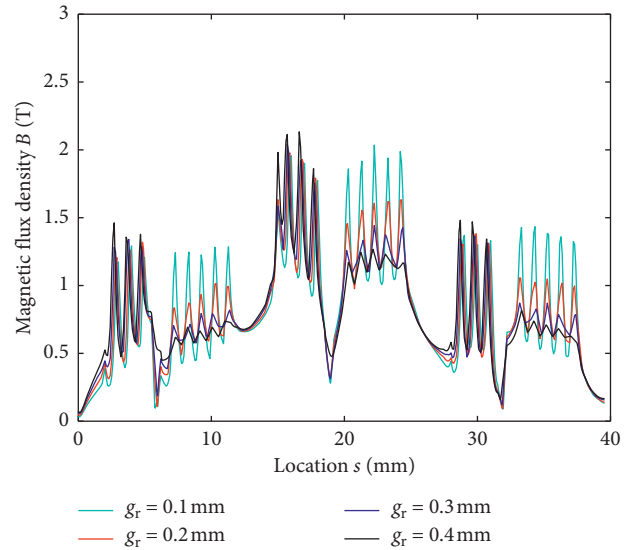


FIGURE 5: Magnetic field distribution with different radial sealing position heights. g_r : radial sealing position height.

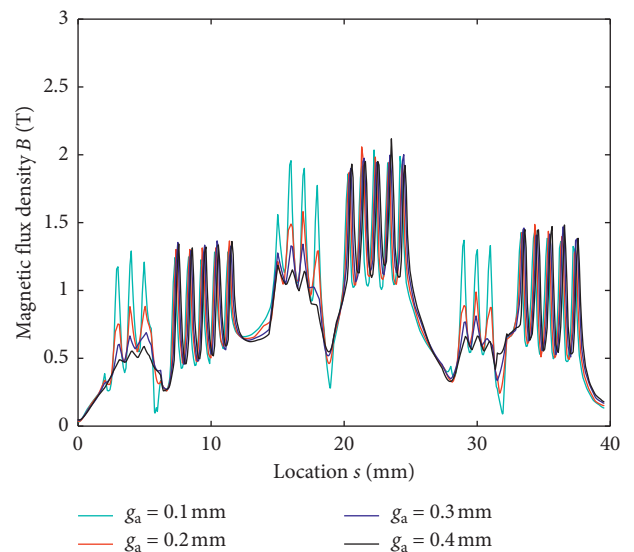


FIGURE 6: Magnetic field distribution with different axial sealing position widths. g_a : axial sealing position width.

From Figure 7, it can be seen that when the radial seal position height is 0.1 mm and the axial seal position width is greater than or equal to the radial seal position height, the theoretical pressure ability of the CSMS reduces with the increasing width of the axial seal position. The reason is that when the pressure ability of CSMS in the axial seal position is less than that in the radial seal position, the theoretical pressure ability of the seal structure is the sum of the pressure ability of the CSMS in the axial and the radial seal positions according to the theory of seal structure. Although the magnetic flux density in the axial seal position reduces with the increase of the height of the axial seal position and the magnetic flux density in the radial seal position enlarges slowly with the increase of the height of the axial seal

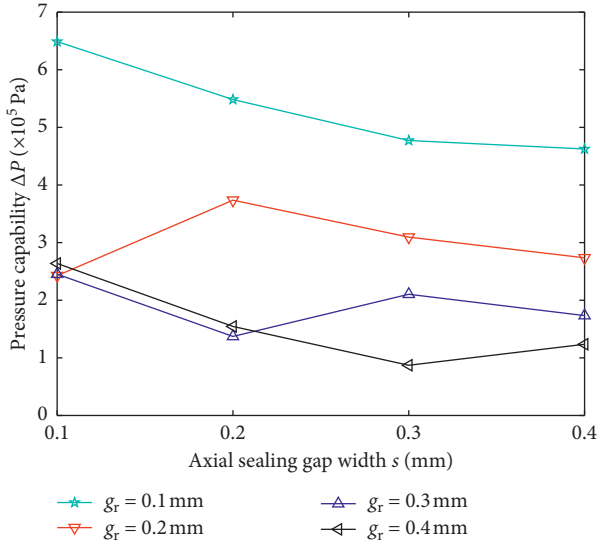


FIGURE 7: Effect of sealing positions on sealing capability. g_r : radial sealing position height.

position as shown in Figure 6, the decrement of magnetic flux density in the axial seal position is much larger than the increment of magnetic flux density in radial seal position. So, the theoretical pressure ability of CSMS reduces with the increasing width of axial seal position.

When the radial seal position height is 0.2 mm which is within the range of the axial seal position width, the theoretical pressure ability of the CSMS enlarges firstly and then reduces with the increase of the axial seal position width. This is because when the axial seal position width is less than the radial seal position height, the pressure ability of the CSMS in the axial seal position is greater than that in the radial seal position. According to the theory of the CSMS, the theoretical pressure ability of the CSMS depends only on the pressure ability of CSMS in the axial seal position. It means that the CSMS in the radial seal position does not work. When the axial seal position is greater than or equal to the radial seal position, the pressure ability of CSMS in the axial seal position is less than that in the radial seal position; the theoretical pressure ability of the CSMS is the sum of the pressure ability of the CSMS in the axial and the radial seal positions according to the theory of CSMS. And the reduction of magnetic flux density in the axial seal position is much less than that in the radial seal position when the axial seal position equals the radial seal position as shown in Figure 6. Therefore, the theoretical pressure ability of the CSMS enlarges firstly as the axial seal position enlarges. And the decrement of magnetic flux density in the axial seal position is much larger than the increment of magnetic flux density in radial seal position when the axial seal position width is larger than the radial seal position height. So, the theoretical pressure ability of CSMS reduces with the increasing width of axial seal position.

When the radial seal position is 0.3 mm, which is within the range of the axial seal position, the theoretical pressure ability of the CSMS structure initially reduces with the increasing axial seal position width, followed by an increase

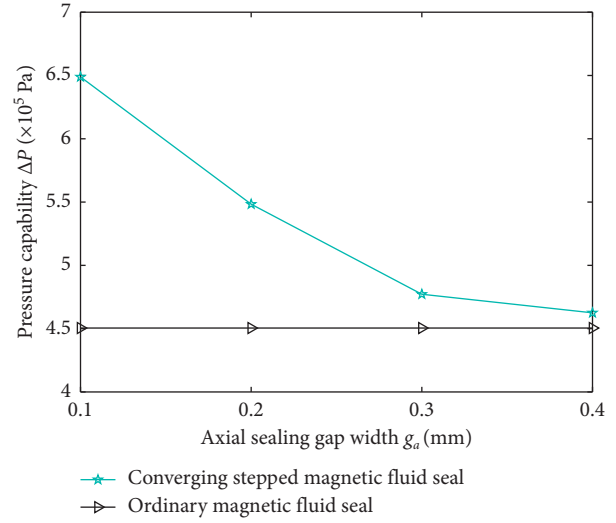


FIGURE 8: Pressure capability comparison between converging stepped seal and ordinary seal.

upon which it begins to decrease once again. This is because when the axial seal position width is less than the radial seal position height, the pressure ability of the CSMS in the axial seal position is greater than that in the radial seal position. According to the theory of the CSMS, the theoretical pressure ability of the CSMS depends only on the pressure ability of CSMS in the axial seal position. It means that the CSMS in the radial seal position does not work. And it can be seen from Figure 6 that the magnetic flux density in the axial seal position reduces with the increase of the height of the axial seal position, so the theoretical pressure ability of the CSMS reduces first with the increase of the axial seal position width. When the pressure ability of CSMS in the axial seal position is less than that in the radial seal position with increasing width of axial seal position, the theoretical pressure ability of the CSMS is the sum of the pressure ability of the CSMS in the axial and the radial seal positions according to the theory of CSMS. And the reduction of magnetic flux density in the axial seal position is much less than that in the radial seal position when the axial seal position equals the radial seal position as shown in Figure 6. Therefore, the theoretical pressure ability of the CSMS enlarges secondly as the axial seal position enlarges. Although the magnetic flux density in the axial seal position reduces with the increase of the height of the axial seal position and the magnetic flux density in the radial seal position enlarges slowly with the increase of the height of the axial seal position as shown in Figure 6, the decrement of magnetic flux density in the axial seal position is much larger than the increment of magnetic flux density in radial seal position. So, the theoretical pressure ability of CSMS reduces lastly with the increasing width of axial seal position.

From Figure 7, it can be seen that when the radial seal position height is 0.4 mm and the axial seal position width is less than or equal to the radial seal position height, the theoretical pressure ability of the CSMS reduces firstly and increases lastly with the increasing width of the axial seal position. The reason is that when the axial seal position

width is less than the radial seal position height, the pressure ability of the CSMS in the axial seal position is greater than that in the radial seal position. According to the theory of the CSMS, the theoretical pressure ability of the CSMS depends only on the pressure ability of CSMS in the axial seal position. And it can be seen from Figure 6 that the magnetic flux density in the axial seal position reduces with the increase of the height of the axial seal position, so the theoretical pressure ability of the CSMS is decreasing firstly with the increasing width of axial seal position. The theoretical pressure ability of the CSMS is the sum of the pressure ability of the CSMS in the axial and the radial seal positions according to the theory of CSMS when the axial seal position width and radial seal position height are equal. Therefore, the theoretical pressure ability of the CSMS enlarges lastly with the increasing width of axial seal position.

Figure 8 shows that when the radial seal position is 0.1 mm and the axial seal position is greater than or equal to the radial seal position, the pressure ability of the CSMS is much greater than that of the OMS. The smaller the axial seal position is, the larger the pressure ability difference between them is. When the axial seal position is 0.1 mm, the pressure ability of CSMS is about 1.5 times that of OMS. The reason is that when the radial seal position is 0.1 mm and the axial seal position is greater than or equal to the radial seal position, the pressure ability of CSMS in the axial seal position is less than that in the radial seal position; the theoretical pressure ability of the CSMS is the sum of the pressure ability of the CSMS in the axial and the radial seal positions according to the theory of CSMS. However, only the CSMS in the radial seal position plays a role for ordinary pressure seal, so the pressure ability of the CSMS is much greater than that of the OMS.

3.3. Effect of Pole Tooth Number on CSMS. When the number of pole teeth in the axial seal position is 1, the magnetic field distribution in the small-sealing seal position of CSMS with different number of pole teeth in the radial seal position is shown in Figure 9.

It can be seen from Figure 9 that the magnetic flux density in the radial and axial seal positions reduces with the increasing width of the pole tooth number in the radial seal position. The reason for this change is that the increase of the number of pole teeth in the radial seal position will decrease the total magnetic resistance of the pole tooth in the radial seal position which causes the decrease of the total magnetic resistance of the magnetic circuit and the decrease of the magnetic potential. According to the magnetic circuit theory, magnetic flux density of the axial seal position reduces as the number of pole teeth in the radial seal position enlarges. On the other hand, when the magnetic resistance in the radial seal position reduces and the magnetic resistance in the axial seal position remains unchanged, the total magnetic flux of the pole tooth magnetic resistance through the radial seal position enlarges relatively, but because the number of pole teeth in the radial seal position enlarges, the total magnetic flux enlarges much faster than that in the pole tooth in the radial seal position. Hence, the magnetic flux density in the pole tooth of the radial seal position reduces.

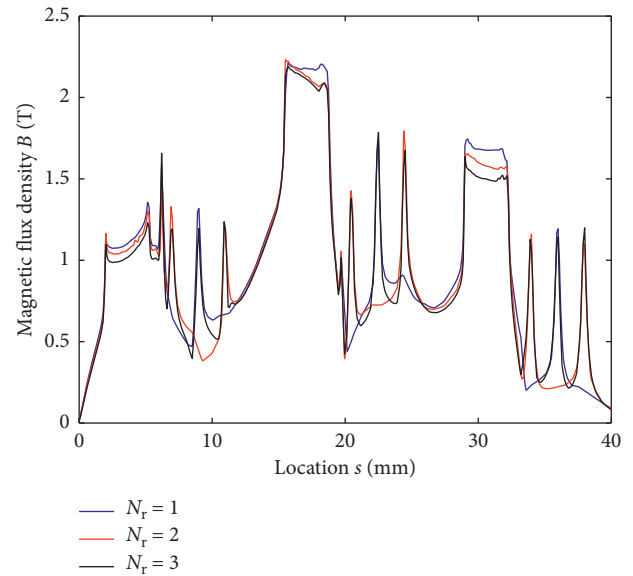


FIGURE 9: Magnetic field distribution with different teeth number in the radial sealing position. N_r : radial teeth.

When the number of pole teeth in the radial seal position is 3, the magnetic field distribution in the small sealing seal position of CSMS with different number of pole teeth in the axial seal position is shown in Figure 10.

It can be seen from Figure 10 that the magnetic flux density in the radial and axial seal positions reduces with the increasing width of the pole tooth number in the radial seal position. The reason for this change is that the increase of the number of pole teeth in the axial seal position will decrease the total magnetic resistance of the pole tooth in the axial seal position which causes the decrease of the total magnetic resistance of the magnetic circuit and the decrease of the magnetic potential. According to the magnetic circuit theory, magnetic flux density of the radial seal position reduces as the number of pole teeth in the axial seal position enlarges. On the other hand, when the magnetic resistance in the axial seal position reduces and the magnetic resistance in the radial seal position remains unchanged, the total magnetic flux of the pole tooth magnetic resistance through the axial seal position enlarges relatively, but because the number of pole teeth in the axial seal position enlarges, the total magnetic flux enlarges much faster than that in the pole tooth in the axial seal position. Hence, the magnetic flux density in the pole tooth of the axial seal position reduces.

According to (2) and (3) and magnetic field distributions as shown in Figures 9 and 10, the effects of the pole tooth number on CSMS radial and axial seal positions on the pressure capabilities of CSMS and the comparison of the pressure capabilities between the CSMS and the OMS under different pole tooth number can be obtained as shown in Figure 11 and 12.

From Figure 11, it can be seen that when the number of pole teeth in the axial seal position is 1, the theoretical pressure ability of the CSMS enlarges with the increasing number of pole teeth in the radial seal position. The reason is that when the number of pole teeth in the axial seal position

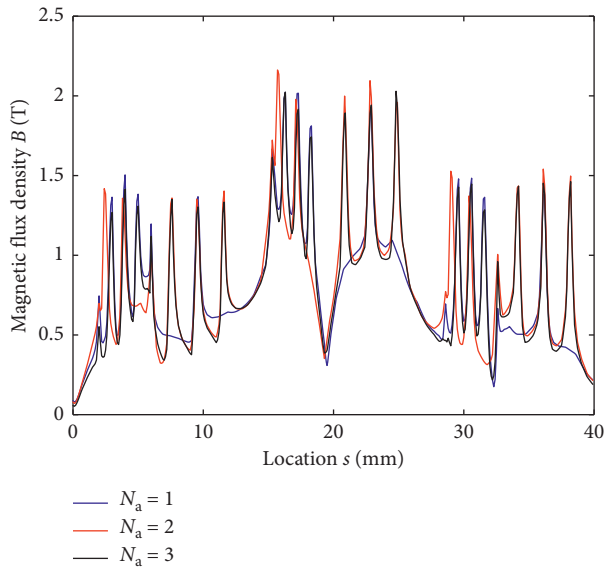


FIGURE 10: Magnetic field distribution with different teeth number in the axial sealing position. N_a : axial teeth number.

is less than or equal to the number of pole teeth in the radial seal position, the pressure ability of CSMS in the axial seal position is less than that in the radial seal position, the theoretical pressure ability of the CSMS is the sum of the pressure ability of the CSMS in the axial and the radial seal positions according to the theory of CSMS. And the increase of total difference of magnetic flux density is much larger than the decrease of magnetic flux density with the increase of the number of pole teeth in radial seal position as shown in Figure 9, so the theoretical pressure ability of CSMS enlarges with the increase of the number of pole teeth in radial seal position.

When the number of pole teeth in the axial seal position is 2, the theoretical pressure ability of the CSMS enlarges with the increase of the number of pole teeth in the radial seal position. This is because when the number of pole teeth in the axial seal position is larger than the number of pole teeth in the radial seal position, the pressure ability of the CSMS in the axial seal position is greater than that in the radial seal position. According to the theory of the CSMS, the theoretical pressure resistance of the CSMS depends only on the CSMS pressure resistance ability in the axial seal position. It means that the CSMS in the radial seal position does not work. When the number of pole teeth in the axial seal position is less than or equal to the number of pole teeth in the radial seal position, the pressure ability of CSMS in the axial seal position is less than that in the radial seal position; the theoretical pressure ability of the CSMS is the sum of the pressure ability of the CSMS in the axial and the radial seal positions according to the theory of CSMS. And the increase of total difference of magnetic flux density is much larger than the decrease of magnetic flux density with the increase of the number of pole teeth in radial seal position as shown in Figure 9, so the theoretical pressure ability of CSMS enlarges with the increase of the number of pole teeth in radial seal position.

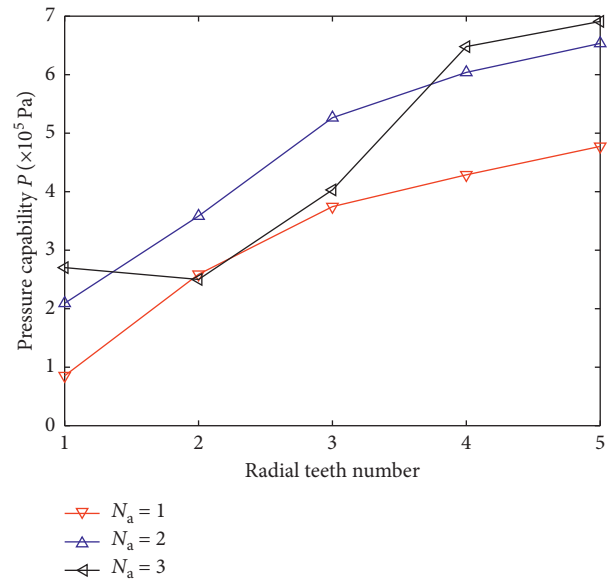


FIGURE 11: Effect of teeth number on sealing capability. N_a : axial teeth number.

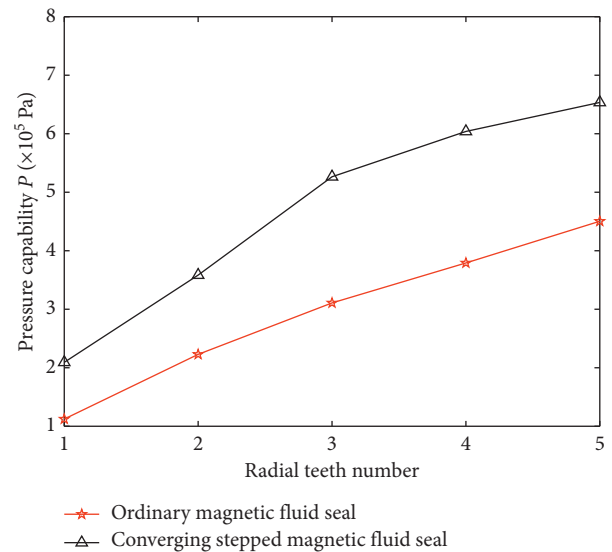


FIGURE 12: Pressure capability comparison between CSMS and OMS.

When the number of pole teeth in the axial seal position is 3, the theoretical pressure ability of the seal structure reduces first and then enlarges with the increase of the number of pole teeth in the radial seal position. This is because when the number of pole teeth in the axial seal position is larger than the number of pole teeth in the radial seal position, the pressure ability of the CSMS in the axial seal position is greater than that in the radial seal position. According to the theory of the CSMS, the theoretical pressure resistance of the seal structure depends only on the CSMS pressure resistance ability in the axial seal position. It means that the CSMS in the radial seal position does not work. So the theoretical pressure ability of the CSMS reduces

with the increase of the number of pole teeth in the radial seal position. When the number of pole teeth in the axial seal position is less than or equal to the number of pole teeth in the radial seal position, the pressure ability of CSMS in the axial seal position is less than that in the radial seal position; the theoretical pressure ability of the CSMS is the sum of the pressure ability of the CSMS in the axial and the radial seal positions according to the theory of CSMS. And the increase of total difference of magnetic flux density is much larger than the decrease of magnetic flux density with the increase of the number of pole teeth in radial seal position as shown in Figure 9, so the theoretical pressure ability of CSMS enlarges with the increase of the number of pole teeth in radial seal position.

Figure 12 shows that when the number of internal pole teeth in the axial seal position is 2, the pressure ability of the CSMS is much greater than that of the OMS. When the number of pole teeth in the radial seal position is 3, the pressure resistance of the CSMS is about 1.6 times that of the OMS. The reason is that when the number of pole teeth in the axial seal position is less than or equal to the number of pole teeth in the radial seal position, the pressure ability of CSMS in the axial seal position is less than that in the radial seal position; the theoretical pressure ability of the CSMS is the sum of the pressure ability of the CSMS in the axial and the radial seal positions according to the theory of CSMS. However, only the CSMS in the radial seal position plays a role for OMS, so the pressure ability of the CSMS is much greater than that of the OMS.

4. Conclusions

By comparing the results of finite element analysis and magnetic circuit design, the reliability of magnetic circuit design is verified. At the same time, the result of magnetic circuit design is slightly larger than that of finite element analysis. The main reason is the existence of magnetic leakage. In order to improve the accuracy of magnetic circuit design, materials with high magnetic resistance can be selected in areas where the magnetic circuit does not pass through. The pressure ability of CSMS with small clearance depends not only on the number of pole teeth in the axial seal position and the axial seal position, but also on the number of pole teeth in the radial seal position and the radial seal position. When the number of pole teeth in the axial seal position is less than or equal to the number of pole teeth in the radial seal position, the pressure ability effect of the CSMS is better than that of the situation in which the number of pole teeth in the axial seal position is smaller than the number of pole teeth in the radial seal position. When the axial seal position is bigger than or equal to the radial seal position, the pressure ability effect of the CSMS is better than that of the opposite situation. Compared with OMS with small clearance, CSMS has greater advantages.

Data Availability

The data in the supplementary file is the text file obtained from the analysis of ANSYS 15. The magnetization curve of

the magnet is measured by the magnetometer. The model in the paper is imported into ANSYS, the material parameters are input, the grid is divided, and a path is defined after solving. The magnetic induction intensity can be mapped to the curve. And output data in text format ga, gr, nr, and na in the file name, respectively, represent the axial sealing position width, the radial sealing position height, the radial teeth number, and the axial teeth number. The first column s is the leakage path length, and the second column A is the magnetic induction intensity at the current point corresponding to s. The following are the steps of data processing. The first step is to find out the peaks and troughs of the curve and calculate the difference between each peak and troughs. In the second step, according to the model and the formula in this paper, the corresponding difference is calculated to get the total magnetic induction strength difference of the seal. The third step is to multiply the total magnetic induction difference and the saturation magnetization of the magnetic fluid to obtain the total pressure resistance of the seal.

Conflicts of Interest

The authors declare that they have no conflicts of interest regarding the publication of this paper.

Acknowledgments

The authors gratefully acknowledge the support of the National Natural Science Foundation of China (Grant no. 51905114), the support of the Science and Technology Project of Guangxi Province (Grant no. 2016GXNSFBA380213), the support of the Innovation Project of Guangxi University of Science and Technology Graduate Education (Grant no. GKYC201901), and the support of the Science and Technology Project of Liuzhou (Grant no. 2017BC20204).

Supplementary Materials

The data in the supplementary file are the text files obtained from the analysis of ANSYS. The magnetization curve of the magnet is measured by the magnetometer. The model in the paper is imported into ANSYS. The material parameters are input, the grid which is divided, and a path which is defined after solving. The magnetic induction intensity can be mapped to the curve, and the output data are in the text format. ga, gr, nr, and na in the file names, respectively, represent the axial sealing position width, the radial sealing position height, the radial teeth number, and the axial teeth number. In the first column, s is the leakage path length, and in the second column, A is the magnetic induction intensity at the current point corresponding to s. The following are the steps of data processing: the first step is to find out the peaks and troughs of the curve and calculate the difference between each peak and trough. In the second step, according to the model and the formula in this paper, the corresponding difference is calculated to get the total magnetic induction strength difference of the seal. The third step is to multiply

the total magnetic induction difference and the saturation magnetization of the magnetic fluid to obtain the total pressure resistance of the seal. (*Supplementary Materials*)

References

- [1] M. Bekovic, M. Trbusic, M. Trlep et al., “Magnetic fluids’ heating power exposed to a high-frequency rotating magnetic field,” *Advances in Materials Science and Engineering*, vol. 2018, pp. 1–7, 2018.
- [2] P. N. Kaloni and A. Mahajan, “Stability and uniqueness of ferrofluids,” *International Journal of Engineering Science*, vol. 48, no. 11, pp. 1350–1356, 2010.
- [3] M. Szczech and W. Horak, “Tightness testing of rotary ferromagnetic fluid seal working in water environment,” *Industrial Lubrication and Tribology*, vol. 67, no. 5, pp. 455–459, 2015.
- [4] H. Wang, D. Li, X. He, and Z. Li, “Performance of the ferrofluid seal with gas isolation device for sealing liquids,” *International Journal of Applied Electromagnetics and Mechanics*, vol. 57, no. 1, pp. 107–122, 2018.
- [5] Y. Mitamura and C. A. Durst, “Miniature magnetic fluid seal working in liquid environments,” *Journal of Magnetism and Magnetic Materials*, vol. 431, pp. 285–288, 2017.
- [6] D.-Y. Kim, H.-S. Bae, M.-K. Park et al., “A study of magnetic fluid seals for underwater robotic vehicles,” *International Journal of Applied Electromagnetics and Mechanics*, vol. 33, no. 1-2, pp. 857–863, 2010.
- [7] H. Urreta, G. Aguirre, P. Kuzhir, and L. N. Lopez de Lacalle, “Seals based on magnetic fluids for high precision spindles of machine tools,” *International Journal Of Precision Engineering And Manufacturing*, vol. 19, no. 4, pp. 495–503, 2018.
- [8] P. Zhang, B. Gu, J. Zhou, and L. Wei, “On hydrodynamic lubrication characteristics of ferrofluid film in a spiral groove mechanical seal,” *Industrial Lubrication and Tribology*, vol. 70, no. 9, pp. 1783–1797, 2018.
- [9] Z. Wang and D. Li, “Theoretical analysis and experimental study on loading process among stages of magnetic fluid seal,” *International Journal of Applied Electromagnetics and Mechanics*, vol. 48, no. 1, pp. 101–110, 2015.
- [10] S. Zhao, Q. Sheng, S. Lin, F. Zhang, and L. Jiao, “The model of seal mechanism for magnetic fluid and related experimental study,” *Mechanika*, vol. 22, no. 4, pp. 260–264, 2016.
- [11] M. Szczech and W. Horak, “Numerical simulation and experimental validation of the critical pressure value in ferromagnetic fluid seals,” *IEEE Transactions On Magnetics*, vol. 53, no. 7, pp. 1–5, 2017.
- [12] M. Szczech, “Experimental study on the pressure distribution mechanism among stages of the magnetic fluid seal,” *IEEE Transactions on Magnetics*, vol. 54, no. 6, pp. 1–7, 2018.
- [13] X. L. Yang and D. C. Li, “Experimental investigation of diverging stepped magnetic fluid seals with large sealing gap,” *International Journal of Applied Electromagnetics and Mechanics*, vol. 50, no. 3, pp. 407–415, 2016.
- [14] X. Yang, P. Sun, F. Chen, F. Hao, D. Li, and P. J. Thomas, “Numerical and experimental studies of a novel converging stepped ferrofluid seal,” *IEEE Transactions on Magnetics*, vol. 55, no. 3, 2019.
- [15] X. Yang, F. Hao, W. Xu et al., “Leakage path study of a diverging stepped magnetic fluid seal with large gap,” *International Journal of Applied Electromagnetics and Mechanics*, vol. 60, no. 3, pp. 327–335, 2019.